PRECIPITATION ESTIMATION FROM REMOTELY SENSED INFORMATION USING ARTIFICIAL NEURAL NETWORK – CLOUD CLASSIFICATION SYSTEM

By

Yang Hong

A Dissertation Submitted to the Faculty of the

DEPARTMENT OF HYDROLOGY AND WATER RESOURCES

In Partial Fulfillment of the Requirements
For the Degree of

DOCTOR OF PHILOSOPHY
WITH A MAJOR IN HYDROLOGY

In the Graduate College

THE UNIVERSITY OF ARIZONA

2003

THE UNIVERSITY OF ARIZONA ®
GRADUATE COLLEGE

As members of the Final Examination Committee, we certify that we have read the dissertation prepared by Yang Hong

entitled

Precipitation Estimation from Remotely Sensed Information using Artificial Neural Network -- Cloud Classification System

and recommend that it be accepted as fulfilling the dissertation requirement for the Degree of doctor of Philosophy

Dr. Soroosh Sorooshian	Date 10/16/03
Dr. W. James Shuttleworth	Date 10/15/03
Dr. Xiaogang Gao	Date 10/20/2003
Dr. Stuart Marsh	Date 10/16/03
Dr. Alfredo R. Huete	Date

Final approval and acceptance of this dissertation is contingent upon the candidate's submission of the final copy of the dissertation to the Graduate College.

I hereby certify that I have read this dissertation prepared under my direction and recommend that it be accepted as fulfilling the dissertation requirement.

Dissertation Director
Dr. Soroosh Sorooshian — Date 10/16/03

STATEMENT BY AUTHOR

This dissertation has been submitted in partial fulfillment of requirements for an advanced degree at The University of Arizona and is deposited in the University Library to be made available to borrowers under rules of the library.

Brief quotations from this dissertation are allowable without special permission, provided that accurate acknowledgement of source is made. Requests for permission for extended quotation from or reproduction of this manuscript in whole or in part may be granted by the head of the major department or Dean of the Graduate College when in his or her judgment the proposed use of the material is in the interests of scholarship. In all other instances, however, permission must be obtained from the author.

SIGNED: 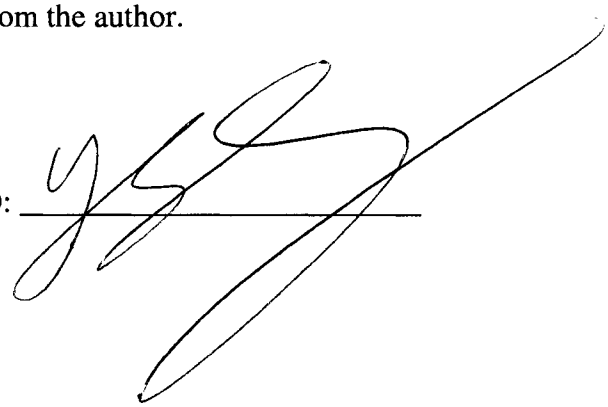

ACKNOWLEDGEMENTS

Many individuals have contributed to this research efforts presented here. This dissertation would be impossible to completed without their their encouragement, support, assistance, cooperation, and friendship. With great pleasure I would like to acknowledge these people.

The utmost thanks and respect are due to Professor Soroosh Sorooshian, my advisor and role model for his confidence and encouragement. His unparalleled expertise and scientific guidance was a pillar of strength to me on numerous occasions. It was his confidence on me, together with his consistent support that gave me the courage and opportunity to overcome obstacles and work on the way toward the completion of this dissertation.

I would like to express my sincere thank and appreciation to my co-advisor Dr. Kuolin Hsu and Dr. Xiaogang Gao for their thoughtful guidance and innumerable suggestions during the entire research effort. Without their support and advice, this work could not be done. My special gratitude and sincere thanks are also due to Professor Jim Shuttleworth, Professor Stuart Marsh, and Professor Alfredo R. Huete for serving on my examination committee, for their comments and assistance throughout the whole processes of degree-pursue. With my deep gratitude I would like to acknowledge Dr. Bisher Iman and Prof. Hoshin Gupta for their unique interesting comments and valuable help.

Thanks are due to my colligates and friends, Dr. Liming Xu, Dr. Jimin Jin, Felipe, Soni, Dr. Yuqiu Liu, Jialun Li, Jianjun Xu, Huilin Yuan, Park, Wolfgang, Ali, Koray, Christie, Terrie, Kim, ..., and numerous other individuals' help and suggestions. My special gratitude and thanks are due to my long time roommate, Kevin A. Dressler, for his very nice attitude on answering countless questions and helps.

Finally, this dissertation is dedicated to my parents, Benyu Chen and TingZhao Hong, for their guidance and patience in teaching me to find the strength within me and to be able to fight with difficulties to reach to my goals. I am very deeply grateful to those dearest to me, my siblings, my niece and nephew, and my girlfriend. I love you all.

The author also thanks for the financial support for this research is from NSF STC for Sustainability of semi-Arid Hydrology and Riparian Areas (SAHRA) (grant EAR-9876800), NASA-EOS (grant NA56GPO185) and NASA-TRMM (grant NAG5-7716). I would like to thank Dank Braithwaite for providing data processing for the research and James, Dean for their computation network support.

TABLE OF CONTENTS

LIST OF ILLUSTRATIONS

LIST OF TABLES

ABSTRACT

Precipitation estimation from satellite information (*VISIBLE, IR,* or *microwave*) is becoming increasingly imperative because of its high spatial/temporal resolution and board coverage unparalleled by ground-based data. After decades' efforts of rainfall estimation using IR imagery as basis, it has been explored and concluded that the limitations/uncertainty of the existing techniques are: (1) pixel-based local-scale feature extraction; (2) IR temperature threshold to define rain/no-rain clouds; (3) indirect relationship between rain rate and cloud-top temperature; (4) lumped techniques to model high variability of cloud-precipitation processes; (5) coarse scales of rainfall products.

As continuing studies, a new version of Precipitation Estimation from Remotely Sensed Information using Artificial Neural Network (PERSIANN), called Cloud Classification System (CCS), has been developed to cope with these limitations in this dissertation. CCS includes three consecutive components: (1) **a hybrid segmentation algorithm**, namely Hierarchically Topographical Thresholding and Stepwise Seeded Region Growing (HTH-SSRG), to segment satellite IR images into separated cloud patches; (2) **a 3D feature extraction procedure** to retrieve both pixel-based local-scale and patch-based large-scale features of cloud patch at various heights; (3) **an ANN model**, Self-Organizing Nonlinear Output (SONO) network, to classify cloud patches into similarity-based clusters, using Self-Organizing Feature Map (SOFM), and then calibrate hundreds of multi-parameter nonlinear functions to identify the relationship between every cloud types and their underneath precipitation characteristics using Probability Matching Method and Multi-Start Downhill Simplex optimization techniques.

The model was calibrated over the Southwest of United States (100°-130°W and 25°-45°N) first and then adaptively adjusted to the study region of North America Monsoon Experiment (65°-135°W and 10°-50°N) using observations from Geostationary Operational Environmental Satellite (GOES) IR imagery, Next Generation Radar (NEXRAD) rainfall network, and Tropical Rainfall Measurement Mission (TRMM) microwave rain rate estimates. CCS functions as a distributed model that first identifies cloud patches and then dispatches different but the best matching cloud-precipitation function for each cloud patch to estimate instantaneous rain rate at high spatial resolution (4km) and full temporal resolution of GOES IR images (every 30-minute).

Evaluated over a range of spatial and temporal scales, the performance of CCS compared favorably with GOES Precipitation Index (GPI), Universal Adjusted GPI (UAGPI), PERSIANN, and Auto-Estimator (AE) algorithms, consistently. Particularly, the large number of nonlinear functions and optimum IR-rain rate thresholds of CCS model are highly variable, reflecting the complexity of dominant cloud-precipitation processes from cloud patch to cloud patch over various regions. As a result, CCS can more successfully capture variability in rain rate at small scales than existing algorithms and potentially provides rainfall product from GOES IR-NEXARD-TRMM TMI (SSM/I) at 0.12°x0.12° and 3-hour resolution with relative low standard error (~=3.0mm/hr) and high correlation coefficient (~=0.65).

CHAPTER 1

RAINFALL ESTIMATION FROM SATELLITES

This chapter is intended to introduce the problem and motivation first, followed by literature review section that was divided into three portions to enhance the understanding of the relevant satellite-based rainfall algorithms. After a brief discussion on the basic concept of lumped model to justify the need for developing a cloud patch-based distributed rainfall model, the objectives of this study are identified and enumerated in Section 1.4, followed by the organization and scope of this dissertation.

1.1Problem Definition and Motivation

1.1.1 Satellite-based vs. Ground-based Rainfall Observation

Precipitation plays a critical role in global energy and mass exchange and motion system. The magnitude of rainfall and its distribution over space and time is one of the most important forcing variables in hydrological and meteorological models. Therefore, accurate measurement of precipitation at different spatial and temporal resolutions is invaluable for a variety of scientific applications. There usually exist two major types of techniques of precipitation observations: (1) ground-based observations, including gauge and radar; (2) satellite-based observations, such as satellite infrared-derived or microwave-derived rainfall estimates.

Rain gauge, as the conventional rainfall observation technique, is the only instrument to give direct measurements of rainfall. Rain gauge provides the best available 'point' measurements of precipitation, however, it may introduce considerable error to extrapolate point values to area-averaged rainfall due to the limitations of the gauge network and the high variation of rainfall field over space and time (Hendrickson-Michaud and Sorooshian, 1993). The development of radar has dramatically increased our ability of acquiring the measurements of rainfall over land. Radar observations are similar to satellite estimation in that they give "snapshot" values in space with high temporal and spatial resolution (~1km and 5~30 minutes). But the disadvantage in using radar data is that they are themselves indirect estimates of rainfall, and are prone to errors of calibration, attenuation, anomalous propagation, etc.

However, both the gauge and radar data availability are limited on land. Radar data are very limited to below 2 km Above Ground Level (AGL) over much of the United States, especially in the West (Maddox et al., 2002). The limitations and impracticality of rain gauge and weather radar network inhibit us from acquiring the temporal/spatial distribution of global precipitation.

Recent advances in rainfall estimation from satellite imagery have been driven largely by two interconnected factors. First, there is the lack of ground-based precipitation measurements over most of the earth's surface. The second factor is the ever-increasing demand by global-scale climate, weather, hydrologic, and water resources studies for more accurate, higher resolution, and longer-duration global precipitation datasets.

Rainfall estimates from satellite data, being area-averaged estimates, are widely used to initialize and validate meteorological models and are the major components of global climatological studies in regions where rainfall measurements are not available from rain gauge and radar. Currently, the precipitation measurements from space borne meteorological satellites have become the only practical means to obtain global coverage of rainfall at near-continuous high spatial resolution.

Since the 1960s, rainfall estimates from satellite imagery have become increasingly defined by the development of satellite technology. In general, there are two types of meteorological satellites: polar-orbiting and geostationary. Polar-orbiting satellites revolve around the Earth from pole to pole. On the other hand, geostationary satellites are stationed so that the satellites are relatively motionless to observers on the Earth at near-continuous temporal resolution. Accordingly, there are two primary sensor data types resulting in two approaches for satellite sensor rainfall measurement: thermal Infrared (IR) and Visible data from geostationary satellite platform such as Geostationary Operational Environmental Satellite (GOES) and passive microwave (MW) radiances from polar-orbiting platforms such as Special Sensor Microwave Imager (SSM/I) and Tropical Rainfall Measuring Mission (TRMM). The first one combines IR and Visible data, called IR/VIS approach and the second approach is called MW rainfall algorithm. In this study, we use the IR algorithms to denote both IR approaches and IR/VIS approaches because the lack of visible data at night has generally restricted to the use of IR data.

1.1.2 Overviews of IR and MW Rainfall Estimation

IR methods were among the first to arrive historically in remote sensing of rainfall estimation (Arkin and Meisner, 1987; Adler and Negri, 1988; Wu et al., 1985). The general assumptions underlying all IR algorithms are that colder cloud tops translate into thicker precipitating clouds, and that these clouds are generally the ones which produce significant rainfall at the surface. The majority of algorithms estimate rainfall by using infrared (IR) images from geostationary satellites because the strength of this approach is that geosynchronous satellites provide measurements with extensive coverage of the earth at relatively high spatial and temporal resolution and continuity.

The reader should keep in mind that the GOES IR data is responding to cloud-top temperature, rather than hydrometers distribution within cloud. Though IR algorithms have been benefited from excellent temporal and spatial sampling imagery from geostationary satellite, but the quantity being sensed from IR radiometers (cloud-top temperature) is indirectly connected to precipitation, particularly at small spatial scales.

In contrast, passive MW sensors with moderate spatial resolution are located only on polar-orbiting satellites, which visit any particular location on the earth surface twice a day at best. Passive MW sensors have the ability to penetrate into the clouds and, hence, the instantaneous rainfall measurements can be derived using radiative transfer models of emission-absorption process within the hydrometeor column.

Although satellite-borne microwave sensors provide more accurate estimates of instantaneous rain rate than IR rainfall algorithms currently, they only provide temporal

resolution twice per day at high latitude and daily coverage over the tropics because the instruments are mounted on low-altitude polar-orbiting satellites. This results in potential temporal sampling errors when attempting to construct longer-term rainfall estimations from these observations (Adler et al. 1993; Ferraro et al. 1999).

1.1.3 Motivation for Current Research

A long time series of precipitation is needed to support a variety of studies, including global change, surface hydrology, and numerical weather and climate model initialization and validation. The World Climate Research programme (WCRP) established the Global Precipitation Climatology Project (GPCP) that is succeeding in producing precipitation estimates on a monthly 2.5^{o}x2.5^{o} lat/long grid over two decades and continuing a routine production a few months after real time. Only since 1996 have daily 1^{o}x1^{o} satellite /IR products using GOES Precipitation Index been archived under the auspices of the Global Energy and Water Cycle Experiment (GEWEX) program (GEWEX, 1996). Because of the lack of fine-scale precipitation data over extended areas, numerous applications remain stymied.

A great deal of research has focused on the development of methods that exploit the strengths of data from both geostationary and polar-orbiting satellites. A number of authors (Adler, 1993, 1994; Vicente and Anderson, 1994; Manobiano et al, 1994; Kummerow and Giglio, 1995; Huffman et al., 1995; Xie and Arkin, 1996; Xu et al., 1999; Sorooshian et al., 2000; Huffman et al., 2001; Todd et al., 2001; Miller et al., 2001;

Kuligowski, 2002;) have made efforts to combine the strengths of both IR and MW by using the MW-based estimates to adjust the GOES-based estimates, mainly for long-term precipitation estimation at coarse spatial resolution. Their results also indicated the potential for developing improved rainfall estimates at shorter time period and higher spatial resolution.

Global precipitation system is distributed over space and time due to the motion of global energy/water and heterogeneity of earth surface. This complicates the task of developing instantaneous surface rainfall estimates at fine pixel scale and, therefore, existing pixel-based algorithms resort to considerable spatial and temporal aggregation to improve the statistical accuracy of the rainfall product. On the contrary, cloud patch-based approaches include synoptic information to screen no-rain clouds. However, the high variability of cloud system and the computational expense on the processing of cloud patch information challenge the application of cloud patch-based algorithms.

Experiments have shown that different cloud types may have similar cloud-top temperatures but are associated with significantly various amounts of rainfall at the ground (Sorooshian et al., 2000), which motivates this paper to classify cloud types and investigate the diverse relations between rain rate distribution and cloud types. Additionally, accurate long-term rainfall estimates at scales (sub-daily estimates at resolutions of 1^{o} down to pixel scale) smaller than the existing coarse resolution products would be highly desirable. Specifically, the motivations initializing this study are:

(a) The need of reliable global rainfall products at higher spatial and temporal resolution than the existing rainfall estimation algorithms;

(b) The limitation of pixel-based rainfall estimation algorithms;

(c) The uncertainty of IR threshold to define rain/no-rain clouds;

(d) The limitations of current segmentation approaches that separate GOES IR imagery into cloud patches;

(e) The necessity to incorporate more informative cloud features at both local-scale and large-scale;

(f) The need of a distributed rainfall estimation model that employs Artificial Neural Network (ANN) to simulate diverse clouds-precipitation processes.

As a matter of fact, these limitations and uncertainty have inhibited further improvement of rainfall estimates from satellites in terms of accuracy and spatial/ temporal resolutions required by current climatological and hydrological research. The requirements of combined MW/IR algorithms that are able to address these limitations and uncertainty, and the need of accurate rainfall estimates with higher spatial and temporal resolutions have motivated this study.

The reminder of this Chapter reviews the satellite-based rainfall algorithms in Section 1.2. Section 1.3 introduces the two categories of rainfall estimation approaches: lumped vs. distributed rainfall estimation models. Section 1.4 presents the objectives of this study. Finally, Section 1.5 briefs the arrangement of chapters in this document.

1.2 Review of Satellite Rainfall Estimation Algorithms

A variety of techniques for precipitation estimation are increasingly defined by the availability of the large amount of latest data from satellites. While most polar-orbiting meteorological satellites have MW, IR, and Visible (VIS) sensors, currently geostationary satellites have only VIS and IR sensors on board due to the weak signal of MW resulted from long distance between the satellites and the Earth's surface. Obviously, VIS measurements are not available during nighttime. Therefore, two primary satellite data, thermal IR and passive MW data, are widely used in the filed of long-term operational satellite rainfall estimation.

1.2.1 IR-Based Satellite Rainfall Estimation Algorithms

A good review of IR rainfall estimation methods is provided in Arkin and Ardanuy (1989), Hsu (1996), and Xu (1997). In general, the strength of IR approaches is that geosynchronous satellites provide measurements with extensive coverage of the earth at relatively high spatial and temporal resolution. All these approaches attempt to correlate the surface rain rate (RR) with IR cloud-top brightness temperatures (IR_{Tb}). From viewpoint of information system, IR algorithms are generally classified into three types: pixel-based, window-based, and patch-based. Figure 1.1 illustrates the IR information extraction from pixel-based, window-based, or patch-based methods. Several examples of these algorithms may clarify this classification further.

1.2.1.1 Pixel-based algorithms

(a) GPI

A good example of pixel-based algorithms is the GOES (Geostationary Operational Environment Satellite) Precipitation Index (GPI) developed by Arkin and his colleagues (Arkin, 1979; Richards and Arkin, 1981; Arkin and Meisner, 1987). GPI is a simple IR algorithm based on the observation of Richards and Arkin (1981) that rainfall is strongly correlated with fractional coverage of cold cloud pixels when averaged over large area (around 2.5^{o} x 2.5^{o}) and/or time. Equation 1.1 is the formula of GPI.

$$GPI=F_cGT \qquad (1.1)$$

Where F_c is the fractional coverage of IR pixels < 235K over a reasonable large domain (50 x 50 km and larger), G is the GPI coefficient equal to 3.0mm/hour, and T is the number of hours over which F_c was compiled. Numerous studies have shown that the GPI yields useful results in the tropics and warm-season extra-tropics at climatological scales (Ebert et al., 1996). Atlas and Bell (1992) mention that the GPI is essentially an area-time integral approach to rainfall estimation. The major advantage of GPI technique is that it is based on IR data that is available frequently over most areas of the globe from geostationary and polar orbiting satellites. The major weakness of the method is that estimation of precipitation from cloud-top temperature is relatively far removed from the physics of precipitation generation process. Monthly precipitation products of GPI for 40N - 40S for the period January 1986 through the present month are available from the

National Oceanic and Atmospheric Administration (NOAA) National Weather Service (NWS) Climate Prediction Center (CPC) website: http://www.cpc.ncep.noaa.gov/products/global_precip/html/wpage.gpi.html.

(b) Auto-Estimator (AE)

In 1998, Vicente et al. presented an Auto-Estimator (AE) algorithm, which utilizes the power law curve to fit IR cloud top-temperature and Rain rate relationship (IR_{Tb}-RR) then adjusted by factors such as temperature gradient. This method is computational easy but suffering in the subjectively selection of data pairs to fit the power law curve and implementation of the single curve into complex cases.

(c) GMSRA

Mamoudou (2001) proposed a GOES Multi Spectral Rainfall Algorithm (GMSRA) that combines information from five GOES satellite channels to optimize the identification of raining clouds and then calibrate rain rate for each indicated raining cloud referenced by its cloud-top pixel temperature.

1.2.1.2 Window-based algorithms

(a) Wu et al. algorithm

As a result of adapting image process techniques, a large body of IR-based algorithms is window-based. In a relatively complex algorithm developed by Wu et al. (1985), 24 features (Table 1.1) are used to retrieve rainfall. Theses features include radiance and texture features computed on windows of both IR imagery and visible

imagery. Pattern recognition techniques and a decision tree are applied to classify clouds into three categories: no rain, light rain, and heavy rain. The window size used in the algorithm is 20 km × 20 km. Many of these features demonstrated their effectiveness in describing rainfall properties, and the algorithm has shown its merit in real applications (Lee et al., 1991).

Table 1.1 Features Used To Characterize IR Cloud Images in Wu et al. algorithm

Feature Number	Features
	Radiance
1	Mean grey level
2	Standard deviation of grey level
3	Maximum grey level
4	Minimum grey level
5	Maximum/minimum grey level ratio
6	Grey level range
	Texture
7	Edge strength per unit area
8	Maximum mean within 4 directions
9	Maximum contrast within 4 directions
10	Maximum angular second moment within 4 directions
11	Maximum entropy within 4 directions
12	Mean value of mean within 4 directions
13	Mean value of contrast within 4 directions
14	Mean value of angular second moment within 4 directions
15	Mean value of entropy within 4 directions
16	Edge strength per unit
17-20	Same features as 8-11 with different separation
21-24	Same features as 12-15 with different separation

(b) PERSIANN

Precipitation Estimation from Remotely Sensed Information using Artificial Neural Network (PERSIANN) is another pixel/window-based approach developed at The University of Arizona (Hsu et al., 1997). A modified Counter Propagation Network (MCPN) is employed to map cloud properties to rainfall. Table 1.2 shows that the inputs

to the MCPN are derived from windows of 3 or 5 sizes to enhance information. By using an updating technique and increasing input information from windows of various sizes, the PERSIANN approach has produced considerably reliable rainfall estimates at daily 1^{o} x 1^{o} resolutions (Sorooshian et al., 2000).

Table 1.2 Inputs to PERSIANN Algorithm

No.	Inputs
1	IR brightness temperature on the calculated pixel
2	Mean IR brightness temperature with window size of 3 x 3 pixels
3	Standard deviation of IR brightness temperature with window size of 3 x 3 pixels
4	Mean IR brightness temperature with window size of 5 x 5 pixels
5	Standard deviation of IR brightness temperature with window size of 5 x 5 pixels
6	Surface type

1.2.1.3 *Cloud patch based algorithm*

(a) GWT and NAWT algorithm

One early example of patch-based algorithms is the Griffith-Woodley Technique (GWT) (Griffith et al., 1978; Woodley et al., 1980). The cloud patch A_c is determined by applying the IR brightness temperature threshold at 253°K. The Negri-Adler-Wetzel Technique (NAWT) is a simplified version of GWT. The GWT must track the cloud patch through its lifetime to find the maximum cloud coverage area, A_m from a series of cloud area A_c, and then derive the rainfall volume. In NAWT, rainfall volume in each time period is assumed is:

$$R_{vol}=k.A_c \qquad (1.2)$$

Where k is a constant calibrated from the least square estimator. Using these simplifications, the R_{vol} can be derived at any instant snapshots instead of waiting till the end of cloud life cycle. Experiments show that NAWT produces comparable results to the GWT method.

(b) CST algorithm

An advanced example of patch-based algorithms is the Convective-Stratiform Technique (CST) by Adler and Negri (1988). This method was designed primarily to estimate deep convective rainfall by identifying convective cells and cirrus clouds with the measurement of *slope*: the temperature difference between cloud coldest pixel and the mean temperature of its neighboring pixels. Then, the rainfall volume is assigned to the convective cell with different rain rate to convective and stratiform components, starting from pixels with low IR temperature to pixels with high IR until the computed rain area is filled.

(c) Cloud Patch Analysis

Another sophisticated Cloud Patch Analysis (CPA) was proposed to estimate rainfall by removing large option of no-rain clouds from IR cloud imagery using an inductive decision tree to identify no-rain clouds (Xu, 1997). Instead of choosing fixed threshold 253^0K to delimit clouds, CPA calibrated the threshold from microwave rainfall and GOES IR data pairs to discriminate rain or no-rain cloud.

1.2.1.4 *IR algorithms summary*

All the above methods primarily attempt to enhance the effectiveness of the input information by reducing mapping **uncertainty** in IR_{Tb}-RR relationships. The uncertainty is largely due to the extreme variation of cloud in brightness, texture, size, etc. Pixel-based methods directly utilize the IR measurements of a single cloud pixel to estimate rainfall. The window-based algorithms consider not only the temperature of a pixel but also some features of the pixels around it—a window—i.e., those features present a "window" of information. The sizes of the selected windows may vary with different algorithms, but they are generally square. However, with much in common, the pixel and window-based algorithms both locally extract and partially utilize information of clouds, thus, these local information suffer inadequate accuracy and uncertainty to identify cloud types in larger scales. This complicates the task of developing instantaneous surface rainfall estimates at the fine temporal and spatial scales and, therefore, the pixel/window-based algorithms resort to accumulation over space and time to obtain reliable rainfall product.

On the contrary, the cloud patch based algorithms include synoptic cloud patch information to identify the cloud types and then to map the cloud-precipitation relations. However, the high variability of cloud system, the difficulty of cloud segmentation, and the computational expense on processing of cloud patch-based information challenge the application of this kind of algorithms.

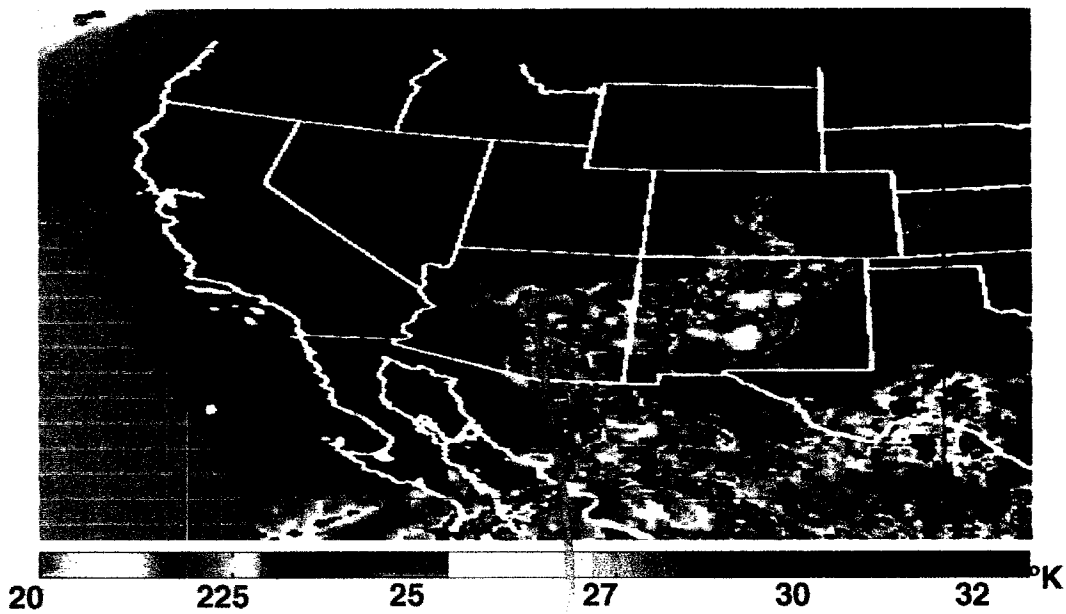

(a) GOES IR cloud image

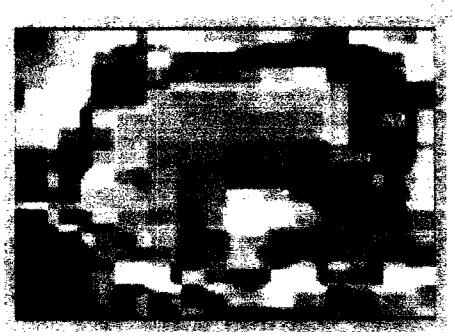

(b) Cloud patch-based synoptic-scale cloud information extraction

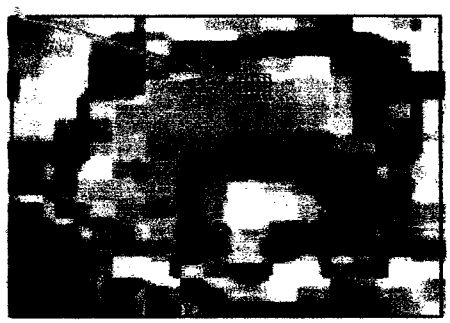

(c) Pixel or window-based local-scale cloud information extraction

Figure1.1 Pixel/window or patch-based information extraction from satellite imagery Note: pixel/window-based algorithms only retrieve local information, however, cloud patch-based algorithms extract the synoptic information.

1.2.2 Microwave-based Satellite Rainfall Estimation Algorithm

Microwave (MW) board channel is defined as the interval of wavelength from 1-10cm (300-3GHz). Compared to visible and IR images, which are only able to detect the radiation reflected or emitted from a cloud top, MW provides more direct and accurate instantaneous rainfall estimates because passive MW sensors have the ability to penetrate into the clouds and, hence, the instantaneous rainfall measurements can be derived using radiative transfer models of emission-absorption process within the hydrometeor column of clouds. The MW associated algorithms fall under three categories: emission, scattering, and the combination of emission and scattering.

Emission MW methods are also referred as lower frequency MW algorithms since they are based on the enhanced emission by raindrop at lower range of MW frequencies. Example of emission algorithms includes Ferrari & Marks (1995) and Berg & Chase (1992).

Scattering MW algorithms are also known as higher frequency MW methods because they are founded upon the attenuation through scattering of upwelling radiation at higher range of MW frequencies by overlying ice particles. The scattering methods can be founded in Adler et al. (1993), Ferrari et al. (1994), and Grody (1991).

The third type or MW algorithms offer a combination of emission and scattering components since the two approaches are somewhat complementary (Wilheit et al., 1991; Ferriday and Avery, 1994; Petty, 1994a,b).

Emission methods are the most physically direct algorithms with respect to the other two approaches, while scattering algorithms are more akin to IR techniques and are biased toward deep convective events. However, the primary disadvantage of using MW algorithms estimates is intermittent availability of estimates and moderate spatial resolution (two overpass a day at best and 12.5km for 85GHZ channel and 25km for 19GHZ and 37GHz in the Special Sensor Microwave Imager (SSM/I)).

1.2.3 Combined Microwave/IR Satellite Rainfall Estimation Algorithms

In summary, IR rainfall algorithms have excellent temporal and spatial sampling, but the physical quantity being sensed from IR radiometers is indirectly connected to surface rainfall. Satellite microwave sensors provide more accurate estimates of rain rate, but they suffer from temporal sampling for daily and monthly rainfall accumulation.

To take advantage of the relative accuracy of the MW estimates and the relative high sampling frequency of IR-based estimates, a number of researchers have developed techniques that combine MW and IR when both are available and then apply adjustments to IR-based estimates at the temporal resolution of IR data, hereafter referred as MW/IR algorithms. These MW/IR approaches fall under four general categories; adjustments of GPI, data merging, probability-matching methods, and regression techniques. The following is the detailed description of the four general categories of MW/IR algorithms.

(a) Adjustments of GPI

Adler et al. (1993, 1994) adjusted the monthly GPI total according to ratio of SSM/I-based rain rate estimates to the GPI IR-based rain rate for 1-month period of coincident pixels. Kummerow and Giglio (1995) used MW rain rate estimates to calibrate the two parameters of GPI-the optimal threshold IR_{Tb} for defining raining area, and the mean rain rate within these areas-to make the total area and volume of the GPI estimates match those of the corresponding MW-based estimates. Xu et al. (1999) calibrated the GPI parameters to minimize total error rather than to preserve area and volume.

(b) Data Merging techniques

Huffman et al. (1995) merged monthly AGPI estimates with MW estimates and rain gauge using their respective estimates error to determine their optimal merging weights. Xie and Arkin (1996) linearly combined the satellite-based estimates and model forecasts to minimize the random error (defined by comparison with rain gauge), and then used the rain gauge analysis to remove the bias in the results locations.

(c) Probability-matching methods (PMM)

Manobiano et al. (1994) used PMM based on the work of Atlas et al. (1990) fitting the cumulative distribution function (CDF) of SSM/I rain rate and IR_{Tb} values and then fitting an equation to the resulting relationship. These equations were interpolated in time for those GOES images that occur between the SSM/I passes, and a weighting of the IR-Based and SSM/I rain rates was also performed to improve the temporal smoonthness of the estimates. Turk et al. (1998) used a similar approach, but keeping the calibration fixed in time and did not weight the resulting estimates with IR-based rates. Anagnostou et al.

(1999) used CDF matching to calibrate separate rain rates for convective and stratiform regions. Todd et al. (2001) also used PMM to match a full month of MW/IR data over 1^{o}-2.5^{o} to develop the CDF curves. Huffman et al. (2001) produced the global precipitation of One Degree Daily (1DD) rainfall products using technique called Threshold-Matched Precipitation Index (TMPI).

(d) Regression techniques

Vicente and Anderson (1994) used multiple linear regression curves to relate SSM/I rain rate estimates to IR_{Tb} values for all of GOES pixels within an SSM/I pixel. To enhance the ability of the technique to handle the nonlinear relationship between IR and rain rate, the data sets were broken up into different IR temperature interval and separate linear regression equation were derived for each interval. Miller et al. (2001) regress the minimum IR_{Tb} within an SSM/I footprint to the SSM/I rain rate to calibrate both a minimum IR_{Tb} rain/no-rain threshold and a regression-based linear relationship with rain rate. Kuligowski (2002) proposes the Self-calibrating multivariate precipitation retrieval (SCaMPR) algorithm to utilize multi-channel IR and satellite-based rainfall data to calibrate linear IR_{Tb}-RR relationship after separating rain/no-rain pixels.

From the viewpoint of function fitting, the adjustment of GPI behaves like a binary function, which carry less amount of information than simple linear regression. Linear, multiple linear, and adjusted linear regression functions all suffer a tendency to underestimate heavy rain rates. Miller et al. (2001) suggested that one possible solution to

this problem is to convert the linear regression into a nonlinear function. Additionally, the nature of regression methods confines its reliable performance only after accumulation over space and time. A distributed model with great number of function regressions is needed to capture the high variation and complexity of dominant cloud microphysical processes at small temporal and spatial scales.

1.3 Lumped vs. Distributed Rainfall Estimation Model

Most of rainfall estimation algorithms fall under two general categories: lumped and distributed model. The GPI (Arkin et al., 1981), AGPI (Adler et al., 1993), UAGPI (Xu et al., 1999), and MIRRA (Miller et al., 2001) all fall under lumped category for they only apply one IR_{Tb}-RR functions to the whole region though with adjustment. GPI is a typical lumped approach since its fixed coefficient of 3mm/hr and raining IR_{Tb} threshold 235K apply regardless of the locations or seasons. The AGPI is a monthly adjustment of GPI; and the MIRRA is a daily adjustment of basic linear IR_{Tb}-MW rain rate relationship. The lumped rainfall algorithms essentially are an area-time integral (ATI) approach. The rain estimates from the lumped techniques suffer one common feature: algorithms cannot reflect the high variation of precipitating clouds and, therefore, model performance relies on the effects of accumulation of temporal and spatial scale to cancel off the estimation errors.

Global precipitation system is distributed over space and time due to the motion of global energy/water and heterogeneity of earth surface. The relation between cloud-top

temperature and surface rainfall rate varies with storm type, season, location, low-level environment, and many other factors that make it impossible to be accurate with a lumped model. Figure 1.2a shows that the relationships between satellite IR temperature and surface rain rate can vary significantly over space and time. More importantly, Figure 1.2b shows diverse relationships exist from cloud patch to patch. As a closer look, Figure 1.3 illustrates the evolution of a cloud life cycle (top) and its corresponding surface rainfall (middle), followed by the calibrated IR_{Tb}-RR functions (bottom). The IR_{Tb}-RR show large variation of precipitation characteristics exists even at different developing stages of same cloud.

It is evident that development of a cloud patch-based distributed rainfall estimation model is needed to capture the large variability of cloud-precipitation relations in order to estimate high quality precipitation at small scales. This is another important objective of this study.

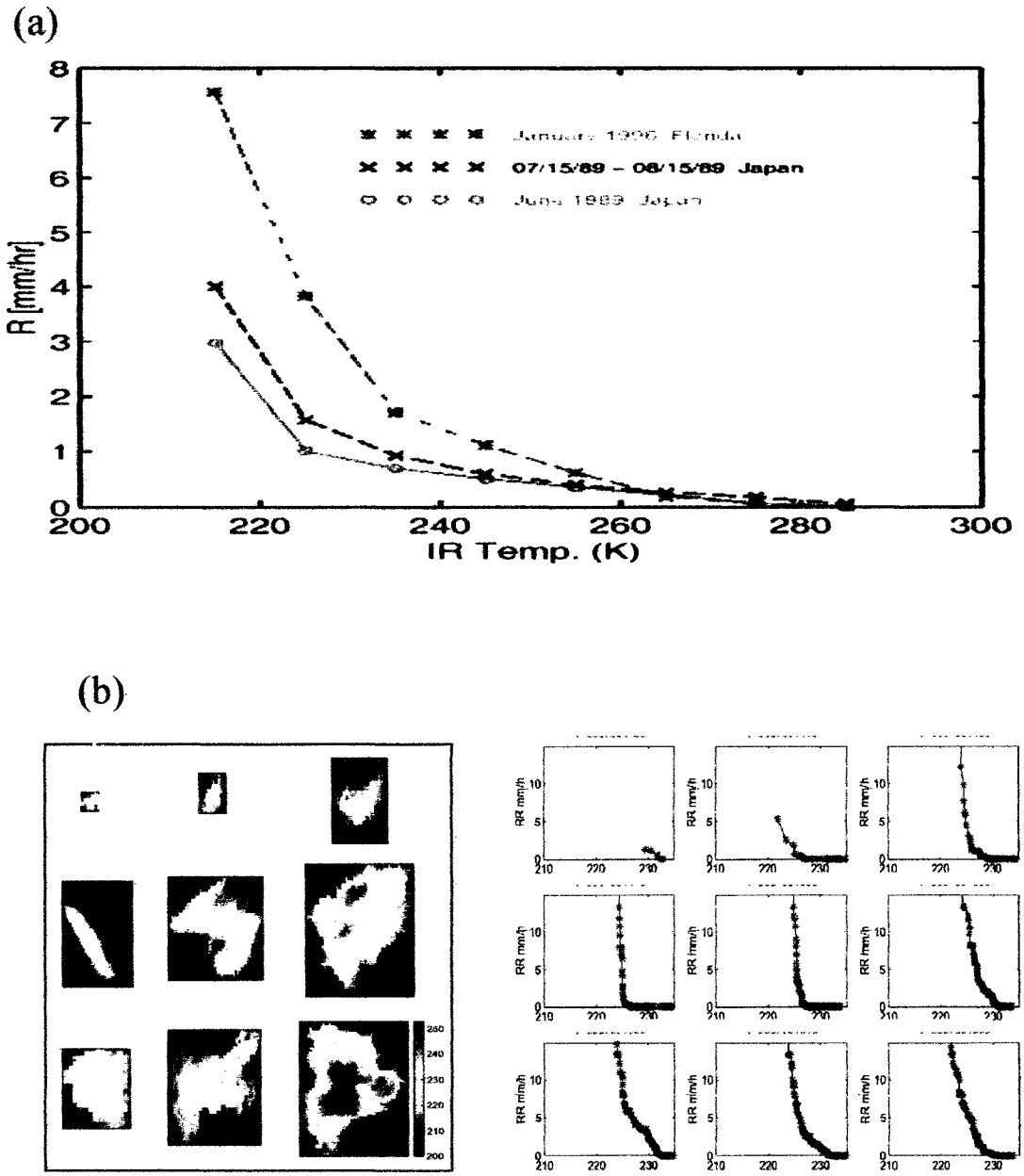

Figure 1.2. Diverse IR temperature and rain rate relationship (IR_{Tb}-RR).

(a): Monthly averaged IR_{Tb}-RR in three case studies (sources: Hsu, 1997)

(b): Cloud patch IR_{Tb}-RR for individual clouds

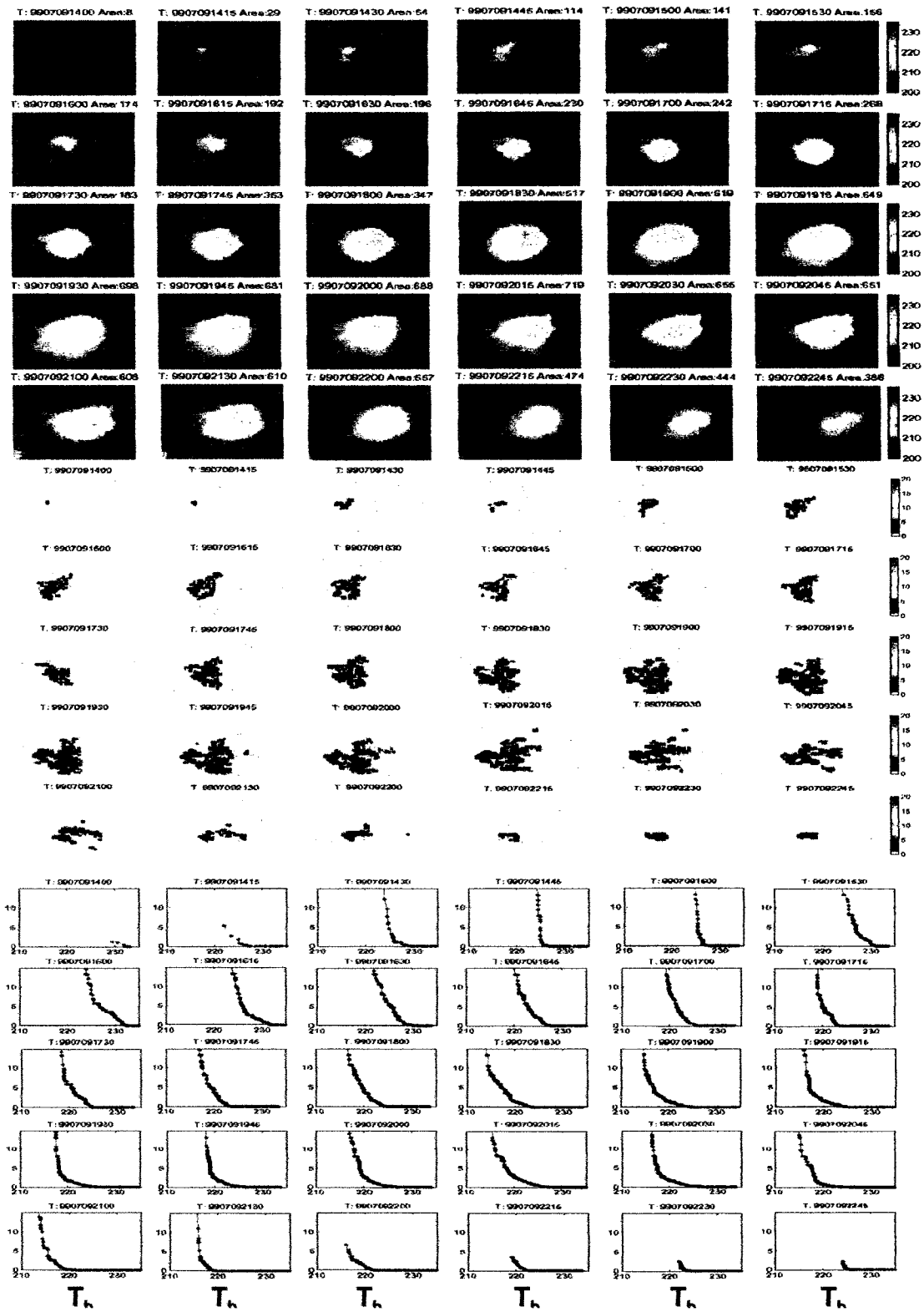

Figure 1.3 Evolution of a cloud life cycle and its corresponding precipitation characteristics. **Top**: cloud evolution; **Middle**: underneath surface rainfall; **Bottom**: brightness temperature-rain rate (mm/hr) curves for each stage.

1.4 Objectives of Current Study

Our overall goal is to develop a distributed MW/IR rainfall algorithm using the strength of ANN to simulate the diverse relationships between various precipitating clouds and surface rainfall in a self-adaptive operational mode. Hence, the proposed rainfall estimation model will be required to posses several important capabilities as listed below:

(1) It must be able to process large amounts of geosynchronous IR and polar-orbiting Microwave Imagery in a real-time mode (because of the huge amount of high spatial and temporal resolution satellite imagery at large coverage);

(2) It must include a sophisticated procedure to segment IR imagery and extract cloud feature information in an automatic mode;

(3) It must function not only as an "analyzer" to classify large amount of cloud patches into well-organized map of cloud types but also as auto-approximator to determine under which conditions the classified satellite cloud clusters are related to the surface rain rates and self-calibrate the highly nonlinear relationships;

(4) It must behave as a distributed model that dispatches the best-fitting function in response to different type of clouds in order to capture the high variation of cloud-precipitation processes at small temporal and spatial scale;

(5) It must possess a "self-calibrating" ability that collects data for an elapsed time period and determines an appropriate function between the predicator(s) of interest and the

observed rain rate, then applies this approximation to subsequent time periods till the calibration is adaptively updated;

(6) It must possess a "self-learning" ability, which can update parameters to improve the model performance with new observations. This feature will enable model to trace the seasonal and regional variability of the precipitation climatoloty and improve the model's transferability.

Hsu et al. (1999, 2002) developed a Self-Organizing Linear Output (SOLO) network for rainfall predication and stream flow forecasting. In this research, a new ANN network, named Self-Organizing Nonlinear Output (SONO), was developed as the core building block of the proposed rainfall estimation model-Cloud Classification System (CCS) to produce rainfall at fine temporal and spatial scale. The CCS includes three consecutive modules:

(A) A hybrid cloud segmentation algorithm, Topographically Hierarchical Thresholding and Stepwise Seeded Region Grow with fast merging (THT-SSRG), which separates cloud imagery into distinctive cloud patches such that each cloud patch behaves like an independent precipitation system;

(B) A cloud feature selection procedure that extracts the precipitation-informative feature information at various cloud height levels;

(C) An ANN module (SONO) that classifies cloud patches into a number of well-organized cloud clusters using Self-Organizing Feature Map (SOFM) and then self-

calibrate the nonlinear relations between the cloud types and their precipitation characteristics.

Module C, SONO, is the core component of CCS and the module A and B are the model preprocessor, which provides cloud patch information and enables CCS to estimate rainfall at patch level instead of pixel level.

As a matter of fact, CCS is a new version of PERSIANN (Hsu et al., 1997, 1999) system. The major difference between the two models includes (1) the input information for CCS is cloud patch-based features vs. pixel/window temperature for PERSIANN; (2) more sophisticated IR imagery preprocessors for CCS than PERSIANN (besides the data normalization and regularization preprocessing, CCS includes module A-cloud segmentation and module B-cloud classification); (3) Modified CPN network or Self-Organizing Linear Output (SOLO) for PERSIANN vs. Self-Organizing Nonlinear Output (SONO) network for CCS; (4) Due to the displacement of pixel to pixel correspondence, PERSIANAN rainfall estimates only at 0.25^{o} x 0.25^{o} vs. CCS at 0.04^{o} x 0.04^{o} spatial scale.

The CCS model behaves as a distributed system with large number of organized cloud-precipitation functions (IR_{Tb}-RR). Each of the relation is derived from different types of clouds and their coincident passive MW rainfall data. Thus each of calibrated IR_{Tb}-RR functions corresponds to different types of clouds instead of a local region. Figure 1.4a shows the scatterplots of randomly selected instantaneous rain rate vs. IR_{Tb} at 0.04^{o} spatial scale from satellite image. Figure 1.4b illustrates the conceptual curves of

lumped rainfall models such as AGPI, linear (Miller, 2001), and nonlinear regression curves, are derived from the same dataset, respectively. Figure 1.4c is the conceptual illustration of a distributed rainfall estimation model, each approximation curve of which is dispatched to model the precipitation characteristics for a particular cloud patch.

From system viewpoint, a simple model inevitably oversimplifies an extremely complicated system. Through the use of methods that synthesize machine-learning and computer-based artificial intelligence techniques with the theory of precipitation processes and practical experience, we present the CCS model that is characterized by significant transience, heterogeneity, and variability to associate rainfall characteristics with the extremely complex and still imperfectly understood cloud system. CCS model also provides possibility to produce precipitation estimate at high spatial resolution because simple pixel-pixel corresponding relationship would lead to spatial displacement due to the long distance of the geostationary satellite from the Earth' surface.

(a) Scatter plots of IR temperature-rain rates

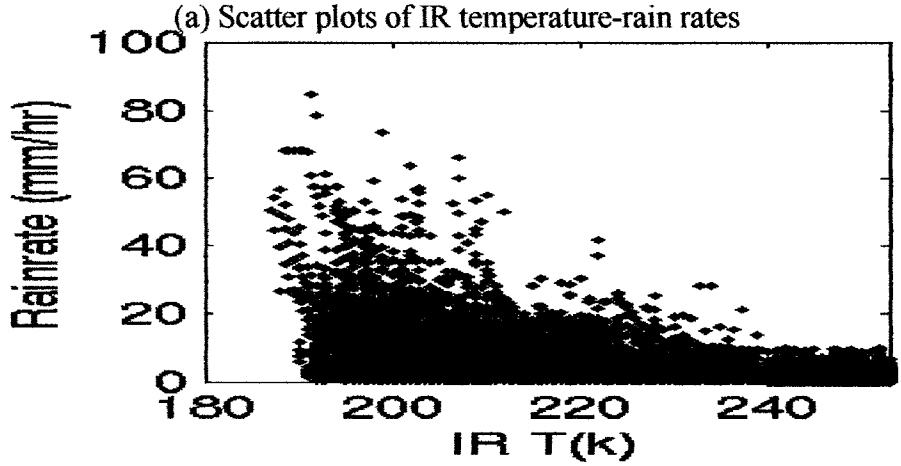

(b) Fitting methods from several lumped algorithms

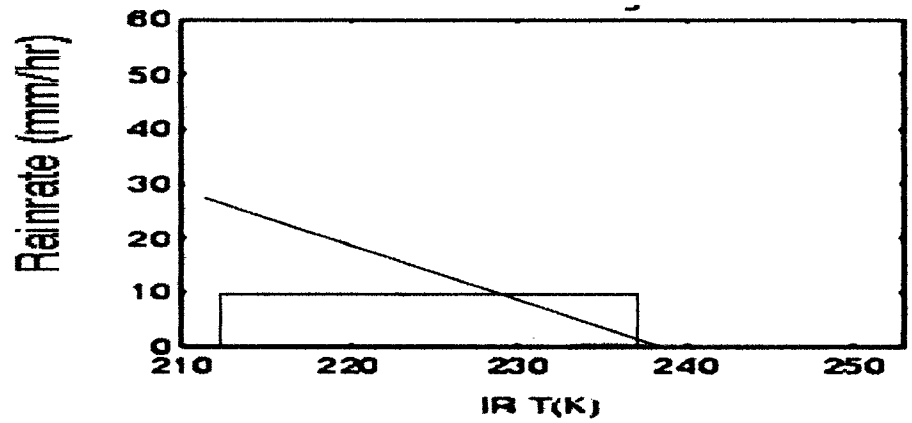

(c) Nonlinear fitting curves from a distributed model

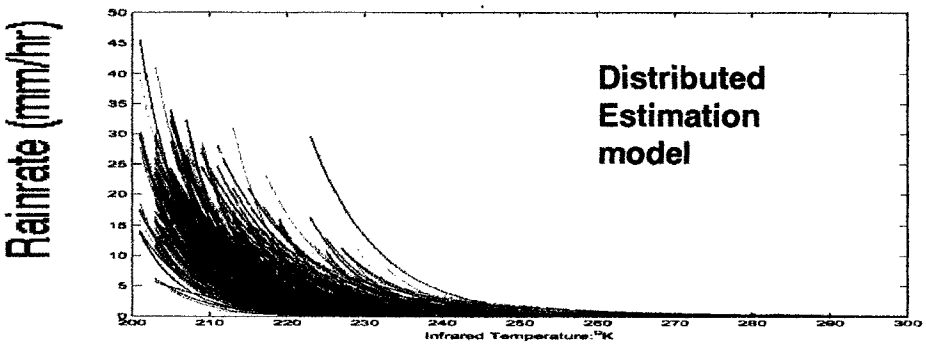

Figure 1.4 Illustration of lumped vs. distributed rainfall estimation model.
(a) Scatter plots of rain rate v.s. IR brightness temperature from training data
(b) Linear (black line), Nonlinear (red curve), and GPI related (blue block) lumped approaches;
(c) Conceptual curves from a distributed rainfall model to represent the high variation of cloud-precipitation relationship.

1.5 Organization of this Document and Scope

The structure of proposed CCS consists two major components: (1) two consecutive input preprocessors (cloud segmentation and cloud feature extraction) to provide cloud patch input information for SONO network; (2) SONO network to classify cloud patches and nonlinearly map the cloud-precipitation relations. The reminder of this document is organized as follows.

Chapter 2 briefly reviews the applications of Artificial Neural Networks (ANN) in hydrology with focus on precipitation first, followed by the description of methodology of the proposed model CCS, focusing on the SONO network. The depiction of the input preprocessors (Cloud Segmentation and Feature Extraction) required by SONO is kept to a minimum with more detailed presentation and implementation in Chapter 3.

The next phase of CCS model development is a primary case study of CCS conducted in the Southwest of United Sates to calibrate network parameters and validate the performance of CCS in Chapter 4. The data and criterion to evaluate model performance are also discussed in this chapter.

In Chapter 5, an adaptive mode of CCS adjusted by observations from TRMM microwave data, is elaborated. Comparison with other relevant algorithms is then devoted to the evaluation of model performance over a broad range of spatial and temporal scales.

Finally Chapter 6 summarizes CCS model and enumerates key contributions of this study, followed by recommendations for future direction of this research.

CHAPTER 2

CLOUD CLASSIFICATION SYSTEM (CCS) FOR RAINFALL ESTIMATION

2.1 Introduction

To date, there are numerous articles that extol the virtues of artificial neural networks (ANN) as computation tools and chalk up impressive performances over conventional techniques. ANN are now widely applied in a broad range of fields, including process control, image processing, signal processing, medical studies, financial predictions, power systems, and pattern recognition, time series forecasting (Croall and Masion, 1991; Tomas and Wyner, 1992; Chen and Khali, 1995; Kosko, 1992; Refenes et al., 1994; Saund, 1989; Schalkoff, 1992; Paola and Schowengredt, 1995; Suykens et al., 1996; Vemuri and Rogers, 1994; Serpico and Roil, 1995; Yoshihisa et al., 1995; Hsu et al., 1996; Govindaraju & Zhang, 2000; Bellerby et al., 2000).

Only during the last decade, researchers in hydrology have shown serious interest in this computational tool (Govindaraju et al. 2000). The ability to learn and generalize "knowledge" from sufficient data make it possible for ANN to solve large-scale complex problems and to apply in hydrology. Among the many ANN architectures proposed and explored in hydrology, the most widely used ones are multilayer feed forward networks (MFNN) (Werbos, 1974; Rumelhart et al., 1982), Self-organizing Feature Maps (SOFM) (Kohonen, 1982), Hopfield networks (Hopfield, 1982), and Counter Propagation

Networks (CPN) (Hecht-nielsen, 1987). Figure 2.1 shows a 3-layer MFNN structure and Figure 2.2 shows a CPN network. The SOFM is the second layer in CPN structure.

However, ANN has remained much like black-box empirical models incapable of explaining their reasoning in a comprehensible manner in most of the applications of ANN rainfall estimation model. For ANN to gain more acceptability and practical use, it is imperative that some part of the reasoning be imparted back to the user. A common ground for combining the advantages of ANN with some interpretation capability of network performance can be achieved by carefully defining the weights transfer functions and input-output functions in the sense of physical understanding. Hsu et al. (1997) designed a Modified CPN (MCPN) for the Precipitation Estimation from Remotely Sensed Information using Artificial Neural Network (PERSIANN) to obtain physically insightful information of weights in SOFM layer (FIG.2.3). However, the output of PERSIANN system is the linear summation of the weights of the linear Grossberg layer, which limits output space expansion of PERSIANN. Another limitation of PERSIANN architecture is that it is only suitable for pixel level rainfall estimation. Given an input pattern of cloud pixel, the output is that pixel's point estimate of rainfall. As matter of fact, these limitations have inhibited further improvement of rainfall estimates in terms of accuracy and spatial and temporal resolutions required by current climatological and hydrological research.

To overcome this limitation and extend PERSIANN to cope with cloud patch–based rainfall estimation from tremendous amount of satellite imagery, a Cloud Classification System (CCS) is developed to cope with satellite IR cloud patch-based information and

to calibrate the various cloud-precipitation relation for each cloud type. CCS consists of two major modules: (a) two consecutive preprocessors—Cloud Segmentation and Cloud Feature Extraction; (b) a Self-Organizing Nonlinear Output map (SONO) network. SONO is the core building block of rainfall estimation model—Cloud Classification System (CCS) proposed in this document.

The goal of this chapter is to give a brief description of application of ANN in hydrology with focus on precipitation estimation and to introduce SONO network for the proposed precipitation estimation model-CCS. The remainder of this chapter is organized as follows: Section 2.2 reviews the applications of artificial neural networks in hydrology, particularly in precipitation estimation. Section 2.3 briefs the structure and functionalities of Counter Propagation Network (CPN) and the Modified CPN (MCPN) implementation in PERSIANN rainfall estimation system. In Section 2.4, the purpose-designed rainfall estimation model-CCS, is presented in the order of data flow: Cloud Segmentation, Cloud Feature Extraction, SONO network (cloud classification and cloud-precipitation mapping). Section 2.5 addresses the training issues of CCS, particularly, the parameters calibration of SONO network.

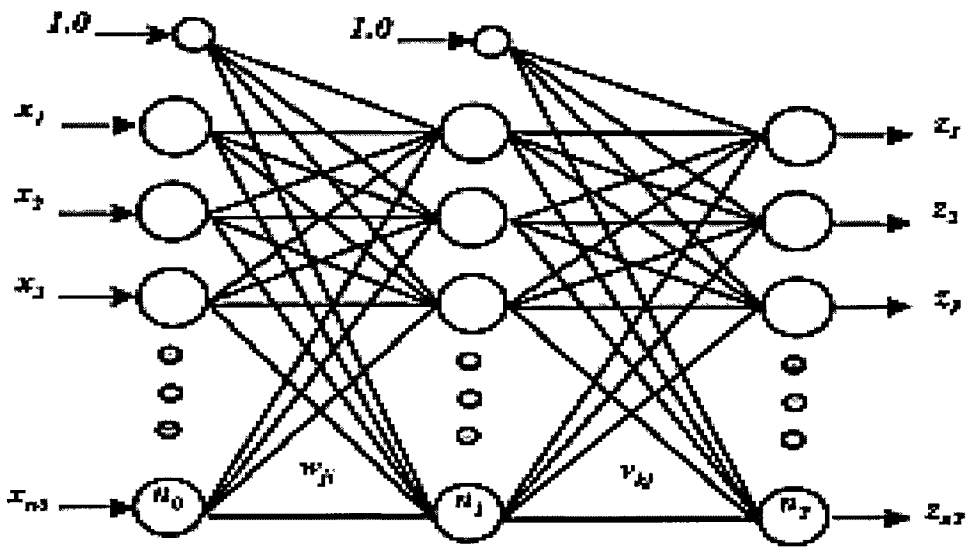

Figure 2.1: The Structure of Multi-layer Feedforward Neural Network (MFNN). (Note: here only show the structure of 3-layer MFNN)

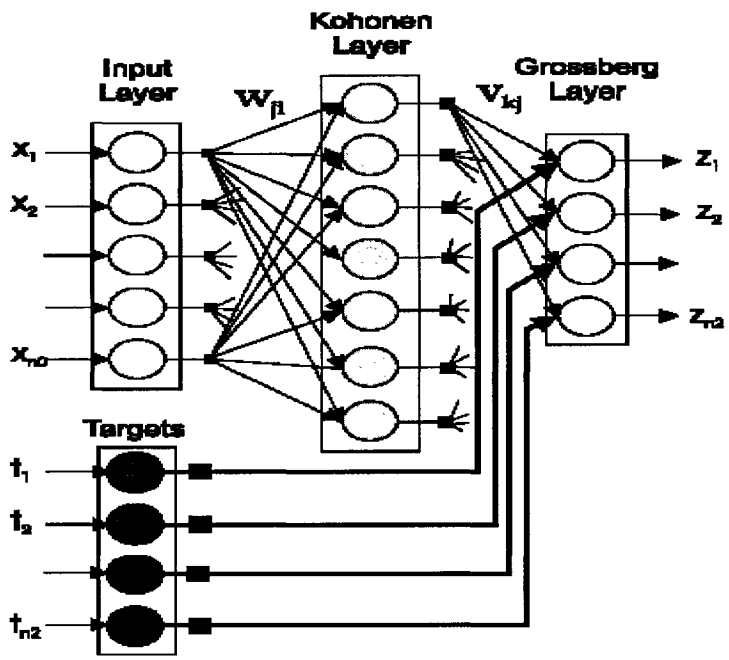

Figure 2.2: The architecture of three-layer Counter Propagation Network (CPN)

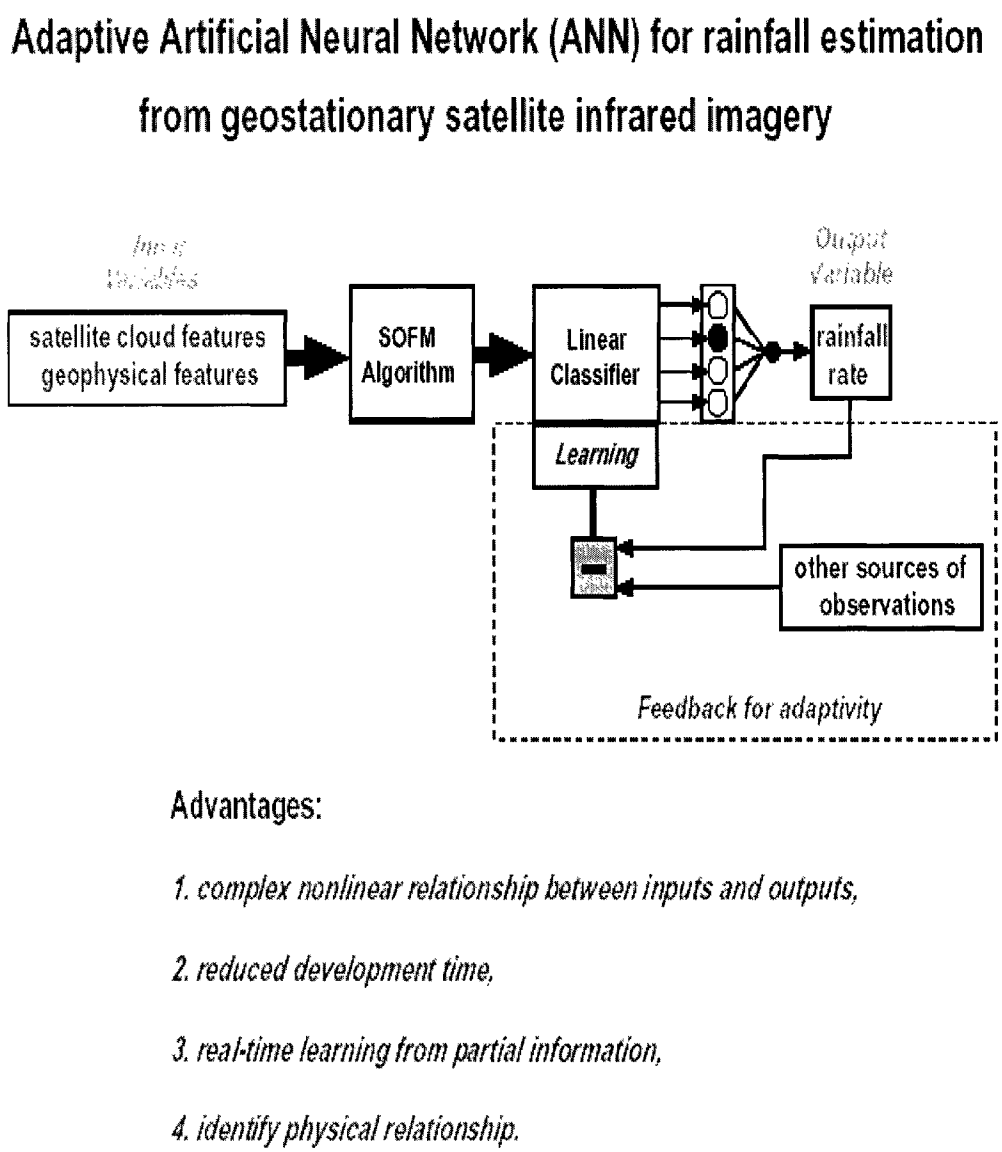

Figure 2.3. The Modified CPN for Precipitation Estimation from Remotely Sensed Information using Artificial Neural Network (PERSIANN)

2.2 Application of ANN in Hydrology

2.2.1 Overview of ANN

The basic notion of artificial neural networks was first formalized by McCulloch and Pitts (1943), inspired by a desire to understand humans and emulate their functioning. The following definition of ANN by Haykin (1994) is an adaptation of an earlier one proposed by Aleksander and Morton (1990): "An artificial neural network is a massively parallel-distributed information-processing system that has certain performance characteristics resembling those of the biological neural networks of the human brain". The development of ANN is based upon the following rules:

1. Information processing occurs at many single elements called nodes, also referred to as units, cells, or neurons.
2. Signals are passed between nodes through connection links.
3. Each connection link has an associated weight that represents its connection strength.
4. Each node typically applies a mathematic transformation called an activation function to its net input to determine its output signal.

ANN is characterized by its architecture that represents the pattern of connection between nodes, its method of determining the connection weights, and the activation function (Fausett, 1994). One way to classify ANN is by the number of layers: single (Hopfield nets); bilayer (Carpenter, Grossberg, and adaptive resonance network); and multilayer (most backpropagation networks). The other way to categorize ANN is based on the direction of information flow and processing: feed-forward (starting from the first

input layer, through 0 or several hidden layer, and ending at final output layer); recurrent (information flowing through the nodes in both directions from the input to output and vice versa). The number of layers and the number of nodes in each hidden layer are defined by problems and determined by a trial-and-error procedure. Figure 2.1 shows a typical configuration of a feed-forward three layers ANN.

It is generally agreed that processing unit of a computer can respond to external stimuli several orders of magnitude faster than a human brain cell. Nevertheless, the sheer number of brain cells and their extremely parallel connection system provide a living brain far superior generalization capability than the world's fastest supercomputer. Initial researches on ANN were prompted by a desire to have computes mimic human learning. Since last two decades, interest in this area picked up momentum in a dramatic fashion with the work of Hopfield (1982) and Rumelhart et al. (1986) and extensive research has been devoted to investigating the potential of ANN as computational tools that acquire, represent, and perform a mapping from one multivariate input space to another (Wasserman, 1989).

2.2.2 Application of ANN in Hydrology

Hydrology is the scientific study of water and its properties, distribution, and effects on the earth's surface, soil, and atmosphere (McCuen, 1997). Hydrologists have been slow to adopt ANN, primarily because practitioners will adopt technologies that have been proven and acceptable (Govindaraju et al. 2000). Therefore, ANN does not have long enough history of hydrological applications. Nevertheless, Applications of ANN in

hydrology have progressed rapidly recently in various areas such as rainfall-runoff modeling, stream flow forecasting, ground water simulation, precipitation estimation, water management policy, hydrologic time series, water quality, and reservoir operations (Govindaraju et al., 2000).

The features of ANN that can be usefully employed in hydrology are: (1) ANN is useful when the underlying problem is either poorly defined or not clearly understood. (2) ANN is advantageous when specific solutions do not exist to the problem posed. (3) Because the weights involved can be updated if new observations are available, ANN is suitable for dynamic system. (4) The ability of ANN to map the non-linear patterns in data make it well suitable to dealing with complex system problems. (5) Owing to distributed processing, errors in the input do not produce significant change in the output. (6) ANN saves on data storage requirements since it is not required to keep all past data in memory.

ANN non-parametric approach presents many advantages over other approximation approaches, particularly, statistical procedures (Sarle, 1994). Hornik et al. (1989) have proved that multiple layers' ANN can approximate any measurable function up to an arbitrary degree or accuracy. Therefore, ANN is called as "universal function approximators". Addtionally, as a non/semi-parametric regression estimator, ANN can model a nonlinear function in a finite number of steps. This ability to extract nonlinear relationship is a very valuable feature of ANN in remote sensing, at least in theory, ANN can improve classification accuracy by 10-30% compared to conventional classification methods (Carpenter et al., 1997).

Govindaraju et al. (2000) edited a book that is the first one exclusively focusing on the various implementation of ANN in hydrology: Roger et al. show how ANN can help us in optimization of number and location of wells and pumping rates in a ground water remediation framework; Rizzo & Dougherty examine the role of ANN and spatial statistics in the problems of subsurface characteristics; Shin & Salas also deal with issues of spatial characterization in the context of precipitation and ground water contamination, while Govindaraju & Zhang use ANN to perform spatial interpolation of saturated hydraulic conductivity; Gupta et al., Markus et al., and Deo & Thirumaliah deal with issues of streamflow forecasting ranging from real time to monthly time scales.

Streamflow is a subject of great interest among hydrologists. Hsu et al. (1994) applied the MFNN in daily streamflow forecasting and compared the performance of ANN to streamflow generated from time-series ARMA and Soil Moisture Accounting model in National Weather Service Runoff Forecasting System (NWSRFS-SMA). The results show that MFFN models can out-perform other models in stream flow forecasting. Hsu et al. (2002) also applied the self-organizing linear output map (SOLO) for daily streamflow predication.

2.2.3 Applications of ANN in Precipitation Estimation

Most hydrologic problems can be viewed as one of forecasting. As one of the most important components of the biosphere, precipitation serves as the driving force for most hydro-meteorological processes. Researchers are often confronted with problems of prediction and estimation of rainfall because precipitation processes exhibit a high degree

of temporal/spatial variability and are further plagued by issues of non-linearity of physical processes and uncertainty of functions approximation.

The application of ANN to practical problems such as signal processing and pattern recognition has shown that the ANN can handle multidimensional, complex data with more accurate results than competing formal statistical methods (Breiman, 1994). Advanced mathematical techniques, combined with real-time data acquisition systems, provide numerous possibilities for controlling complex, distributed, and uncertain dynamical systems such as precipitation processes, particularly in situations where a good model of the system is not available, and an approximate model of the system must be identified using on-line data. For the particular case of precipitation estimation, ANN has a number of features that make it useful.

1) The high variation of cloud microphysical system result in precipitation processes being highly nonlinear and complex. In modeling a complex system, many different levels of difficulty may be involved in design and decision making, such as complexity, nonlinearity, high dimensionality, and uncertainty. The combination of parallel inputs and the hidden layer enables the network to approximate the relationship between predictors and predictands more closely than any linear methods. Linear methods can be adapted to find nonlinear relationships through the use of transforms, dummy binary variables, nonlinear combination of real variables, and so on. However, these adaptations of linear methods require extensive trial-and-error selection on the part of the user, while

the neural network requires much less subjective intervention to find these relationships.

2) There is still much that is not understood regarding the short-term, small-scale behavior of precipitation and its interaction with orography and other sources of forcing. The self-learning nature of ANN allows it to generate estimates for any desired location without extensive prior knowledge of all of the processes involved (though knowledge of which variables might be relevant is important; without a basic understanding of the underlying physics, reliable prediction is impossible). Linear methods such as regression also posses this feature, but as has already been pointed out, these methods require a degree of advanced knowledge or analysis if non-linearity is to be account for.

French et al. (1992) applied three-layer feedforwad ANN (MFFN) model with Back Propagation Algorithm (BPA) to forecast rainfall intensity fields at a leading time of 1 hour with the current rainfall as input. But the performance over the testing data set was not satisfactory. Tohma and Igata (1994) employed a three-layer ANN to estimate rainfall fields based on visible and infrared remote sensing cloud images in the heavy rainfall area of Hokkaido, Japan, over 12 x 12 pixels at 5 km resolution domain. They reported that the ANNs could map the relationship between remotely sensed images of clouds and the rainfall intensities.

Navone and Ceccato (1994) have used two MFFN models to predict the summer monsoon rainfall (SMR) over India. The resulting hybrid network was shown to perform 40% more accurately than the best linear statistical methods using the same data. Zhang

et al. (1997) propose that ANN need to employ in groups when the transformation from the input to output space is complex. Kuligowski and Barros (1998) present an ANN approach for short-term precipitation estimation using feedforward architecture with upper atmospheric wind direction and antecendent precipitation data from rain gauge network to generate 0-6 hour precipitation forecast for a target location.

Hsu et al. (1996, 1997, 1999) have developed a modified counter propagation network (MCPN) for transformation satellite infrared images to rainfall rates by using a Kohonen hidden layer and a linear Grossberg output layer in the three-layer structure. An interesting feature was that the connection weights in hidden and output layers could be trained separately. The MCPN output the rain rate over the predication pixel. A recursive process of competitive node selection and weights adjustment is updated by repetitive sequential processing of the partially available new observation data. The results indicated that MCPN provided good estimation of rainfall rates over 1.0^{o} x 1.0^{o} pixel resolution and yielded informative insights into the functional relationships between the input variables and the rain rate (Sorooshian et al., 2000). The next section briefly describes the application of CPN and MCPN in rainfall estimation.

2.3 PERSIANN Rainfall Estimation System

2.3.1 Introduction

Hsu et al. (1996) summarized the suitability of ANN architectures in remote sensing precipitation estimation. In comparison CPN and MFNN, the MFNN outperforms the CPN in its nonlinear mapping capability. Although the CPN also has the potential to

approximate a continuous nonlinear function to within certain accuracy, the number of processing elements in the SOFM is expected to have many more nodes than the MFNN's hidden nodes. However, the CPN may have more than hundred times lower training cost than MFNN, in term of training time and complexity in finding optimal connection weights. The property of the CPN is particularly important because a large amount of satellite data from the GOES images and rainfall observation are to be used in the ANN model for the model calibration. Another reason to choose CPN architecture is the good classification performance of SOFM. Besides, the CPN posses the capability to visually explain the input/output relationship from the training results of the topological feature map on the SOFM layer and the output weights on the Grossberg layer. For these reasons, Hsu et al. (1996) modified the CPN as the core building block of precipitation estimation model: Precipitation Estimation from Remotely Sensed Imagery using Artificial Neural Network (PERISANN).

2.3.2 Counter Propagation Networks (CPN)

The CPN (Hecht-Nielsen, 1987b; 1988; and 1990) is a hybrid three-layered network, which combines two basic networks together: Kohonen self-organization feature maps (SOFM) (Kohonen, 1982) and Grossberg linear networks (Grossberg 1969; 1971). The SOFM has competitive units operating under unsupervised learning in the input-hidden layer. The Grossberg linear layer is a supervised learning layer, with the units between the hidden and output layers being fully connected and uses the Widrow-Hoff learning rule (Widrow and Hoff, 1960) in network training. The structure of a CPN is depicted in

Figure 2.2. Compared to the MFNN, the CPN requires significantly less training time and is therefore more suitable for situations that involve a large amount of data in training.

$$d_j = [\sum_{i=1}^{n0} (x_i \; w_{ji})^2]^{1/2} \quad where \quad j = 1, \ldots n_1 \tag{2.1}$$

As shown in Figure 2.2, $\mathbf{x}=[x_1, x_2, \ldots, x_{n0}]$ denotes the input vector which is normalized in [0,1]; $\mathbf{y}=[y_1, y_2, \ldots, y_{n1}]$ is the hidden output; and $\mathbf{z}=[z_1, z_2, \ldots, z_{n2}]$ is the network output. The w_{ji} denotes the weight connecting from input node *i* to hidden node *j*; v_{kj} indicates the weight connecting from hidden node *j* to output node *k*. The hidden layer performs the distance calculation of input vector and input-hidden connection weights as follows: the competition occurs in the hidden layer, which assigns a single node that has minimum distance d_c between the inputs and input-hidden connection weights of hidden node j as the winner. That is:

$$d_c = \min(d_j), \quad where \; j = 1, \ldots, n \tag{2.2}$$

After the competition, the winner takes over all outputs in the hidden layer. The output from the hidden layer associated with the winning node, I_c, is assigned $y_c=1.0$, and $y_j=0$ are placed to all j other than I_c. y_j is listed below:

$$\begin{aligned} y_j &= 1.0, \quad if \quad j = I_c \\ y_j &= 0, \quad otherwise \end{aligned} \tag{2.3}$$

The output at the output layer is computed from the weighted summation of the hidden node outputs y_j. Because only $j=I_c$ is activated in the hidden layer, z_k is then simply equal to v_{kc} in the calculation.

$$z_k = \sum_j v_{kj}\, y_j = v_{kj}, \quad if \quad j = I_c$$
$$z_k = 0, \quad otherwise \tag{2.4}$$

The training procedure for CPN is also performed separately in two stages: the SOFM layer and Grossberg linear layer training. The first stage is an unsupervised training procedure for training the SOFM. Training connection weights in the Kohonen layer will describe at next section. The second stage is a supervised training procedure to specify for the hidden-output Grossberg linear layer only.

The simple linearity of (2.4) makes the training of Grossberg layer relatively easy. A sequential training mode moves the Grossberg connection weights to minimizes the matching error between CPN generated pattern and output pattern. The current output target pattern is $[t_1[p], t_2[p], ..., t_{n2}[p]]$, where n_2 is the number of output nodes on the Grossberg layer. The matching error of the output is defined in equation 2.5.

$$\begin{aligned} F[v] &= \sum_{k=1}^{n2} [t_k(p) - z_k(p)]^2 \\ &= \sum_{k=1}^{n2} [t_k(p) - v_{kj}\, y_j(p)]^2 \end{aligned} \tag{2.5}$$

From Equation 2.4, the relationship between z_k and y_j is linear; therefore, the weights of the Grossberg linear layer, v_{kj}, can simply be calculated by finding the optima of a linear least square (LLS) using gradient derivates method.

$$\Delta v_{kj} = -\frac{\partial F[v]}{\partial v_{kj}} = -[t_k(p) - v_{kj}\, y_j(p)]\, y_j(p) \tag{2.6}$$

The weight update is taken from the negative gradient direction of matching error associated with the update weight, v_{kj}, as shown in equation 2.7. Adaptation of the weight v_{kj} follows the Widrow-Hoff learning rule:

$$\begin{aligned} v_{kj}^{new} &= v_{kj}^{old} + \beta\,[\,t_k(p) - z_k(p)]\; y_j(p) \quad if \quad j = I_c \\ v_{kj}^{new} &= v_{kj}^{old} \qquad\qquad\qquad\qquad otherwise \end{aligned} \tag{2.7}$$

Where the learning step size, β, is between 0 and 1. The value of $y_j(p)$ is dependent on the competition of SOFM layer. It is assigned a value of 1.0 in the winner node, I_c, which has minimum distance between inputs, **x**, and SOFM connection weight, **w**. The value of $y_j(p)$ is 0.0 in all nodes other than the winner node. As a result, only the weights at $j=I_c$ are adjusted; other weights remain the same.

Finally, a lookup table is formed by the CPN. The function mapping of the CPN proceeds to find the SOFM node, n_j, which has the closest matching distance between input vector, **x**, and SOFM weights, **w**. Then the Grossberg Layer output weights, $\mathbf{v_j}$, are selected, which represent the mean value of output mapping functions for input values clustered in the n_j node of SOFM layer.

2.3.3 The Modification of CPN in PERSIANN Application

The core of PERSIANN system is a Modification Counter Propagation Network (MCPN) that improves function approximation capability of CPN to a continuous function from input space x to output space z ($z=f(x)$) while the CPN only presents a discrete function , which limits the output space as discrete functions to the number of nodes in network structure design (Hsu, 1996). In order to distinguish two different

inputs that have selected the same SOFM node, Hsu modified the CPN by changing equation 2.3 as the following:

$$\begin{aligned} y_j &= 1 - d_j, \quad \text{if } j \in \Omega, \ \Omega \text{ centers at } I_c \\ y_j &= 0, \quad \text{otherwise} \end{aligned} \tag{2.8}$$

Equation 2.8 assigns SOFM output value, y_j, which is a variable of the distance between input pattern and its connection weights as d_j. An activation range of neighborhood node, Ω, surrounding the winner node on the SOFM layer is assigned as 3 or 5 window size. From Equation 2.8, each node in SOFM forms a small cluster; inside the cluster, a linear interpolation of input-output variables is calculated by the weighted combination of SOFM outputs within the range of Ω.

On the Grossberg layer, the output values, z_k, are estimated from the weighted summation of the outputs from SOFM layer, y_j. This associated output node on the Grossberg layer is only connected to those nodes inside the Ω in the SOFM layer. Hence, the MCPN output, z_k, can be represented as follows:

$$\begin{aligned} z_k &= \sum_j v_{kj} \, y_j, \quad \text{if } \ j \in \Omega \wedge k = I_c \\ z_k &= \varnothing, \quad \text{otherwise} \end{aligned} \tag{2.9}$$

The training of MCPN is basically the same as CPN due to their linearity of network structure and functionality. From Equation 2.9, the relationship between z_k and y_j is linear; therefore, the weights of the Grossberg linear layer, v_{kj}, can also be calculated by finding the optima of a linear least square (LLS) using gradient derivates method. The MCPN differs from CPN is that the weights on the Grossberg layer inside the Ω and $k=I_c$

are adjusted; other weights remain intact instead of adjustment of weights corresponding to $k=I_c$.

2.3.4 Summary and Discussion

ANN has remains much like black-box empirical models incapable of explaining their reasoning in a comprehensible manner in most of the applications of ANN rainfall estimation model. For ANN to gain more acceptability and practical use, it is imperative that some part of the reasoning be imparted back to the user. A common ground for combining the advantages of ANN with some interpretation capability of network performance can be achieved by carefully defining the weights transfer functions and input-output functions in the sense of physical understanding. The PERSIANN system yielded reasoning insightful information of weights in SOFM layer. However, the output of PERSIANN system simply is the linear summation of the weights of the linear Grossberg layer and the weights of the hidden layer (SOFM). Another limitation of PERSIANN architecture is that it was designed for pixel level rainfall estimation. Given an input pattern of cloud pixel, the output is that pixel's grid estimate of rainfall. The linear functionalities of PERISANN in Grossberg layer limit its output space extension.

To overcome this limitation and extend PERSIANN capability to cope with cloud patch–based rainfall estimation from satellite imagery, an ANN network, Self-Organizing Nonlinear Output network (SONO), is designed to explore the cloud patch-based rainfall estimation. SONO is the extension of Self-Organizing Linear Output map (SOLO) whose structure has been designed for rapid, precise, ad inexpensive estimation of network

structure/parameters and system outputs, as well as estimates of their uncertainty (Hsu et al., 2002). More important, SOLO provides additional insight into the underlying input-output processes, thereby extending its usefulness beyond forecast applications. Besides inheriting these high standards of network performance and accuracy of SOLO, the structure of SONO improves SOLO function approximation performance and network flexibility to enable it to approximate the highly nonlinear relationships of cloud-precipitation system and to estimate rainfall of cloud patch instead of pixel at possible smallest temporal and spatial scales from satellite images.

Combined with preprocessors, SONO network is the core building block of the proposed rainfall estimation model-Cloud Classification System (CCS), described in Section 2.4. The proposed CCS also differs from previous ANN rainfall model such as Bellerby et al. (2000) since instantaneous rather than accumulated rainfall is the desired product. Although validation procedures may require accumulated monthly values, the goal of CCS is to generate actual instantaneous estimates at a higher spatial resolution than current techniques.

2.4 Cloud Classification System

2.4.1 Motivation

Hsu et al. (1996) selected CPN as an appropriate method for rainfall rate estimation from satellite imagery due to its simple but effective structure and their ability to cope with large amount of data. Whereas, function approximation abilities of CPN are not good compared with MFFN.

Summarily, the limitations of CPN in rainfall estimation are: (1) discrete function approximation: the mapping between input (x) and output (z) variables is a series of discontinuous values denoted by the weights of Grossberg layer node related to the SOFM layer winning node; (2) linearity: the relationship between the weights (v_{kj}) in Grossberg layer and the output variables is linear; (3) single point to point input-output relationship: the input-output function only produce one single value for each node at output layer by averaging the summation of products of connection weights of winning nodes in Grossberg layer; (4) coarse resolution: the pixel-to-pixel correspondence prohibits the rainfall estimates at high spatial resolution due to displacement or impacts of other climatic factors.

Hsu et al. (1996) designed Modified CPN (MCPN) to improve CPN function approximation from discrete to continuous functionality. However the limitations of 2, 3, and 4 in CPN network structure remind to constrain the capability of MCPN to capture the highly nonlinear continuous relationships between cloud patches and surface rainfall. Particularly, the basic CPN structure prevents MCPN from constructing an appropriate ANN mode for rainfall estimation from satellite imagery at cloud patch level rather than pixel point level. Based upon previous studies, a new version of PERSIANN network, called PERSIANN-Cloud Classification System (PERSIANN-CCS, in short as CCS), is designed to develop a distributed cloud patch-based rainfall estimation model that achieves the objectives as specified in chapter 1.

2.4.2 The Layout of CCS Model Structure

Figure 2.4 shows the architecture of CCS. CCS consists of two basic modules: (1) the input preprocessor module that process satellite imagery and provide cloud patch-based input features; (2) the Self-Organizing Nonlinear Output (SONO) module that classifies cloud patches into different cloud clusters and calibrates the nonlinear relationships of cloud-precipitation. SONO network is an ANN model that could run in two modes: fixed parameter mode and adaptive mode.

According to the order of data flow, the CCS is comprised by five procedures. The names and functions of each procedure are as follows: (a) cloud segmentation procedure that segments the satellite IR image into separated cloud patches; (b) cloud feature extraction procedure that provides the input features of cloud patch and its rainfall information; (c) the SOFM classification that organizes each cloud patch and corresponding rainfall information into certain cluster; (d) Probability Matching Method (PMM) that matches the cloud-precipitation data distribution for each classified cloud cluster and its corresponding surface rainfall; (e) nonlinear mapping procedure that approximates the cloud-precipitation relationship and, finally, predict rainfall estimates.

The procedures (a) and (b) belong to the first module: input preprocessors and the procedures (c), (d), and (e) comprise the ANN module: SONO network. The two preprocessors enables SONO network to produce precipitation estimates at cloud patch level by preparing the input variables of cloud patches. The SONO network performs two basic functions as "switchboard" and "approximator". The SOFM functions as a "switchboard" to turn "on" or "off" the units of the nonlinear output layer, i.e., the SOFM classifies each cloud input vector and determines to which unit in the Nonlinear Output

layer it must be routed for approximation of cloud-precipitation relationship. After turned "on" by SOFM classifier, the "approximator" in the Nonlinear Output map approximates the cloud-precipitation relationship and estimates rainfall.

As any other three-layer ANN network, the SONO consists of three layers, input layer, SOFM classification layer, and the Nonlinear Output layer. The mathematical depiction of SONO is as follows. The input layer is comprised of n_0 neural units, $\mathbf{x}=[x_1, x_2,..., x_{n0}]$ that denotes the variables of input vector normalized in [0,1]. The second SOFM classification layer is comprised of n_1 neural nodes $\mathbf{y}=[y_1, y_2, ..., y_{n1}]$; and the weight w_{ji} denotes the weight connecting from input node x_i to SOFM node y_j. In the third Nonlinear Output layer, $\mathbf{z}=[z_1, z_2, ..., z_{n2}]$ is the network output and weight vector $v_{kj}=[vkjl,$ *where* $l=1, ..., n_3])$ indicates the multidimensional weights connecting from hidden node y_j to output node z_k. The following sub-sections detail the methodology in the order of model data flow. Section 2.4.3 briefs the preprocessors (cloud segmentation and feature extraction). Section 2.4.4 and Section 2.4.5 describes the SOFM classifier of SONO network and the Nonlinear Output approximator of SONO network, respectively. Finally, Section 2.4.6 discusses the training of CCS model for the value of the network parameters (i.e., connection weights linking the nodes) are determined by the process of calibration.

2.4.3 The Input Preprocessors: Cloud Segmentation and Feature Extraction

The inputs of PERSIANN system are features of a pixel from IR cloud brightness temperature imagery, and the output is rainfall estimate of that pixel. Since the proposed

rainfall estimation method is coping with the input pattern of cloud patch rather than a pixel, it is necessary to preprocess the satellite IR imagery into cloud patches.

The first preprocessor, Cloud Segmentation, segments satellite IR imagery into separated cloud patches. Assumed the pixel number of a separated cloud patch pattern (p) is *N*. And then the second preprocessor extracts the cloud feature X as well as collects the cloud-top temperature IR_m and surface rainfall RR_m, if available, for pixel m where m=1, ..., *N*. The input pattern p of cloud patches includes information of three vectors:

$$p\{[x_i], [IR_m], [RR_m]\}, \text{ where } i=1,\ldots,n_0;\ m=1,\ldots,N(p) \qquad (2.10)$$

Where $[x_i]$ is the input feature vector of cloud pattern p; $[IR_m]$ is the IR brightness temperature vector within cloud p; and $[RR_m]$ is the observation of rainfall rate vector corresponding to $[IR_m]$ within the same cloud p. N(p) is the number of pixels belonging to cloud pattern. Thus, the two preprocessors enable CCS to model precipitation estimation at cloud patch level by providing the patch-based input pattern to SONO network. The detailed procedures of the two processors will be described in next chapter.

2.4.4 The Self-Organizing Feature Mapping (SOFM) Classifier of SONO Network

The SONO network (see Figure 2.5) is the core building block of CCS rainfall estimation model, which consists of two major modules: a Self-Organizing Feature Mapping classification layer and a Nonlinear Output approximation layer.

The SOFM classification layer performs the distance calculation of input vector *x* and connection weights *w* in SOFM layer as following equation 2.11.

$$d_j = [\sum_{i=1}^{n0} (x_i - w_{ji})^2]^{1/2} \quad where \quad j = 1, \ldots n_1 \qquad (2.11)$$

The competition occurs in the SOFM classifier layer, which locates a node that has minimum distance d_c between the inputs x and connection weights of SOFM node j as the winner node.

$$d_c = \min(d_j), \quad where\ j = 1,\ldots,n_1 \tag{2.12}$$

After the competition, the winner node takes over all outputs in the SOFM layer. The output from the SOFM layer associated with the winning node, I_c, is assigned y_c=1.0, and y_j=0 are placed to all nodes other than I_c. y_j is listed below:

$$\begin{aligned} y_j &= 1.0, \quad if \quad j = I_c \\ y_j &= 0, \quad otherwise \end{aligned} \tag{2.13}$$

The SOFM functions as a "switchboard" to turn "on" or "off" the activity of node in the nonlinear output layer. The winning node I_c turns "on" its counterpart node in nonlinear output layer to be active for processing.

2.4.5 Nonlinear Output Layer of SONO Network

After turned "on" by SOFM classification layer, the node in nonlinear output layer will firstly match the cloud-precipitation data pairs using Probability Matching Method (PMM) approach and then calibrate a nonlinear function to estimate rainfall for cloud patch.

2.4.5.1 Cloud-Precipitation Data Distribution by Probability Matching Method (PMM)

The essence of the PMM proposed by Atlas et al. (1990) is to select the data pairs of radar R_i and reflectance Z_i in the cumulative distribution functions (CDF) such that their

CDFs match (see equation 2.14). The pairs of matching (R_i, Z_i) then determine the climatological Z-R relation provided that CDF of R and Z are representative of certain season and region.

$$\frac{\int_0^{R_i} P(R)dR}{\int_0^{\infty} P(R)dR} = \frac{\int_0^{Z_i} P(Z)dZ}{\int_0^{\infty} P(Z)dZ} \tag{2.14}$$

In our cloud-precipitation study, the data pairs of RR_m and IR_m are from the same cloud type clustered by SOFM classifier and, therefore, we assume that the data may represent observation values from an individual cloud patch through its lifetime or from those cloud patches with similar geophysical features at any other areas or time periods. Therefore, the CDF probability match of data pairs (IR_m and RR_m) is written as:

$$\frac{\int_0^{RR_i} P(RR)dRR}{\int_0^{RR_{max}} P(RR)dRR} = \frac{\int_{IR_{max}}^{IR_i} P(IR)dIR}{\int_{IR_{max}}^{IR_{min}} P(IR)dIR} \tag{2.15}$$

Where RR_{max} is the upper limit of rain rate and IR_{min} and IR_{max} indicate the coldest IR cloud-top temperature and warmest temperature, respectively. The regression of data pair (RR_m and IR_m) using PMM constitutes the climatological cloud-Precipitation (IR_{Tb}-RR) relation. Note that it is important that the CDFs of IR and RR be from the same cloud type or that they are representative of the same population of cloud-precipitation events. PMM approach enables us to approximate the highly nonlinear relationship of data pairs (IR and RR) from the same or similar cloud-precipitation events.

2.4.5.2 Nonlinear Cloud-precipitation Relationship Approximation

We define the nonlinear function for cloud-precipitation events as

$$Z_m = f(\Theta, IR_m, RR_m),\ m=1, \ldots, N(p) \tag{2.16}$$

Where Θ is the parameter set for the nonlinear function *f;* the output Z is rain rate estimates from function *f,* and the data pairs of (IR_m and RR_m) are the observation data from the same cloud pattern. To incorporate the parameter set Θ into the SONO network, we assign the parameter set Θ as connection weight vector v_{kj} in Nonlinear Output layer.

$$v_{kj}=[v_{kjl}] = v_{kjl},\ where\ l=1, \ldots, n_3. \tag{2.17}$$

Where V_{kj} denotes the connection weights linking from j^{th} node in SOFM layer to k^{th} unit in the Nonlinear Output layer. Then the nonlinear relationship function for cloud pattern p is written as

$$Z_m = f(v_{kjl}, IR_m) = v_{kj1} + v_{kj2} \times \exp[v_{kj3} \times (IR_m + v_{kj4})^{v_{kj5}}],\ where\ m=1, \ldots, N(p); \tag{2.18}$$

This nonlinear rainfall estimation function is derived from an exponential function with five parameters [v_{kjl}], l=1,2, ..., 5. The use of power-law relation between cloud-temperature and precipitation rates was suggested by the study of Gagin et al. (1985) and was used previously by Martin et al. (1990) and Goodman et al. (1994). The form of the equation 2.18 is partially referred from the Auto-Estimator (AE) by Vicente et al. (1998). The AE, equation 2.19, is a power law function calibrated with selected data pairs from heavy rainfall events.

$$R=1.1183 \times 10^{11} \times exp(-0.036382 \times IR) \tag{2.19}$$

AE function has only two parameters and the single function is applied into various precipitation events though with adjustment from Precipitable Water (PW) and IR local

pixel features such as texture. Equation 2.18 has 3 more parameters in order to increase the fitting ability of function approximation at the certain IR range from warm 270°K to super cold 180°K. More importantly, with the cloud patches classified into n_1 clusters by SOFM, Equation 2.18 shows larger variation of fitting curves that could cover the whole feasible training data domain as identified in model calibration of Chapter 4.

In summary, CCS functions as follows: (1) CCS segmentation preprocessor firstly segments IR imagery and obtain a separated cloud patch p; (2) CCS feature extraction preprocessor computes the input features x of the p; (3) according to the features, the SOFM classifies the cloud patch p into j^{th} connection unit w in SOFM layer and turn on the counterpart of k^{th} unit in Nonlinear Output layer; (4) the Nonlinear output layer calibrates and computes the rainfall estimates Z.

The rainfall estimates Z for cloud pattern p is thus computed from the nonlinear equation of the SOFM node outputs y_j, the weights vector v_{kjl} of nonlinear output layer, and the IR vector.

$$z_{kjm} = \sum_{j}^{n_1} y_j . f(v_{kjl}, IR_m) = \sum_{j}^{n_1} y_j \times \{v_{kj1} + v_{kj2} \times \exp[v_{kj3} \times (IR_m + v_{kj4})^{v_{kj5}}]\} \ \ if \ \ j = I_c$$
$$Z_{kjm} = 0 \ \ otherwise$$
$$where \ m = 1,..., N(p)$$

(2.20)

Where j is the winning node in the SOFM layer; k is the counterpart node of j in Nonlinear Output layer and is turned "on" by SOFM "switchboard". The values of the network parameters i.e., connection weights such as w and v, are determined by the process of training.

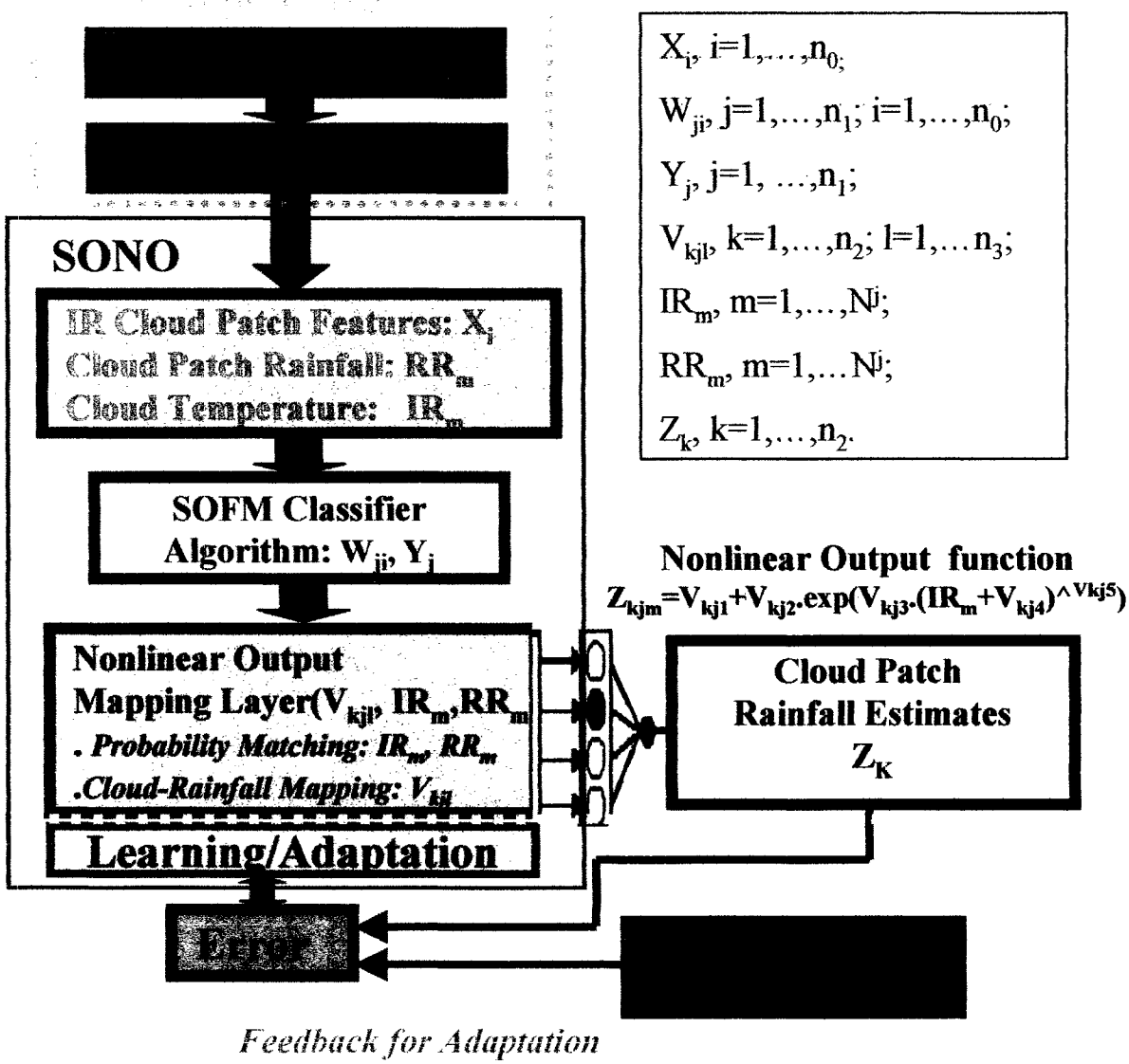

1.complex nonlinear Grossberg mapping layer,
2.Nonlinear approximation of cloud –rainfall relationship,
3.cloud patch level rainfall estimation system,
4.more precipitation-oriented information included,
5.all the advantages inherited from MCPN in Fig. 2.3.

Figure 2.4. The Architecture of Self-Organizing Nonlinear Output (SONO) network

(as a core building block of Cloud Classification System for Precipitation Estimation from Remotely Sensed Information using Artificial Neural Network)

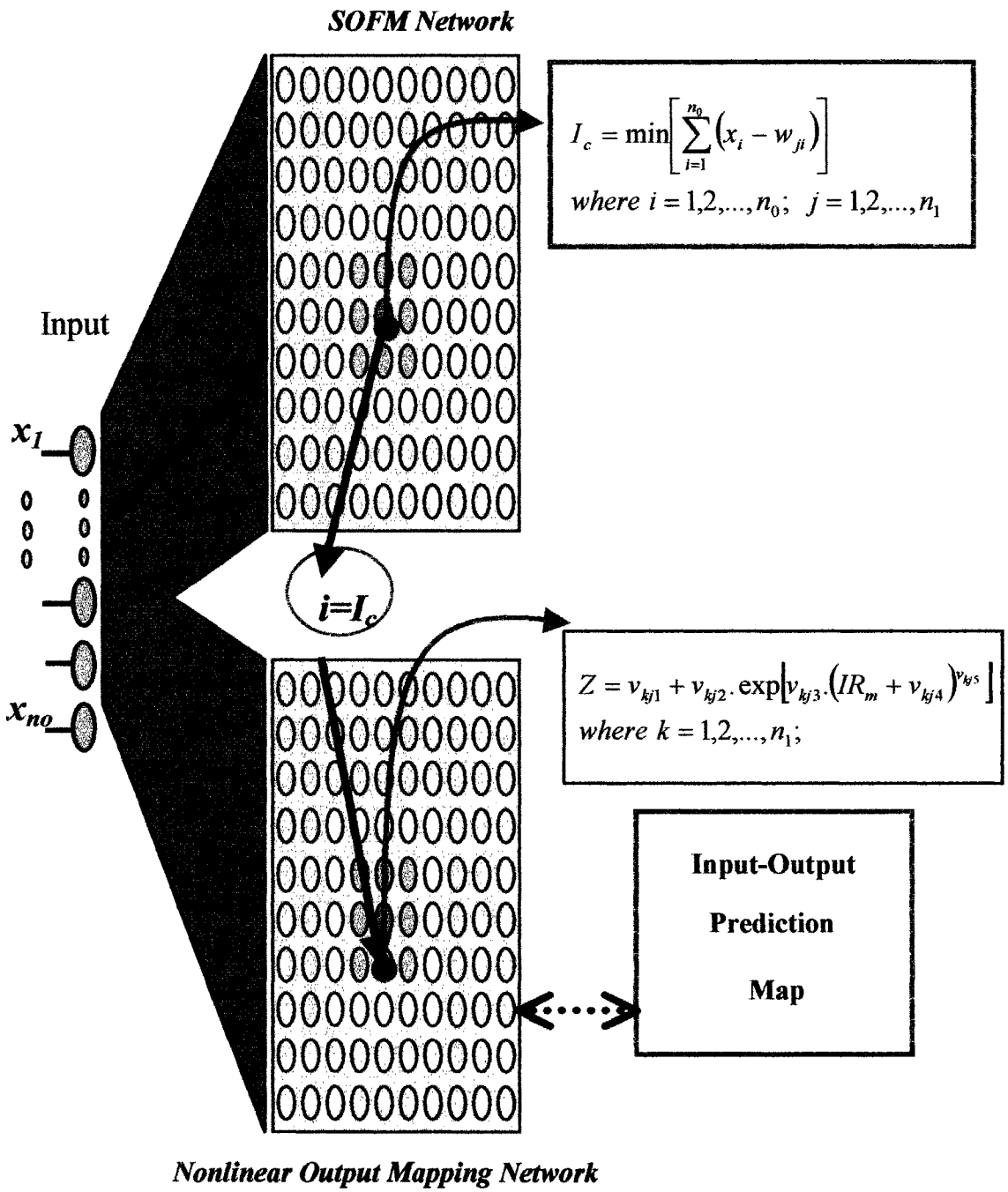

Figure 2.5 Self-Organizing and Nonlinear Output (SONO) in CCS model

2.5 Training of CCS Model

The structure of CCS in this study includes two modules (input preprocessors and SONO network). Only the SONO network involves training of parameters. SONO network consists of two components: the SOFM classifier and the Nonlinear Output approximator. The SOFM classifier performs an unsupervised clustering using a technique called the self-organizing feature map (SOFM) [Kohonen, 1982]. The function of SOFM, as the name suggests, is to achieve classification of the input variables i.e. cloud features on the basis of a set of representative training (input) data vectors. The SOFM organizes the input vector x onto a discrete one- or two-dimensional SOFM weights w map, which preserves the topographic order of the inputs space (Hecht-Nielsen, 1990). The Nonlinear Output component maps the organized cloud clusters to precipitation output space. A powerful feature of SONO is that the training of the two components could be decoupled, which enables the network to rapidly process large volume of satellite data.

The training procedure for SONO is described separately in Section 2.5.1 for the SOFM classifier and Section 2.5.2 for Nonlinear Output map training. The first stage is an unsupervised training procedure for the SOFM. The second stage is a supervised training procedure to specify the Nonlinear Output map using Multi-Start Downhill Simplex (MSDS) optimization technique (Duan et al., 1993).

2.5.1 Training of SOFM Layer

The weights w, indicting the cluster centers of the SOFM map, must be trained to well organized cloud patches into clusters. Defining n_0 denotes the dimension of the input feature vector x and n_1 denotes the node number of the hidden SOFM layer, the procedure for training the SOFM weights vectors $w_j = [w_{j1}, \ldots, w_{jn0}]$ $j=1,2,\ldots,n_1$ is conducted as follows:

Step 1: randomly initialize the connection weights for each hidden nodes *w(0)*;

Step 2: For each input vector x_i, the 'distance' between the normalized input vector and each hidden layer (SOFM) node is calculated as

$$d_j = \left[\sum_{i=1}^{n0}(x_i - w_{ji})^2\right]^{0.5} \quad j = 1, \ldots, n_1 \tag{2.21}$$

Where the n_0 denotes the dimension of the input vector x and n_1 denotes the node number of the hidden SOFM layer.

Step 3: Select the winning node I_c such that $d_c = \min(d_j)$, $j=1,\ldots,n_1$; (2.22)

Step 4: Update the connection weights of all hidden nodes in the neighborhood of the winning node as follows (the nodes outside $\Lambda_c(t)$ remain the same as before):

$$w_j(t) = w_j(t-1) + \eta(t)[x - w_j(t-1)] \quad \text{if } j \in \Lambda_c(t)$$

$$w_j(t) = w_j(t) \quad \text{otherwise} \tag{2.23}$$

Where t is the training iteration index, $\eta(t)$ is the learning rate, and $\Lambda_c(t)$ defines the neighborhood size around the winning node I_c.

Step 5: Decrease the learning rate $\eta(t)$ and the neighborhood size $\Lambda_c(t)$:

$$\eta(t) = \eta_0[1.0 - (t/T)]$$

$$\Lambda_c(t) = \Lambda_0 [1.0 - (t/T)] \tag{2.22}$$

Where T is the total number of training iterations and the initial settings are $\eta_0 = 0.2 \sim 0.5$ and $\Lambda_0 = n_1/2$, i.e. half of the hidden node size. Repeat step 2-5 several times until the values of the weights w stabilize.

SOFM hidden layer functions as a clustering map to classify the cloud patches with similar combination of features into same node. The off-line training of SOFM hidden layer weights results in an organized clusters map. Each node of the SOFM map represents a cloud type with certain combination of input features.

2.5.2 Training of Nonlinear Output Layer: Multi Start Downhill Simplex

The linearity of CPN and MCPN Grossberg layer enable the training of weights simply implements the gradient search to solve the optimal for the objective functions in PERSIANN system. However, in this study, the Equation 2.20 is a multi-parameters nonlinear function that requires global search optimum algorithms instead of local search algorithms such as gradient search.

A number of global search algorithms have been developed to find the global optimal or near global optimal for multidimensional nonlinear equations. The main disadvantage of those global search algorithms is the convergence to the best values requiring a great deal of iterations and training time, particularly for multi-layers Artificial Neural Network with multi-dimensional weights matrix. Duan et al. (1992) and Hsu et al. (1997) have proved that the Multi-Start Downhill Simplex (MSDS) is capable of finding optimal results with relatively short training time and fast convergence. The

MSDS algorithm also has both local and global search characteristics, and is not easily trapped by multiple local optima.

The connection weights of the nonlinear layer are trained either by using sequential training or batch training. Adaptation of the weights follows the Widrow-Hoff learning rule. Batch training mode sends all the training data to the SONO model at once. Each of the pattern **x**(p) triggers a winning node, I_c, in the SOFM layer and activates SOFM output y_j. Sequential training is listed as below:

$$v_{kjl}^{new} = v_{kjl}^{old} + \beta\{ \sum_{m=1}^{N^j} [t_{km}(p) - z_{km}(p)].\, y_j(p) \} \quad if \quad j = I_c,$$
$$v_{kjl}^{new} = v_{kjl}^{old} \qquad otherwise \qquad (2.24)$$
$$where \ \ j = 1,...,n_1, k = 1,...,n_2, l = 1,...,n_3; \beta \ is \ learning \ rate.$$

A sequential training mode moves the connection weights v_{kjl} to minimize the matching error between generated pattern z(p) and output pattern t(p). Let the current output target pattern is $[t_1[p], t_2[p], ..., t_{n2}[p]]$, where n_2 is the number of output nodes on the Output layer. An objective function F_k is defined as equation 2.25.

$$F_k[\, v_{kjl}] = \frac{1}{2}\,[t_k(p) - z_k(p)]^2 = \frac{1}{2}\sum_{m=1}^{N_j}[t_{km}(p) - z_{km}(p)]^2 = \frac{1}{2}\sum_{m=1}^{N_j}\sum_{j=1}^{n_1}\,[t_{km}(p) - y_j(p).f(v_{kjl}, IR_m^j)]^2$$
where $l = 1,...,n_3$;
(2.25)

The objective function equation 2.25 is a multi-parameter nonlinear function of vector $[v_{kjl}]$, the weights vector $[v_{kjl}]$ of which cannot be solved by setting the derivatives of the function F_k as did for the conventional linear CPN network. To find the optimal values of the weights v_{kj}, we apply the non-linear MSDS global search algorithm. MSDS uses a multi-start version of the Downhill Simplex search algorithm (Nelder and Mead,

1965) to search for the global optimum in the super-dimensional output weights space. This algorithm is similar to the genetic algorithm (GA) in that it involves a population of search points in an improvement direction, but uses a different strategy from GA in its selection of improvement points.

The Downhill Simplex algorithm begins with a geometric Simplex consisting of n+1 points in an n-dimensional parameters space, and evolves the Simplex in the direction of improving function value by the procedures of reflection, extension, contraction, and shrinking until the stopping criteria has been reached.

The Simplex only uses one start of n+1 points in n-dimensional parameters while the improved MSDS uses multi-start to search the optima. Thus the MSDS algorithm has both local and global search characteristics, and is not easily trapped by minor optimal. The MSDS algorithm used in the training is outlined below:

Let the weights parameters space be n-dimensional and nSim denotes the number of simulation. The nSTART indicates the number of starts of MSDS algorithm. Specify a small enough value for group convergent criterion (GCC) (eg. $GCC=10^{-8}$).

Step 1) Let nSIm=0 and specify the number of restarts of the MSDS algotirhm: nSTART.

Step 2) initialize the "Simplex":

Randomly initialize m=n+1 points in the feasible n-dimensional weights space. The set of m points is called a "simplex". Estimate the objective function F_i at each point x_i, $\{(x_i,F_i)$, i=1,..,m and $W_{min}<x_i<W_{max}\}$. The

feasible space weight space is defined by $W_{min}<x_i<W_{max}$, for i=1,…,m, where W_{min} and W_{max} are the lower and upper limits on the weights.

Step 3) sort the Simplex and identify the worst point:

Sort the m points in order of increasing function value, such that j=m has worst error function value, into array $D=\{(x_j,F_j),j=1,\ldots m\}$.

Step 4) find the centroid:

Compute the centroid of the, g, of the first n points.

Step 5) test the reflection point:

Find the reflection point $r=2x_m - g$. If the function value F(r) less than $F(x_m)$, then go the step 6; otherwise, go the step 7.

Step 6) test the extension point:

Find the extension point $e=3x_m -2g$. If the F(e)<F(r), let x_m=**e**; otherwise, let x_m=**r**; go to step 9.

Step 7) test the contraction point:

Find the contraction point c=(g+xm)/2. If F(c)<F(xm),let xm=c and go to step 9; otherwise go to step 8.

Step 8) shrink the simplex:

Shrink the simplex by $x_j^{new}=(x_1+x_j^{old})/2$, j=2,…,m. Go to step 9.

Step 9) test of the convergence:

If the group convergence value (GCV) of the simplex is smaller than the GCC, let nSIM=nSIM+1 and go to step 10. If not, go to step 2. The GCV

measures the size of the region spanned by the m points of the simplex and is defined as:

$$\text{GCV} = \left[\prod_{k=1}^{n} \frac{x_{\max}^{k} - x_{\min}^{k}}{W_{\max} - W_{\min}} \right]^{1/n}$$

Where $x_{\max}^{k}$ is the maximum of all m points at parameter k;

$x_{\min}^{k}$ is the minimum of all m points at parameter k.

Step 10) test for termination of training iterations:

If nSIM=nSTART then stop; otherwise save the best point and go to step 1.

2.6 Summary

SONO network is the core building block of the proposed precipitation model CCS in this study. The preprocessors of CCS such as cloud segmentation and cloud feature extraction enables SONO network to produce rainfall estimates at cloud patch level. The combination of SONO and its preprocessors constitutes the proposed rainfall estimation model. This chapter detailed the structure and training of SONO network but only briefly depicted the CCS preprocessors. Therefore, next chapter will present detailed information about the preprocessors (cloud segmentation and cloud feature extraction).

CHAPTER 3

THE CCS PREPROCESSORS: CLOUD SEGMENTATION AND CLOUD FEATURE EXTRACTION

3.1 Introduction

The proposed Cloud Classification System (CCS) includes two major modules: Input preprocessors (Cloud segmentation and cloud feature extraction) and the core network-Self-Organizing Nonlinear Output (SONO). The first module functions as preprocessors to enable SONO to estimate rainfall at cloud patch level instead of pixel level. As an automated system, the first step of CCS is to perform IR image segmentation to clearly separate the cloud patches of interest. The next step involves features identification and extraction, and then, propagates all the information into SONO network to map cloud-precipitation relationships.

In Chapter 2, the structure of CCS model is presented with focus on SONO. In this Chapter, the preprocessing module of CCS is described in detail. Section 3.2 introduces the first preprocessor: cloud segmentation. Section 3.3 describes the second one: cloud feature extraction.

3.2 Cloud Patch Segmentation

A long-standing problem of great interest among the meteorological and hydrological communities has been how to segment the cloud imagery with various

intentions such as cloud feature extraction, cloud type classification, and other cloud-related studies like cloud dynamics or wind detection. This Section reviews the segmentation methods firstly and then proposes a new segmentation approach, namely, Topography Hierarchical Thresholding and Stepwise Seeded Region Growing with fast merging (THT-SSRG), followed by some application examples of the new segmentation method.

3.2.1 Satellite IR Cloud Imagery

A cloud is defined as "a visible aggregate of minute particles of water or ice, or both, in the free air". Clouds cover about half of the earth at any given time (*International Cloud Atlas,* Volume I World Meteorological organization, 1956). The pattern of clouds seen from space fluctuates strongly as they form, dissipate, and move in conjunction with the fluid motion of the air.

Clouds in the atmosphere can be identified by a human observer on the ground or by an aircraft. However, what one can see from these vantage points is limited to the immediate surroundings of the observer. It is impossible to observe visually the full extent and structure of many clouds. Meteorological satellites provide a viewpoint from which the broader shapes and forms of clouds can be seen. In particular, they allow the primary precipitation-producing clouds to be recognized and characterized. Since the largest source of clouds is from satellite such as GOES, AVHRR etc., the interpretation of weather satellite imagery has generally required the experience of well-trained meteorologist. However, it is not always feasible to have an expert meteorologist on hand

when such interpretation is needed. Especially, it is impossible while large amount of satellite imagery processing required at automatically weather forecasting system, like precipitation estimation system and meteorological modeling. Therefore, the availability of an automated segmentation system of satellite cloud images would be quite desirable.

3.2.2 Segmentation Approaches Overview

Image segmentation is one of the most important tasks in image processing and analysis, having a wide range of applications. A large variety of segmentation algorithms have been developed. Based on an excellent survey of current approaches (Fu and Mei, 1981; Shaw and Lohrenz, 1992; Pal, 1993). These techniques can be categorized into the following categories.

(1) Amplitude thresholding(AT)

As the simplest and widely used approach, AT uses single threshold to divide the IR image into regions of above- and below- threshold of brightness temperature. This merely requires a comparison of the pixel data to the threshold values. Lee and Chung showed that AT would usually produce good results in only bi-modal images where the image consists of only object and the background (Moghaddamzadeh, 1997). Even in this kind of images, detected segments are not necessarily continuous (Moghaddamzadeh, 1997). The main problem with this method is in selecting the appropriate threshold because for complex images like cloud imagery, choice of a universal threshold to clearly separate various cloud patches is impossible, particularly in multi-cold cores of connected cloud images; besides, elimination of thresholds plays an important role in designing automatic

image segmentation.

(2) Connected Component Labeling (CCL)

CCL examines the connectivity of pixels with their neighbors and then labels the connected sets of pixels as one segment. This method only applies when an image contains objects whose intensity level has large difference with background intensity.

(3) Boundary-based segmentation

Boundary-based segmentation includes the widely used techniques of edge-detection and Hough transforms. Image boundary is detected by the thresholding local texture variation and then linked into contours that delimit the objects from background (Gonzalez and Woods, 1992). Problems of use of boundary-based segmentation approach are the high possibility of unclosed edges and the over detection of edge by simply thresholding the local texture variation with Gaussian derivatives.

(4) Region-based segmentation

Region-based approach involves grouping of pixels that satisfy certain predefined homogeneity threshold (Ho, 2001). These algorithms rely on the postulate that neighboring pixels within one region have similar value. This leads to the class of algorithms known as region growing. The general procedure is to compare one pixel with its neighboring regions. If a criterion of homogeneity is satisfied, the pixel is determined to belong to the region. However, different similarity threshold settings may lead to different segmentation results (Ho, 2001). Another disadvantage is the numbers of regions is predefined thus fixed in the beginning. This is impractical for images having an unknown number of objects.

(5) Template matching

Template matching method segments an image by matching it against templates from a given list and isolating objects that match expected shapes.

(6) Clustering-based approaches.

Clustering of characteristic features applied to image segmentation is the multidimensional extension of the concept of thresholding. Several approaches have been proposed, such as fuzzy-c-mean (FCM) and K-means. The main advantage of these approaches is that the problem of setting thresholds can be avoided by using iterative processes. However, under-segmentation occurs since pixels within the same cluster may not be adjacent, for example, distant cloud patches could be assigned into same cluster because of similar brightness temperature.

With reference to the definition of segmentation (Fu and Mei, 1981), image segmentation, generally, is a process of partitioning an image into some regions such that each region is homogeneous and none of the union of two adjacent regions is homogeneous. In another words, the objects or regions in the segmentation images are characterized by connected pixels of **similar values**. Therefore, the above methods are not applicable to highly textured images with large range of values such as cloud images (Adams, 1994). From the coldest top to its edge, a cloud patch may consist of very cold and warm pixels, of sharp and weak gradients, and of variety of textures and shapes. For example, the poleward end of a cloud might have deeper convection, and hence brighter clouds, than the equatorward end. Additionally, clouds are natural physical phenomena

that are involved in the processes of formation, growth, shrinking, breakup, and fallout. Therefore, it is rather difficult to segment cloud images with the above existing algorithms.

3.2.3 Objective of Desired Cloud Segmentation Approach

Historically, the usually used approach for cloud segmentation is amplitude thresholding. In several cloud segmentation studies, the thresholds were chosen between 235~253K to discriminate clouds and clear sky. One early example of patch-based segmentation is the GWT (Griffith et al., 1978; Woodley et al., 1980), in which a cloud patch is defined by applying the temperature threshold of 253°K on IR imagery. Later, Xu (1997) proposed a Cloud Patch Analysis (CPA) calibrating the threshold to discriminate rain/no-rain cloud for particular region using data from GOES IR and microwave rain rate estimates. The result is about 243K. A more advanced algorithms entitled as segmentation of satellite imagery using Hierarchical Thresholding Segmentation (HTS) is introduced by Peak (Peak and Tag, 1994). HTS constructs a bottom-up hierarchical threshold tree to split children regions from parent regions occupying the same area at lower thresholds, and then uses neural network to decide whether to keep or prune the splits.

Clouds exhibit a wide variety of size, shape, texture, height, and coldness. For complex images like cloud, however, it is impossible to select a threshold that will correctly segment a cloud image (Peak, 1994); besides, elimination of thresholds plays an important role in designing automatic image segmentation to process huge amount of

satellite images.

In light of the above analysis, several objectives must be taken into account for developing an efficient IR cloud patch segmentation algorithms. They are described as follows.

(1) Elimination of thresholds. How to choose appropriate thresholds for various images is not easy. Elimination of thresholds plays an important role in designing an automatic image segmentation scheme to identify cloud, non-cloud area.

(2) Continuous closed edge. A segment (cloud patch) must be composed of a continuous collection of adjacent and touching pixels. This is a very important criterion that is not met in many approaches (Moghaddamzadeh, 1997). Closed cloud patch boundaries are basically requirement and their identification is important.

(3) Complete segmentation. Every pixel in image must be assigned to a segment or background when any segmentation algorithm terminates.

(4) Automated process. For large amount of satellite IR imagery, manual setting and tuning during each segmentation process is impractical.

(5) Clear separation. Clear and distinctive separation of adjacent cloud patches enables CCS model to identify informative cloud features such as geophysical features (coldness), geometric features (size, shape), and texture features.

Existing segmentation algorithms only partially satisfy the above objectives. In order to develop an efficient image segmentation algorithm specifically for cloud satellite imagery, we proposed a Topography Hierarchical Thresholding and Stepwise Seeded Region Growing (THT-SSRG) combined possible merging post-processing. This

algorithm falls under a hybrid segmentation category since it integrates the hierarchical thresholding, region growing, and merge/split techniques.

3.2.4 Methodology of Cloud Segmentation (THT-SSRG)

3.2.4.1 Definition of Terms

In this context, IR cloud imagery is the 3D depiction of a climate variable-cloud-top brightness temperature g(x, y, t), where x and y are the spatial dimensions, longitude and latitude respectively; t is the snapshot time. Segmentation and texture analysis reduces the dimensionality of the climate field by two, converting the original 3D g(x, y, **t**) problem into 2D g(x, y) at *t* time point problem.

(a) Seed

A seed is a cloud pixel with the relatively coldest temperature within each cold region and a cloud patch grows from seeds till terminated by predefined stop criterions.

(b) Connectivity

The growing direction from seeds is called connectivity. For 2 dimensional images, the usually used connectivity is 4-connectivity or 8-connectivity. 4-connectivity determines that pixels are connected only if their edges are connected along the horizontal or vertical direction while 8-connectivity means that pixels are connected if their edges or corners connected along the horizontal, vertical, or diagonal direction. Figure 3.1 illustrates connectivity for 2 or 3 dimensional image. 8-connectivity is chosen in this study because it grows region more spatially compact.

(a) (b)

2-dimension Connectivity: (a) 4 Connectivity; (b) 8 Connectivity

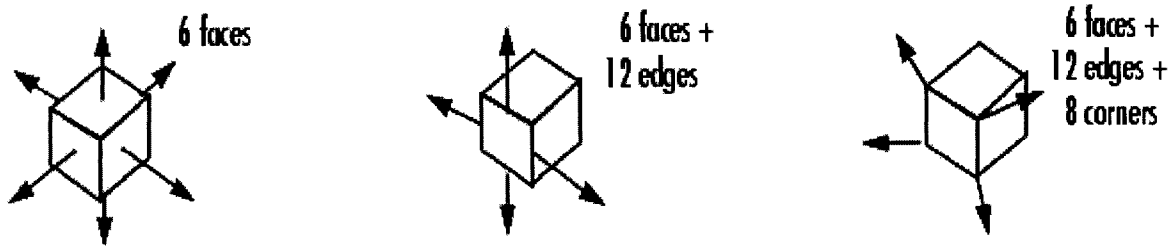

(a) (b) (c)

3-dimension connectivity: (a) 6 Connectivity; (b) 18 Connectivity; (c) 26 Connectivity

Figure 3.1 Illustration of connectivity for segmentation algorithms.

(c) External Boundary, Internal Boundary, and Current Regions

In order to monitor the pixels joining the region, especially while a pixel neighbors two or more regions, we introduce the following terminology: Current Region (CR), Internal Boundary (IB), and External Boundary (EB). CR is a region under segmenting. IB is defined as the boundary produced by the set of connected outermost pixels of the current region. EB is the set of un-segmented pixels adjacent to the current region.

(d) **Topography of Cloud Imagery**

The IR brightness temperature represents the height of the cloud according to the lapse rate, which determines the temperature decreases generally along with cloud height increase in the troposphere (Equation 3.1). As a three-dimensional object, the minimum brightness temperature of cloud visually appears as cloud overshooting top from the satellite view.

$$\tau(z) = -\frac{dT}{dz} \qquad (3.1)$$

When $\tau(z)$ is applied to a mass of dry air, it is called the dry adiabatic lapse rate (DALR) and approximately 9.8K/km (David, 2000). The actual lapse rate $\tau(z)$ in the atmosphere will generally differ from the DALR. Because of the latent heat given to the air by condensation of the water vapor, the temperature drops off less rapidly with height (by about 6~9K km^{-1}) at the wet adiabatic lapse rate than it does at the DALR. In all, the range of lapse rate is about 6~10K km^{-1}.

(e) **Segments**

Conventionally, a segment is defined as a collection of adjacent pixels having similar values. The large variation of temperature gradients within a cloud patch necessitates that

we modify the definition of segment to suit the cloud segmentation: *A segment is defined as a collection of adjacent pixels having similar values or gradual change in values.* The gradual change of cloud temperature is defined as Temperature Interval (TI).

(f) **Temperature Interval (TI)**

We add the gradual change in pixel gray value to define the cloud segment besides similar values to fit the specific cloud imagery segmentation issue. Now the problem is how to quantify the gradual change as a temperature interval to monitor the process of cloud region growing. TI is derived from the approx relationship between cloud-top brightness temperature and the cloud-top height. Equation 3.2 regards cloud-top height change (z) as the function of temperature change by transposing from Equation 3.1 and, therefore, derives a range of TI and its corresponding cloud-top height difference in Table 3.1.

$$dz = - dT / \tau(z) \qquad (3.2)$$

Table 3.1 IR brightness Temperature Intervals and its approximate height difference

Temperature Interval	Minimum height difference (km)	Maximum height difference (km)
1K	0.1	0.166667
2K	0.2	0.333333
3K	0.3	0.5
4K	0.4	0.666667
5K	0.5	0.833333
6K	0.6	1
7K	0.7	1.166667
8K	0.8	1.333333
9K	0.9	1.5
10K	1.0	1.666667

The value of TI is chosen based upon the knowledge of lapse rate and the efficiency of processing speed. Larger TI will decrease the computation time but will increase the

possibility of under-segmentation of clouds regions. On the contrary, smaller TI will increase the processing cost and result in over-segmentation. TI is defined as 3K to fit the specific cloud imagery segmentation issue because any two adjacent cloud pixels with temperature difference less than 3K possibly belong to same cloud patch due to their minor height difference (0.3~0.5km). The small value of TI, 3K, tends to result in over-segmentation but a post-processing procedure such as merge/split could solve over-segmentation.

(g) **Topographical Hierarchical Thresholds (THT)**

Given a cloud image, we define the temperature minima as T_{min} and the temperature that discriminates cloud from clear sky as T_{max}. The THT series is defined as:

$$THT_m = T_{\min} + TI \cdot i \;; i = 1,2,...,M; \;\; where \;\; M = \| (T_{\max} - T_{\min}) / TI \| \qquad (3.3)$$

Where TI is temperature interval as 3K and $\| \; \|$ takes the integer values.

3.2.4.2 The Processes of THT-SSRG Algorithm

Here the hierarchical thresholding in THT-SSRG performs topographically top-down hierarchical thresholding from cloud-top cold core to cloud warm edge, which is different from Peak's HTS bottom-up hierarchical thresholding (Peak, 1994). The segmentation algorithm sets up a series of hierarchical thresholds ranging from cloud global minimum temperature (T_{min}) to the warmest 253K, the choice of which is based upon previous studies (Griffith et al., 1978; Woodley et al., 1980; Xu, 1997) that usually selected thresholds between 235~253K to screen clouds out from clear sky.

Given a cloud image, the algorithm locates the global T_{min} and detects the first set of

seeds (illustrated by cross marker) then starts to iteratively expand each seed's area one neighborhood size at a time by absorbing the bordering/warmer pixels under the control of THT series till touching other regions or clear sky. THT induces a directional growing such that pixels of colder temperature will be absorbed first. Additionally, the 8-connectivity ascertains that the same growing speed toward the 8 neighboring pixels thus makes the resulted regions more spatially compacted than 4-connectivity. Figure 3.2 shows an example of cloud segmentation using the THT-SSRG method. The following is a list of steps of THT-SSRG segmentation approach.

(1) Automatic initial seeding from T_{min}

Given a new IR cloud image input, the series of topographical hierarchical thresholds, THT, is computed with Equation 3.3 and the initial seeds are located at the cold core starting from T_{min}.

(2) Stepwise seeded region growing and hierarchically seeding new seeds

This process starts with seeds located at cold cores of cloud-top brightness temperature, which has been numerically labeled as a region and then grows starting from colder to warmer region till reach the $THT_1 = T_{min} + TI$;

Assume that the process completes m step then all the pixels with temperature colder than THT_m are labeled as cloud regions after the m^{th} step, now two sub-processes need to complete in this iteration: one is to grow existing seeded regions till reaching the threshold THT_{m+1}; the second is to detect possible new seeds for new regions. The following (3) is the detailed explanation.

(3) Iteratively growing current regions and hierarchically seeding new regions

We assume that at step m there are n_1 current regions represented by a set of Ai and numerically labeled as i=1, 2, …, n_1.

$$A^m = \{A_1^m, A_2^m, ..., A_i^m, ..., A_{n1}^m\} \tag{3.4}$$

The coldest top temperature for each cloud region is defined as:

$$CT_i = \min_{(x,y)\in A_i^m} \{g(x, y)\} \tag{3.5}$$

Where $g(x, y)$ is the temperature of the pixel (x, y). At each step, the algorithm completes two tasks. One is to grow the existing regions A^m till reaching the threshold THT_{m+1}; the other is to label emerging seed(s) for new regions.

To grow the existing regions, let T^m be the set of all as-yet unallocated cloud pixels and T^m borders at least one of the current regions at step m. T^m is actually the external boundary (EB) of existing regions according to the definition of EB.

$$T^m = EB = \{(x, y) \notin \bigcup_{i=1}^{n} A_i^m \text{ AND } NB(x, y) \cap \bigcup_{i=1}^{n} A_i^m \neq \phi \} \tag{3.6}$$

Where $NB(x, y)$ is the set of immediate neighbors of the pixel (x, y) at 8 connectivity. If $NB(x, y)$ intersects just one of the existing regions, A_i^m, algorithm partitions pixel (x, y) into region A_i^m; If NB(x, y) intersects more than one region, a decision of partition into which region is made with $\delta(x, y)$, a measure of the difference (similarity) between (x, y) and the intersected region. In this case $\delta(x, y)$ is defined as:

$$\delta_i(x, y) = | g(x, y) - CTi | \tag{3.7}$$

Pixel g(x,y) is assigned into region A_i^m so that δ_i(x, y) is minimum. If equal situation happens, we classify the pixel into the region with larger size. If all fails, though rarely,

we just randomly assign this single pixel to either region. All those pixels intersected with more than one region are potential boundary pixels. We label the intersected regions as bordering regions to mark possibility of region merge during post processing.

After complete the segmentation of all $(x, y) \in EB$, the EB becomes the IB and new EB forms automatically. Thus, repeat of this process will eventually reach the current THT_{m+1} and complete the task of growing existing regions.

After completion of the first task: growing all spatially connected cloud pixels into existing regions, there comes the second task: detecting possible seeds for new emerging clouds. A new seed is confirmed if a pixel is colder than THT_{m+1} but isolated from any one of existing regions A^m (Equation 3.8).

$$Seed_{new}^{m} = \{\, g(x,y) < THT_{m+1} \text{ and } NB(x,y) \cap \bigcup_{i=1}^{n} A_i^m = \phi \,\} \qquad (3.8)$$

We simply numerically label new seeds as n+1, n+2, …, n_2. The new seeds will act the same as existing regions to absorb connected cloud pixels at next step. Therefore, after complete the m+1 step, the cloud segments are:

$$A^{m+1} = \{A_1^{m+1}, A_2^{m+1}, \ldots, A_i^{m+1}, \ldots, A_{n1}^{m+1}, \ldots, A_{n2}^{m+1}\} \qquad (3.9)$$

(4) Repeat the process 3 till the $THT_m >= T_{\max}$ according to equation (3.3)

(5) Final tuning of segmentation: examination of regions merging

After obtaining the initial segmentation, the set of segmented regions are:

$$A = \{A_1, A_2, \ldots, A_n\} \qquad (3.10)$$

A final stage, region merging, is needed to examine the adjacent regions with the labels of bordering regions to resolve the over-segmentation. Labeling the bordering regions

during previous stage speeds up the region merging process by only examining those labeled bordering regions. If a region A_i borders one region A_j, we merge the two regions only if their height difference $|(CT_i - CT_j)|$ is less than TI as defined in 3.2.4.1(f). If a region A_i borders multiple regions with height difference less than TI, we use the dissimilarity criterion proposed in Hierarchical Stepwise Optimization Algorithm (HSWO) (Beaulieu, 1989). The dissimilarity (cost) function:

$$\delta_{i,j} = \frac{Ni \cdot Nj}{Ni+Nj} |(CT_i - CT_j)| \tag{3.11}$$

where N_i and N_j are the number of pixels of neighboring regions A_i and A_j; and CT_i and CT_j correspond to the cloud coldest temperature of A_i and A_j, respectively. HSWO computes the degree of dissimilarity with every bordering region and then merge region A_i and A_j such that the merging cost of δ_{ij} is the smallest. This criterion is superior to other statistical measures in terms of computation because merging cost is calculated only using the number of pixels and minima temperature of each region, needlessly to compute standard deviation, average of each region, or other measures. The two regions having smallest cost is merged in each step of iterative merging. This merging process is guided by marked bordering regions and is automatically terminated when there are no more bordering regions with height difference $|CT_i-CT_j|$ less than TI to be merged.

3.2.5 The Application of the THT-SSRG Algorithm

Figure 3.3 is a snapshot of GOES IR image and its segmented cloud patches, indicated by cross marker, using THT-SSRG algorithm. For the same IR image, Figure 3.4 shows the under-segmentation results using the Amplitude Thresholding method that

simply connects several individual cloud patches into one. Under-segmentation leads to the difficulty to define and extract cloud feature information, particularly for geometric features and texture features. The biased information will likely propagate noise into system and induces uncertainty of rainfall estimation.

Figure 3.5 shows several individual cloud patches randomly selected from Figure 3.3. Each cloud patch is well separated from background and is clearly an individual cloud-precipitation system. Figure 3.6 shows some segmented cloud patches located at Las Vegas during a storm events July 8, 1999.

As a hybrid method, THT-SSRG retains all advantages of Seeded Region Grow-fast execution and robust segmentation (Adams, 1994). Meanwhile THT-SSRG eliminates manual selection of seeds in SRG. The additional advantages of this method are:

(1) Fully automatic process;

(2) Clear and distinctive delineation of individual cloud patch boundary;

(3) Eliminating uncertainty of ignorance of the raining warm clouds;

(4) In addition to horizontal features, it is capable to extract vertical information of a cloud patch by applying features extraction at different temperature (height) levels, for example, 220K, 235K, and 253K. The features at different temperature levels could supply the meaningful signals toward precipitation estimation.

This segmentation method is fully automatic and flexible. As a hybrid segmentation method, it incorporates the strength of seeded region growing to apply into cloud image with the help of topographically hierarchical thresholds, which guarantees the automatic and dynamic seeding in different cloud height levels instead of manual seeding.

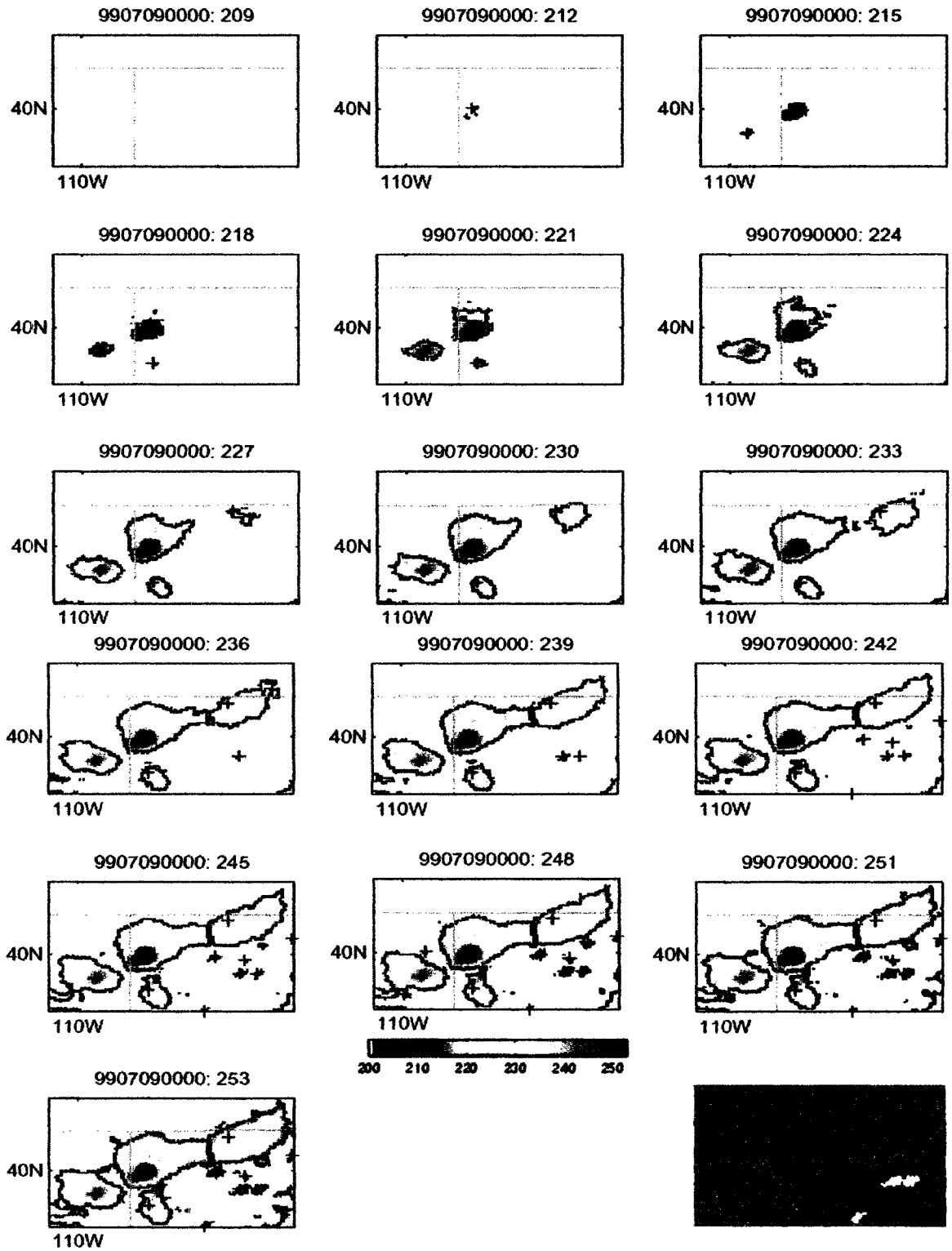

Figure 3.2. The cloud patch segmentation process using THT-SSRG (the "+" denotes the seed; the last plot of cloud patch is resulted from Amplitude Thresholding algorithm).

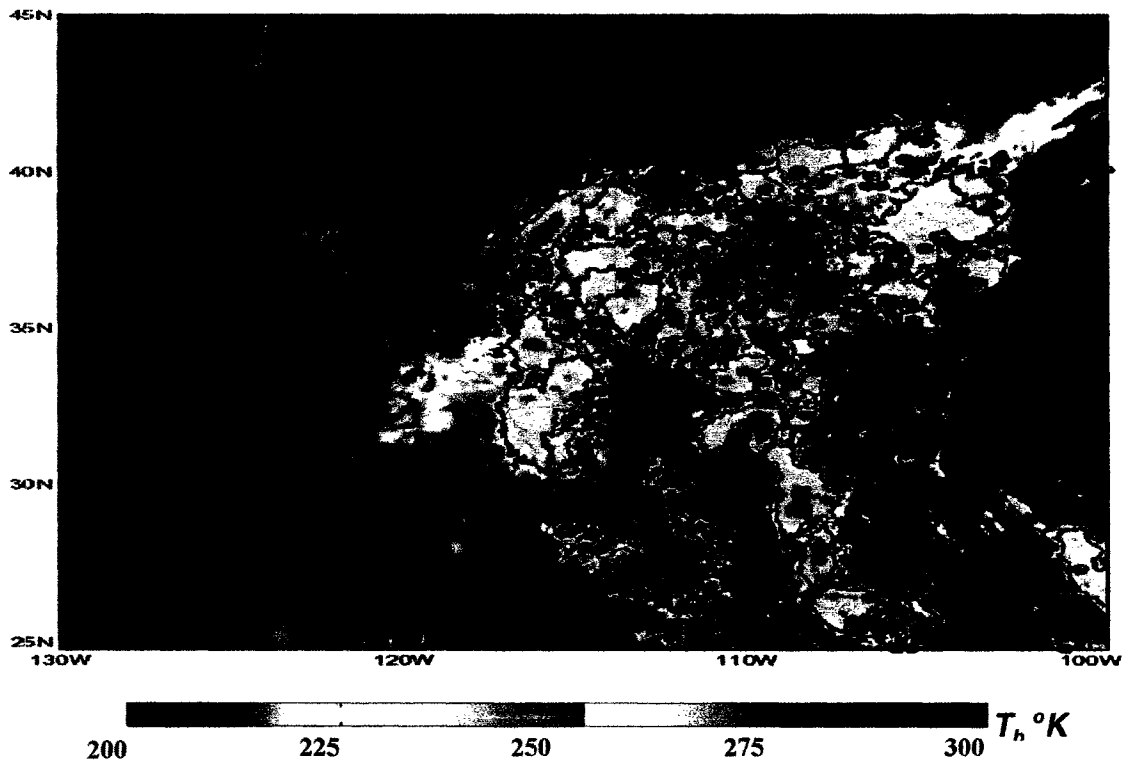

Figure 3.3 Segmented cloud patches from GOES IR image using THT-SSRG algorithm (UTC: 0000, July 9, 1999 and the cloud patch marked by 'cross').

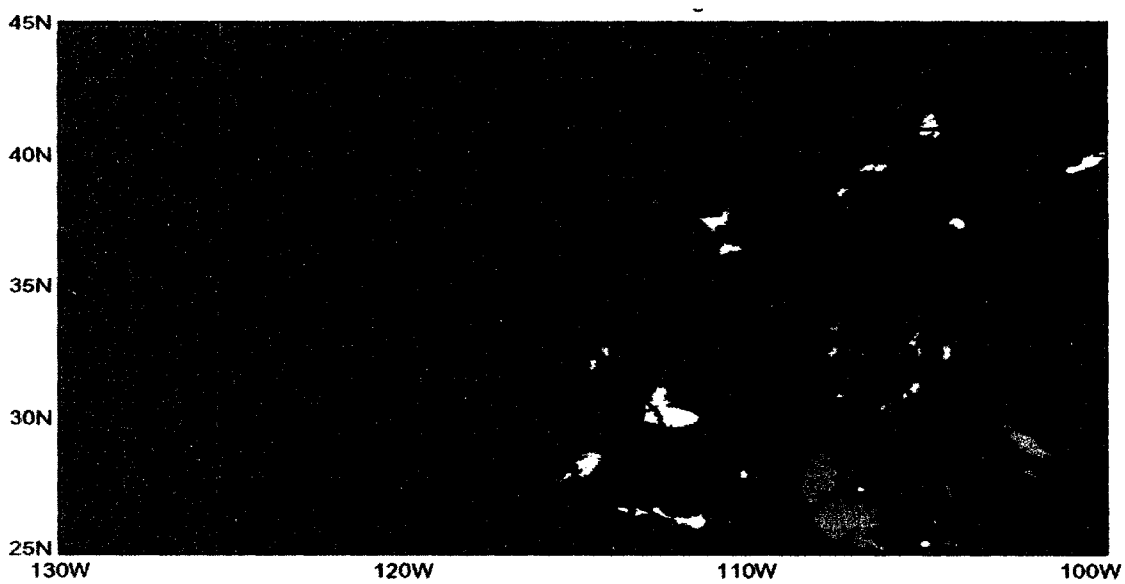

Figure 3.4 Segmented cloud patches using Amplitude Thresholding algorithm for the same IR image at Figure 3.3.

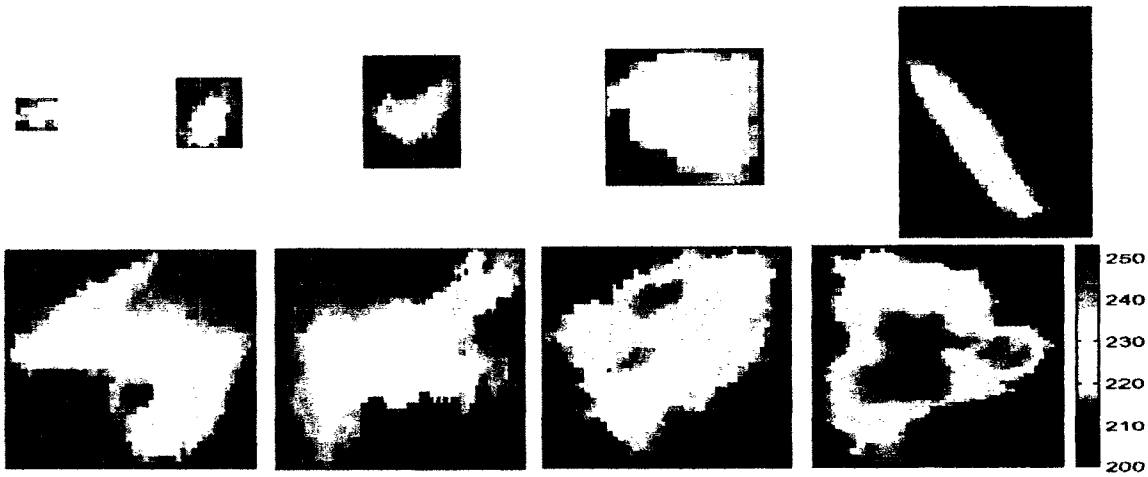

Figure 3.5 Randomly selected individual cloud patches from Figure 3.3

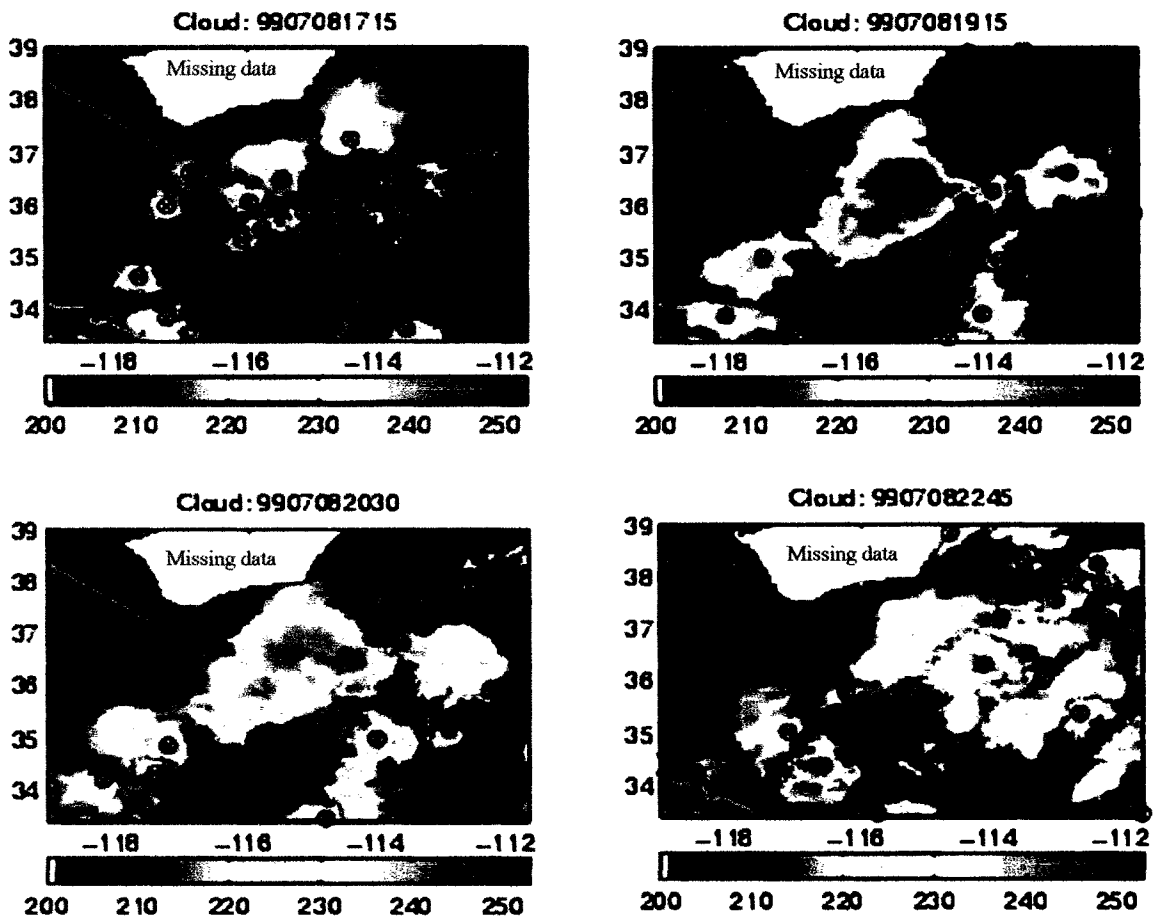

Figure 3.6 The GOES Infrared Cloud Imagery and segmented cloud patches using THT-SSRG algorithm at various snapshots (cloud shooting top is marked by circle and cross).

3.3 Cloud Features Definition and Extraction

After the completion of cloud patch segmentation, the second module for CCS is the cloud feature extraction to prepare the input for SONO network. This section describes and explains some feature candidates.

3.3.1 Cloud Feature Overview

At any given time about 60% of the earth's surface is masked by cloud of one form or another (Sumner, 1988). These clouds associate with large range of scales from meters to thousands of kilometers (in three dimensional atmosphere) and various types of evolutional processes (forming, developing, and dissipating).

Table 3.2. The cloud patch input feature candidates for the CCS model

Coldness Features of Cloud Patch:
(1) Minimum temperature of a cloud patch (T_{min})
(2) Mean temperature of a cloud patch (T_{mean})
Geometric Features
(3) Cloud patch area (AREA)
(4) Perimeter (PERI)
(5) Cloud Patch Shape Index (SI)
(6) Eccentricity (ECCT)
(7) Compactness (COMP)
(8) Boundary Steepness (BS)
(9) Rectangularity (RECT)
Texture features (referring the brightness temperature texture)
(10) Standard deviation of cloud patch (STD)
(11) Mean value of local standard deviation of cloud patch ($MSTD^5$)
(12) Standard deviation of local standard deviation of cloud patch (STD^5_{std})
(13) Gradient of cloud cold top brightness temperature (TOPG)
(14) Gray images' texture (Angular second moment, Contrast, entropy etc.)
Dynamical Features
(15) Moving speed of cloud patch (MSPD)
(16) Moving direction of cloud patch (MDRT)
(17) Life stage factor (L)

The previous studies verified the idea that clouds picture from space could be typed (Barrett, 1981) based on its presenting features. The characteristics of clouds, important to interpretation, are size, texture/structure, brightness, and dimensions. The features selected in this research are grouped in four categories: coldness features, geometric features, texture features, and dynamic features (see Table 3.2). The first category is associated with the cloud brightness temperature; the second is derived from the geometric properties of cloud patch; the third one is texture variation of cloud brightness temperature; and the last one are clouds moving features derived after cloud patch tracking.

3.3.2 Description of Cloud Features

To mathematically explain some of the features, the total number of pixels of a cloud patch is denoted as N, and the top temperature of pixel i is denoted by T_i. Certain features are explained as follows.

(1) *Minimum temperature of a cloud patch ($T_{min:}$):* $T_{min} = \min_{(x,y)\in A_k} \{g(x, y)\}$ *(3.11)*

(2) *Mean temperature of a cloud patch: (T_{mean}):* $T_{mean} = \sum_{(x,y)\in A_k} \{g(x, y)\}/N$ *(3.12)*

(3) Cloud patch area (A_k): $A_k = N * pixel\ resolution$ *(3.13).*

(4) *Shape index (SI):* SI is defined as the ratio of the geometric inertia momentum of a cloud patch (I) to that of a round patch with a same size (I_o):

$$SI=I/I_0 \qquad (3.14)$$

where

$$I = \sum_{i=1}^{N} [(x_i - G_x)^2 + (y_i - G_y)^2] \qquad (3.15),$$

(x_i, y_i) is the coordinate of pixel I,

(G_x, G_y) is the geometric center of the cloud patch, and

I_0 is the geometric inertia of a round patch with the same area.

Given a certain size of cloud patch, the rounder shape patches give smaller shaping index. A perfect circular cloud patch consists smallest SI value of one.

(5) *Boundary Steepness (BS)*: BS measures how steeply the temperature increase along the boundary of a cloud patch.

$$BS = \frac{\sum_{i=1}^{N} \mu(i)}{N} \qquad (3.13)$$

For a cloud patch, N is the number of pixel along the 235K boundary, and $\mu(i)$ is the distance from pixel I on the 253K boundary to a corresponding position of the warmer 253K boundary.

(6) Standard deviation of cloud patch temperature (STD):

$$STD = \{ \sum_{(x,y) \in A_k} [g(x, y) - T_{mean}]^2 / (N-1) \}^{1/2} \qquad (3.16)$$

(7) Mean value of the local standard deviation of cloud temperature ($MSTD^5$):

$$MSTD^5 = \sum_{i=1}^{N} STD_i^5 / N \qquad (3.17)$$

where STD_i^5 is the standard deviation of brightness temperature with window size of 5 x 5 window centered on pixel i.

(8) Standard deviation of local standard deviation of cloud temperature (STD^5_{std}):

$$STD^5_{std} = [\sum_i (STD^5_i - MSTD^5)/(N-1)]^{1/2} \quad (3.18)$$

(9) Gradient of cloud top temperature (TOPG): TOPG is mean temperature

TOPG measures how steeply the temperature increase around the cloud's shooting top indicated by T_{min}. to define TOPG, a cloud shooting boundary is derived by applying a warmer threshold, 15°K above T_{min}, to the cloud patch under study. Then. TOPG is defined as average pf temperature gradients from shooting top (T_{min}) to every pixel on the shooting top boundary.

$$TOPG = \sum_{i=1}^{N} \frac{15}{\mu(i)} / N \quad (3.19)$$

Where N is the number of pixels on the shooting top boundary, and $\mu(i)$ is the distance from pixel i on the boundary to the shooting top (T_{min}).

(10) Gray image texture (Maximum Angular Second Moment: MASM):

Texture information is characterized by a set of gray level cooccurrence matrices $H_{d,\phi}$, with the element $h(i,j)_{d,\phi}$ as the estimate of the probability that gray level i and gray level j are located at a distance d, angle ϕ, with a fixed direction (Haralick et al., 1973). The cooccurrence matrices $H_{d,\phi}$ delineate the texture information of an image on various scales and directions. Angular second moment (ASM) of the cooccurence matrix located at various distances and directions are:

$$ASM_{d,\phi} = \sum_i \sum_j [h(i,j)_{d,\phi}]^2 \quad (3.20)$$

The ASM features computed at various directions are usually redundant. In our case, only one index is selected according to their ability to identify no-rain cloud patches is listed below:

$$MASM = \frac{\max}{\phi}\{ASM_{\phi} \mid \phi = 0^{o},45^{o},90^{o},135^{o}\} \qquad (3.21)$$

(11) Dynamical features

To obtain these types of features requires the track cloud patch movements. Once the cloud patches are tracted, the moving speed is calculated by dividing the distance of cloud patch centers at consecutive images by the time interval; and the moving direction is the direction of joint axis of the two centers. The life stage factor denotes the growing or decaying stages. The stage factor is jointly decided by the change of T_{min} and cloud patch area along the evolution of cloud patch.

The features are calculated at three vertical height levels 220K, 235K, and 253K (Figure 3.7 and Feature 3.8). Default values are assigned for cloud at non-existing height level. For instance, the *AREA* feature of a warm cloud patch (T_{min}>235K) only computed at existing height level 253K and the default value 0 is assigned to non-existing higher levels. The vertical information will be interpreted and propagate into the cloud types classification. The features calculated at hierarchical vertical levels will emphasize information at different aspects of a cloud patch. Generally, the features at 253K level give overall information of a defined cloud; the features at 235 K level emphasize cloud cold regions with higher possibility of precipitation release; and the features at 220K

level supply information which focus on the super cold core of the cloud (cloud overshooting top).

3.4 Summary

This Chapter described the two preprocessors, Cloud Segmentation and Feature Extraction for the proposed CCS rainfall estimation model. In next Chapter, a primary case study of CCS is conducted to calibrate parameters of CCS network after testing all of the features candidates described in Table 3.2.

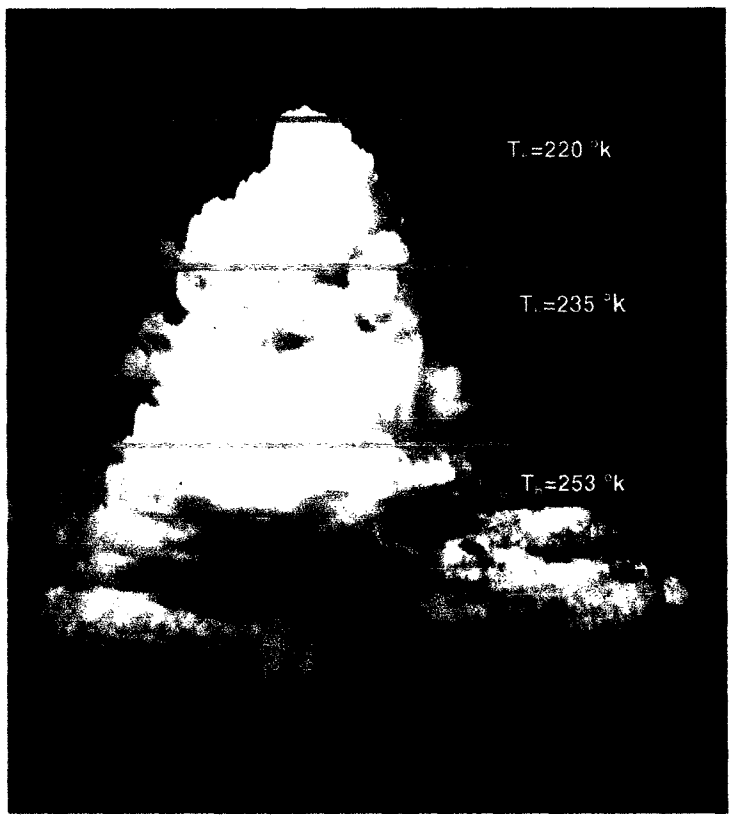

Figure 3.7 Feature extraction at 3 height levels of cloud patch.

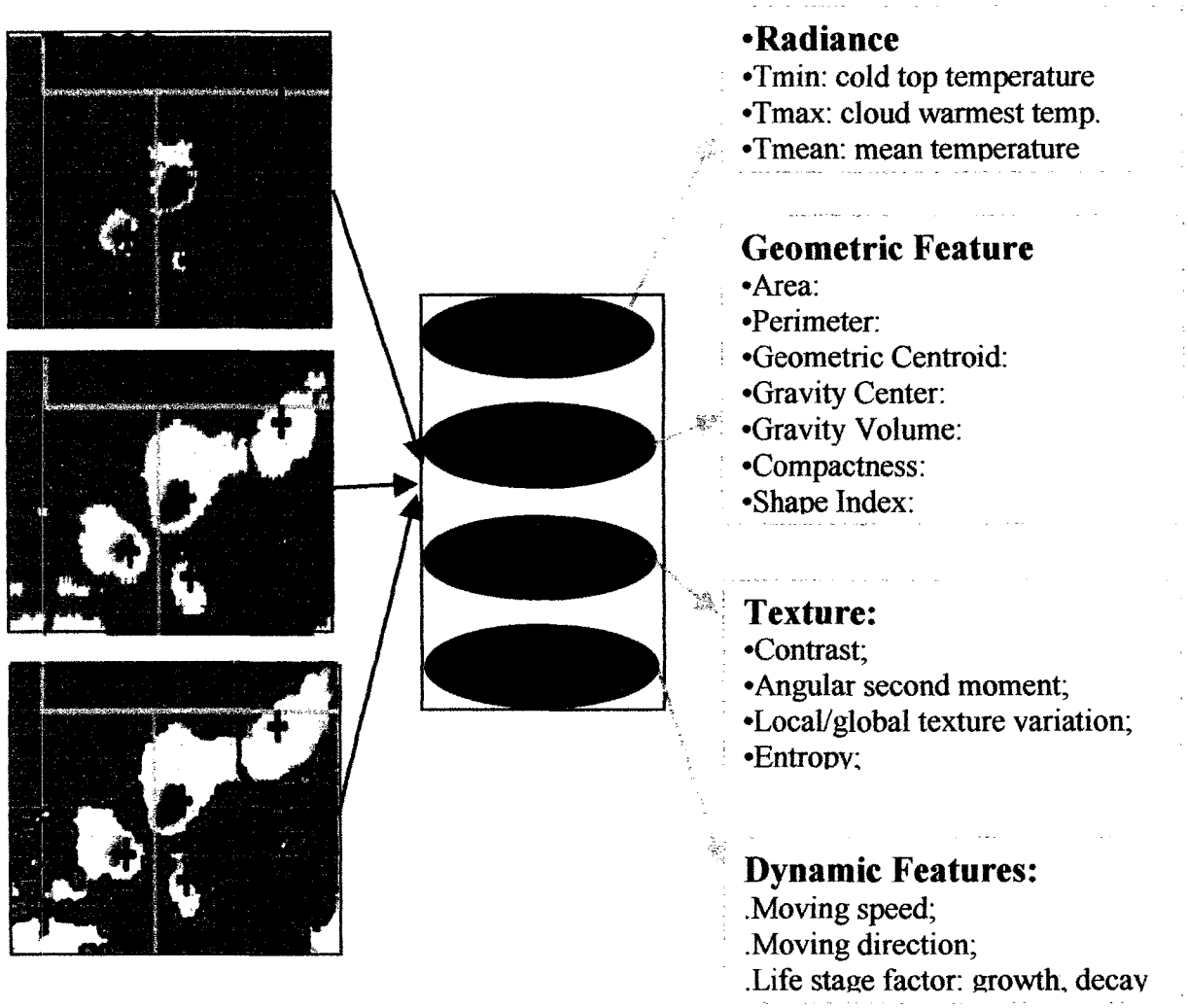

Figure 3.8 Four categories of cloud feature extraction at various cloud heights.

CHAPTER 4

CALIBRATION OF CLOUD CLASSIFICATION SYSTEM

4.1 Introduction

As mentioned in previous chapters, the network parameters of the proposed CCS rainfall estimation model need to be calibrated with high quality observation data. In this chapter, we present a case study of CCS for small-scale rainfall estimation (down to the instantaneous and pixel scale). The CCS model is calibrated using a 30-day period of data (June 1999 located at 25°-45°N and 100°-130°W region) and then tested on other time periods. In section 4.2 of this Chapter, the study area and input preprocessing are described. Section 4.3 presents the CCS network structure. Section 4.4 analyzes the insight into the relationship between cloud feature inputs and output rain rates/rain-volume distribution yielded by the design of the CCS model structure. Section 4.5 describes the verification methods for satellite rainfall estimation. Section 4.6 provides the results of preliminary validation, conducted over a range of time and space scales. Section 4.7 evaluates the model performance when applied at the cloud patch level. Section 4.8 concludes this chapter and discusses the possible improvements in CCS model.

4.2 Study Areas and Data Preprocessing

4.2.1 Study Area and Date for CCS model Calibration

The US Southwest region (25°-45°N and 130°-100°W) is selected for the model development and testing studies (Fig.4.1). IR brightness temperature images were collected by GOES satellite at every 30 minutes. Rainfall data are NCEP Stage IV hourly data collected by NEXRAD, operated by the U.S. National Weather Service, available at the NOAA website (http://dipper.nws.noaa.gov/hdsb/data/nexrad/nexrad.html). These data are 0.04° x 0.04° latitude/longitude resolution. CCS model was initially trained in "batch mode" with 30 days data (June, 1999) then applied to other time periods (July, 1999) to validate the model performance.

4.2.2 Data Preprocessing

4.2.2.1 Data Range Transformation

In any ANN model development process, familiarity with the input data is of the utmost importance (Kasstra and Boyd, 1995). Generally, different input variables span different ranges since each of them represents varying geophysical or statistical features. To ensure that all variables receive equal attention during model calibration, they should be scaled to uniform ranges that are commensurate with limits of the activation functions (Masters, 1993).

For example, the original input pattern is $X_i=[x_{i1},x_{i2},\ldots,x_{in}]$ for n input variables. By defining the lower limits as $L=[l_1,l_2,\ldots,l_n]$ and upper limits as $U=[u_1,u_2,\ldots,u_n]$, the value range of transformed input X` by the lower and upper limits is [0 1]:

$$X_i`=\frac{X_i}{U-L}=\left[\frac{x_{i1}}{u_1-l_1},\ldots,\frac{x_{in}}{u_n-l_n}\right]=[x`_{i1}, x`_{i2},\ldots, x`_{in}]. \text{ Where i=1, ..., m.}$$

4.2.2.2 Data Filtering and Regularization

To reduce overlapping information in the input pattern space, a filtering and regularization approach was designed by Hsu (1996). For this study, the data filtering is especially imperative because warm and small-sized clouds are dominant but unimportant due to their tiny contribution of rainfall. Large portion of CCS network space would be occupied by the over-abundant yet minor important information if without proper pre-screening. Data filtering and regularization ensure that the network space could be proportionately representative of the importance of training data domain by propagating equally weighted input values. To start, predefined regular grids are defined from all input variables. Each variable is divided into 10 equally spaced grids, and the grid center is used to represent all the data located in each grid. By passing all the calibrating input data through those grids, grids counted with at least one data are preserved; grids with no data in them are discarded. All the selected grid center data are then placed as input data to train the connection weights in the CCS model.

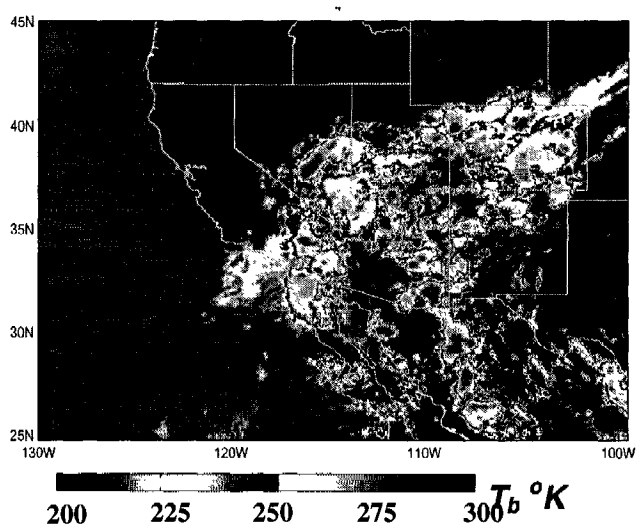

(a) GOES 8/9 satellite IR brightness image

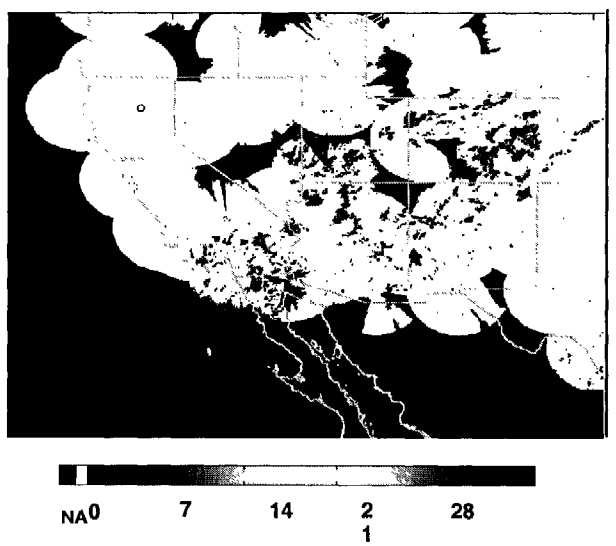

(b) NEXRAD network radar rainfall map

Figure 4.1 Calibration Domain for CCS over 25°-45°N and 130°-100°W region at 0.04° x 0.04° spatial resolution

4.3 Calibration of CCS Model

4.3.1 Feature Selection

The detailed segmentation procedure is descried in Section 3.2. The vital requirement for successful estimation of rainfall using this model is the selection of input variables that provide sufficient information to enable proper discrimination of cloud patch types.

In this study, a primary selection of cloud features is listed in Table 4.1. Figure 4.2 illustrates the relationships between the selected cloud features and rainfall/raining-probability of cloud patches from the training data in June 1999. These features exhibit various sensitivities to rainfall and raining-probability. Additionally, Section 4.5 also quantitatively discusses that these features yield insight into the relationship between input features and cloud-rainfall characteristics. Using the cloud rainfall and cloud raining-probability as two of the criterion, the features selected in this research are included in three categories: coldness features, geometric features, and texture features. The first category includes T_{min} and T_{mean} associating with the cloud brightness temperature; the second is derived from the geometric properties of cloud patch including *AREA* and SI; the third one is texture variation of cloud brightness temperature including *STD*, $MSTD^5$, STD^5_{std}, *TOPG*, and *ASM*. All these features are detailed in Section 3.3.

Excluding the global features (T_{min} *and TOPG*), all the other features are hierarchically calculated at vertical cloud height levels of 220K, 235K, and 253K. Default values are assigned for clouds at non-existing colder level (see Fig. 4.3). For instance, the *AREA* feature of cloud patch (outlined by box) in Figure 4.3a only computed at existing height levels 253K and 235K, the default value of 0 assigned to level 220K.

The vertical information will be interpreted and propagated into the cloud type classification. Features calculated at hierarchical vertical levels emphasize information at different aspects of a cloud patch. Generally, features at the 253K height level give overall information of a defined cloud; features at the 235 K level emphasize clod cloud regions with higher possibility of precipitation release; features at the 220K level supply information that focuses on the super cold core of the cloud (cloud overshooting top).

Table 4.1. The selected cloud patch input feature for the CCS model

Coldness Features of Cloud Patch:
(1) Minimum temperature of a cloud patch (T_{min})
(2) Mean temperature of a cloud Patch (T_{mean})
Geometric Features
(3) Cloud patch area (AREA)
(4) Cloud Patch Shape Index (SI)
Texture features (referring the brightness temperature texture)
(5) Standard deviation of cloud patch (STD)
(6) Mean value of local standard deviation of cloud patch ($MSTD^5$)
(7) Standard deviation of local standard deviation of cloud patch (STD^5_{std})
(8) Gradient of cloud cold top brightness temperature (TOPG)
(9) Gray images' texture (Angular Second Moment)

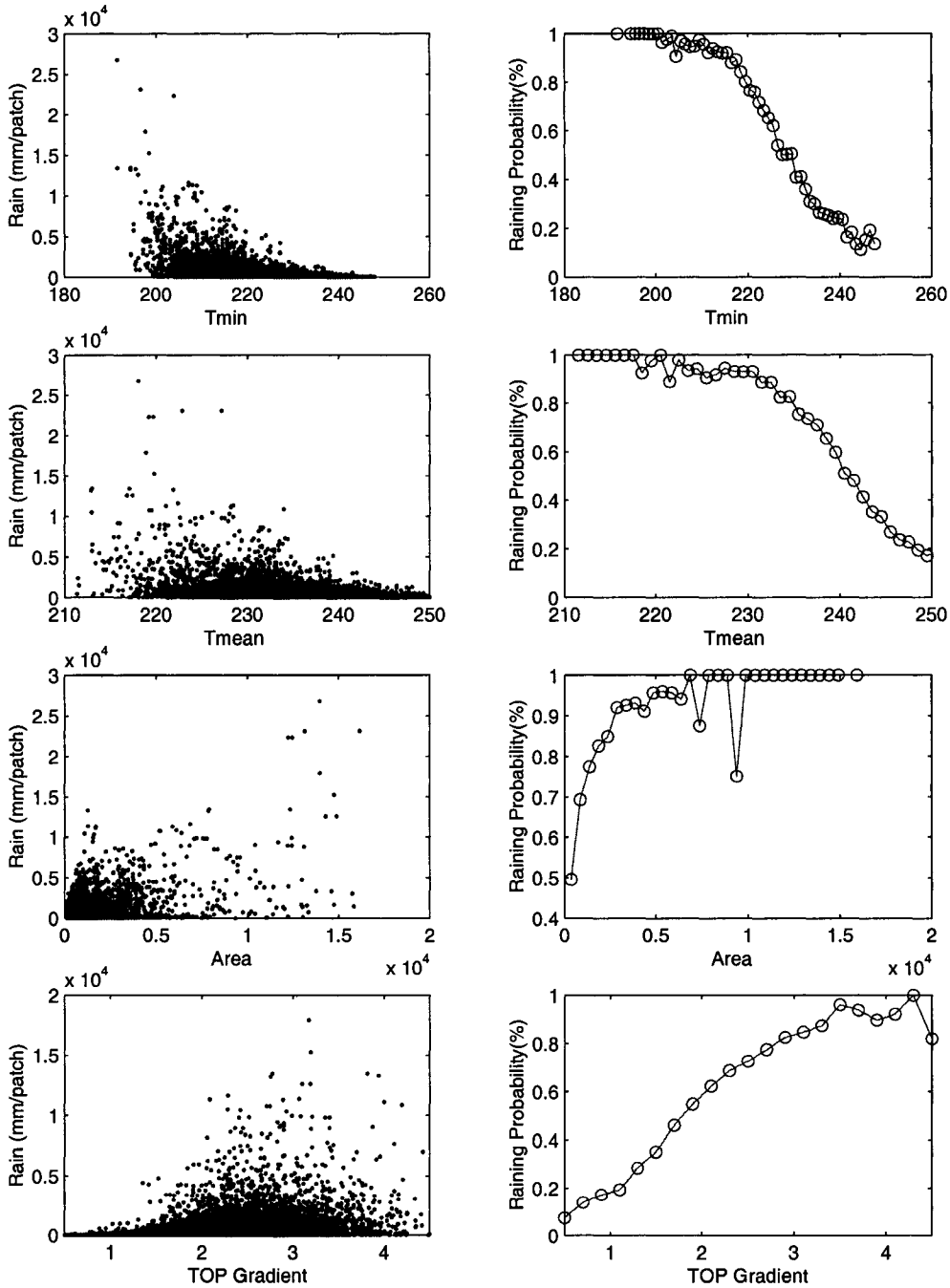

Figure 4.2: Relationships between cloud features and rainfall volume (left column) and raining probability (right) of cloud patches (based on the training data).

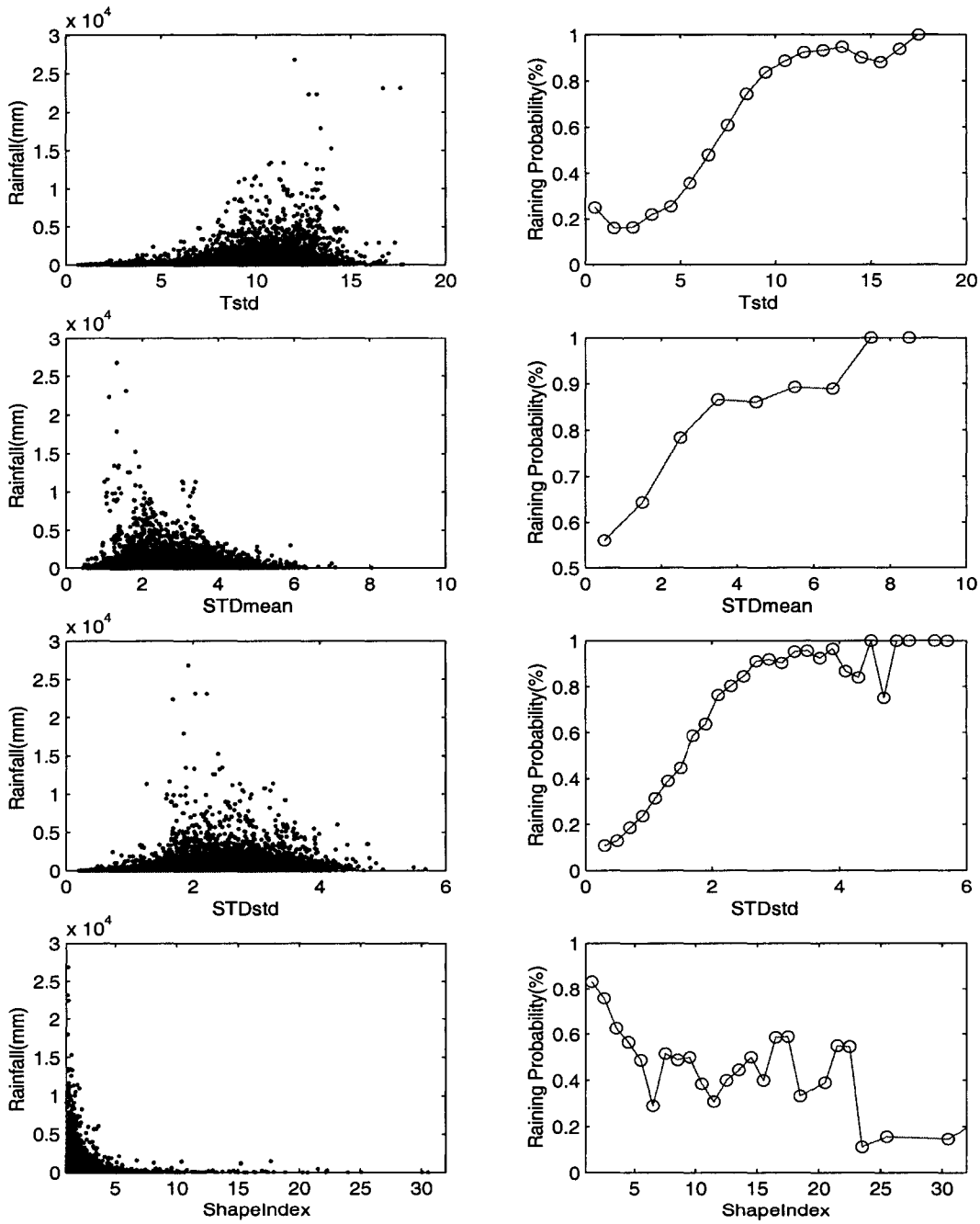

Figure 4.2: continued from previous page.

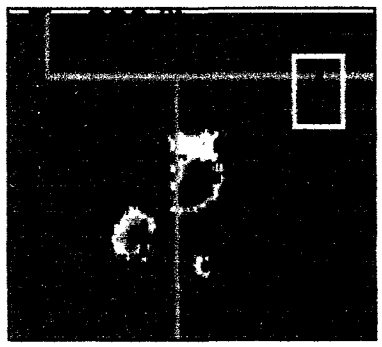

(a)

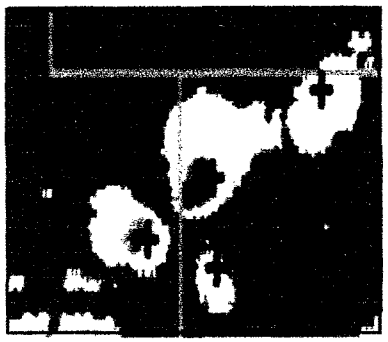

(b)

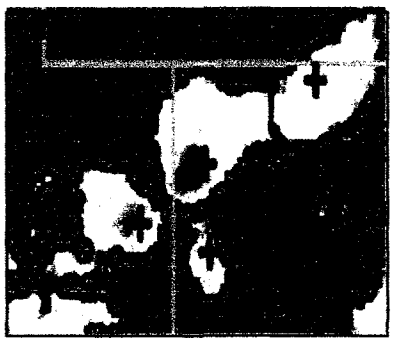

(c)

Figure 4.3: Cloud patch feature extraction at three incremental temperature levels (a) T=220K height level; (b) T=235K height level; (c) T=253K height level.

4.3.2 CCS Model Architecture

To implement CCS model, the cloud feature input and the number of nodes in SOFM layers must be specified. The model structure used to generate the rainfall estimates reported in this study is shown in Fig 4.4. The CCS, a satellite-based cloud type classification and rain estimation system, consists of three relevant procedures in the order of data flow: (a) a hybrid cloud segmentation algorithm (THT-SSRG) which separates cloud images into cloud patches; (b) a cloud feature selection procedure which extracts the precipitation-informative feature information at various cloud height levels; (c) a Self-Organizing Nonlinear Output (SONO) network which groups cloud samples into a number of well-organized cloud types and identifies the classified cloud types and their characteristics of surface rainfall distribution. The CCS network structure consists of 23 normalized input cloud features (Table 4.1) in the input layers and 400 nodes arranged in a 20 x 20 matrix in the SOFM classification layer (Fig4.4(c)), as well as a nonlinear output cloud-precipitation relationship mapping layer (Fig 4.4(d)).

4.3.3 The Calibration of SONO Architecture

The structure of SONO includes three layers: a cloud feature input layer, SOFM cloud classification layer, and Nonlinear Output cloud-precipitation mapping layer (see Figure 4.4 (b, c, d)). A powerful feature of the SONO network is that the training of SOFM layer and Nonlinear Output mapping layer could be decoupled, which enables the network to rapidly process a large volume of data. The detailed calibration of SONO is presented in the last Section of Chapter 2.

4.3.3.1 Calibration of SOFM Classification Layer

After feature extraction procedure, an unsupervised clustering using of a technique called self-organizing feature map (SOFM) (Kohonen, 1982; Hsu et al., 1997, 1999) is selected to classify the cloud patches into organized map of cloud clusters on basis of the cloud features under categories of coldness, geometry, and texture (Table 4.1). As its name suggests, SOFM organizes cloud input features to a discrete two-dimensional SOFM connection weights map, which preserves the topographic order of the inputs space (Hecht-Nielsen, 1990).

The SOFM firstly performs the distance calculation of input feature vector x and connection weights w as equation 4.1.

$$d_j = [\sum_{i=1}^{n0} (x_i - w_{ji})^2]^{1/2} \quad where \quad j = 1, \ldots n_1 \tag{4.1}$$

The competition occurs in the SOFM classifier layer, which locates a node that has minimum distance d_c between the feature vector and connection weights of node j in SOFM layer as the winner node.

$$d_c = \min(d_j), \quad where \; j = 1, \ldots, n_1 \tag{4.2}$$

Here, the SOFM clustering algorithm is used to sort out the similarity in the cloud features, while feature vectors similar to each other are classified in the same group. In each classified cloud feature group, the selected patch features are very similar. SOFM classification essentially enables CCS to search for a different curve for each cloud cluster that is characterized with similar cloud features. Thus, CCS is also a cloud patch-

based distributed rainfall estimation system that dispatches the best matching curve for each cloud patch to estimate rainfall.

The training of connection weights of the SOFM layer results in an organized clusters map (detailed in Section 2.5.1). Each node of the SOFM map represents a cloud type that consists of similar cloud features.

4.3.3.2 Calibration of Nonlinear Output Layer

The output layer has the same number and arrangement of nodes as the SOFM layer (See Figure 4.4 (d)); each node has one-to-one correspondence with its counterpart in the SOFM layer. Based on this arrangement, it can detect and map the cloud-precipitation distribution relation for each cloud cluster classified by the SOFM.

For each cloud cluster, coincident data pairs of GOES IR_{Tb} and the collocated surface rainfall (RR) from ground observation were collected. To derive an optimized IR_{Tb}-RR relationship for each cloud cluster, the Probability Matching Method (PMM) of Atlas et al. (1990) is used to match the histograms of coincident RR (from high to low rain rate) and IR_{Tb} (from cold to warm) observations such that the proportion of the RR distribution above a given rain rate is equal to the proportion of the IR_{Tb} distribution below the associated IR_{Tb} threshold value.

After histograms match of IR_{Tb} and RR data pairs, each classified SOFM group (j) is specified a nonlinear exponential function to fit the IR_{Tb}-RR relationship as follow:

$$RR^j = v^j{}_1 + v^j{}_2 \cdot \exp[v^j{}_3 \cdot (IR_{Tb} + v^j{}_4)^{v^j{}_5}] \tag{4.3}$$

Where RR is the rainfall rate (mm/hour),

IR_{Tb} is the cloud top brightness temperature (^{o}K), and

v^{j}_{1}, v^{j}_{2}, v^{j}_{3}, v^{j}_{4}, and v^{j}_{5} are parameters with respect to SOFM group j.

Because the IR_{Tb}-RR function is nonlinear, regression parameters cannot be found by linear least searching algorithm. A "batch" training procedure based on Multi-Start Downhill Simplex (MSDS) is used (Johnston and Pilgrim, 1976; Singh, 1995; Duan et al., 1992). Simplex procedure is a direct search approach, which could converge fast to the parameter with a minimum cost function. However, there is no guarantee for locating the parameters in a global optimal solution. Duan et al. (1992) demonstrated that the Downhill Simplex procedure has a single-start failure probability of approximately 65% whereas the MSDS procedure reduces failure rate 1 in 100 (99% success) with only 12 starts to find the global optimal. The training procedure for this portion is detailed in Section 2.5.2.

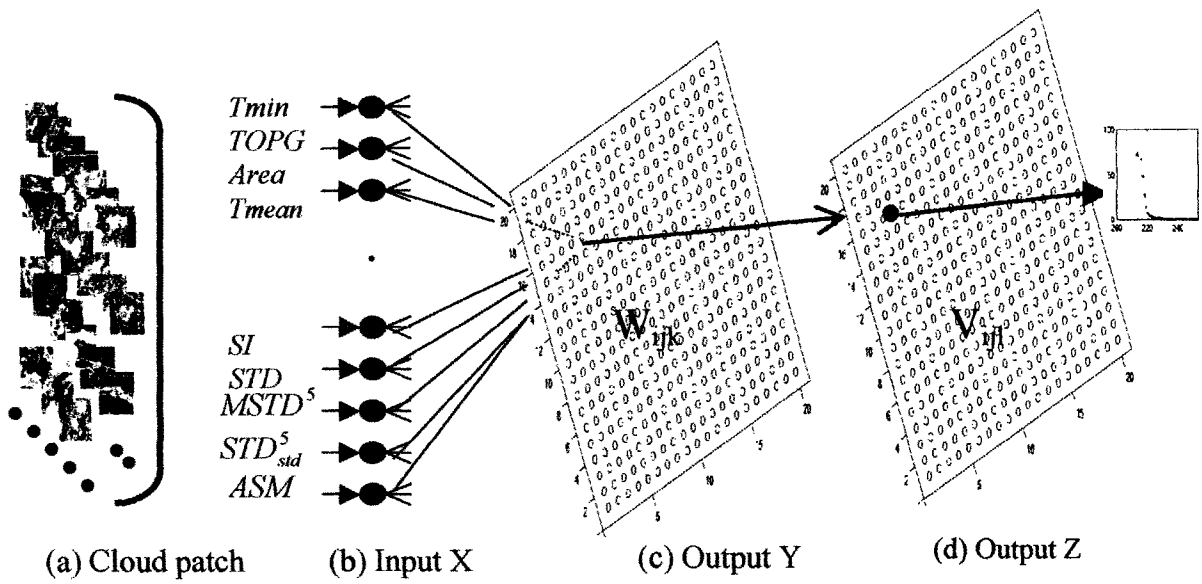

Figure 4.4 The CCS model structure: (a) cloud segmentation; (b) input layer-features of cloud patch; (c) Cloud classification SOFM layer; (d) the output layer: IR_{Tb}-RR distribution curves map corresponding to nodes of cloud types in (c).

(Note: X is cloud feature input; Y and Z are the output from SOFM and nonlinear Output layer, respectively; W and V are the connection weights for two layers' nodes. Where i=1,..., 20; j=1,...,2; l=1,...,5.)

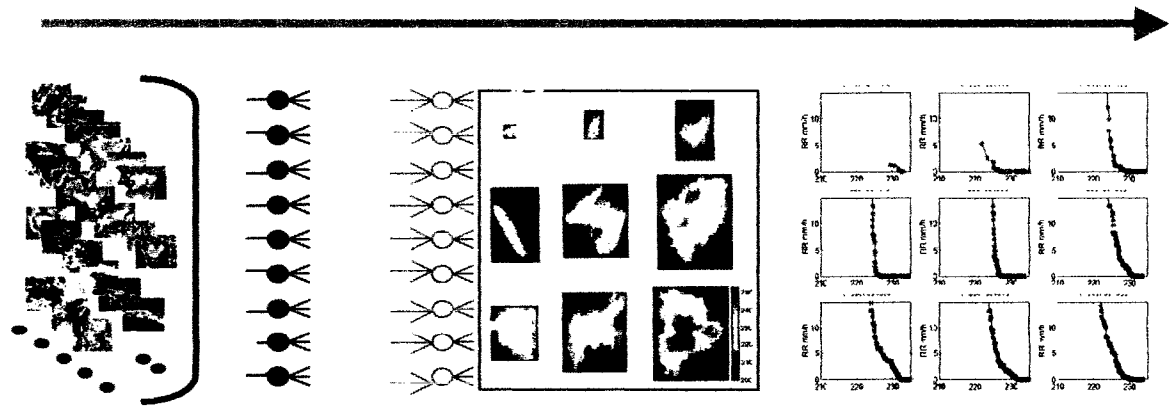

Figure 4.4 (continued) The data flow of CCS model: (a) cloud segmentation; (b) cloud feature extraction; (c) cloud classification; (d) IR_{Tb}-RR distribution matching and fitting curves calibration for each classified cloud cluster.

4.4 Insights Provided by CCS Model

The key to successful use of CCS with neural network training is to identify a broad and informative set of input features (input variables) that, taken together, provide adequate discrimination to clearly classify every cloud patch into its most similar cluster and, therefore, construct a nonlinear mapping function to approximate each properly classified cloud-precipitation situation.

4.4.1 Sample Distribution on SOFM Nodes

The SOFM and Nonlinear Out mapping layer are both designed with 20 x 20 nodes arrangement. Each node represents a classified cloud type. After extensive calibration, the SOFM organizes the cloud patches into different nodes. As shown in Figure 4.5, each of the SOFM node contain various number of cloud patch samples. The minimum number of cloud patch samples in nodes is 51 and the maximum is 855. The distribution of cloud sample number mimics the percentage of occurrence of different cloud types. For instance, the nodes holding small and warm clouds construct the tall peak of cloud samples in figure 4.5.

4.4.2.Theoretical Cloud Clusters

As mentioned in Section 3.3, cloud patch features are selected from the following three categories: coldness, geometric, and texture features. In each feature space, it is literally easier to specified it into 2-3 sub-categories, such as T_L, T_M, and T_H refer to the low (cold), medium, and high (warm) temperature clouds, A_L, A_M, A_H refer to the small,

medium, and large size of clouds, and S_L and S_H refer to the low texture variation (stratiform) and high texture variation (convective) clouds, respectively. In addition, patch averaged rain-rates are specified as R_L (low averaged rain rate), R_M (medium averaged rain rate), and R_H (high averaged rain-rate); Patched rainfall (volume) is assigned as V_L (low total rain volume), V_M (medium rain volume), and V_H (high rain volume). R unit is mm/hr per pixel within cloud; V unit is mm/hr per cloud patch. The three categories (T, A, and S) constitute 18 (3x3x2) theoretical clusters of clouds. The theoretical cloud clusters and its precipitation characteristics are examined in Table 4.3 using the calibration data sets of this study.

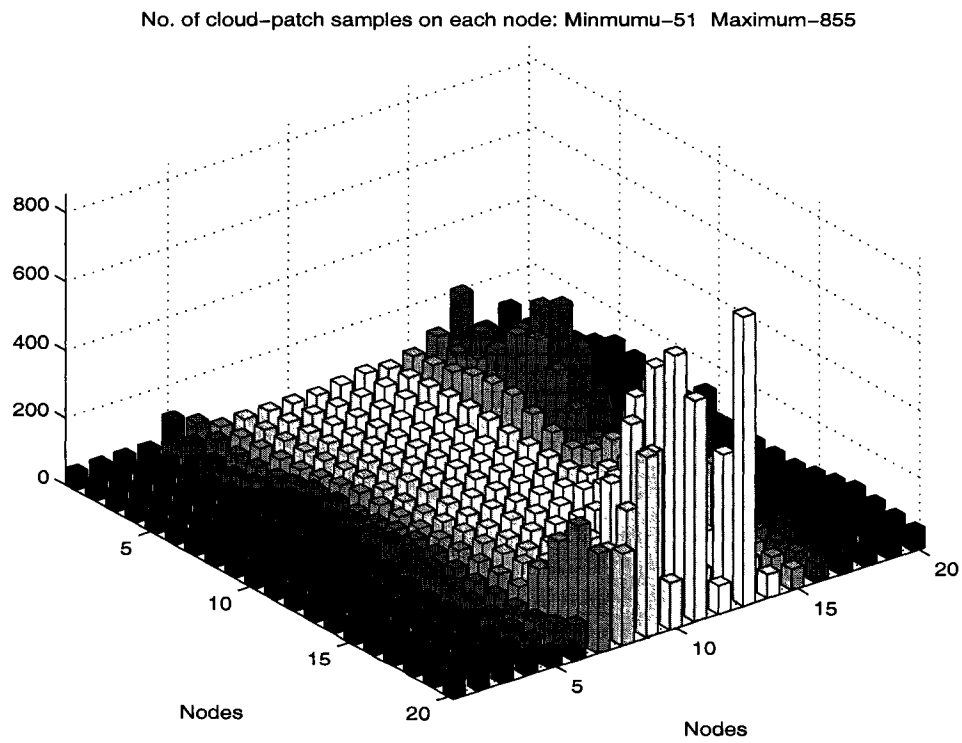

Figure 4.5 Number of cloud patch samples located on node of SOFM map after training

4.4.3.The CCS Classified Cloud Clusters and Their Precipitation Characteristics

The success of the CCS model is dependent on the coupling of two components: the classified cloud types on the SOFM layer and the corresponding IR_{Tb}-RR distribution curves on the "output map". After extensive calibration, Figure 4.6 illustrates the value distribution of cloud features on 20 x 20 matrix of SOFM map. Figure 4.6a shows the contour map of cloud patch average rainfall volume (from monthly training data set) associated with 20 x 20 nodes of SOFM. Figure 4.6b shows the contour map of cloud patch average rain rate associated with the same 20x 20 nodes of SOFM while figure 4.6c-g and Figure 4.6i show the some corresponding maps of the input features of cloud types: c-shape index (SI); d-minimum temperature (T_{min}); e-gradient of cloud top (TOPG); f-mean of local texture variation ($MSTD^5$); g-cloud area (Area); i-overall cloud texture variation (STD).

Table 4.2 Connection weights values of input features and precipitation characteristics for seven typical cloud clusters on SOFM layer

	T_{min} (K)	Area (Pixel)	TOPG	$MSTD^5$	SI	STD	Rain rate (mm/pixel)	(mm/patch) Rain volume
Cluster 0	>245	<100	<0.5	<0.5	>15	<2	<0.1	<10
Cluster 1	235~245	100~1000	~1	1	5~10	<4	0~0.5	<100
Cluster 2	235~245	100~1000	~3	3.5	~5	4~8	0.5~0.1	<1000
Cluster 3	215~235	500~4000	~1	2.5	1~3	6~8	0.1~0.5	500~2000
Cluster 4	215~235	500~4000	~3.5	4	~4	8~10	1~1.5	1000~2500
Cluster 5	<215	1000~3500	~4.5	5	1~3	8~14	1.5~4.5	2000~3500
Cluster 6	<215	1500~5000	~1.5	3	1~3	>10	0.5~1.5	3000~6000

First, notice that the SOFM process has organized the cloud patches so that seven significant clusters can be identified on the output map (see Figure 4.7a). Figure 4.8b shows plots of the typical IR_{Tb}-RR curves from Figure 4.7a. Table 4.2 summaries the

coupling of IR_{Tb}-RR curves on "output" layer and the features on SOFM layer. The "output map" of IR_{Tb}-RR distribution curves matches the input feature maps well.

Comparison of GOES cloud-top temperature in the IR images against collocated radar images has demonstrated that convective thunderstorms are characterized by very low cloud-top temperature (195-210K) and rapid change in texture of the cloud-top surface. From the satellite-based infrared cloud images, cloud types at various heights are visually detectable. Well-developed convective clouds are usually with cold overshooting top, tight temperature gradient, and large local pixel temperature variations. This type of clouds usually produces a large amount of rainfall in a short time period within few hours. Stratiform clouds, on the other hand, contain mild temperature gradient and low local pixel temperature variations. Mild rains or no-rain are usually associated with such kind of layered cloud. From the visual features, human are able to recognize the difference between these two cloud types effectively. Similarly, if the features from the cloud systems are adequately extracted, through an effective classification system, we will be able separate different cloud systems more effectively, and hence improve our understanding of cloud rainfall relationship.

Following Table 4.2, the seven typical IR_{Tb}-RR cluster (Figure 4.7a) represent the convective and stratiform precipitation system to their cloud clod top pixel temperature and patch size are explained below:

- **Cluster 0 (T_H-S_L):** warm no-rain cloud; the coldest temperature is higher than 245°K.

- **Cluster 1 (T_H-S_L):** The coldest patch pixel temperature is around 235°K ~ 245°K, in addition that the texture index are low (TOPG: ~1; MSTD[5]: ~1; STD: <4). As presented in Figure 4.7b, this type of cloud patches consists of very mild slope of T_b-R distribution. The averaged patch rain-rate is around 0~0.5 mm/hr, while the patch rain volume is lower than 100 mm/hr-patch. This type of cloud patches is classified as low (warm) stratiform clouds.
- **Cluster 2 (T_H-S_H):** The coldest pixel temperature of this group is similar to that of the cloud group in Cluster 1. The texture index, however, are much higher (TOPG: ~3; MSTD[5]: ~3.5; STD: 4~8). The slope of the T_b-R distribution is steeper than cluster 1's. The averaged pixel rain-rate in the patch is around 0.5~1.0 mm/hr, the total rain volume (~1000 mm/hr-patch) is about 10 times higher than Cluster 1's. This type of cloud is classified as low (warm) convective clouds.
- **Cluster 3 (T_M-S_L):** The coldest patch pixel temperature is around 215°K ~ 235°K and the texture index are low (TOPG: ~1; MSTD[5]: ~2.5; STD: ~6-8). Averaged pixel rain-rate is around 0.1~0.5 mm/hr, accumulated patch rain rate is around 500~2000 mm/hr. As presented in Figure 4.7b, this type of cloud patches consists of mild slope of T_b-R curve and is classified as medium-height stratiform clouds.
- **Cluster 4 (T_M-S_H):** The coldest patch pixel temperature is around 215°K ~ 235°K and the texture index are higher (TOPG: ~3.5; MSTD[5]: ~4; STD: ~8-10). Averaged pixel rain-rate is around 0.5~1.0 mm/hr, and accumulated patch rain-rate is around 1000~2500 mm/hr. As presented in Figure 4.7b, this type of cloud

patches consists of steeper slope of T_b-R curve and is classified as medium-height convective clouds.

- **Cluster 5 (T_L-S_H):** The coldest patch pixel temperature is lower than 215°K and the texture index are higher (TOPG: ~4.5; MSTD[5]: ~5). Averaged pixel rain-rate is around 1.5~4.5 mm/hr, and accumulated patch rain-rate is around 2000~3500 mm/hr. As presented in Figure 4.7b, this type of cloud patches consists of steeper slope of T_b-R curve and is classified as medium-height convective clouds.
- **Cluster 6 (T_L-S_L):** The coldest patch pixel temperature is lower than 215°K and the texture index are low (TOPG: ~1.5; MSTD[5]: ~3). Averaged pixel rain-rate is around 0.5~1.5 mm/hr, and accumulated patch rain-rate is around 3000~6000 mm/hr. As presented in Figure 4.7b, this type of cloud patches consists of mild slope of T_b-R curve and is classified as height stratiform clouds.

When area (A_L, A_M, A_H) is considered in the six clusters to further categorize the output map, it becomes 18 clusters. Consequently, all of the cloud patches from training domain fall under 18 typical cloud types according to a combination of ranked categories (Table 4.3). All other cloud types are the transitional zones among the 18 clusters.

Table 4.3 The 18 typical cloud types and their precipitation characteristics.

Cloud types	S_L(stratiform)			S_H(convective)		
	A_L	A_M	A_H	A_L	A_M	A_H
T_L	No rain	R_L/V_L	R_L/V_L	R_L/V_L	R_M/V_L	R_L/V_M
T_M	R_L/V_L	R_L/V_M	R_L/V_M	R_M/V_L	R_H/V_M	R_M/R_M
T_H	R_M/V_L	R_M/V_M	R_M/V_H	R_H/V_M	R_H/V_H	R_H/V_H

4.4.4.The Distribution of Rain/no-Rain Thresholds

Another interesting feature provided by CCS is the derivation of IR rain/no-rain thresholds (*IR_{Tb}-Thd*) from the IR_{Tb}-RR output map, by defining the IR_{Tb} that corresponds to the rain rate 0.1mm/hr as optimum *IR_{Tb}-Thd*. Different *IR_{Tb}-Thd* values represent the substantial variation in the relationship between cloud characteristics and rain rate that result from pronounced variability of clouds and precipitation processes over space and time.

The derivation of the *IR_{Tb}-Thd* map (Figure 4.8) reflects the variation of *IR_{Tb}-Thd* in various cloud types clusters. Considering the six clusters in Figure 4.7a, the average *IR_{Tb}-Thd* is very warm in cluster 0 (around 250K) and very cold in cluster 6 (below 225K). Cluster 1, 2, 3, 4 and 5 correspond with *IR_{Tb}-Thd* values of approx 240K, 245K, 235K, 240K, and 230K, respectively. The majority of the nodes' no-rain thresholds range between 230K-240K, which accounts for 80 percent of rainfall in this case study. Warm raining clouds do exist in cluster 1 with approx 250K no-raining thresholds, but their rain rate is small and contribute only about 2-5% percent to total rainfall.

The transitional value of *IR_{Tb}-Thd* existing from node to node provides compelling evidence for the previous studies such as AGPI (Adler et al., 1993) and UAGPI (XU et al., 1999), which calibrated the optimum *IR_{Tb}-Thd* for regional scale applications. However, CCS illustrates more variability and flexibility since the *IR_{Tb}-Thd* is derived from cloud-to-cloud instead of from region-to-region.

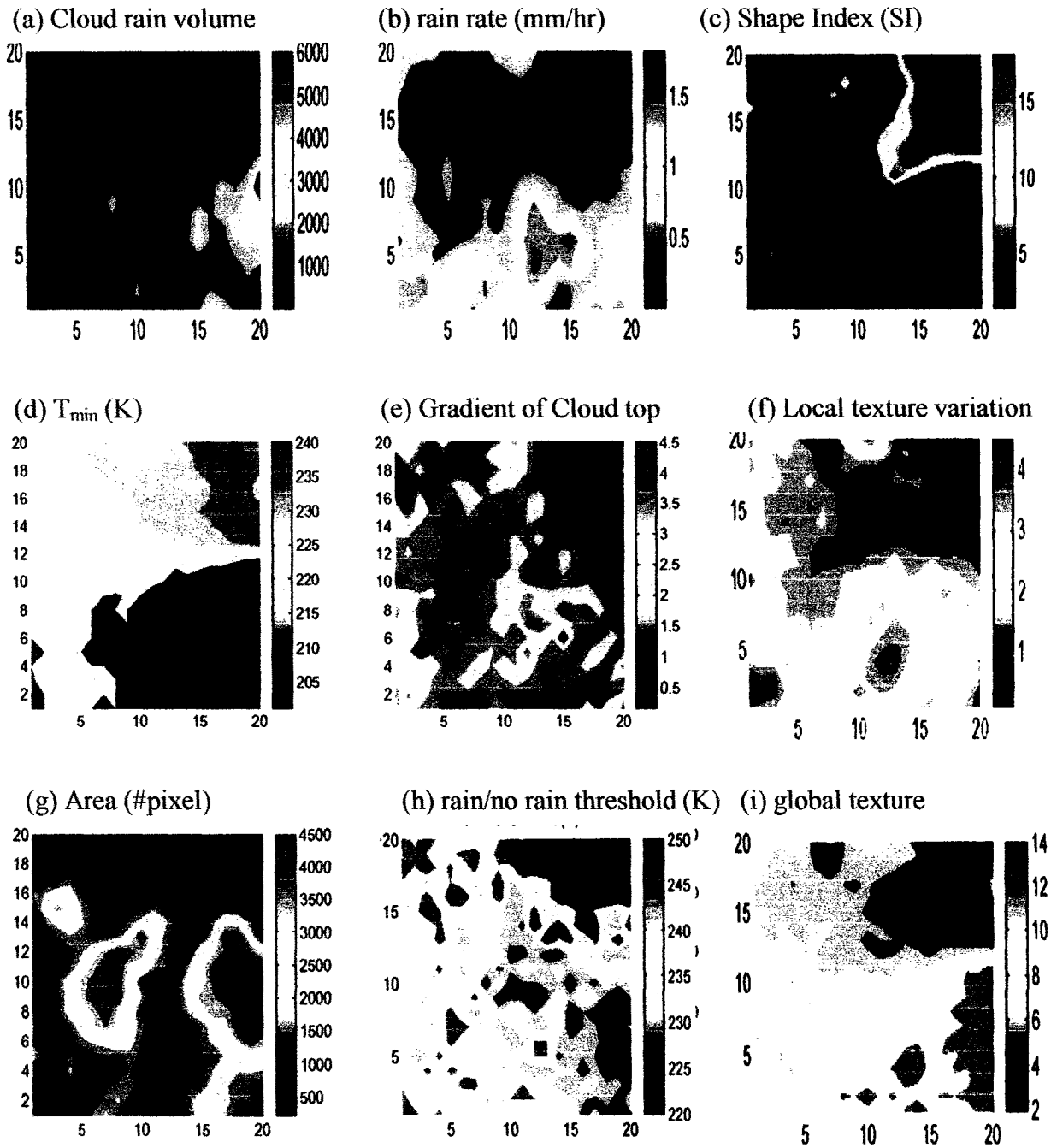

Figure 4.6: Contour maps of rainfall (a-b) and contour maps of connection weights on 20 x 20 SOFM classification layer to each cloud input features (c-i) after training.

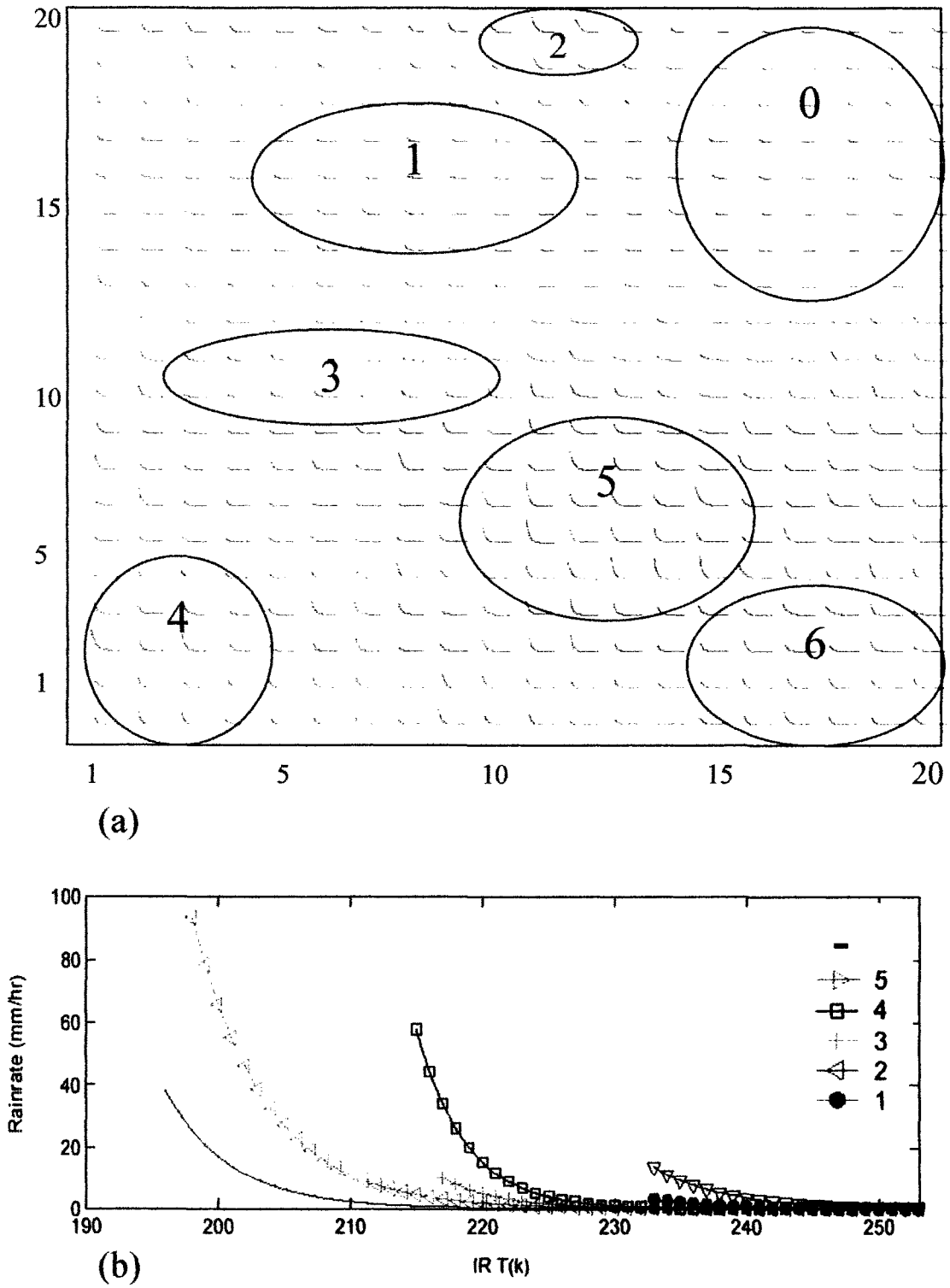

Figure 4.7: (a) the CCS 'output' IR_{Tb}-RR estimation curve map and its significant clusters, each curve corresponding to a node at SOFM layer; (b) the typical IR_{Tb}-RR curves corresponding to clusters in (a).

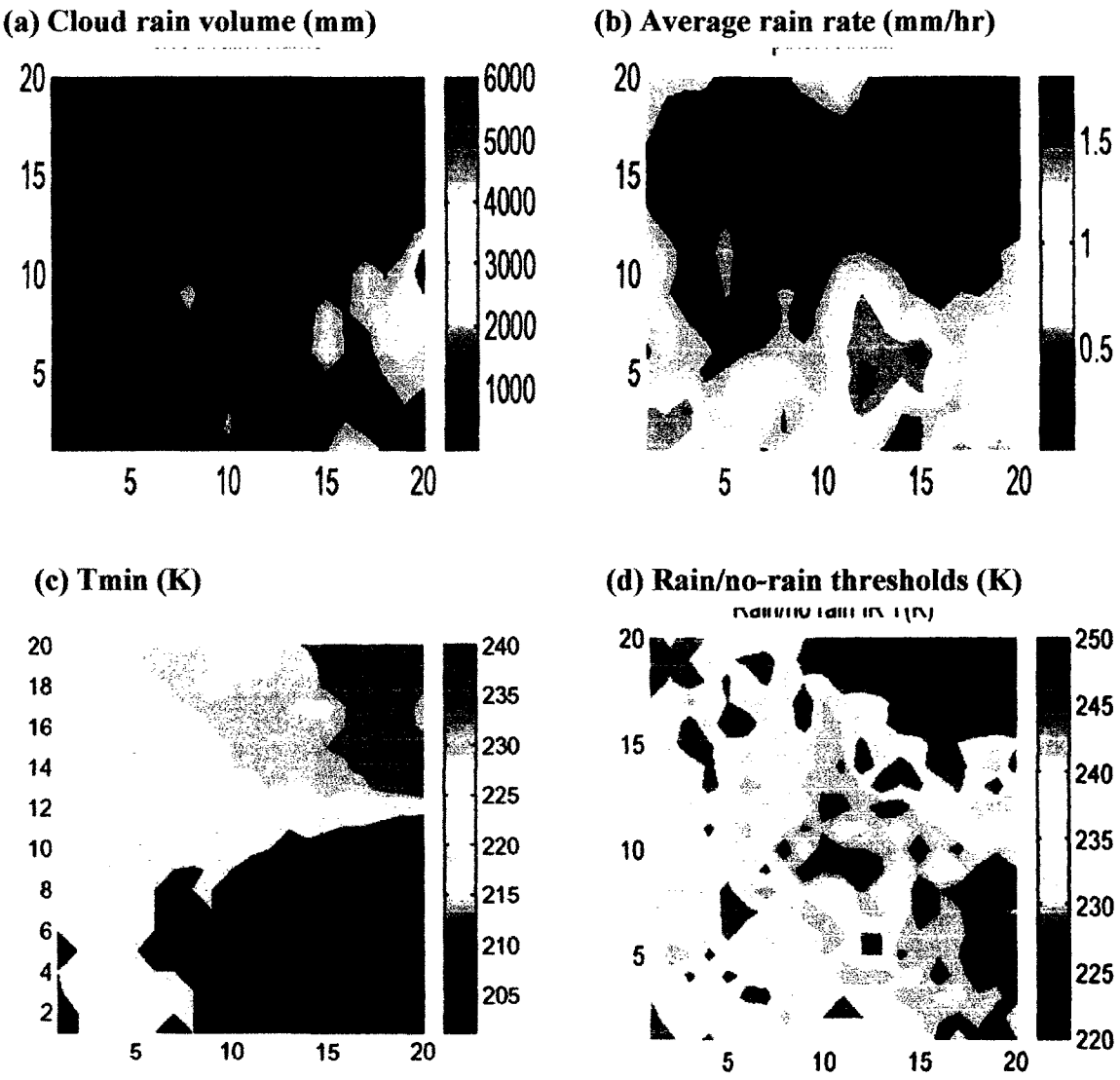

Figure 4.8. The contour maps of cloud rainfall volume, averaged rain rate, cloud top coldest temperature, and rain/no-rain thresholds on 20 x 20 nodes of SOFM classification layer after calibration of CCS model.

4.5 Verification Methods

A great deal of work has been done to validate climate-scale precipitation estimates against observation data with the usual statistics measurements of accuracy such as *bias, correlation coefficient*, and *root-mean-square-error*. For the quantity of interest in climate-scale, rainfall is accumulated over space and time (approx 2.5°, monthly, for example) so that the erroneous estimates on smaller spatial and temporal scales could cancel out each other.

Near real time satellite precipitation are becoming increasingly available and interesting to the wider community. Due to the high variability of rainfall system in small spatial and temporal scales, it is important to assess their accuracy and limitations by expending the validation from quantitative measurements to categorical verification such as the correspondence between the estimated and observed occurrence of rainfall events and success of the detection of raining pixels.

4.5.1 Validation Data

The main sources of rainfall "truth" data for satellite algorithm validation are observations from rain gauges and radar rainfall. The preliminary assumption behind the "truth" data is the observational error is random (unbiased) and is much smaller than the algorithm error. Rain gauge is the only instrument to give direct measurements of rain accumulation. However the 'point' measurements and temporal accumulation of gauge from minutes to hours are likely to be unrepresentative of satellite "snapshot" estimates. Radar observations are similar to satellite estimation in that they give "snapshot" in time

and area values in space with relatively high temporal and spatial resolution (~1km and 5~30 minutes). The disadvantage of radar data is that they are themselves indirect estimates of rainfall, and are prone to errors of calibration, attenuation, anomalous propagation, reflectivity-to-rain rate conversion, etc.

The most appropriate choice of validation data depends on the availability of the data, the resolution of the satellite estimates, and the needs of the users. For high temporal and spatial resolution satellite rainfall estimates, gauge-corrected radar estimates are generally preferable because merging of gauge and radar data within grid boxes reduces some of the random noise and regularizes the spatial distribution. The U.S. Next Generation Radar (NEXRAD) (WSR-88D) rain-gauge composite data (published by NCEP) is available at high spatial (4 x 4 km^2) and temporal (hourly) resolution, which makes it "ideal" for evaluation of the CCS estimates.

4.5.2. Verification Approaches

Subjectively, the very first step to validate precipitation estimates is to plot the estimates alongside the observations in order to visually compare the two. This subjectively visual comparison is called eyeball verification. The objective verification methods fall under two categories: continuous and categorical verification methods.

4.5.2.1. Continuous Verification Methods

The most commonly used statistics in the validation of satellite estimates are the continuous verification statistics measure the accuracy of continuous variable such as rain

amount and rain intensity. Defining M as satellite modeling estimates and G as ground data with data sample N, the continuous verification methods are described as follows:

- Correlation coefficient (CORR): the CORR measures the degree of correspondence between the estimated and the observed distributions and it is independent of bias. The definition of CORR is reference from the work of Achutuni and Borneman (1998) in the evaluation of the Interactive Flash Flood Analyzer (IFFA)

$$\mathrm{CORR} = \frac{N\sum_{i=1}^{N} G_i M_i - \sum_{i=1}^{N} G_i \sum_{i=1}^{N} M_i}{\sqrt{\left(N\sum_{i=1}^{N} G_i^2 - (\sum_{i=1}^{N} G_i)^2\right)\left(N\sum_{i=1}^{N} M_i^2 - (\sum_{i=1}^{N} M_i)^2\right)}}$$

- Bias (mean error): the satellite modeling estimates minus the ground data, averaged over the data set. Thus positive indicates over-estimation and vice versa.

$$\mathrm{BIAS} = \frac{\sum_{i=1}^{N}(M_i - G_i)}{N} = \bar{M} - \bar{G}$$

- Mean absolute error (MAE): the MAE measures the average of the error.

$$\mathrm{MAE} = \frac{\sum_{i=1}^{N}|M_i - G_i|}{N} = |\bar{M} - \bar{G}|$$

- Ratio: The ratio of mean of model rainfall to the mean of observation

$$\mathrm{Ratio} = \frac{\sum_{i=1}^{N} M_i}{\sum_{i=1}^{N} G_i}$$

- Root Mean Square Error (RMSE): the RMSE also measures the average magnitude of error but gives greater weights to the larger values.

$$\text{RMSE} = \sqrt{\frac{1}{N}\sum_{i=1}^{N}(M_i - G_i)^2}$$

- Bias as Ratio of Mean (BRM): the BRM is the measure of error in percentage of the averaged rainfall values

$$\text{BRM=BIAS/}\frac{\sum_{i=1}^{N} M_i}{N} = \frac{\sum_{i=1}^{N}(M_i - G_i)}{N} \Big/ \frac{\sum_{i=1}^{N} M_i}{N} = (\bar{M} - \bar{G})/\bar{M}$$

- Skill: this is a normalized parameter that takes into account the absolute error between estimation and the ground truth data divided by the sum of both. The best performance of the model is when the value SKILL is near one:

$$\text{SKILL} = 1 - \frac{\sum_{i=1}^{N}\frac{|M_i - G_i|}{(M_i + G_i)}}{N}$$

- The Linear Error in Probability Space (LEPS): Potts et al. (1996) designated LEPS to measure the error in probability space instead of in the unit of the variable itself.

$$\text{LEPS}=\frac{1}{N}\sum_{i=1}^{N}|\,CDF(M_i) - CDF(G_i)\,|$$

Where CDF is the cumulative density function of the variable.

Any of the above continuous verification methods can be used along with other methods to measure the degree of accuracy of rain amount or rain intensity.

4.5.2.2. Categorical Verification Methods

Categorical verification statistics measure the correspondence between the estimated and observed occurrence of events instead of amount/intensity of events. Most are based on a 2 by 2 contingency table of yes/no events (see Table 4.4).

Table 4.4 Rain / No Rain contingency table

		Ground Measurements G	
		Rain	No Rain
Modeling estimates M	Rain	Q1 (hits of yes)	Q3 (false alarms)
	No Rain	Q2 (misses)	Q4 (hits of no)

- Probability of detection (POD): This parameter measures the probability of detection of rain from the satellite model where some rainfall was observed. The best performance of the model is when POD is value one:

$$\text{POD} = \frac{Q_1}{Q_1 + Q_2}$$

- False Alarm Ration (FAR): the FAR gives the fraction of observed non-raining events that were diagnosed as raining ones. This parameter measures the relationship between the cases where rain was estimated but not observed and the total observed rainfall cases. The best value expected from this measure is zero:

$$\text{FAR} = \frac{Q_3}{Q_1 + Q_3}$$

- Threat Score (TS), also known as Critical Successive Index (CSI): the CSI measures the fraction of all events of estimated and/or observed that were correctly diagnosed. The indication of algorithm performance is same as the POD.

$$\text{CSI (TS)} = \frac{Q_1}{Q_1 + Q_2 + Q_3}$$

4.6. Preliminary Verification of CCS

4.6.1 Application to Daily Rainfall Estimation

4.6.1.1 Model Performance at Different Spatial Resolutions

Two days CCS derived rainfall estimates on 8-9 Jul 1999 over region 30°-40°N and 100°-120°W were compared with collocated NEXRAD radar rainfall. Maps of the daily rainfall estimates for these two days are shown in Figure 4.9 at 0.04° x 0.04° spatial resolution. Figure 4.10 shows the scatterplots and the statistical comparison of the two daily CCS estimates vs. radar at four different spatial scales (0.04°, 0.12°, 0.5°, and 1.0°). It shows that the correlation coefficient is above 0.5, 0.6, and 0.7 for the resolution at 0.04°, 0.12° and 0.24°, respectively.

4.6.1.2 Comparison with GPI and PERSIANN Algorithms

The performance of CCS daily rainfall is compared with that of GPI and PERSIANN after re-mapping to PERSIANN highest spatial resolution-0.25°x25°. CCS outperforms PERSIANN, especially with respect to correlation coefficient, which improves from 0.59 to 0.79 at July 8th and from 0.65 to 0.71 at July 9th (Table 4.5). The Figure 4.11 shows that PERSIANN rainfall estimates more averaged and less variation in spatial distribution but CCS demonstrates higher texture of rainfall distribution, which explains that the CCS estimates result in better correlation with Radar rainfall

distribution. In addition to the comparison with GPI, both the CCS and PERSIANN show significant improvement from GPI, particularly in the correlation and ratio.

Table 4.5 Inter-comparison statistics between GPI, PERISANN, and CCS estimates vs. gauge-radar observed rainfall

Daily 0.25^0x0.25^0	8 Jul 1999: 25^0N-45^0N; 100^0-125^0W			9 Jul 1999: 25^0N-45^0N; 100^0-125^0W		
	RMSE (mm)	Ratio	CORR	RMSE (mm)	Ratio	CORR
GPI	4.25	0.61	0.367	4.86	0.55	0.595
PERSIANN	2.89	1.17	0.590	3.27	1.21	0.650
CCS	2.03	1.01	0.790	2.12	1.05	0.715

Note: Originally, GPI (Arkin and Meisner, 1987) is calculated at large scale 2.5^0x2.5^0 grid and UAGPI (Xu et al., 1997) at 25km and above. In this study, all GPI and UAGPI were computed at 0.04^0x0.04o scale then aggregate into the desired resolution for the purpose of comparison. The GPI related algorithms were selected for comparison because they are infrared algorithms that have experienced popular use. It should be pointed out that this comparison is primarily for highlighting some of the improvements that we believe accrue from the CCS such as a distributed rainfall estimation model to dispatch the best-fitted nonlinear curve for different cloud patches to estimate rainfall.

The daily estimates, displayed in Figure 4.9 and 4.10, show that CCS achieved correlation coefficients of 0.55, 0.6, 0.72, and 0.80 for the approx 4-, 12, 50, 100-km grids, respectively. Shown in Figure 4.11 and Table 4.5, the comparison with GPI and PERSIANN of daily rainfall shows that CCS significantly outperforms both algorithms at correlation coefficient, root-mean-square error, and bias for 25km grids.

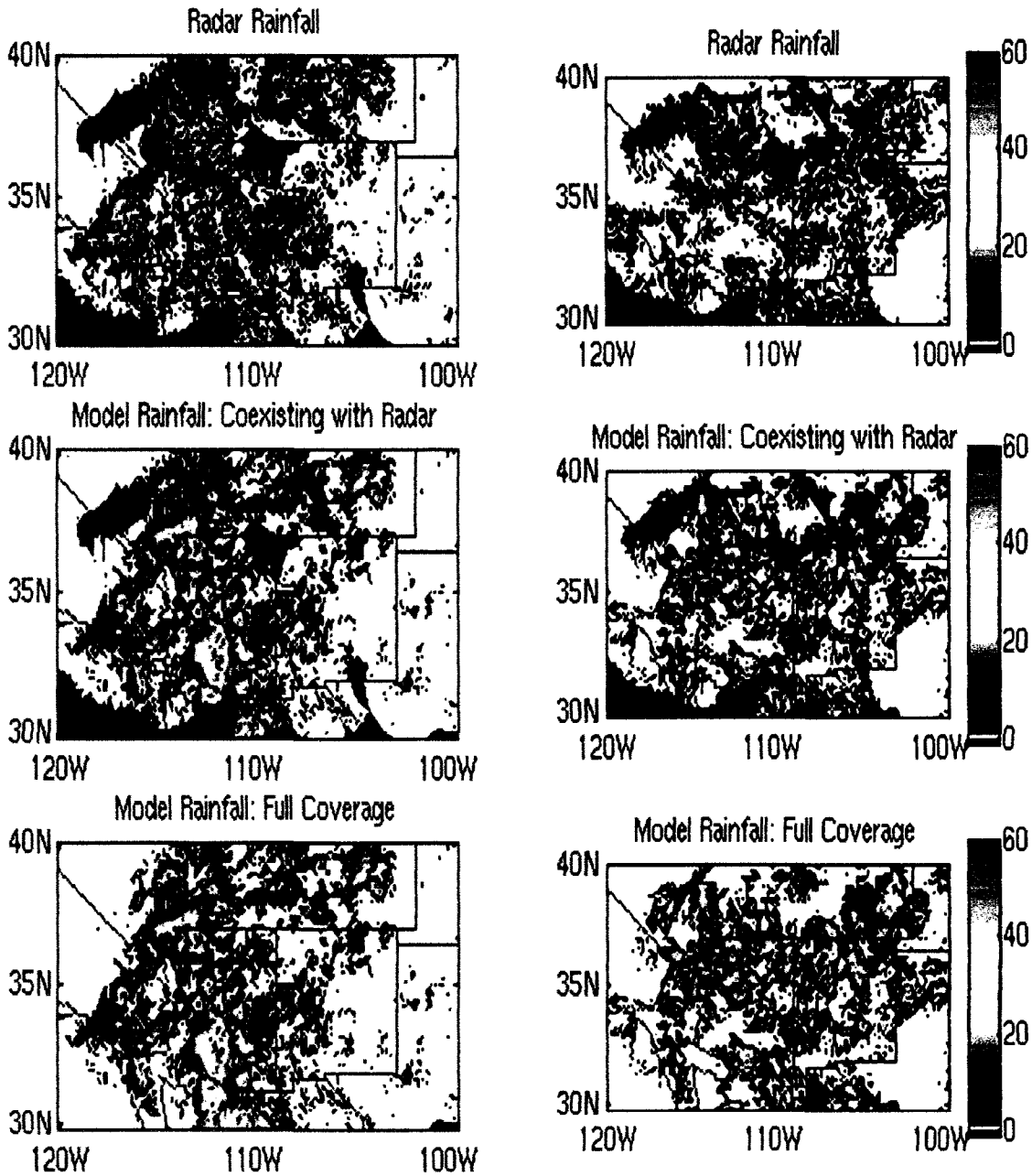

Figure 4.9. Plots of Radar vs. CCS-derived daily rainfall at 0.04° x 0.04° spatial scale for a region located at 30°-40°N and 100°-120°W on (left) 8 Jul 1999 and (right) 9 Jul 1999.

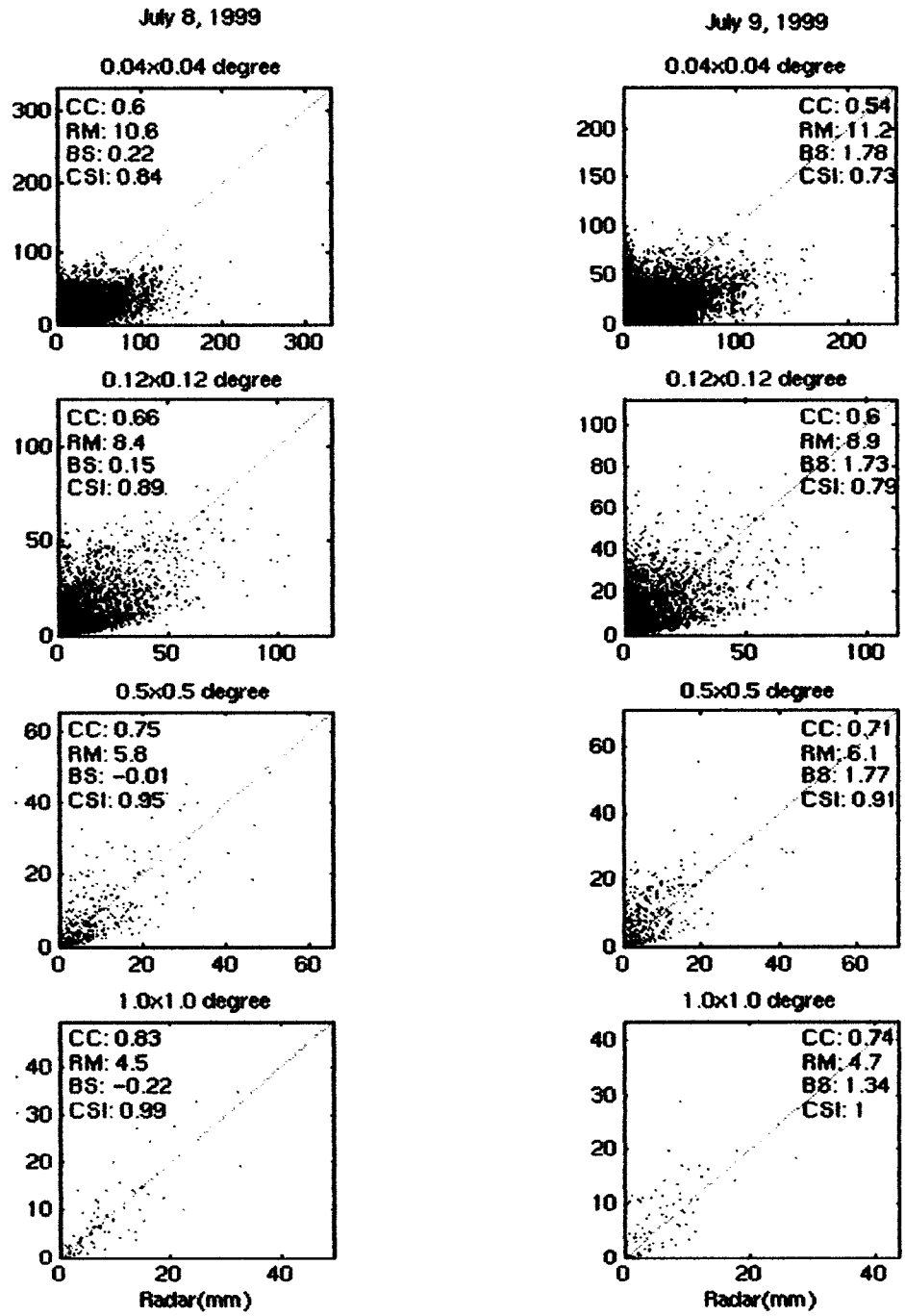

Figure 4.10. Scatterplots of Radar vs. CCS-derived daily rainfall totals at different spatial scales for a region located at 30-40°N and 100-120°W on (left) 8 Jul 1999 and (right) 9 Jul 1999.

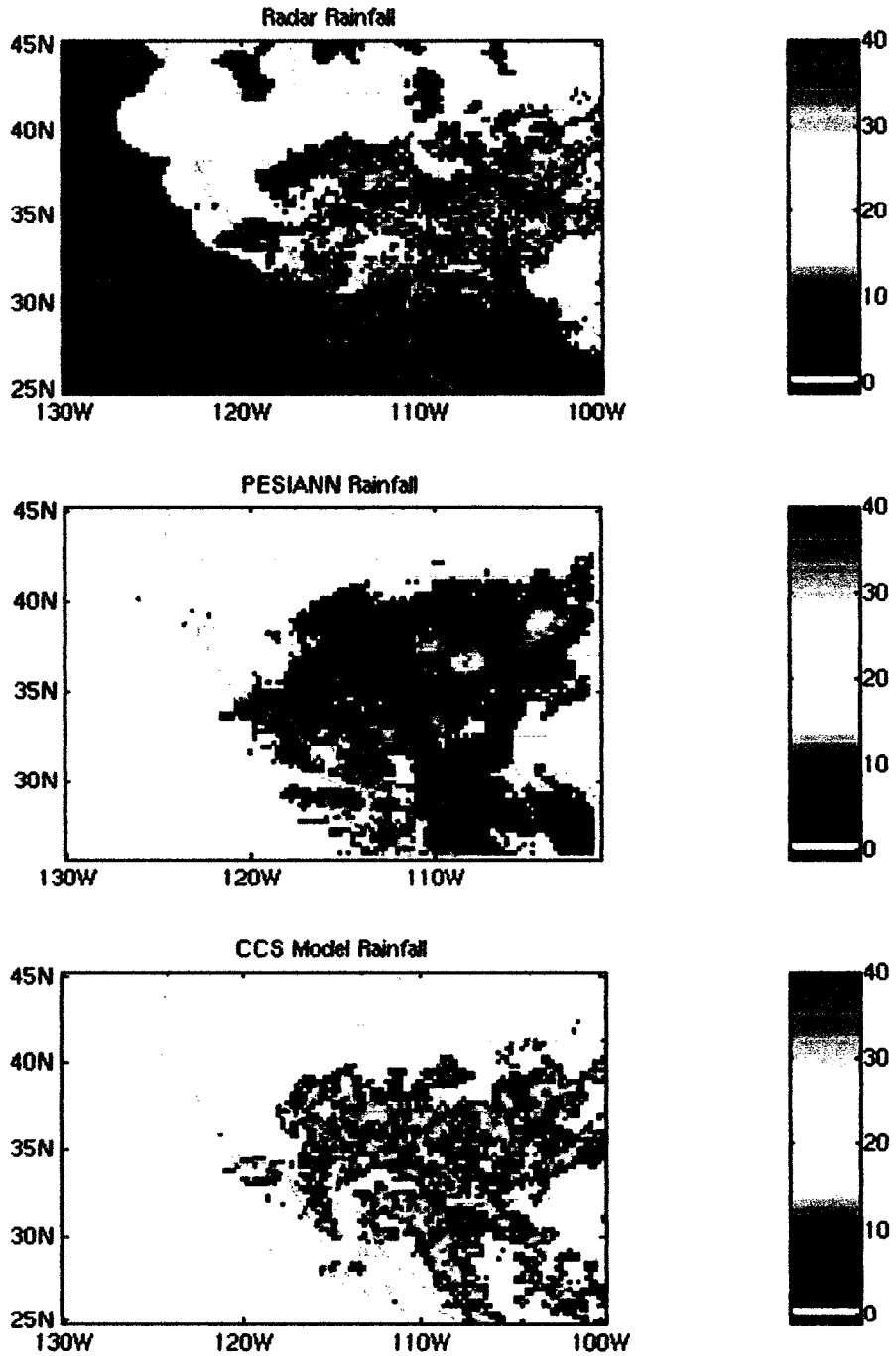

Figure 4.11. Comparison of CCS with Radar, PERSIANN daily rainfall total at 0.25° x 0.25° on July 9 1999

4.6.2 Application to Hourly Rainfall Estimation

The cases presented above compared the accuracies of CCS method with regard to producing estimates of daily rainfall. The goal, however, is to provide accurate rainfall estimates at high spatial and temporal resolution. Clearly, it is much more difficult to produce accurate estimates of hourly rainfall than of temporal accumulated rainfall because, for the latter case, the accumulation process favors to cancel the random estimation errors. Two storm cases studies were selected with the purpose showing the effectiveness of CCS to provide reliable rainfall estimations for flash flood caused by very intense and short-lived convective systems in summer season.

4.6.2.1 Comparison with PERSIANN in a flash flood storm event

For US southwest region, PERSIANN system provides operational hourly rainfall estimates at around 25km resolution. The proposed CCS is compared with PERSIANN in instantaneous rainfall estimates from flash flood storms of 8 July 1999 at the Las Vegas, Nevada. This intense flash flooding storm from 1400 through 1900 UTC (0600 a.m. through 1100 a.m. local standard time) were reported to cause the worst flooding in the Las Vegas vicinity of 20^{th} century, with two deaths and $20 million in property damage. At the instantaneous timescale (at 25 km spatial resolution), CCS estimates again show a substantial improvement in estimate accuracy and detection of rain/no-rain pixels in comparison to the PERSIANN (Table 4.6). During the near five-hour flash flood event, the correlation coefficient of CCS is 0.59 vs. 0.47 of PERSIANN; the root-mean-square error of CCS is 1.27 vs. 2.67 of PERSIANN. CCS also demonstrates the advantage over

PERSIANN to estimate rainfall at scales smaller than 25 km. The time series of rain rate and statistical indices, illustrated on Figure 4.12, show how CCS better captures the instantaneous variability of rain rate than PERSIANN in this flash flood storm.

Table 4.6 Statistics for CCS and PERSIANN estimates of instantaneous rain rate, under a range of spatial resolutions, compared with Radar observation

	CCS				PERSIANN			
Resolution	RMSE	CORR	Ratio	CSI	RMSE	CORR	Ratio	CSI
4 x 4 km	2.72	0.51	1.10	0.53	N/A	N/A	N/A	N/A
12x12 km	2.01	0.55	1.09	0.64	N/A	N/A	N/A	N/A
25x25 km	1.27	0.61	1.07	0.67	2.67	0.47	1.17	0.55

4.6.2.2 Rio Grande basin flash flood storm

Figure 4.13 shows maps of hourly rainfall time series derived from CCS vs. radar at 0.04° x 0.04° spatial scale from UTC 0000 to 0500 on 4th July 1999 over Rio Grande basin located at 32°-37°N and 103°-107°W. The scatterplots are shown at Figure 4.14. The averaged comparison statistics of hourly estimates are presented in Table 4.7.

Table 4.7 Comparison statistics between CCS instantaneous rainfall estimates vs. gauge-radar at different spatial scales over a region located at 32°-37oN and 103°-107oW for UTC time 0000 to 0500 on 4th July 1999 storm period.

Spatial scales	#Pixels	RMSE (mm)	Ratio	CORR	POD	FAR	CSI
0.04° x0.04°	18900	2.79	1.15	0.458	0.779	0.209	0.641
0.12° x0.12°	2100	2.30	1.11	0.513	0.782	0.202	0.654
0.50° x0.50°	120	1.36	1.06	0.656	0.840	0.176	0.696
1.00° x1.00°	30	0.84	1.06	0.709	0.941	0.118	0.737

In summary, the hourly estimates of the cases studies show that CCS improves from PERSIANN and achieved relative high correlation coefficients and low bias at different spatial scales. Particularly, CCS demonstrates consistent good performance at scales less than 25km grids.

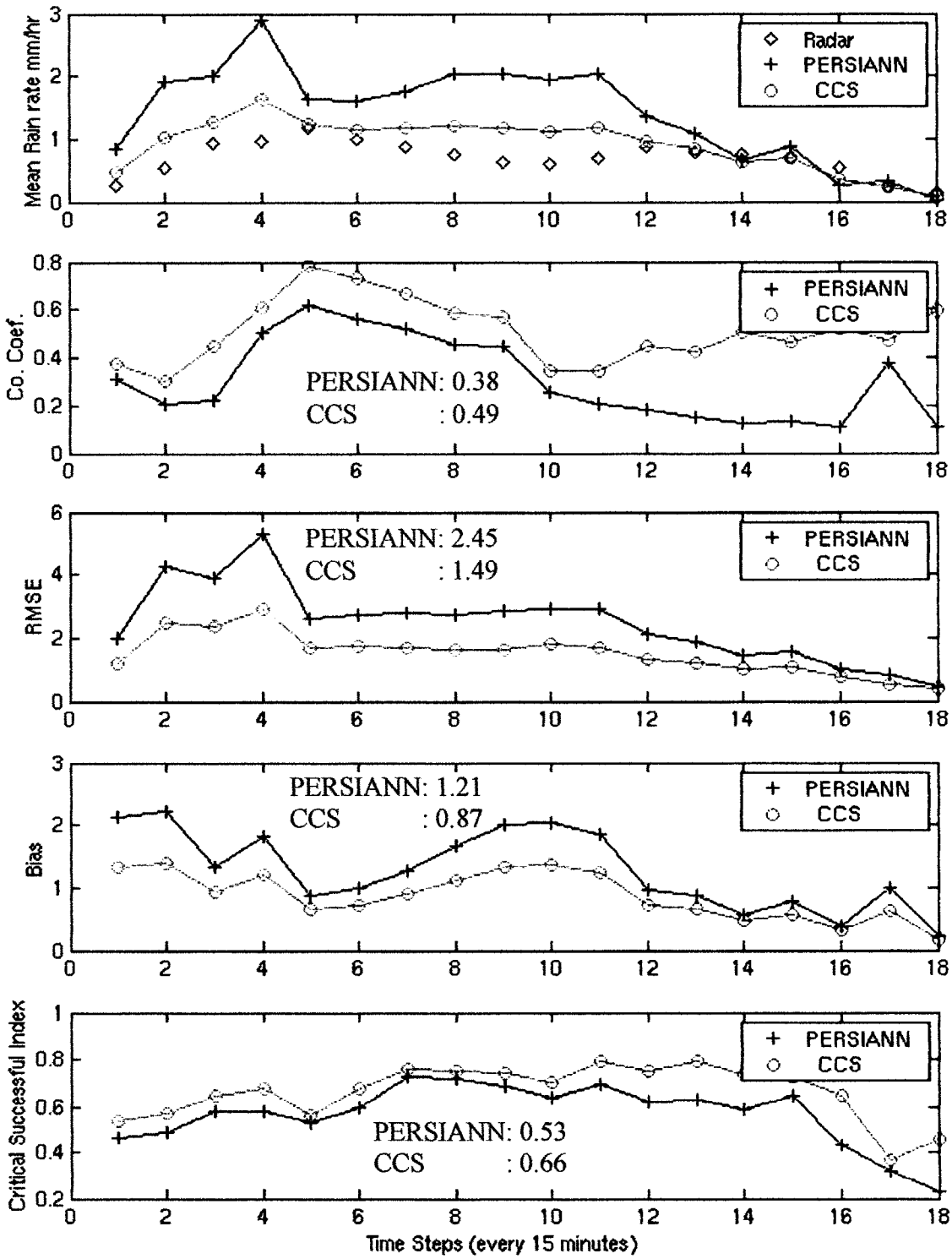

Figure 4.12 Time series of instantaneous rain rate from radar, PERSIANN, and CCS and evaluation indices from PERSIANN and CCS over the Las Vegas vicinity flash flood storm from UTC 1400 through 1900 event, 8 July 1999.

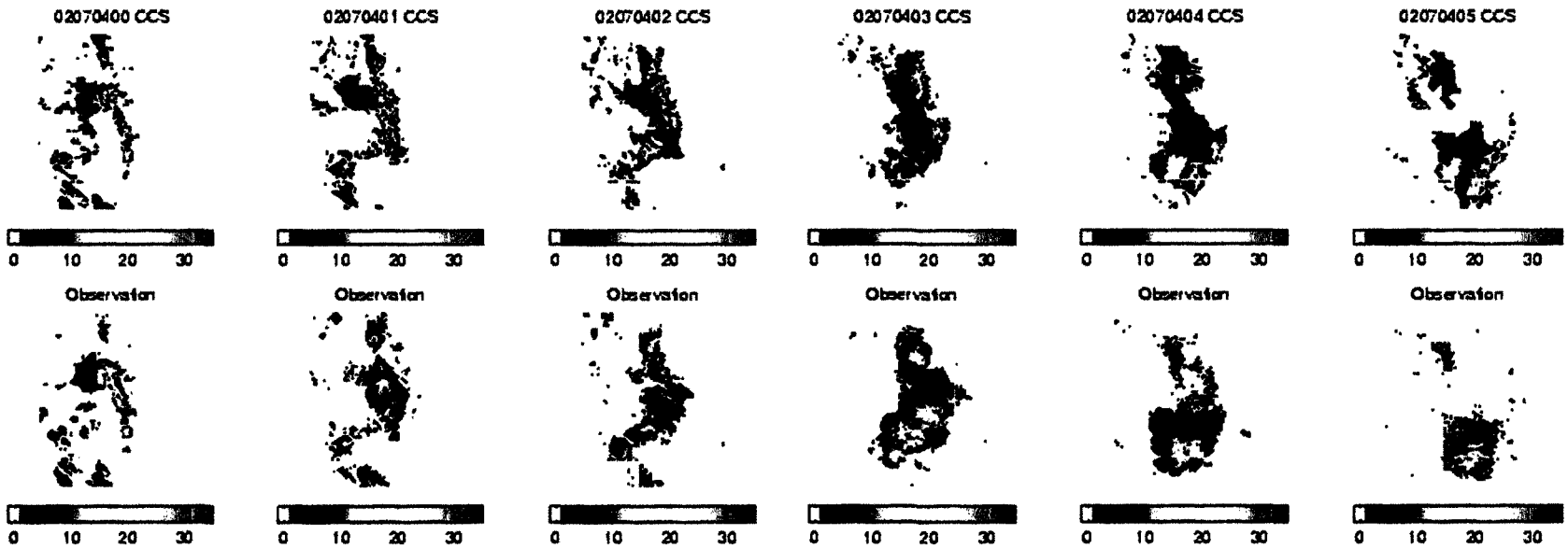

Figure 4.13 Time series of hourly rainfall of CCS vs. radar at 0.04° x 0.04° spatial scales over Rio Grande.

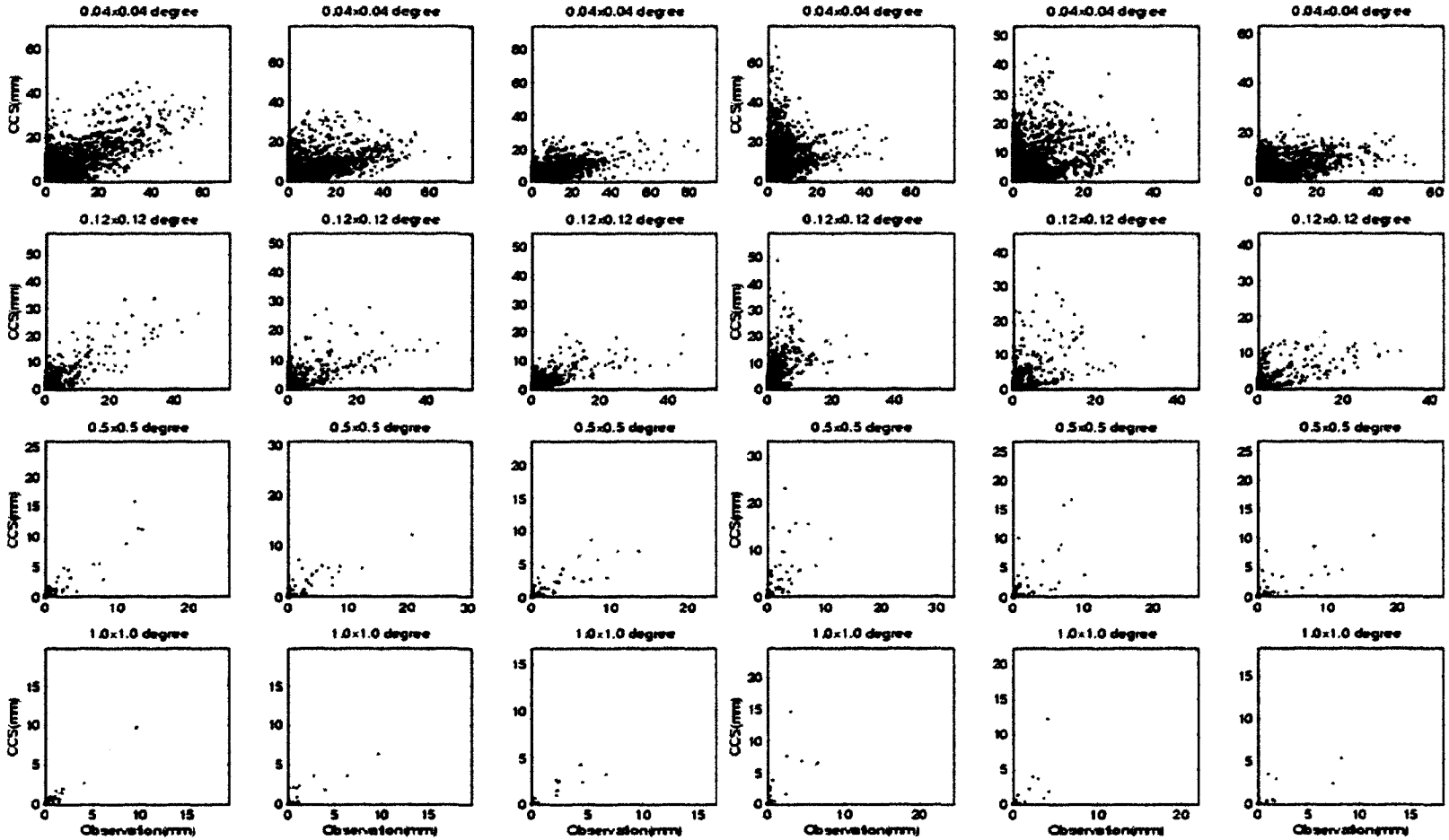

Figure 4.14 Scatterplots of hourly rainfall time series of CCS vs. radar at 0.04°, 0.12°, 0.5°, 1.0° spatial scales at Rio Grande.

4.7. Application to Cloud Patch Level

4.7.1 CCS: A Cloud Patch-Based Distributed Rainfall Estimation Model

One cloud patch was selected to demonstrate how the CCS model responds to diverse precipitation behaviors at different cloud life stages. The rainfall event from this cloud lasted about 10 hours from UTC 1400 to 2300 on 9 July 1999. Figure 4.15a shows the evolution of cloud patch and Figure 4.15b shows the CCS model distributes the most suitable IR_{Tb}-RR curve for each stage of cloud dynamical development processes to estimate rainfall. CCS functions like a distributed rainfall estimation system, which consists variety calibrated sub-models in response to one particular cloud during different life steps. On the contrary, lumped model estimates the rain rate with only one universally averaged regression function over the whole life cycles of cloud, which necessitates large accumulation to cancel off the estimation errors.

4.7.2 Lumped vs. Distributed Rainfall Estimation Model

Reference from the concept of distributed hydrological modeling, most of rainfall estimation approaches fall into two general categories: lumped or distributed model. Diverse clouds are distributed in space and proceeding in time. A single function to approximate such a complex system for rainfall rate retrieval is appealing but has very limited application because of large variety of physical processes associated with rain generation. Correspondingly, our analysis of cloud patches and measure of cloud patch-based rainfall must also be analyzed in a spatial-distributed and time-dependent way.

Figure 4.16a shows the distribution of training instantaneous rain rate vs. IR temperature at 0.04° spatial scale from GOES satellite image and NEXRAD radar rainfall. Figure 4.16b plots all the 400 nonlinear IR_{Tb}-RR curves calibrated from CCS model. Figure 4.16c illustrates the conceptual curves of lumped rainfall models derived from the same dataset.

The design of CCS network structure enables it behaves as a distributed system with large number of IR_{Tb}-RR functions. The size of nodes (groups) in the SOFM determines how fine classification of the input cloud-patches are categorized. The higher the size of clusters in SOFM, the finer the cloud patch features are specified into dissimilar groups. Likewise, if only few SOFM groups are selected, we would expect to receive a very broad classification. An extreme case of the group size is one classification group, which as we would expect that all the cloud patch features are assigned to a same category. In this case, it goes back to the lumped technique that would be difficult to tell the difference between the large and small patch features, so as to tell difference of the cold cloud features from the warmer clouds. Because all kinds of cloud patches are grouped in one, with variety of cloud systems, using one single IR_{Tb}-RR relationship to represent all possible cloud system and rainfall relationships can be risky and would expect that the prediction can be unsatisfactory.

As shown in Figure 4.16b, the number of IR_{Tb}-RR approximation functions is 400 arranged as 20 x 20 two-dimension nodes at SOFM layer in CCS model structure. Each of functions was derived from certain type of clouds and its' coincident rainfall observation data. Thus each IR_{Tb}-RR function corresponds to certain type of cloud

instead of a local region. Given different kinds of cloud patches, the CCS model dispatches the best-approximated IR_{Tb}-RR function for each cloud to produce rainfall instead of using single one-for-all regression curve. Figure 4.16 clearly demonstrates that a simple regression function couldn't completely represent the complex of precipitation system. Instead, a distributed system provides the capability to capture the high variability of rainfall at high spatial and temporal resolutions.

(a) Cloud evolution from developing to dissipating

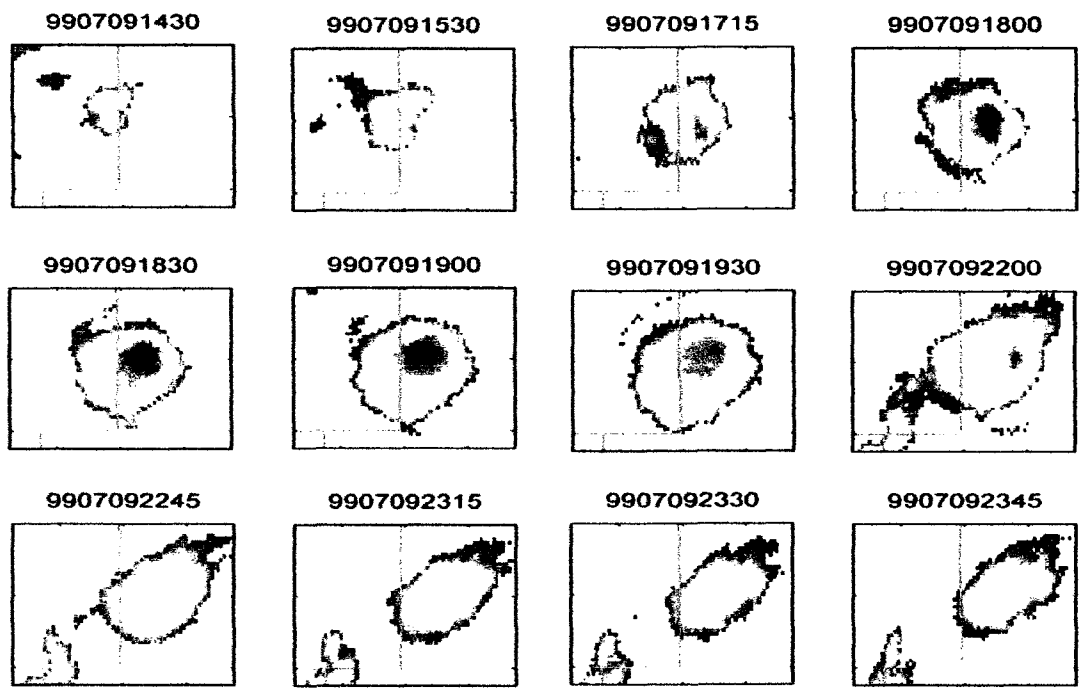

(b) IR_{Tb}-rain rate (m/hr) curves changing along with cloud evolution stages

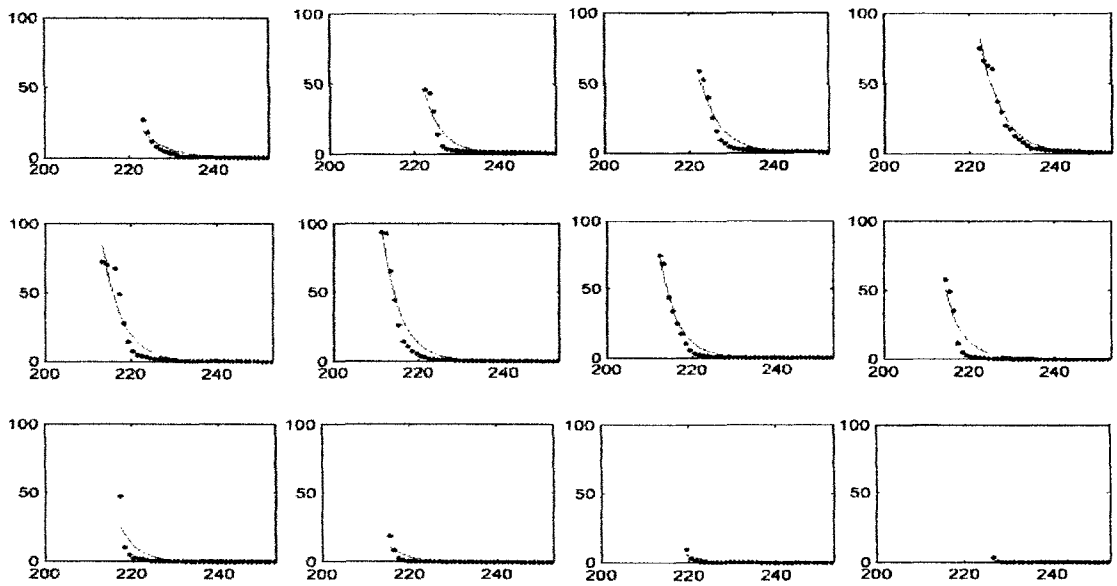

Figure 4.15: A storm event (a) Cloud evolution from beginning to end; (b) The rainfall approximation curves corresponding to each cloud development stage.

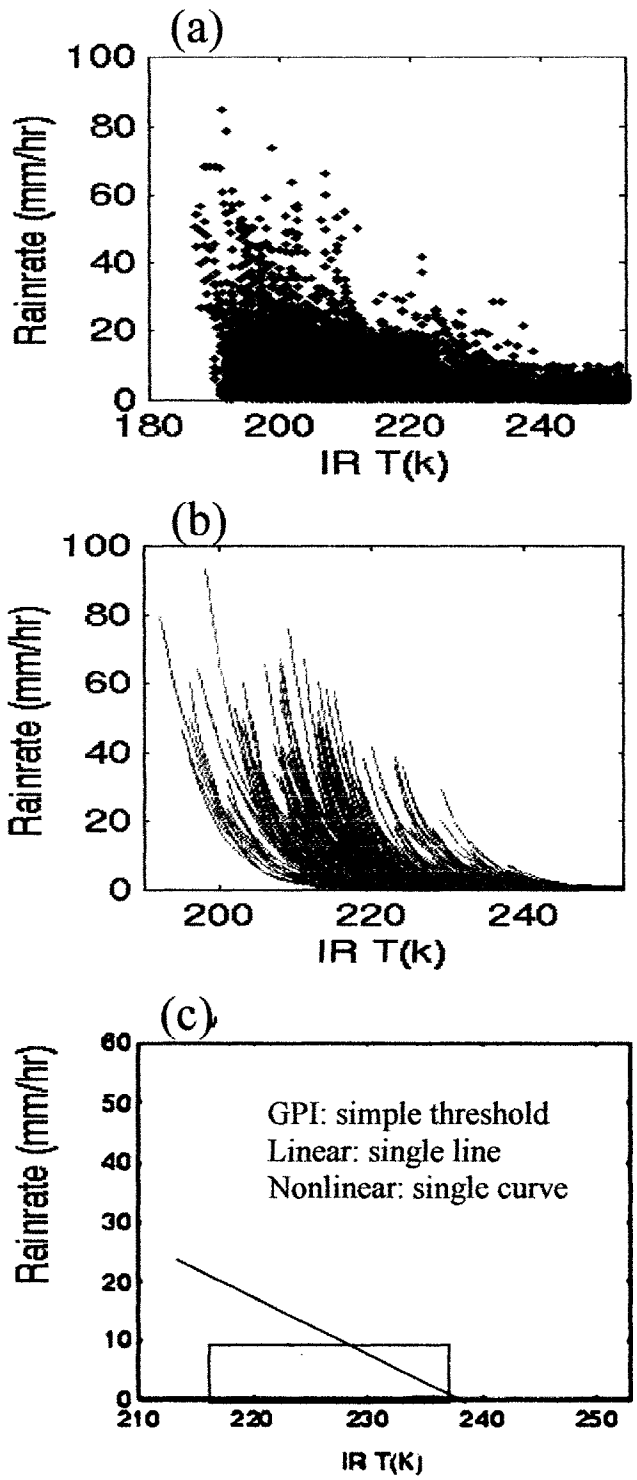

Fig 4.16 Illustration of lumped vs. distributed rainfall estimation model
(a) The distribution of calibrated IR and rain rate data; (b) The IR-Rain rate curves resulted from distributed CCS model; (c) The IR-Rain rate curves from various lumped model: GPI-Box, linear-Line, or nonlinear-Curve.

4.7.3 Patch Rainfall Validation

During the evolution process of a convective cloud, the IR temperature and rain rate distribution from the initial stage to the dissipated stage of cloud patch is significantly different. Figure 4.15a illustrates the evolution stage of a convective cloud patch from UTC 1400 through 2300, 9 July 1999. Figure 4.17a plots the time series of coldest temperature of cloud overshooting top and cloud area coverage from that convective cloud patch. Patch-averaged rainfall rate and patch rainfall volume derived from CCS are compared with radar (Figure 4.17b).

It is interesting to note that the correlation coefficients of 0.96 and 0.93 are exceptionally high for satellite method and that the estimate bias is small. As a matter of fact, Figure 4.16 and Figure 4.17 demonstrate one of the most important advantages of CCS is that it behaves as a distributed rainfall estimation model by responding to each precipitating cloud patch with different IR_{Tb}-RR functions. Figure 4.15 also implied that a single function (lumped techniques) would not catch the high temporal variation of the convective cloud-rainfall processes. The distributed CCS model dispatches the best-matching function to estimate rainfall for each specific clod patch, whereas lumped approaches produce rainfall estimates with their universally calibrated functions. Therefore, those lumped approaches tend to rely temporal or spatial accumulation to lower resolutions, such as 1^{o} x 1^{o} monthly (daily).

(a) Time series of minimum temperature of cloud patch overshooting top and cloud patch area from a convictive cloud patch

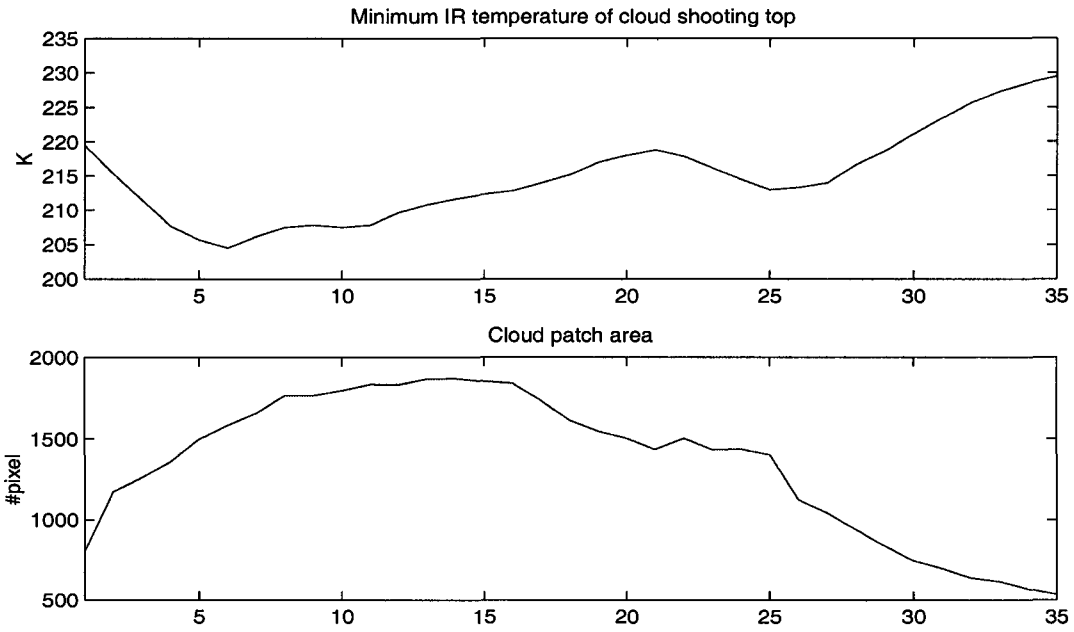

(b) Time series of rain rate and rain volume from convictive cloud patch

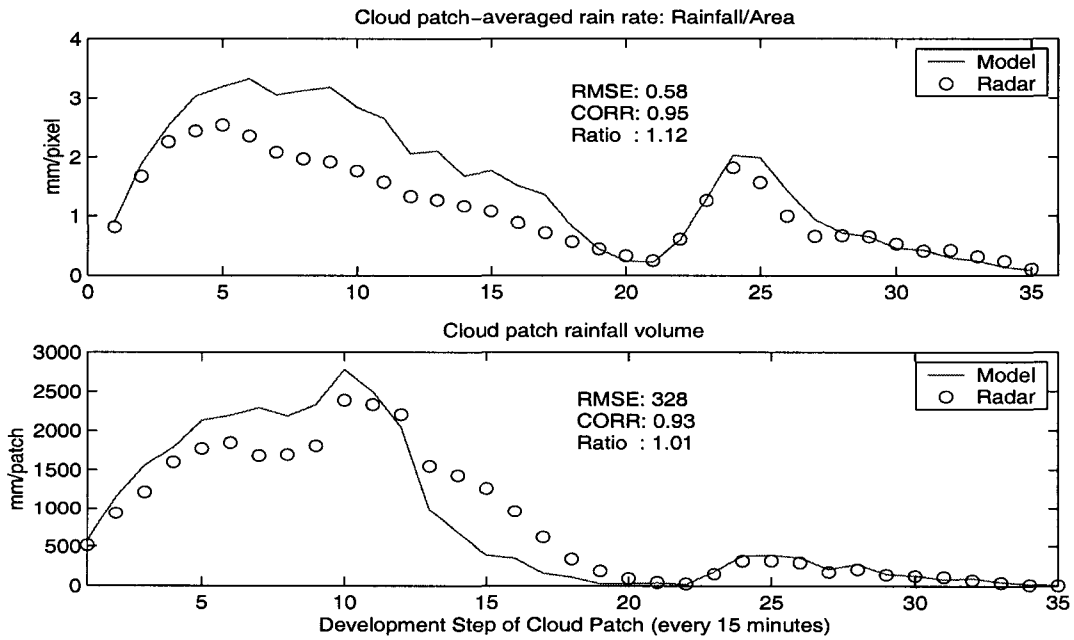

Figure 4.17 Evolution of a convective cloud patch from UTC 1400 through 2300, 9 July 1999 (a) IR temperature and area coverage; (b) rain rate and rainfall volume.

4.8. Summary and Discussion

In this study, the proposed rainfall estimation mode, CCS, is calibrated and validated to explore high spatial resolution (as high as 0.04^{o} x 0.04^{o}) precipitation estimation using cloud patch-based information, including the radar and satellite IR images. This system is based on the synthesis of computer-based artificial intelligence techniques with the theory of precipitation processes and practical experiences. The performance and capability of this model (at daily and hourly timescales and 0.04^{o}, 0.12^{o}, 0.24^{o}, 0.5^{o}, 1.00^{o} spatial scales, and, additionally, cloud patch level) have been demonstrated. Key features of the model are listed as follows:

(1) Utilization of multiple sources of information,

(2) Capability to process large amount of satellite data,

(3) Sophisticated segmentation of satellite images into separated cloud patches,

(4) Selection of meaningful feature information extracted from cloud patches,

(5) Successful classification of cloud patches into well-organized cloud clusters,

(6) Capability to estimate high rainfall events using multi-parameter nonlinear function to approximate the cloud-precipitation relationships.

(7) A distributed model to account for the limitations of lumped rainfall estimation techniques,

(8) Highly sensitivity to the development stages of convective cloud,

(9) Provision of insights into the manner in which the explanatory cloud features interact to give rise to a variability in rainfall,

(10) Potential to provide rainfall at high resolution.

The preliminary evaluation of CCS demonstrated the potential of the algorithm to capture high variation of rain rates at smallest possible temporal and spatial scales given current satellite data. The validation of CCS model performance also successfully provides insight into the diverse IR_{Tb}-rain rate relationships between cloud types and output rainfall distribution. The eventual goal of CCS is to develop a satellites operational model, adapted with instantaneous microwave rain rate, to produce high quality precipitation at fine spatial and temporal resolution. A need for a long-term investigation involving a much larger study region is critical for this goal. In our next Chapter, an operational model adjusted by microwave rain rate on North American region with one year's every half-hour data training will be discussed.

CHAPTER 5
A COMBINED MW/IR ADAPTIVE CLOUD CLASSIFICATION SYSTEM FOR RAINFALL ESTIMATION (MIRACCS)

5.1 Introduction

The high frequency and high spatial resolution of the satellite rainfall estimates, as well as the broad area that they cover, make them uniquely complementary to rain gauge and radar measurement. For large areas of the globe, near-continuous precipitation products from satellite-based rainfall estimation model at high spatial and temporal resolutions would be invaluable for numerous applications in meteorology and hydrology. Therefore, the ability to update model behavior from new observable sources is necessary to enable the proposed CCS model to estimate rainfall over extended area and time. There are two critical components for model adaptation: (1) the new observation data for adaptation; and (2) the adaptability of model structure. The adaptability of model structure enables the model to incorporate new data observation to adjust the model parameters and, meanwhile, to preserve the quality of pre-calibrated model behaviors in some extent. The parameter updating from new observation is imperatively important in short-term rainfall retrieval.

The possible sources of new data for updating the CCS model include satellite-derived observations (such as polar-orbiting microwave rainfall estimates), ground-based observations (such as rain gauge and surface radar), and/or meteorological model-derived rainfall. Ground-based observations are, usually, limited on land. Thus, the satellite-based observations provide the possibility to adapt the land-only-calibrated rainfall model over extended areas such as ocean and radar-blocked mountainous regions.

Since the training data set for CCS in previous chapter is only one month (June 1999) covering 25°-45°N and 100°-130°W area in previous chapter, broader coverage and longer time period are needed to enable CCS model to adaptively estimate rainfall over extended areas. This chapter describes the development of an adaptive CCS rainfall estimation system that combines TRMM Microwave/IR Rainfall Algorithm using Cloud Classification System (MIRACCS) for precipitation estimation at high temporal/spatial resolution. The MIRACCS is an operational system that inherits the nature of CCS descried in previous chapter and adaptively combines the TRMM TMI microwave data and ground radar rainfall data to predict rainfall estimates at extended regions and periods that are beyond the continent and not sampled by the rainfall observation instruments.

The rest of this Chapter is organized as follows: the adaptability of CCS rainfall model is presented in Section 5.2 firstly, followed by Section 5.3 to review the MW/IR rainfall estimation algorithms. Section 5.4 describes the experimental design of the adaptive CCS model-MIRACCS. Section 5.5 validates the results of MIRACCS over a range of spatial and temporal resolutions, followed by analysis of model performance

over time and space domain. This Chapter is concluded with a brief summary in Section 5.6.

5.2 Adaptability of CCS Model

5.2.1 Model Adaptation

The high variation of earth surface conditions, climate, geography, and energy flux transportation etc. over time and space necessitates that the proposed rainfall model has the adaptability to adjust model behavior from newly available data sources such as radars, rain gauges, meteorological modeling results, or rainfall derived from lower temporal frequency but more accurate polar-orbiting microwave satellite data. The adaptability would be critical quality in rainfall estimation to generalize a model to behave more precisely and sensitively in response to temporal and spatial variations.

The Self-Organizing Nonlinear Output (SONO) network structure of CCS model enables us to adaptively train the model either by adjusting the existing cloud-precipitation functions on the nonlinear output space (the first method) or by dynamically adding new node in SOFM layer to incorporate additional cloud clusters into system (the second method). The advantages of SONO network of CCS model are as follows:

1. Stability. Only the clusters that were activated are influenced by new input data. The rest of the network is completely unaffected by the current input. Additionally, the discrete division of nodes arrangement inherently makes the network stable in response to noisy information.

2. Plasticity. SONO structure is able to grow or shrink in response to changes of input data. The dynamic alteration in the number and structure of the SOFM nodes enables it to cope with non-stationary data more efficiently than static networks.
3. Speedup of adjustment. As only subset of SOFM clusters is involved while adaptation occurs, the training process speeds up, especially for large-sized network.

5.2.2 Adaptability of Cloud-Precipitation Functions

The Nonlinear Output layer of SONO network inlcudes a group of cloud-precipitation multi-parameter nonlinear functions for cloud patch rainfall estimation. While in adaptive mode, any new observations could be used, together with existing observations, to adaptatively adjust the function, namely the IR_{Tb}-RR curve.

A "batch" calibrating procedure based on Multi-Start Downhill Simplex (MSDS) is applied to obtain the fixed estimates of the IR_{Tb}-RR curve parameters. In subsequent applications, those parameters could be recursively updated through an adaptive training procedure that makes small adjustments to the parameters based upon new observation, which enables this model to preserve previous trained behaviors and, meanwhile, adjust to seasonal and regional variations of the cloud-precipitation relations. Figure 5.1 illustrates the adjustment of curves. Curve 1 indicates the new observation data is similar with existing pattern. Curve 2 shows only partial new observation data available at low rainfall region. Therefore, the adaptive curve only adjust the low rainll region and

maintain the same at high rainfall region. Curves 3 and 4 show the adaptation of new observation data at both high and low rainfall regions.

5.2.3 Adaptability of SOFM Structure

When hydrologic model is applied in different seasons or regions, the need of tuning of the structure or/and paramters of this model is necessary. In our case if there is a new cloud pattern emerging, the option to include the new cloud type is to re-organize the SOFM map by increaing its number of nodes. For example, figure 5.2 shows that the SOFM size is increased to cope with trainig data from smaller to bigger domains. In previous Chapter, a 20 x 20 nodes of SOFM matrix was originally trained using one month US Southwest region data (25^{o}-45^{o}N and 100^{o}-130^{o}W) in June 1999. The new SOFM of the adaptive CCS model in this Chapter is 40 x 40 nodes of Matrix to represent the one year whole United States data (10^{o}-50^{o}N and 65^{o}-135^{o}W) in 2002.

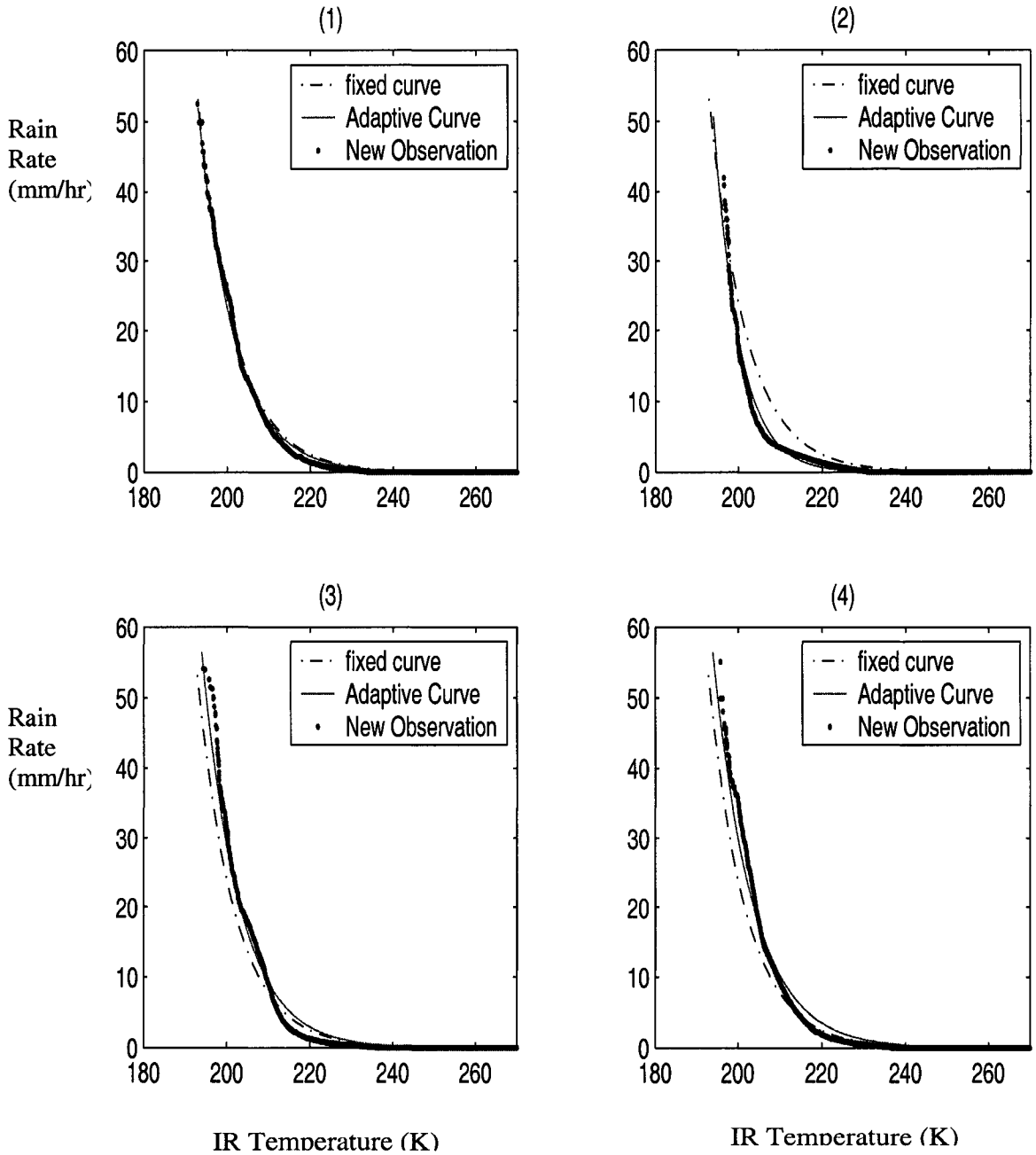

Figure 5.1 Illustration of adaptability of cloud-precipitation (IR_{Tb}-RR) functions in Nonlinear Output layer of SONO network.

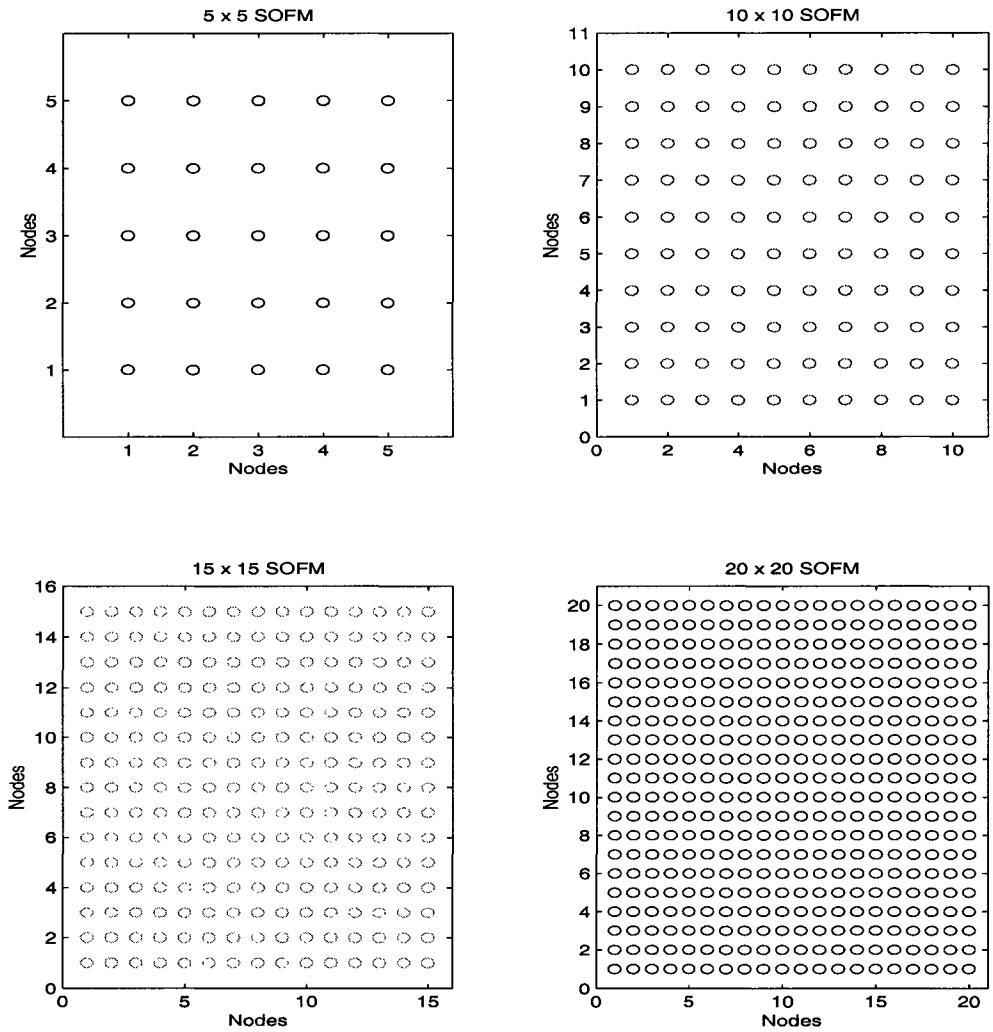

Figure 5.2 Illustration of adaptability of SOFM layer's nodes arrangement. (*Note: 15x15 SOFM structure is used by PERSIANN rainfall system. The 20x20 SOFM layer is used by CCS (fixed parameters) in previous Chapter and 40x40 SOFM used by MIRACCS in this Chapter*)

5.3 Overview of Combined MW/IR Rainfall Algorithms

IR rainfall algorithms have been benefited from excellent temporal/spatial sampling, but the quantity being sensed from IR radiometers (mostly cloud-top temperature) is indirectly connected to precipitation, particularly at small spatial scales. Satellite-borne microwave (MW) sensors provide more accurate estimates of rain rate, but they suffer in poor temporal resolution of two passes per day at best.

To take advantage of the relative accuracy of the MW estimates and the high sampling IR-based estimates, a number of researchers have developed techniques for using the MW to adjust the later when both are available and then to apply the adjustments to IR-based estimates regardless of the availability of MW data (termed as MW/IR algorithms). Adler et al. (1993) developed an adjusted GPI (AGPI) in which a correction factor is derived from the comparison of MW and GPI estimates for coincident time slots over some extended period (e.g., one month). This correction is then retrospectively applied to all the hourly GPI estimates during that period. Xu et al. (1999) have extended AGPI to develop the Universal Adjusted GPI (UAGPI) method in which both the monthly IR threshold and IR conditional rain rate are optimized using coincident MW and IR data, again over extended monthly periods. Todd and Kniveton (1999) developed this principle further by calibrating the IR-rain rate relationship at each 1^{o} x 1^{o} grid cell using coincident IR and MW data. Huffman et al. (2001) demonstrate a similar algorithm for global rainfall estimates. Miller et al. (2001) approximated linear regression function from coincident MW and IR data pairs. Results suggested a nonlinear relationship would better cope with high rain rate events.

Given certain study area, most of these MW/IR approaches fall into two general categories: lumped and distributed systems. The widely tested and applied techniques like the AGPI can be referred as lumped algorithm: after collecting data for an elapsed time period, they are used to determine **an** appropriate relationship between the predicators(s) of interest and the passive MW rain rate. The resulted relationship is then applied into subsequent time periods. The AGPI and UAGPI fall under lumped category because they only calibrated one set of optimization parameters that only involve two parameters: IR rain/no-rain threshold and average rain rate for study area. The rain estimates resulted from these existing techniques featured with simplex of characteristics in constrained functional flexibility and systematic invariability demonstrate one thing in common: algorithms perform reliably only at accumulated time/space scales like daily/100km or above. A distributed MW/IR rainfall estimation model is needed to represent the highly variation and complexity of cloud-precipitation processes.

Recently, Todd et al. (2001) introduced a MW/IR algorithm using Probability Matching Method (PMM) to derive different IR_{Tb}-RR curve for each sub-region perhaps with smoothing while insufficient data are available. This geographically distributed IR_{Tb}-RR functions are then applied to IR imagery at full temporal resolution.

As described in Chapter 4, the CCS algorithm itself is a distribution model based on not geographical region but cloud clusters classified by Self-Organizing Feature Map. The philosophy behind this is that each cloud pattern behaves its own characteristics of precipitation. However, large amount of cloud patterns could occur in the same region to cancel off the advantage of region-based distributed rainfall model. In our cloud type-

based distributed rainfall model, each of the resulted cloud-rainfall relationship is solely calibrated from the same cloud cluster. More importantly, the cloud-pattern-based distribution model provides higher adaptive ability and portability, which improve the model performance for large area of globe.

5.4 Combined MW/IR Algorithm using CCS for Estimation of Precipitation (MIRACCS)

5.4.1 Data and Application Area

The possible data sources for updating the model include satellite-based observations (such as polar-orbiting microwave rainfall estimates), ground-based observations (such as rain gauge and surface radar), and/or meteorological model-derived rainfall. Ground-based observations are, usually, limited on land. Thus, the polar-orbiting satellite-based observations such as SSM/I and TRMM TMI provide the possibility to adapt the land-only-calibrated rainfall model over extended areas such as ocean and radar-blocked mountainous regions. The SSM/I is widely used for this kind of algorithms due to its better temporal sampling.

It is well known that rainfall from sun-synchronous polar-orbiting satellites, i.e. SSM/I, are subject to bias in regions for which the diurnal cycle of rainfall is pronounced (Bellerby et al., 1998). The non sun-synchronous Tropical Rainfall Measuring Mission (TRMM) provides sampling of the complete diurnal cycle of rainfall over some extended areas and the rainfall estimates are more likely accurate than SSM/I (Kummerow et al., 1998). Additionally, TRMM TMI microwave rainfall estimates (highest spatial resolution

at 12 x 12km) has higher spatial resolution than SSM/I data (highest at 25 x 25km). A combination of high spatial resolution, high accuracy, and the absence of sun-synchronicity make the TRMM microwave rainfall data an ideal candidate for use in this MIRACCS model development.

The observed datasets used for MIRACCS at present are described in Table 5.1. Figure 5.3 shows the training data space domain covering from 135°W-65°W and 10°N-50°N. While Radar covers most of the land of training domain, the TRMM TMI Microwave data cover both land and ocean area. The IR brightness temperature images were collected by GOES 8/9 satellites at each 30 minutes interval. The radar rainfall data were collected by the network of NEXRAD radars operated by the U.S. National Weather Service in hourly temporal resolution. Both radar and IR data are 0.04° x 0.04° latitude by longitude, which is the highest spatial resolution from GOES satellite IR band.

Table 5.1 GOES IR, TRMM, and radar data used for the adaptive CCS model

	Data	Area	Description
I	TRMM 2A12	135°-65°W and 10°-50°N	Provides rainfall rate and the vertical structure of hydrometeors based upon the nine channels of the TRMM microwave imager (TMI) at 0.12° x 0.12° scale
II	WSR-88D radar network	135°-65°W and 10°-50°N	Stage IV hourly 0.04° x 0.04° rainfall data collected by the network of NEXRAD radars operated by the NCEP at NOAA in the year of 2000 year
III	GOES IR	135°-65°W and 10°-50°N	Long-wave Infrared (10.7um) data provided by GOES-8, GOES-9/10 30 minutes 0.04° x0.04° scale in the year of 2000
IV	GOES IR	130°-100°W and 25°-45°N	Long-wave Infrared (10.7um) data provided by GOES-8, GOES-9/10 at 30 minutes 0.04° x0.04° scale in June and July 1999
V	WSR-88D radar network	130°-100°W and 25°-45°N	Stage IV hourly 0.04° x 0.04° rainfall data collected by the network of NEXRAD radars operated by the NCEP at NOAA in June and July 1999

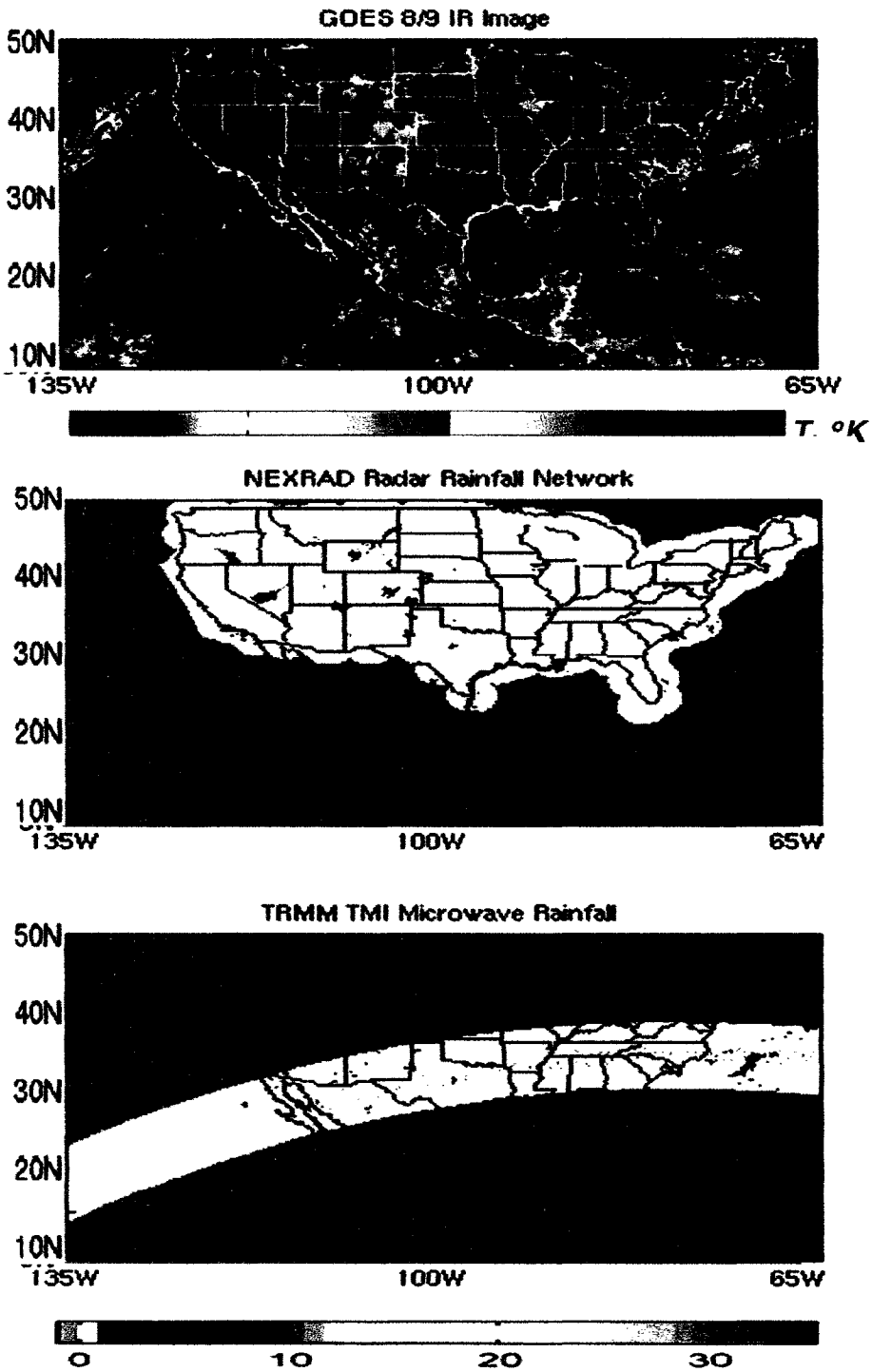

Figure 5.3. The study area for MIRACCS operational model

Note: GOES IR covers whole area with every 30 minutes samples; TRMM TMI microwave rainfall coverage (bottom) complements REXRAD rainfall network (middle).

5.4.2 The Structure of MIRACCS

To implement the MIRACCS, the input cloud features and the number of nodes in SOFM hidden layer must be specified. MIRACCS is an adaptive mode of CCS calibrated in previous Chapter using datasets IV and V in June 1999. Then the extended region dataset I and II (10^{o}-50^{o} N and 135^{o}-65^{o}W) are selected for the adaptive model-MIRACCS. The detailed information of CCS is presented at Chapter 2, 3, and 4.

As an adaptive mode of CCS, MIRACCS is based on the CCS model and uses the TMI 2A12 product provided by the low-inclination orbiting TRMM satellite to regularly update network parameters. The model structure used to generate the rainfall results reported is illustrated in Fig. 5.4 and the flow diagram in Fig.5.5. The system produces estimates of rainfall at 0.04^{0}x0.04^{0} pixel of the IR brightness temperature image provided by GOES satellite at every 30 minutes, meanwhile the system parameters are adjusted by the TRMM microwave rainfall estimates.

First, the system segments the GOES IR imagery into separated cloud patch and then compute the selected cloud features, as described in Chapter 4.3. Next, the first portion of SONO network, named the Self-Organizing Feature Map (SOFM), is used to classify these cloud patches into a larger number of groups associated with different precipitation characteristics. For each group, a multi-parameter nonlinear function is developed to map the cloud-precipitation relations, namely IR_{Tb}-RR rainfall estimation function.

The system operates in two modes: simulation and update. In simulation mode, the surface rain rate at the 0.04^{o} x 0.04^{o} resolution is estimated every 30 minutes from the GOES satellite infrared images using the previously calibrated SONO network

parameters. In update mode, the parameters of SONO are adjusted using the simulation error at any pixel for which a coincident TMI instantaneous rainfall estimate is available.

As a test of rainfall estimation at the smallest possible spatial scale, a disaggergration of TRMM MW to 0.04^{o} from 0.12^{o}, described in the next section, also conducted.

5.4.3 Downscaling TRMM Microwave Rainfall Data

The TRMM MW data's smallest spatial scale is around 0.12^{o}. The maximum rain rate is about 35mm/hr according to the definition of TMI rain rate retrieval algorithms at that resolution. The NEXRAD network shows that the rain rate could reach as high as 100mm/hr at 0.04^{0} pixel scale. The Passive MW retrieval algorithm prohibits high rain rate estimation at scales smaller then 0.12^{o} pixel resolution. Thus, a possible solution is to choose a disaggregation method to drive TMI microwave data to rain rate higher than 35mm/hr at scales smaller than 0.12^{o}. The method we used is the IR weighted disaggregation of rainfall according to the classified IR_{Tb}-RR curves from MIRACCS. The procedure to disaggregate TMI data is as the following:

1): Pre-train MIRACCS system to quantify cloud-type-based IR_{Tb}-RR curves at 0.04^{o} scale using IR and NEXRAD Radar data;

2): Locate the nonlinear curve *j* from MIRACCS for the collocated TMI (0.12^{o}) and IR (0.04^{o}) data such that one TMI pixel grid represented by 3x3 IR grids;

3): Calculate the rain rate according to the curve *j* for the 3x3 sub grids: $RR_i=f_j(IR_i)$, where i =1,2,..,9 and f_j is the j^{th} RR-IR_{Tb} curve from MIRACCS model;

4): Calculate the disaggregation weights: $w_i = RR_i / \sum_{i=1}^{N} RR_i$, where N =9;

5): Compute the disaggregated TMI at 0.04° scales: $T_i^{0.04} = w_i . T^{0.12} . N$, where $T_i^{0.04}$ is the disaggregated TMI data at sub grid i, $T^{0.12}$ is the TMI observation data at 0.12° pixel resolution. This $T^{0.12}$ is disaggregated into $T_i^{0.04}$ and the distribution of $T_i^{0.04}$ is based upon the characteristics of j^{th} curve.

6): Apply the disaggregated TMI $T^{0.04}$ rainfall data to adjust the MIRACCS model at 0.04° x 0.04° high spatial resolution.

The procedure of accumulation of N $T_i^{0.04}$ into $T^{0.12}$ is exactly reverse:

$$T_{accu}^{0.12} = \sum_{i=1}^{N} T_i^{0.04} / N = \sum_{i=1}^{N} w_i . T^{0.12} . N / N = \sum_{i=1}^{N} [(RR_i / \sum_{i=1}^{N} RR_i) . T^{0.12} . N / N] = T^{0.12}$$

5.4.4 The Comparison between CCS and MIRACCS Model

The CCS and MIRACCS share the same model structure and network parameters. However, the CCS model was calibrated with much smaller training space and time domain. Larger training domain means that more cloud clusters are possibly included. Therefore, the size of MIRACCS layer is increased (from 20 x 20 to 40 x 40) to incorporate the new cloud-precipitation clusters from the training data domain. The use of polar-orbiting TRMM TMI microwave rainfall data enables MIRACCS to estimate rainfall over ocean and mountainous areas where gauge and radar coverage are very sparse. Table 5.2 summarizes the comparison of the fixed parameters CCS model and the adaptive parameter MIRACCS network.

As a matter of fact, MIRACCS is an adaptive model of CCS. The adaptation conducts both at the new observation and the SOFM structure.

Table 5.2 Comparison of CCS and MIRACCS rainfall estimation model

	CCS	MIRACCS
Space	25°-45°N and 100°-130°W region	10°-50°N and 65°-135°W region
Time	One month training data (June 1999)	Six months (every even month in 2002), plus the CCS time training domain
Data	GOES 9 IR, Radar rainfall, and Gauge rainfall	GOES 8/9 IR, Radar rainfall, and Gauge rainfall, TRMM microwave rainfall
SOFM	20 x 20 matrix	40 x 40 matrix

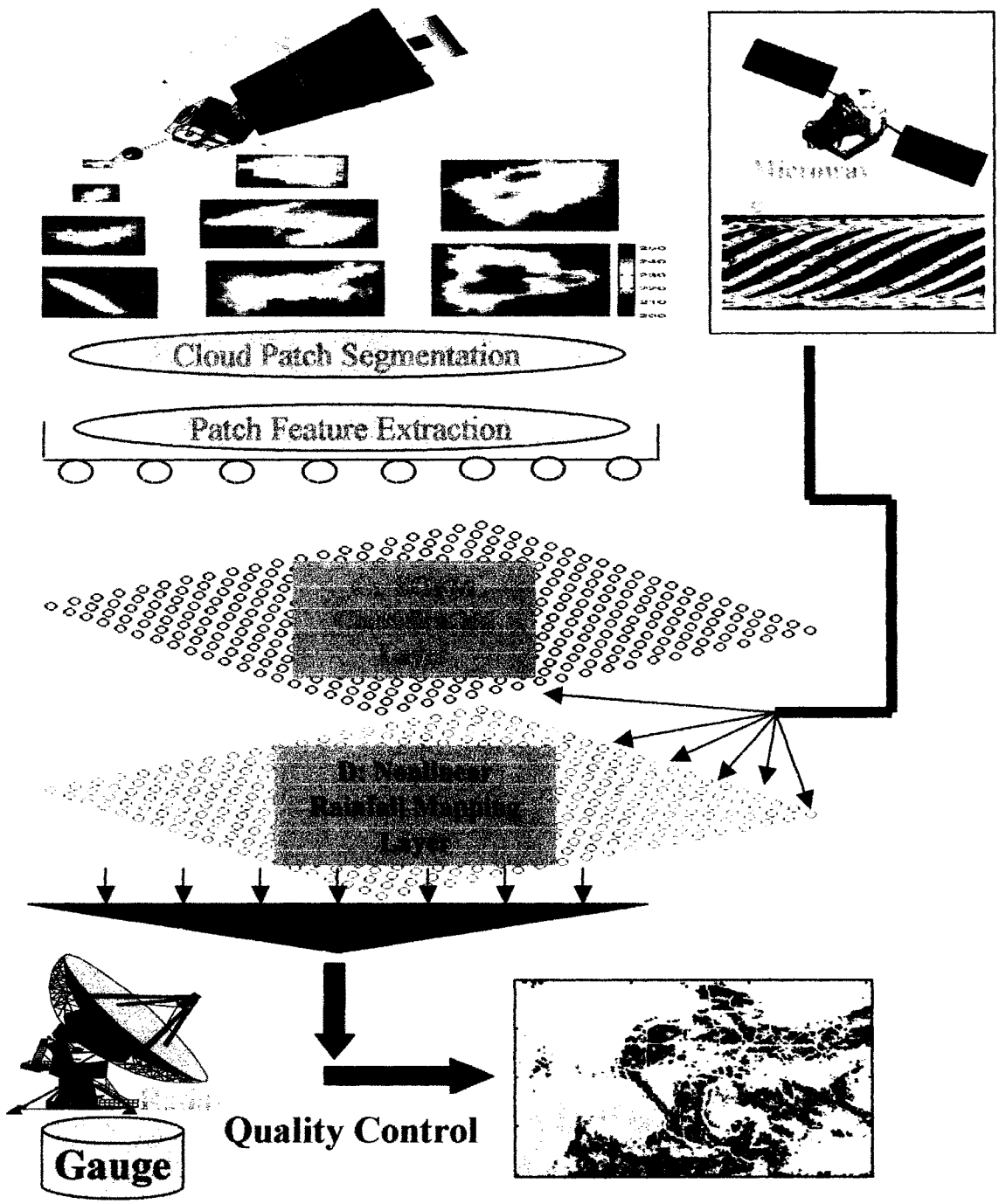

Figure 5.4. The architecture of operational MIRACCS model:
(a) Cloud patch segmentation; (b)Cloud patch feature extraction;
(c) Cloud classification: self-organizing feature map layer;
(d) The output layer: IR_{Td}–RR distribution curves
MIRACCS is adjusted by TRMM microwave and validated by ground observation.

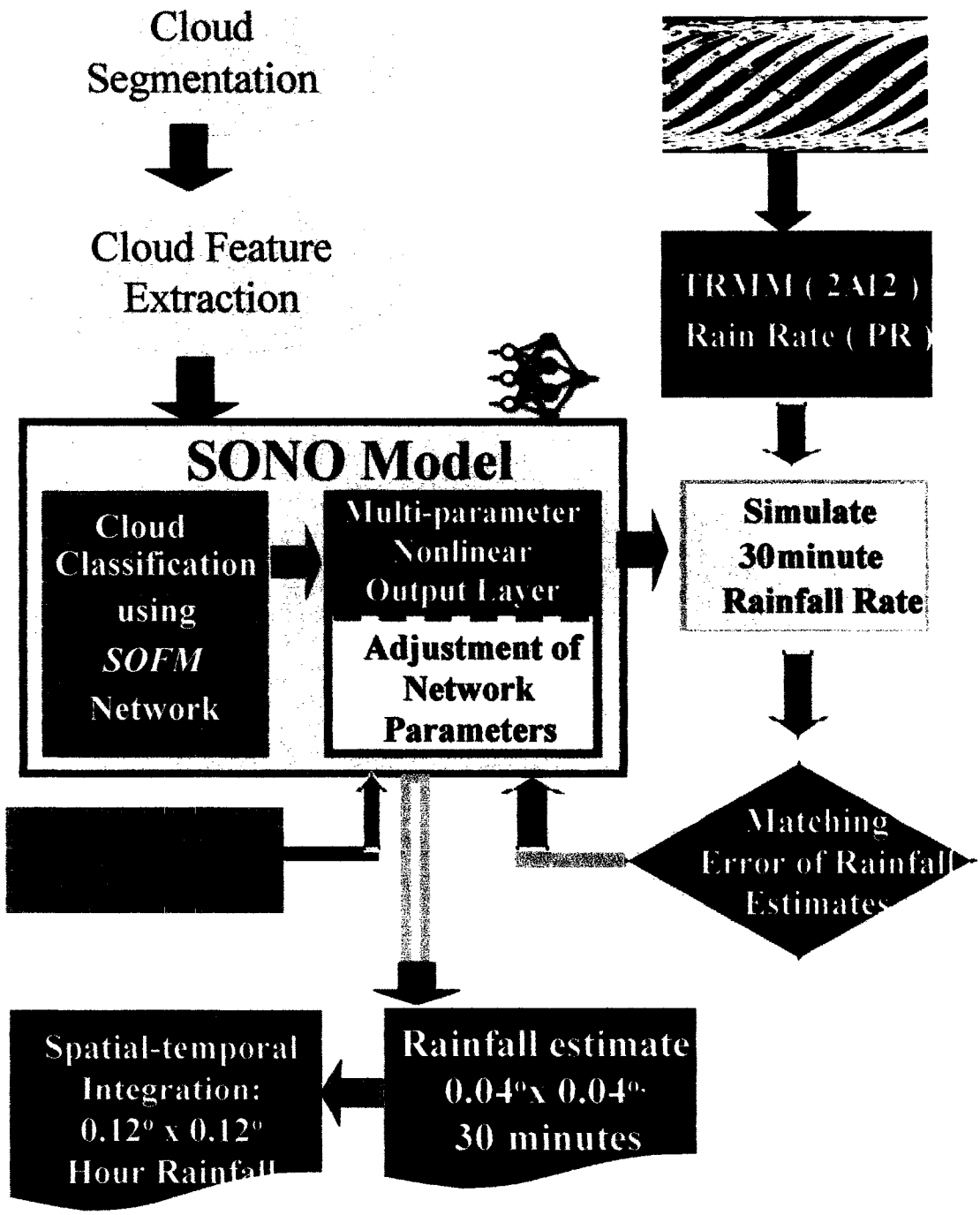

Figure 5.5. Flow diagram of the structure of the MIRACCS system

5.5 Verification of MIRACCS Algorithm

5.5.1. Comparison of Adaptive Model vs. Fixed Model

The CCS model was initially trained in "batch mode" using 30 days of data (June 1999) from the GOES satellite data and NEXRAD network. The adaptive MIRACCS estimation mode, in which the IR_{Tb}-RR function parameters are recursively updated with new information before computing the precipitation, was compared with non-adaptive estimation mode.

Figure 5.6 indicates the locations of two cloud patches (A and B) that we track their life cycle development from beginning to dissipating. Figure 5.7 and Figure 5.8 show the results comparison between GPI, Single Curve Method (SCM), Fixed CCS and Adaptive MIRACCS for cloud patch A and B, respectively. The SCM, like the Auto-Estimator (Vicente, 1998), is a lumped model that approximates a single power law nonlinear IR_{Tb}-RR curve with the Radar/IR data pairs during the whole calibrating domain. On the contrary, both CCS and MIRACCS are distributed estimation algorithms, which allocate the best-approximated IR_{Tb}-RR function to estimate rainfall by judging the type of instantaneous cloud patch.

Both CCS and MIRACCS models function like a distributed rainfall estimation system, which consist a variety of calibrated sub-models in response to one particular cloud during different life steps. The results in Figure 5.7 and 5.8 show that distributed models perform better than the lumped model such as GPI and AE (a power law fitting curve introduced as Auto-estimator [Vicente et al., 1998]).

In comparison with fixed CCS model, the adaptive MIRACCS estimates are superior both in the representation of temporal distribution and in accuracy of rainfall values, particularly the CORR in rain rate/rain volume improved to about 0.9. The RMSE and BIAS also reduced significantly while the BIAS appears from under estimated to overestimated, which could be explained by the adaptation of the IR_{Tb}-RR curves illustrated in Figure 5.8(c, d, e, f). Both curves (c), fixed CCS model, and (d), adaptive MIRACCS model, refer to the rainfall estimation curves at cloud life stage 10. Similarly, fixed CCS model curve (e) and adaptive MIRACCS curve (f) refers to the rainfall estimation functions at 15^{th} stage of cloud life cycle. The adaptive model demonstrates the capability of MIRACCS to capture the diverse variation of cloud-precipitation system in very short-term or instantaneous temporal scale.

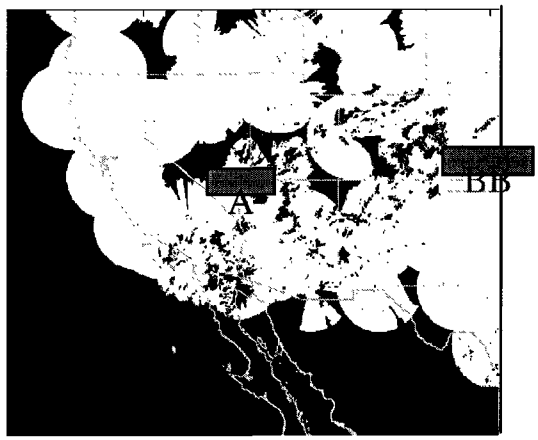

Figure 5.6 The locations of two cloud patches A (left) and B (right) for adaptive studies

(a) Cloud A: hourly averaged rain rate times series: UTC 1700-2200, July 8 1999

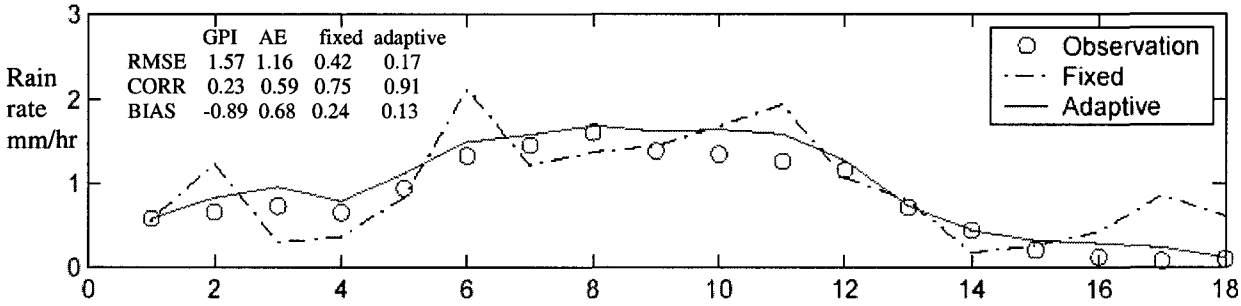

(b) Cloud A: hourly rainfall times series (mm/patch): UTC 1700-2200, July 8, 1999

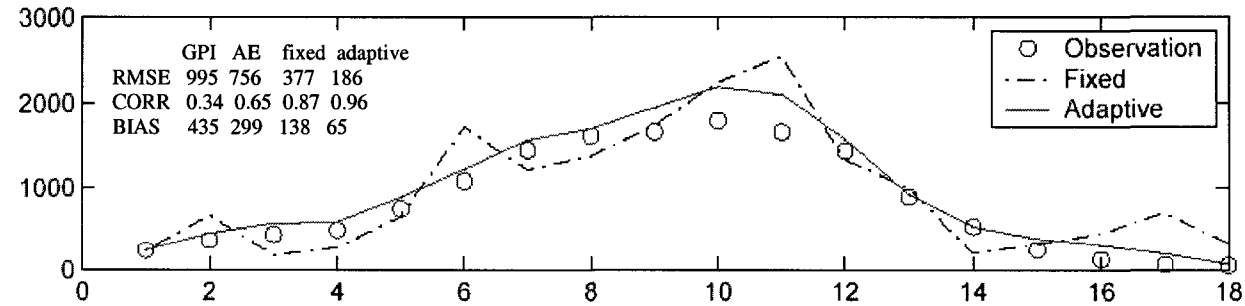

Evolution time steps of cloud patch A (every 15 minutes)

Figure 5.7 Statistical comparisons of different rainfall algorithms vs. observation for Cloud patch A

(a) Cloud B: every 15 minutes rainfall time series: UTC 1400-2345, July 9 1999

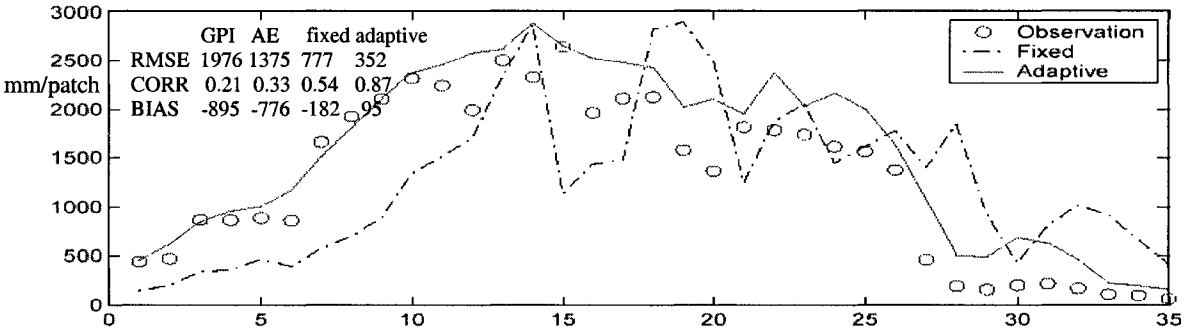

(b) Cloud B: Every 15 minutes rain rate time series: UTC 1400-2345, July 9 1999

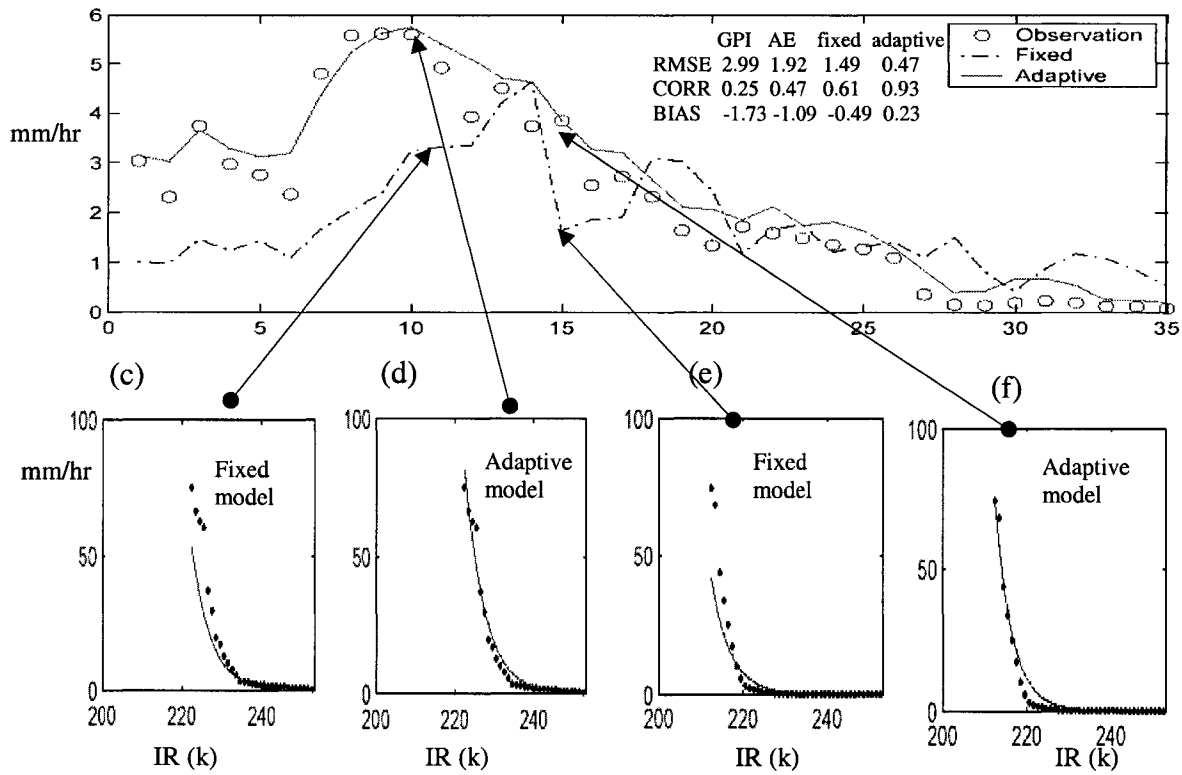

Figure 5.8 Investigation of adaptive and fixed estimation mode for cloud B
(a-b): Plots of time series of CCS estimates at adaptive and fixed parameters modes vs. observation for rain rate and rain volume, respectively;
(c-d): IR_{Tb}-RR distribution curve from fixed and adaptive modes at time point 10 of cloud patch B life stage, respectively;
(e-f): IR_{Tb}-RR distribution curve from fixed and adaptive modes at time point 15 of cloud patch B life stage, respectively.

5.5.2. Comparison of Instantaneous Rainfall Estimates

Two case studies are examined here with independent NEXRAD network radar rainfall and TRMM Microwave rain rates at different spatial scales. Case I is located at Florida south semi-island (22°-26°N and 79°-83°W) at UTC 0145 9 Jul 2002 and case II is located at Texas coast (26°-30°N and 93°-97°W) at UTC 0445 16 Jul 2002. The reason to choose these cases is that the co-availability of IR, Radar, and, most importantly, TMI rain rates data. The comparison of Case I is summarized in Table 5.3 and Figure 5.9; case II summarized in Table 5.4 and Figure 5.10 (Note: $MIRACCS^R$ means the MIRACCS estimates are compared with Radar and $MIRACSS^T$ are compared with TRMM TMI rain rate. TMI^R is the inter-comparison between TMI and Radar).

Both cases demonstrate high correlation and low bias between TMI and Radar data. MIRACCS estimates show favorable performance comparison with TMI at both cases due to MIRACCS being TMI adjusted algorithm. At smallest scale, the average correlation coefficient is 0.5 with 0.55 Critical Successive Index while the performance is more reliable at increasing spatial scales.

Table 5.3. Statistics comparison of MIRACCS estimates vs. Radar/TMI data at region 22°-26°N and 79°-83°W for Case I: UTC 0145 9 Jul 2002 at different spatial scales

Spatial scales		CORR	RMSE	Ratio	POD	FAR	CSI
0.04°x0.04°	$MIRACCS^R$	0.54	2.69	0.89	0.68	0.31	0.46
0.12°x0.12°	$MIRACCS^R$	0.62	2.11	0.88	0.74	0.16	0.58
	$MIRACCS^T$	0.69	1.94	0.91	0.75	0.07	0.70
	TMI^R	0.75	1.56	0.97	0.72	0.11	0.68
0.5°x0.5°	$MIRACCS^R$	0.77	0.71	0.80	0.74	0.12	0.67
	$MIRACCS^T$	0.84	0.68	0.82	0.79	0.05	0.78
	TMI^R	0.93	0.49	0.98	0.78	0.06	0.73
1.0°x1.0°	$MIRACCS^R$	0.85	0.49	0.87	0.86	0.0	0.85
	$MIRACCS^T$	0.86	0.42	0.89	0.95	0.0	1.0
	TMI^R	0.96	0.19	0.98	0.91	0.0	0.86

Note: $MIRACCS^R$ means the MIRACCS estimates compared with Radar and $MIRACSS^T$ compared with TRMM TMI rain rate. TMI^R is the comparison between TMI and Radar. The mean radar rain rate at 0.12x0.12 is 0.92mm and TMI is 0.90mm.

Table 5.4 Statistics comparison of MIRACCS estimates vs. Radar/TMI data at region 26°-30°N and 93°-97°W for Case II: UTC 0445 16 Jul 2002 at different spatial scales

Spatial scales		CORR	RMSE	Ratio	POD	FAR	CSI
0.04°x0.04°	$MIRACCS^R$	0.46	4.01	0.60	0.78	0.26	0.62
0.12°x0.12°	$MIRACCS^R$	0.51	3.48	0.62	0.80	0.18	0.67
	$MIRACCS^T$	0.57	3.20	0.62	0.87	0.12	0.76
	TMI^R	0.60	3.60	1.22	0.84	0.10	0.78
0.5°x0.5°	$MIRACCS^R$	0.60	2.92	0.59	0.84	0.17	0.71
	$MIRACCS^T$	0.66	2.42	0.59	0.90	0.10	0.80
	TMI^R	0.71	2.84	1.24	0.88	0.03	0.88
1.0°x1.0°	$MIRACCS^R$	0.71	2.47	0.62	1.0	0.18	0.82
	$MIRACCS^T$	0.79	1.37	0.72	1.0	0.09	0.90
	TMI^R	0.84	1.90	1.41	0.93	0.0	0.91

Note: $MIRACCS^R$ means the MIRACCS estimates compared with Radar and $MIRACSS^T$ compared with TRMM TMI rain rate. TMI^R is the comparison between TMI and Radar. At 0.12° pixel scale, radar mean is 1.90 mm/hr and TMI mean is 1.82 mm/hr, the number of points is 1044

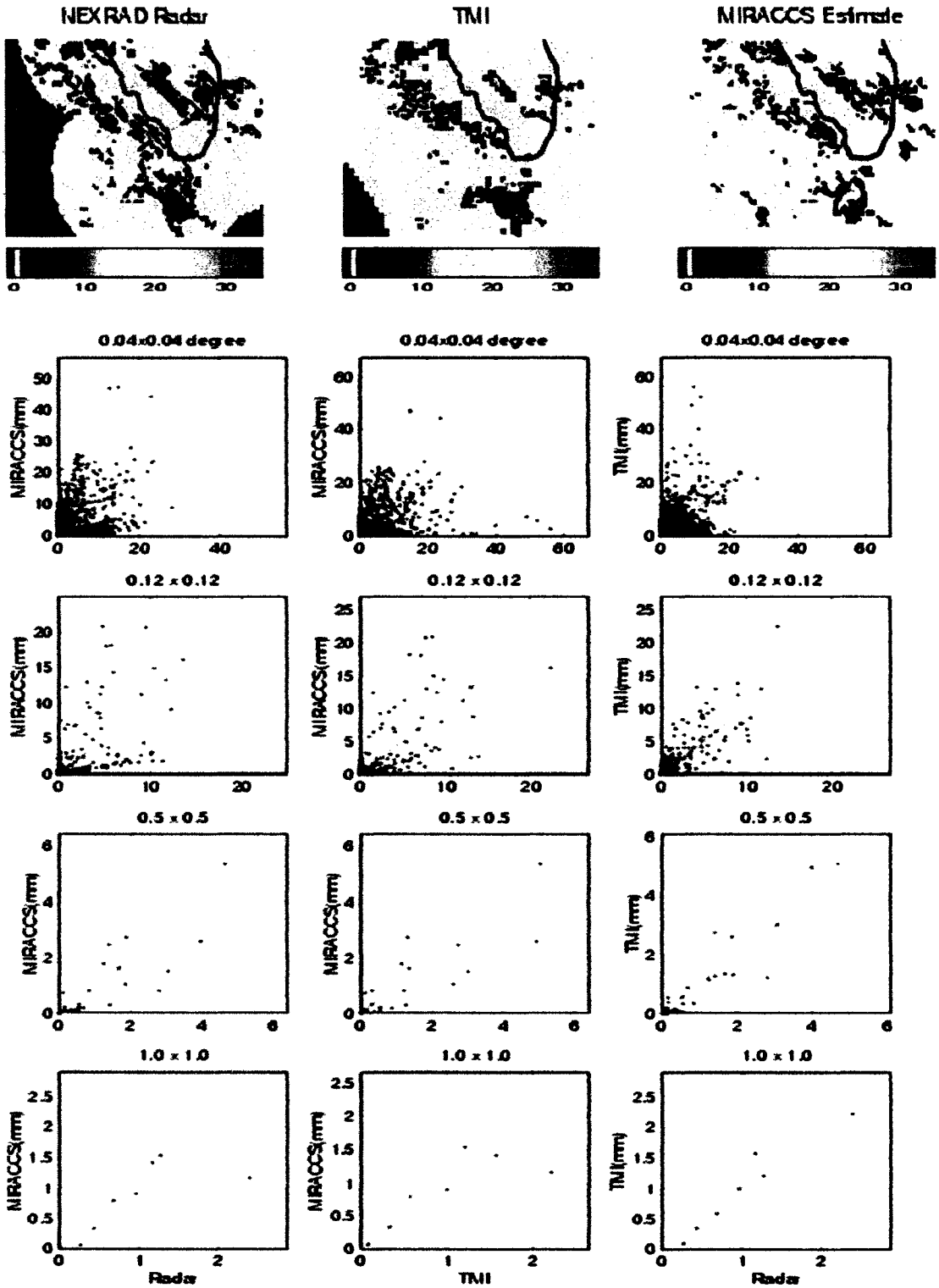

Figure 5.9. Top: plots of instantaneous rainfall derived from MIRACCS, radar, and TMI at UTC 0145 July 9, 2002; Scatterplots of instantaneous rainfall at different spatial scales: left (MIRACCS vs. Radar), middle (MIRACCS vs. TMI), right (TMI vs. Radar). The statistics are listed in Table5.3.

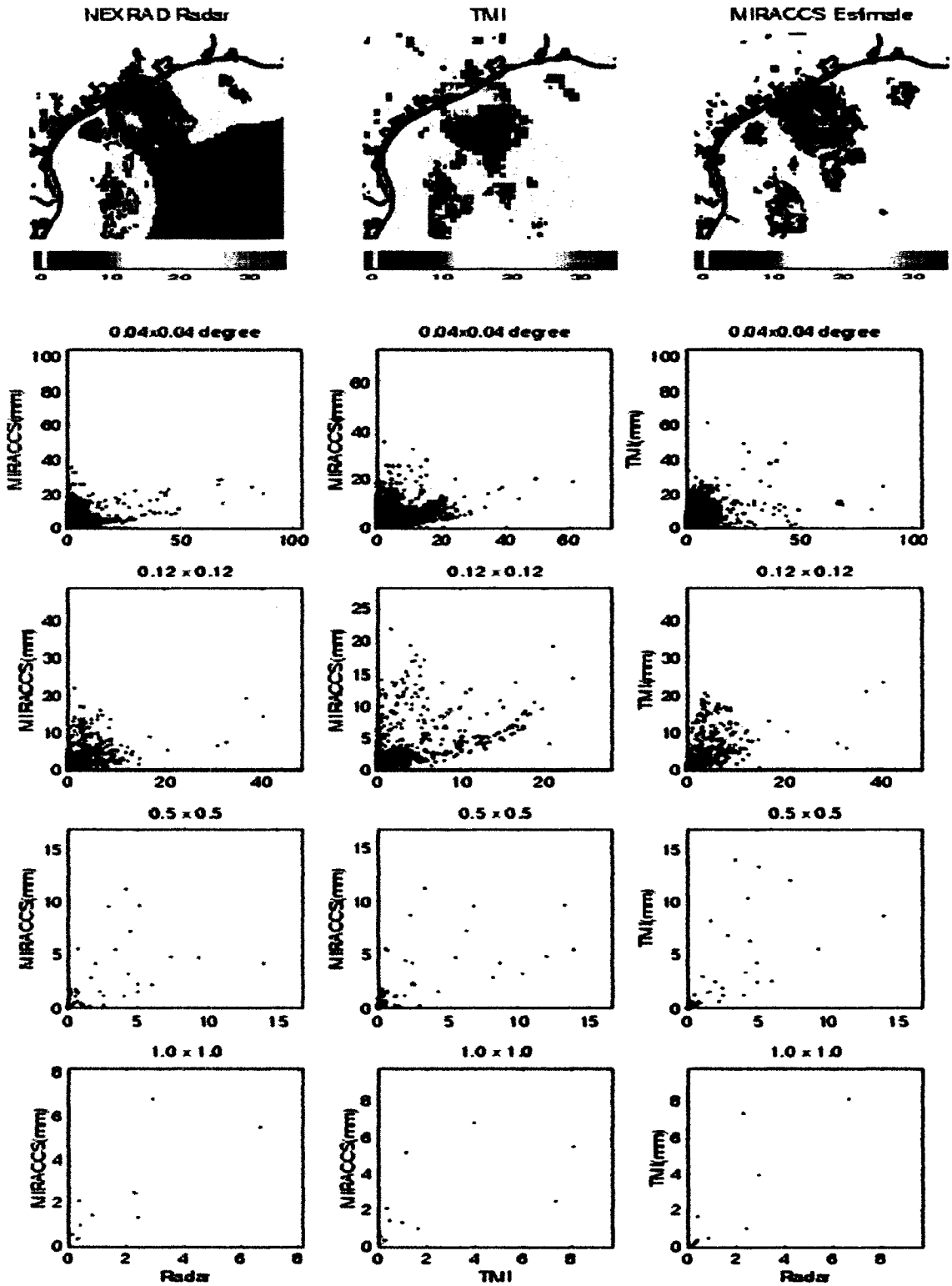

Figure 5.10 Top: Plots of instantaneous rainfall derived from MIRACCS, radar, and TMI at UTC 0445 July 16, 2002; Scatterplots of instantaneous rainfall at different spatial scales: left (MIRACCS vs. Radar), middle (MIRACCS vs. TMI), right (TMI vs. Radar). The statistics are listed in Table5.4.

5.5.3 Evaluation of Sub-daily Time Series Estimates

UAGPI (Xu et al., 1999) and MIRACCS are both cloud patch-based rainfall algorithms that are trained using satellite microwave estimates and ground-truth observation. However, UAGPI is a lumped rainfall model and uses simple binary function that assigns all pixels an averaged rain rate if the temperature of those of pixels is colder than certain threshold. On the contrary, MIRACCS is a distributed rainfall model that classifies the cloud-precipitations system into hundreds of clusters, each of which contains cloud patches with similar precipitation behaviors, and then search a multi-parameter nonlinear function for each individual cluster to approximate the cloud-precipitation relation. Accordingly, MIRACCS dispatches the best-fitted function (possibly timely adjusted if observations available) of the 1600 nonlinear functions (40 x 40 nodes in SOFM layer) to estimate rainfall for every cloud patch. Therefore, the MIRACCS can much more successively capture variability in rain rate at short-term time scales.

Statistics comparison of UAGPI and MIRACCS are conducted in sub-daily scales for six 1^{o}x1^{o} grids located at Texas and Florida, respectively. Figure 5.11 shows the locations of the selected boxes. Fig. 5.12.1-3 shows the time series plots of four grids at hourly, 3-hourly, and 6-hourly temporal integration over Texas. Fig. 5.12.4 plots the scatter plots of Texas time series at hourly, 3-hourly, 6-hourly, and daily rainfall at four grids for July 1-10 2002. Figure 5.13 shows the time series plots and scatter plots for the Florida grid II. Statistic comparison of two time series is presented at Table 5.5 and Table 5.6 for 1^{o}x1^{o} boxes located at Texas and Florida, respectively.

UAGPI consistently under-estimates rainfall compared to radar over the 1^{o} x 1^{o} grids and, therefore, results in larger RMSE and BIAS than MIRACCS. MIRACCS estimates demonstrate higher correlation coefficient than UAGPI, especially at time scales less than 6-hour. At larger time scales, i.e. daily, UAGPI and MIRACCS perform similarly at correlation coefficient and Critical Successive Index (CSI) but the BIAS and RMSE are much more favorable for MIRACCS.

Table 5.5. Statistics comparison of time series averaged 1^{o} x 1^{o} MIRACCS estimates vs. radar located Texas grid IV 29^{o}-30^{o}N and 99^{o}-100^{o}W at 1, 3, 6 hourly, and daily intervals from 1 Jul 2002 to 10 Jul 2002.

Time interval	Radar mean	RMSE (mm)		CORR		Bias (mm)		CSI	
		UAGPI	MIRACCS	UAGPI	MIRACCS	UAGPI	MIRACCS	UAGPI	MIRACCS
Hour	1.32	1.51	1.19	0.52	0.73	-0.62	-0.18	0.62	0.78
3 hours	3.96	4.23	2.12	0.61	0.80	-1.86	-0.55	0.77	0.95
6 hours	7.93	7.56	5.02	0.63	0.81	-3.72	-1.10	0.89	0.98
Daily	31.71	23.21	12.97	0.68	0.86	-14.93	-4.40	1.0	1.0

Table 5.6. Statistics comparison of MIRACCS time series averaged 1^{o} x 1^{o} estimates vs. radar data located at 35^{o}-36^{o}N and 80^{o}-81^{o}W Florida grid II at 1, 3, 6 hourly, and daily intervals from 1 Jul 2002 to 10 Jul 2002

Time interval	Radar mean	RMSE (mm)		CORR		Bias (mm)		CSI	
		UAGPI	MIRACCS	UAGPI	MIRACCS	UAGPI	MIRACCS	UAGPI	MIRACCS
Hour	0.607	1.14	0.60	0.517	0.78	-0.21	-0.05	0.53	0.76
3 hours	1.822	2.72	1.31	0.614	0.827	-0.69	-0.12	0.74	0.92
6 hours	3.645	3.63	1.96	0.727	0.916	-1.36	-0.35	0.87	0.96
Daily	14.579	6.25	3.64	0.924	0.946	-4.85	-1.02	1.0	1.0

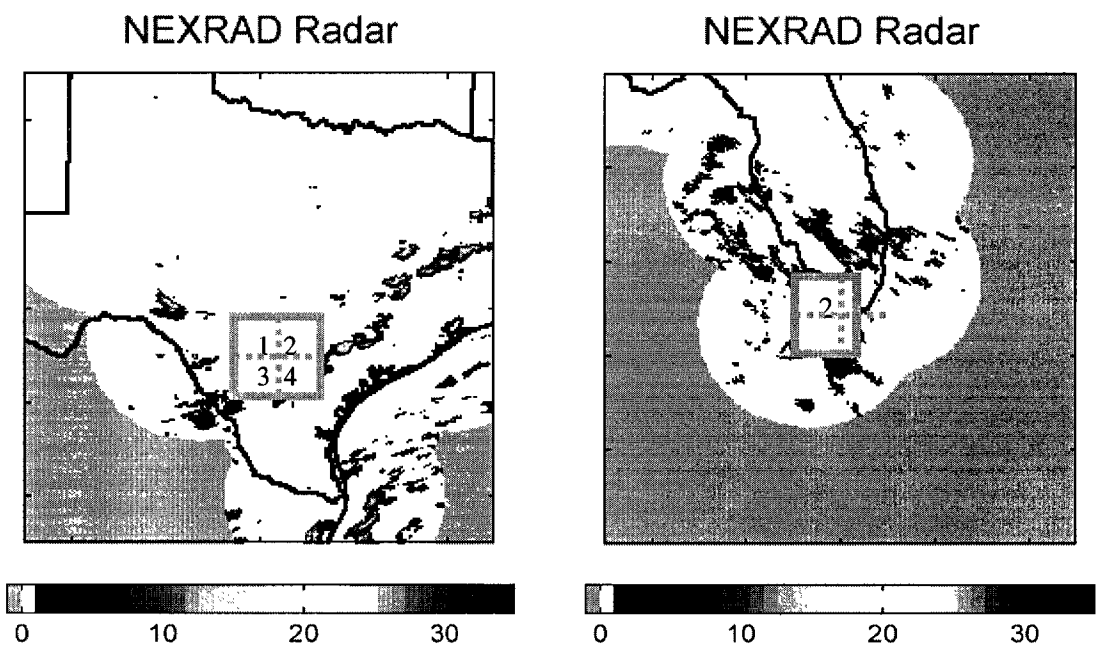

Figure 5.11. Overlapping areas between MIRACCS hourly rainfall products and NEXARD data over the Texas and Florida regions.
Left: Texas four 1^{o} x 1^{o} grids located at 28^{o}-30^{o}N and 98^{o}-100^{o}W;
Right: Florida four 1^{o} x 1^{o} grids located at 34^{o}-36^{o}N and 80^{o}-82^{o}W.
(*Note: Grids with indices 1-4 are grids with scatterplots and time series plots shown in Fig.5.12 and Fig. 5.13*)

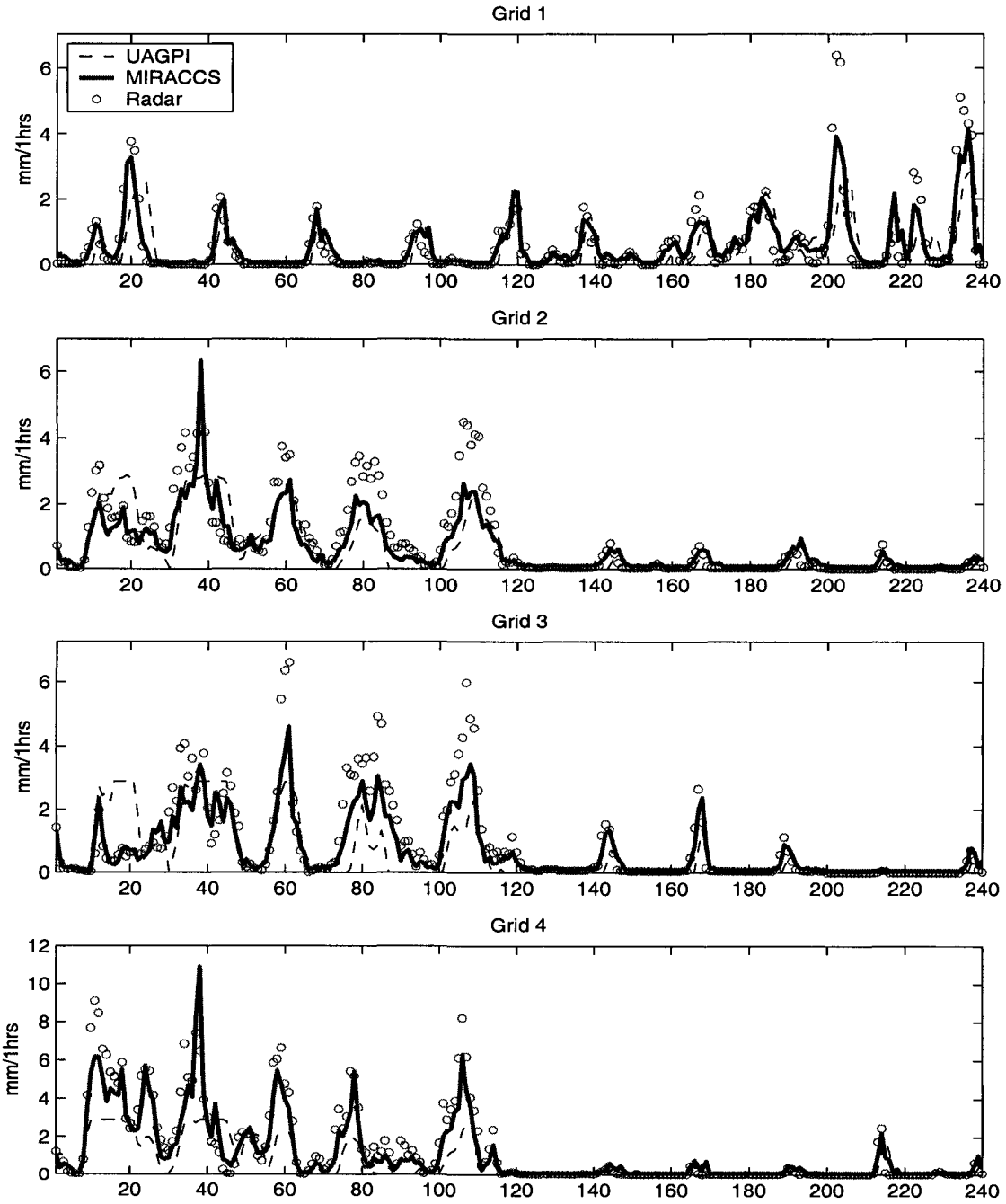

Figure 5.12.1 Time series plots of hourly rainfall at four 1^{o} x 1^{o} grids for July 1-10 2002 located at Texas 28^{o}-30^{o}N and 98^{o}-100^{o}W region.

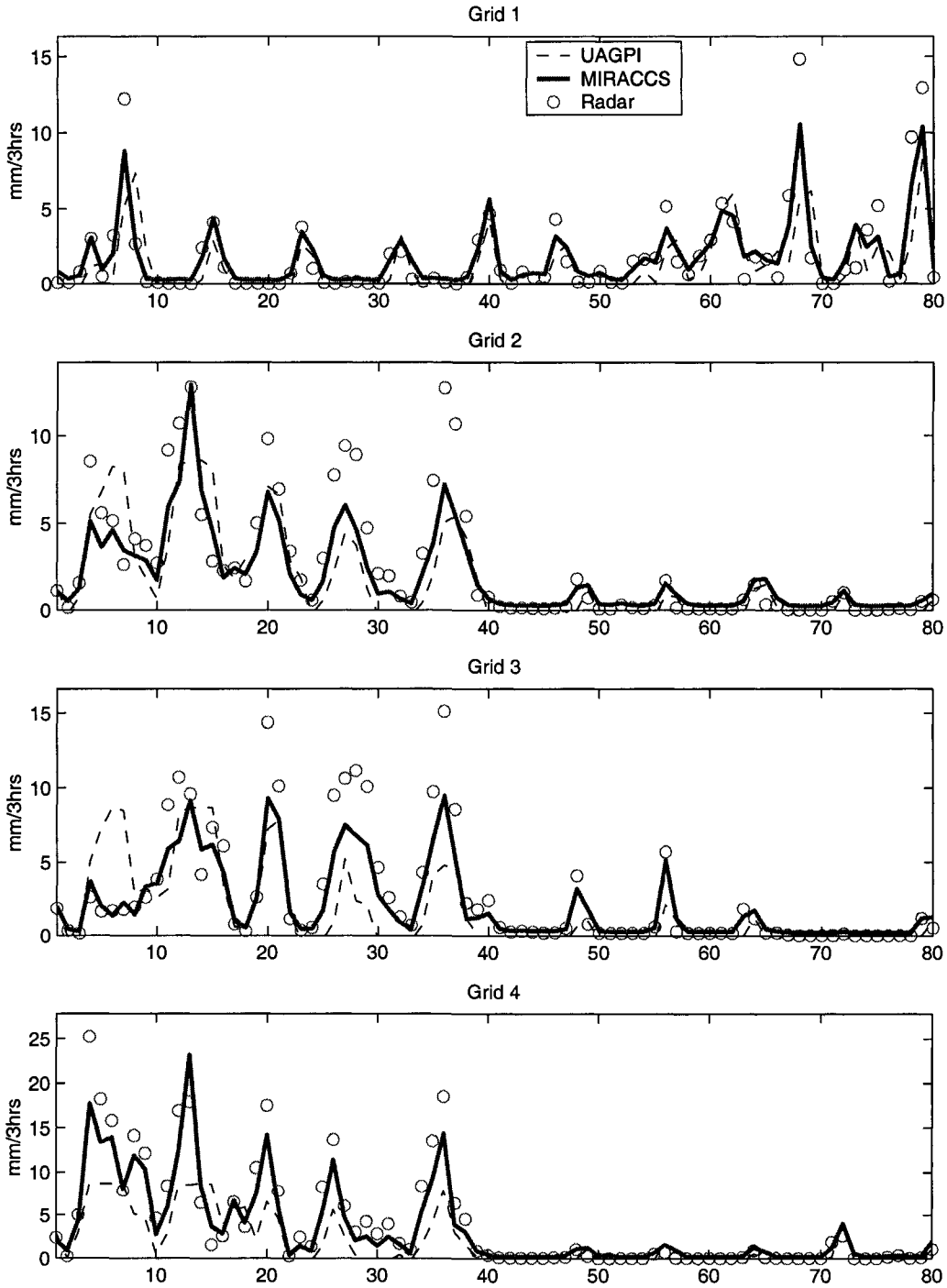

Fig. 5.12.2 Texas time series of 3-hour rainfall at four 1^{o} x 1^{o} grids for July 1-10 2002 located at Texas 28^{o}-30^{o}N and 98^{o}-100^{o}W region.

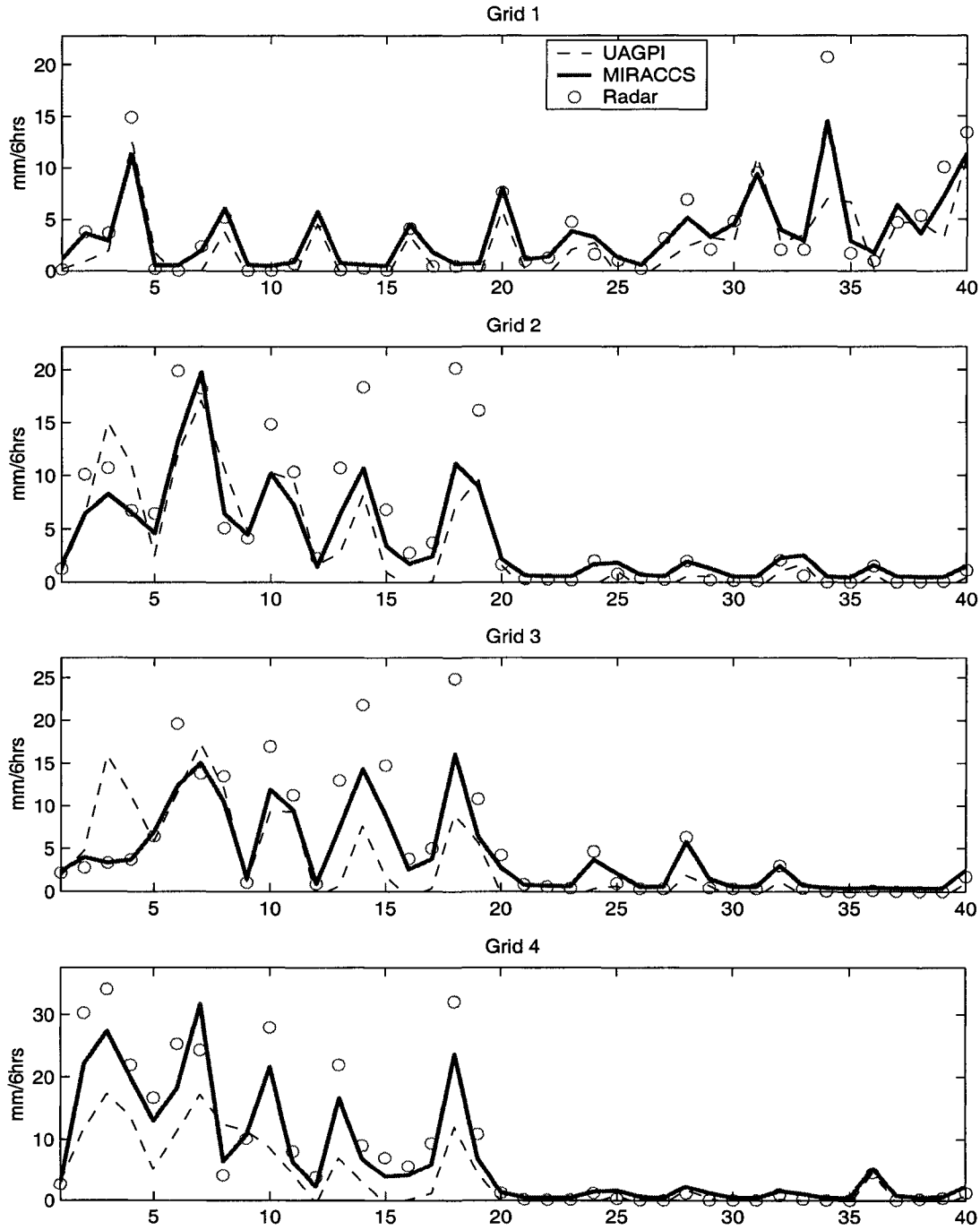

Figure 5.12.3 Texas time series of 6-hour rainfall at four 1°x1° grids for July 1-10 2002 located at Texas 28°-30°N and 98°-100°W region.

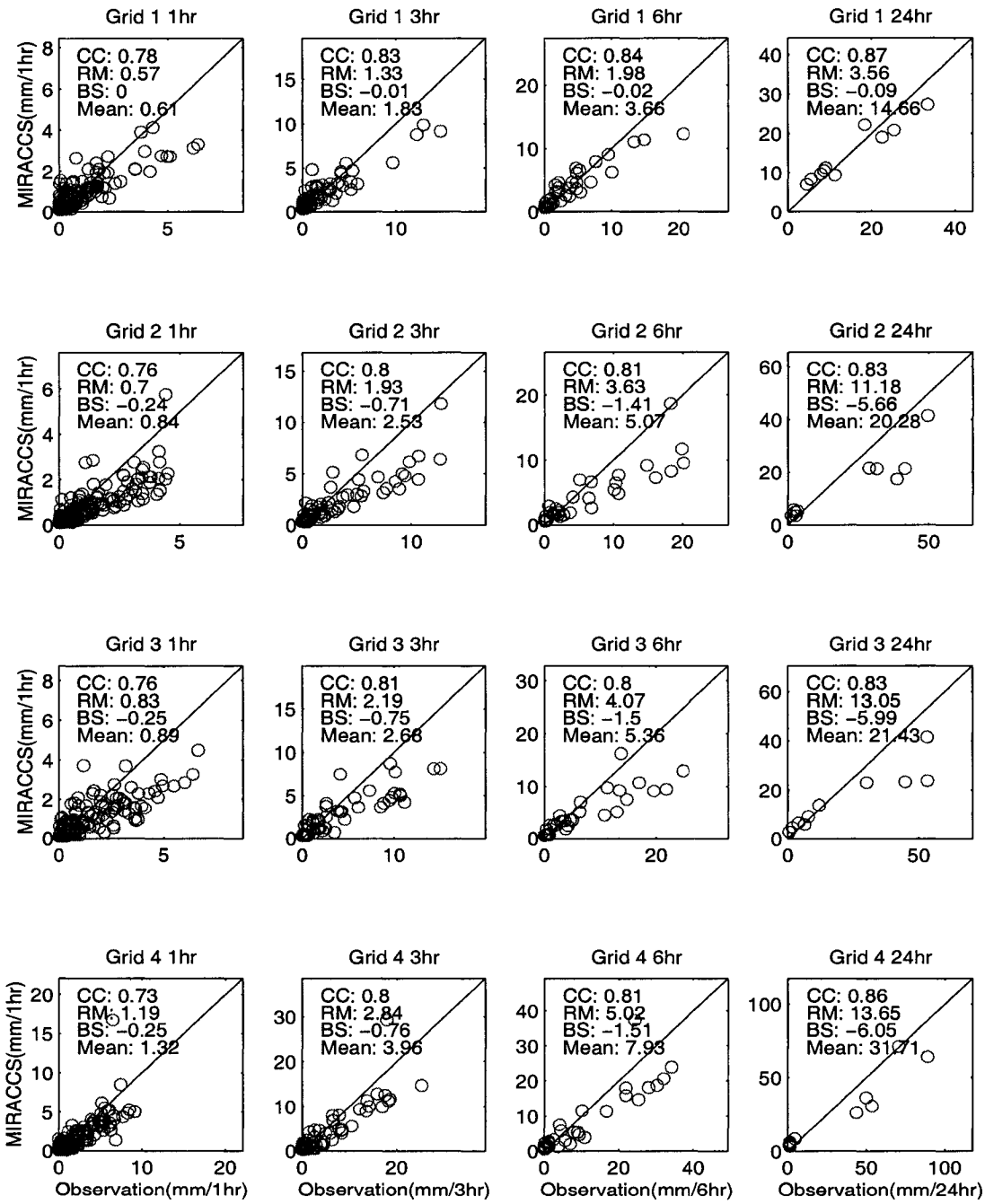

Figure 5.12.4 Scatterplots of Texas time series of hourly (1hr), 3-hour, 6-hour, and daily rainfall against radar at four 1^{o} x 1^{o} grids for July 1-10 2002 located at Texas 28^{o}-30^{o}N and 98^{o}-100^{o}W region.

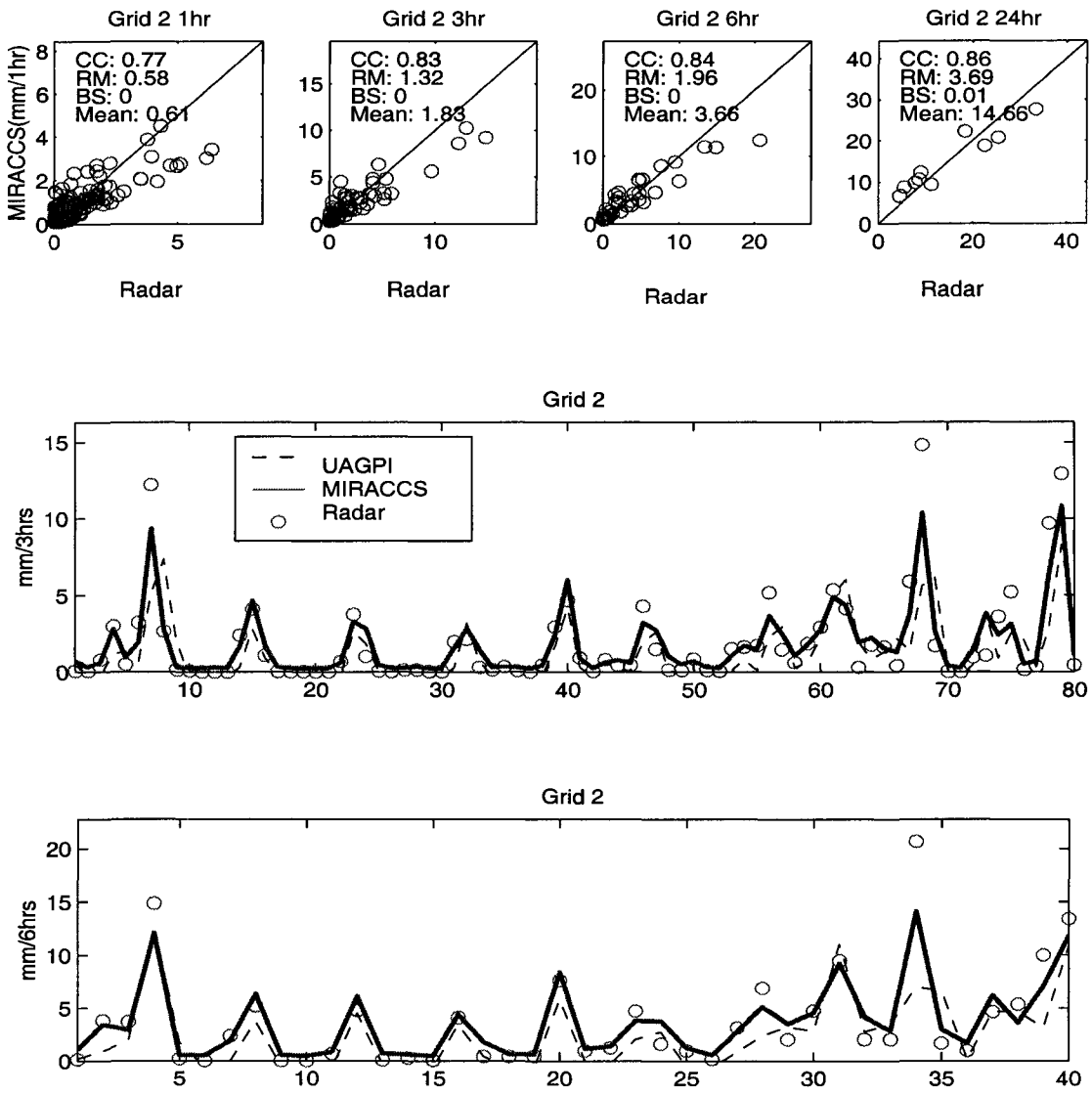

Figure 5.13: Rainfall estimation at Florida 1°x1° grid II located at 35°-36°N and 80°-81°W.

Top: Scatter plots of MIRCCS vs. Radar at different time intervals;

Middle: Plot of 3-hour rainfall time series MIRACCS and UAGPI estimates vs. Radar;

Bottom: Plot of 6-hour rainfall time series MIRACCS and UAGPI estimates vs. Radar.

5.5.4 Daily and Monthly Rainfall Evaluation

One of the goals of development MIRACCS is to provide rainfall product for North American Monsoon Experiment (NAME) project at summer season. Figure 5.14 and Figure 5.15 show two daily rainfall maps over North American in July 1st and July 5th 2002, respectively. Evaluation results show low error and, particularly, high correlation coefficient in daily heavy rainfall.

To assess the model performance at longer duration such as daily or even monthly level, a regional monthly (July 2002) rainfall estimation study was conducted at a 10^{o} x 10^{o} region located at central Texas plain (30^{o}-40^{o}N and 105^{o}-115^{o}W) with good quality of observation data—NEXRAD radar network fro comparison (Maddox, 2002). Rainfall estimation was produced at hourly basis and then accumulated to daily and monthly total while maintaining the original spatial resolution at 0.04^{o} x 0.04^{o} lat/long.

Figure 5.16 shows the statistical comparison of daily estimates time series derived from UAGPI, AE, and MIRACCS vs. radar data, including the daily-averaged statistical information. Figure 5.17 shows the monthly rainfall accumulation at 0.04^{o} x 0.04^{o} pixel resolution and Figure 5.18 shows the scatter plots of monthly rainfall total derived from AE, UAGPI, and MIRACCS vs. Radar observation.

The IR algorithm Auto-Estimator can catch the high rain rate events but with pronounced overestimation, resulting in large RMSE and bias while UAGPI can not catch high rainfall but with better performance accumulated over space/time than AE. The MIRACCS inherits both the sensitively nonlinear behavior of AE and also the advantage of microwave rain rate calibrated UAGPI approach while, additionally, it is a

distributed rainfall estimation model in that each IR_{Tb}-RR relationship corresponds to certain cloud type and is adjusted by passive MW rain rate. Therefore, the MIRACCS outperforms AE and UAGPI with respect to overall statistics both at small and accumulated large time/space scale.

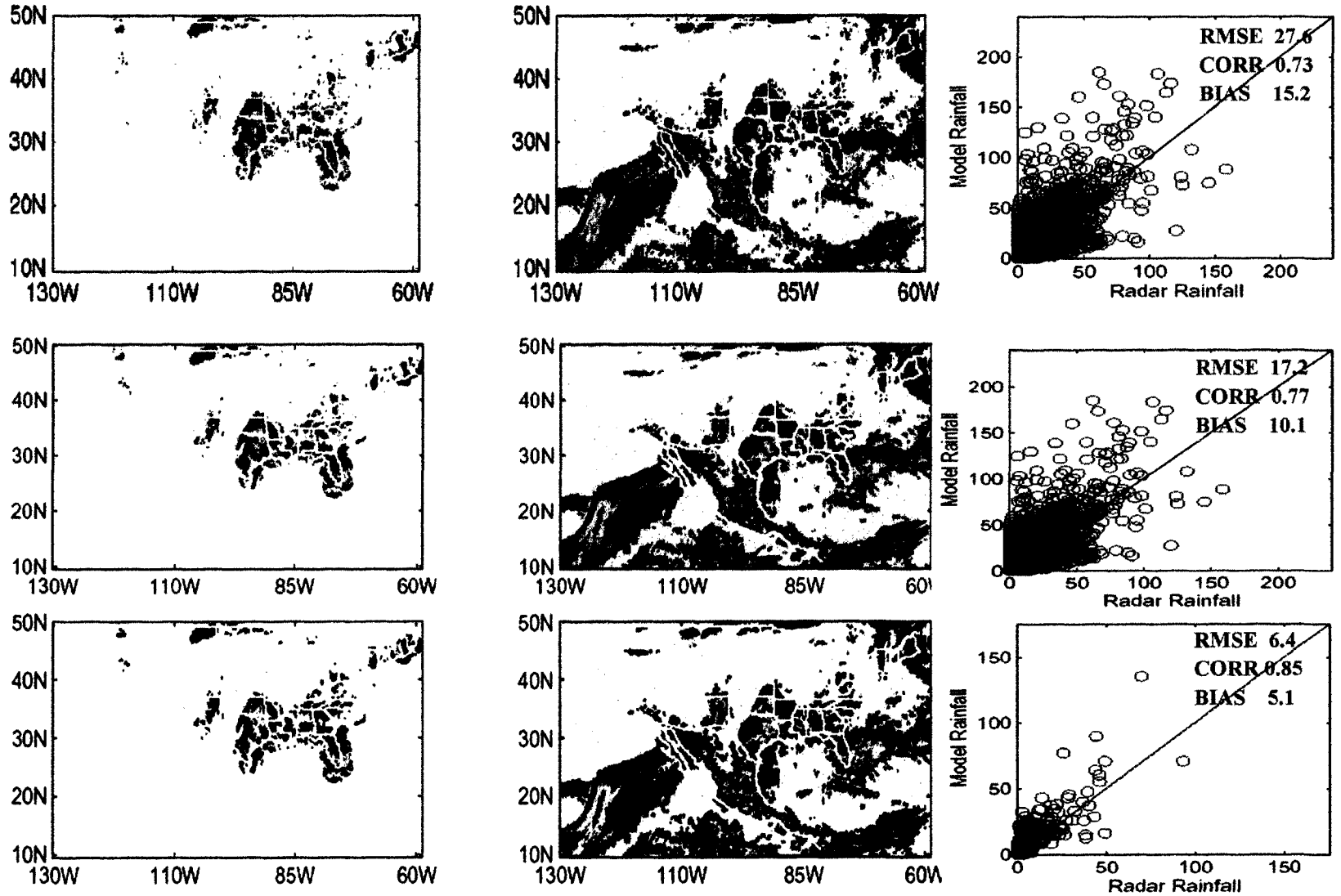

Figure 5.14 Comparison of daily rainfall derived from model vs. NEXRAD radar over the North American Monsoon Experiment region (10-50°N and 65-135°W) in July 1st 2002 at 0.04° (top), 0.12° (middle), and 0.24° (bottom) spatial resolutions.

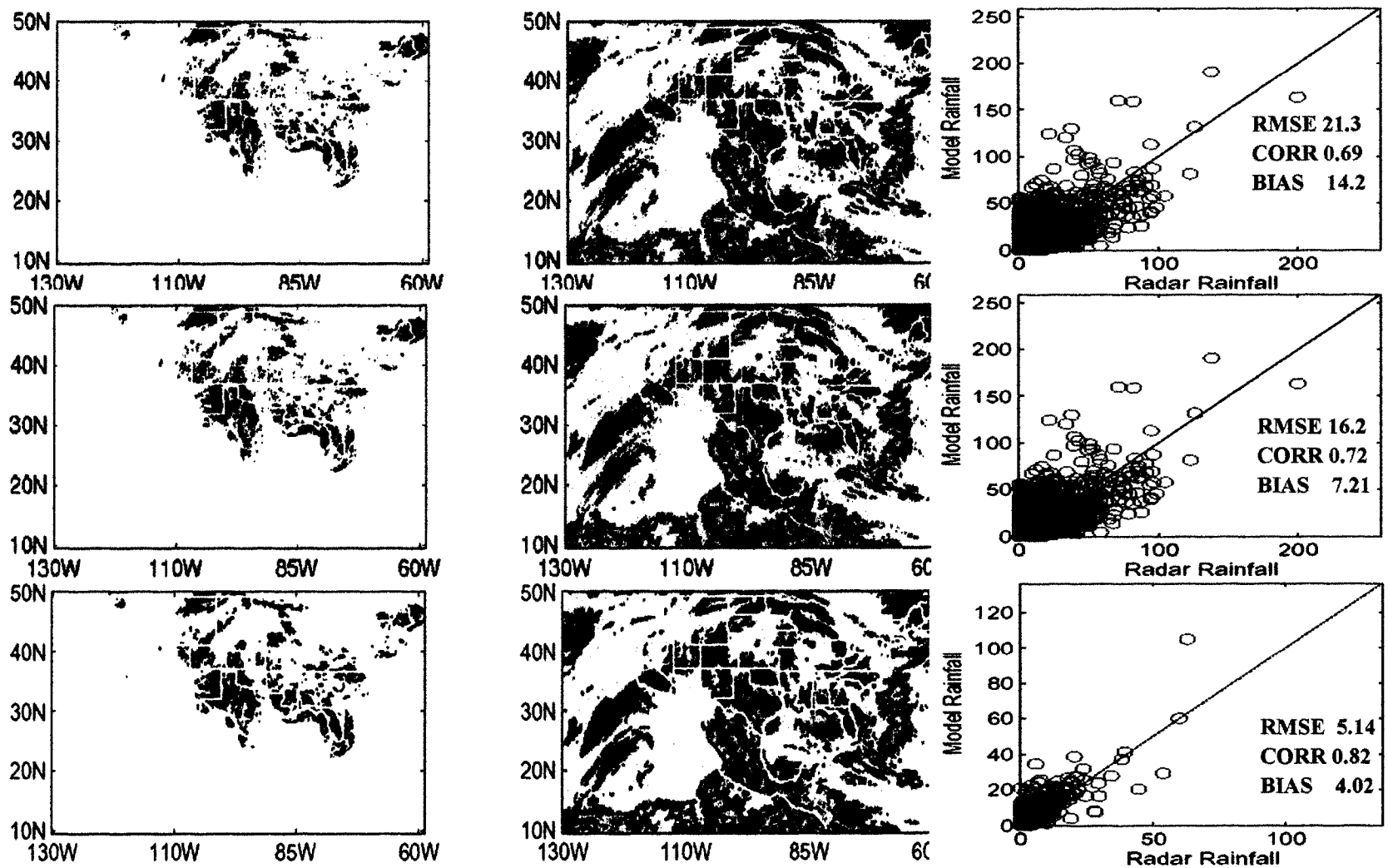

Figure 5.15 Comparison of daily rainfall derived from model vs. NEXRAD radar over the North American Monsoon Experiment region (10-50°N and 65-135°W) in July 5th 2002 at 0.04° (top), 0.12° (middle), and 0.24° (bottom) spatial resolutions.

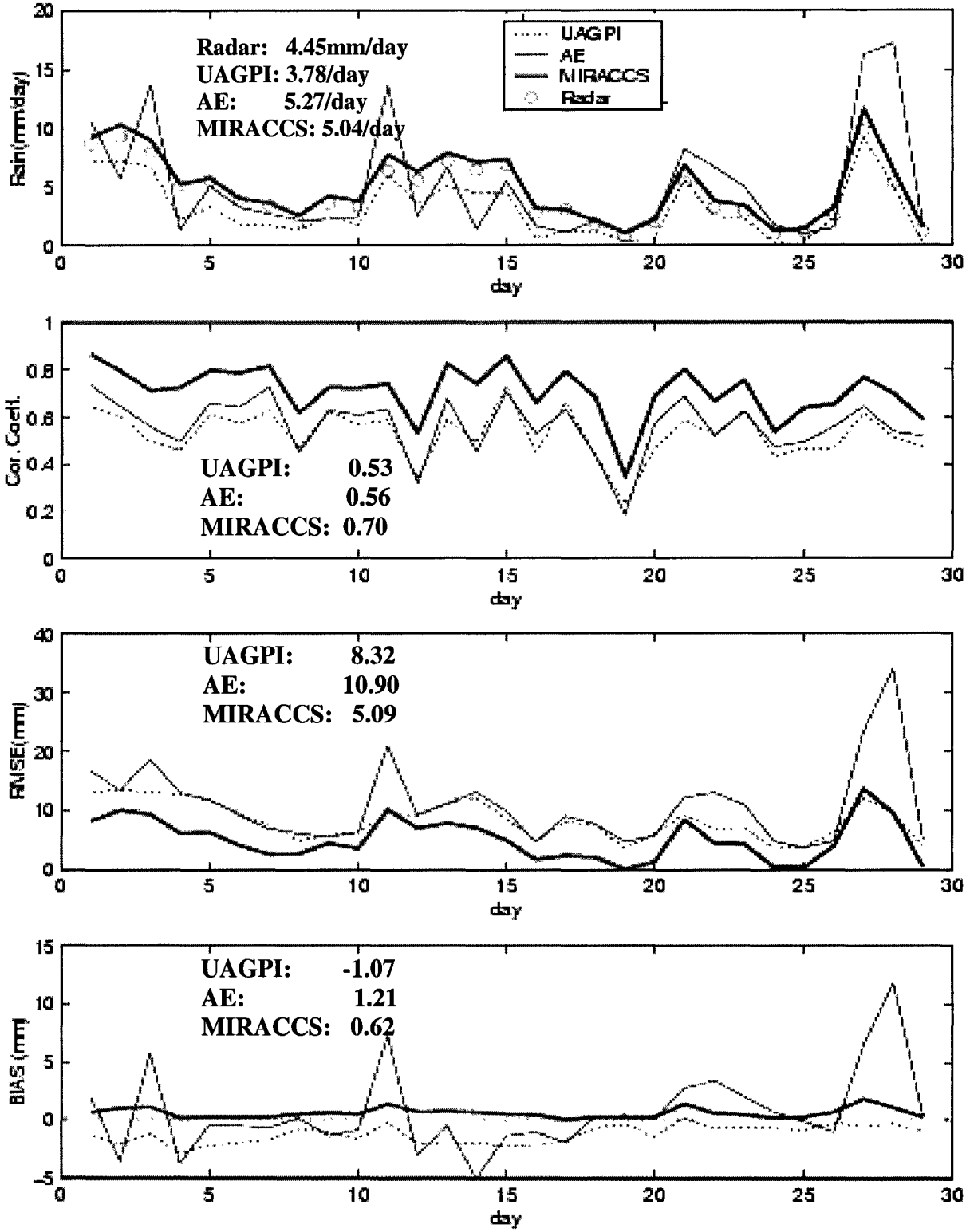

Figure 5.16 Plot of the time series of daily rainfall derived from radar, AE, UAGPI, and MIRACCS and their daily comparison statistics (CORR, MSE, BIAS, POD, FAR, CSI, and SKILL Score) over 30-40°N and 105-115°W Southwest of USA in July 2002.

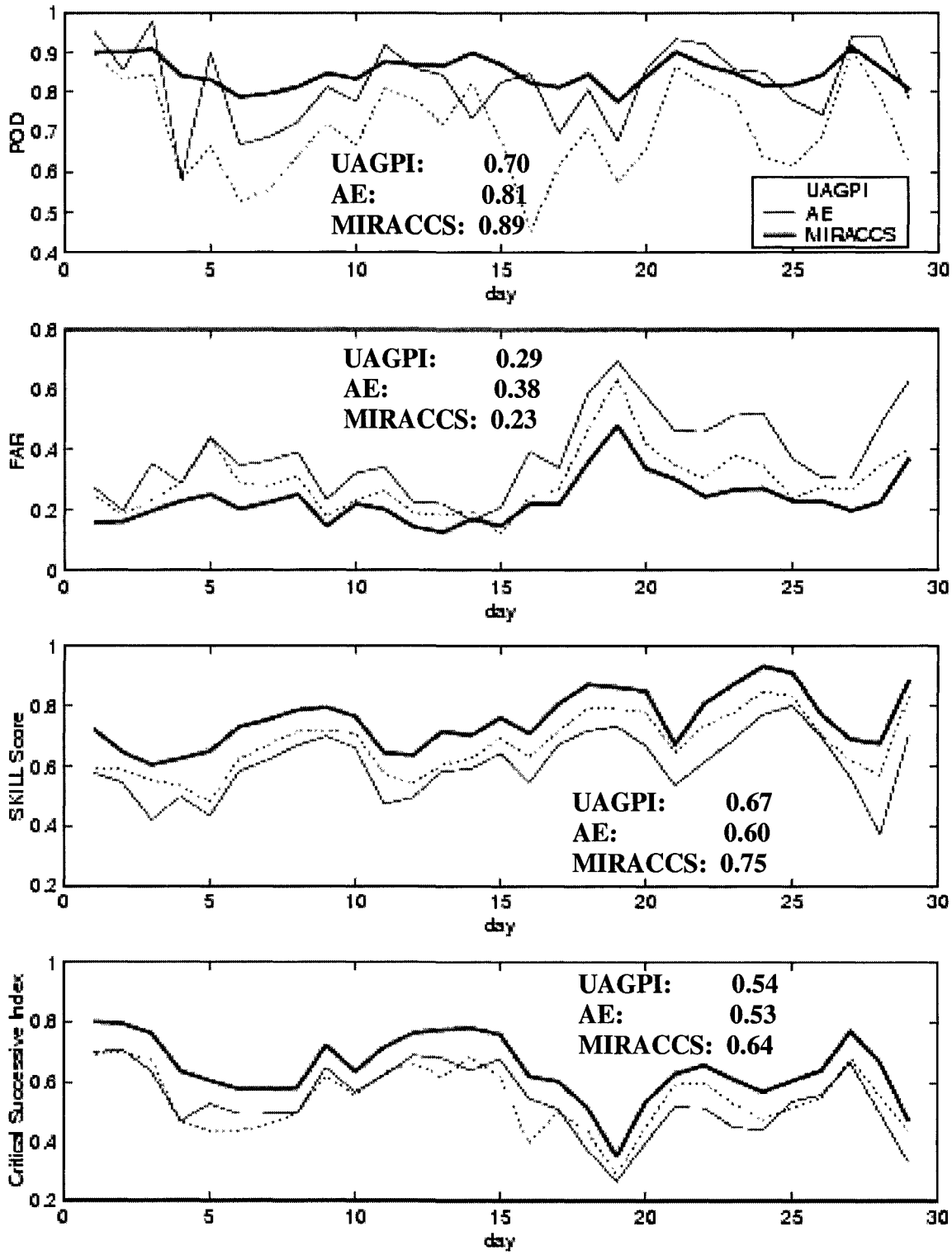

(Continue) Figure 5.16 Plot of the time series of daily rainfall derived from radar, AE, UAGPI, and MIRACCS and their daily comparison statistics (CORR, MSE, BIAS, POD, FAR, CSI, and SKILL Score) over 30°-40°N and 105°-115°W Southwest of USA in July 2002.

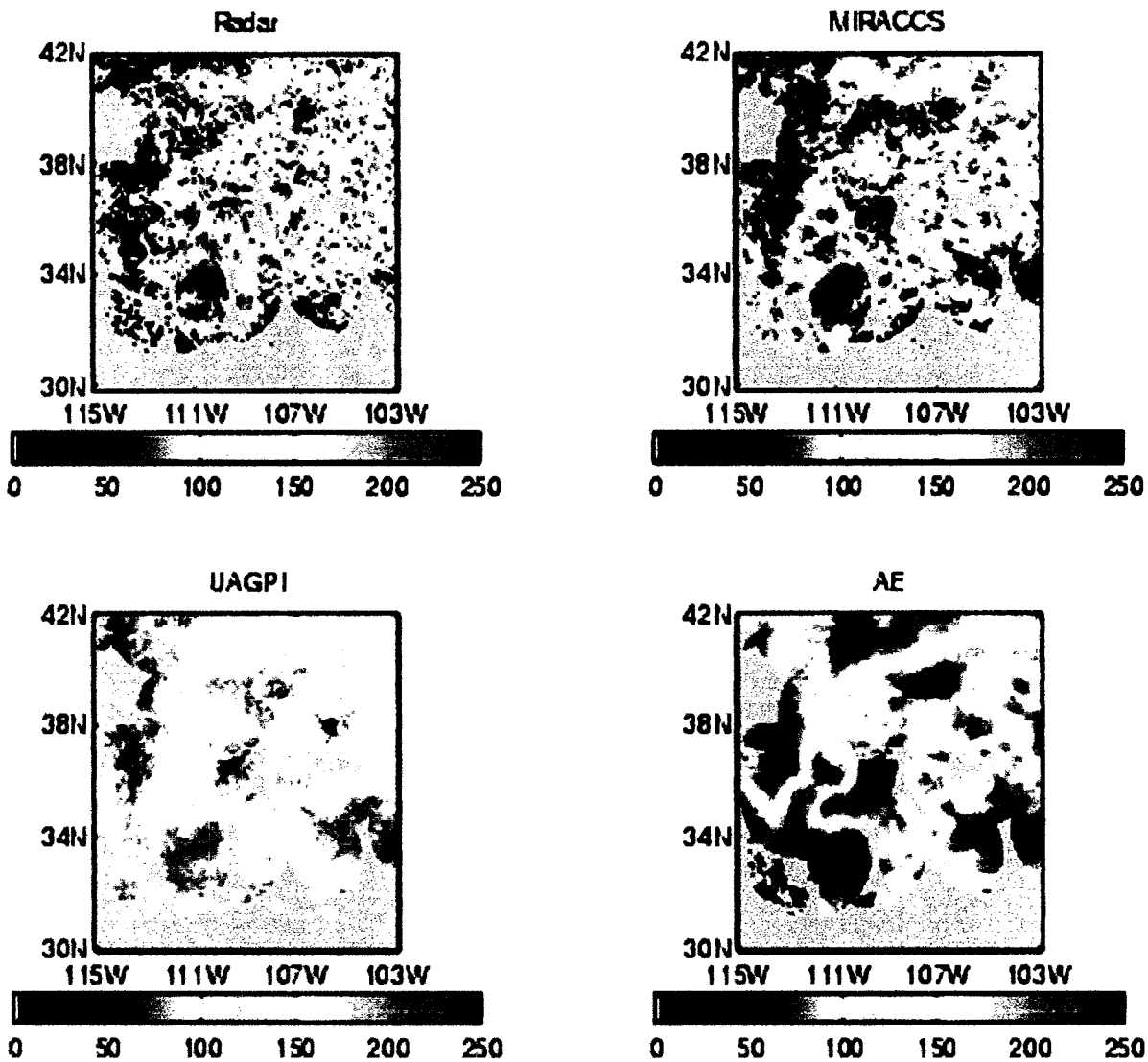

Figure 5.17: The comparison of July 2002 monthly rainfall total derived from MIRACCS, UAGPI, and AE vs. Radar at 30°-40°N and 105°-115°W region

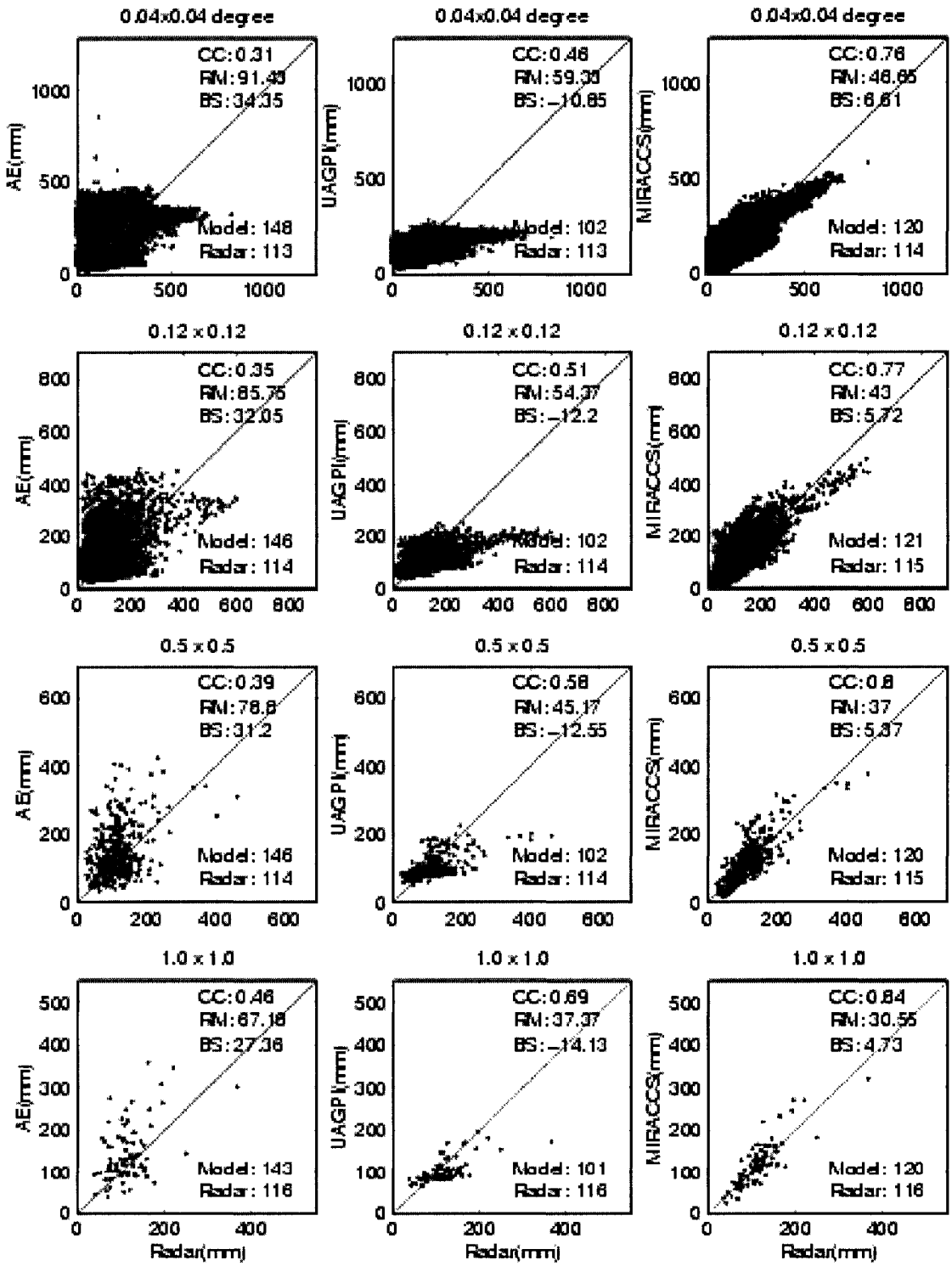

Figure 5.18 Scatterplots of Jul 2002 monthly rainfall total derived from AE, UAGPI, and MIRACCS vs. Radar at 30°-40°N and 105°-115°W region

5.5.5 MIRACCS Model Performance over Space and Time

Finally, we compare the MIRACCS products with NEXRAD radar over a range of temporal and spatial scales for long-term period to investigate the consistency and uncertainty of the model. The region is located at Rio Grande and San Pedro basins at 30°-40°N and 105°-115°W for July 2002 whole month. Figure 5.19 shows the correlation coefficient and standard error over range of temporal/spatial resolution (from 0.04° x 0.04° hourly to 1.0° x 1.0° daily). Results show that the temporal integration of rainfall data reduces the standard error more effectively than spatial aggregation. Large uncertainty of standard error exists among 0.04°-0.12° and hourly-3 hour spatial/temporal range. For correlation coefficient, the spatial averaging improves the correlation coefficient more efficiently than temporal integration, particularly the correlation coefficient increased to 0.63 from 0.53 while rainfall data aggregated from 0.04° to 0.12° scale at hourly time interval. The uncertainty of correlation coefficient is mostly located in the spatial range of 0.04° to 0.12° while the correlation coefficient is quite stable at lower spatial resolution. This indicates that the model involves large uncertainty to produce rainfall at spatial scales less than 0.12°. We believe that results are due to the unavailability of microwave data at spatial scales smaller than 0.12° and partially from the displacement of IR images from the surface rainfall due to very high altitude of geostationary satellites.

In summary, the model performance analysis shows that the MIRACCS model has the potential to provide reliable rainfall products at 0.12 and 3 hours spatial/temporal scale with relative high consistence at standard error (3.0mm/hr) and correlation (0.65).

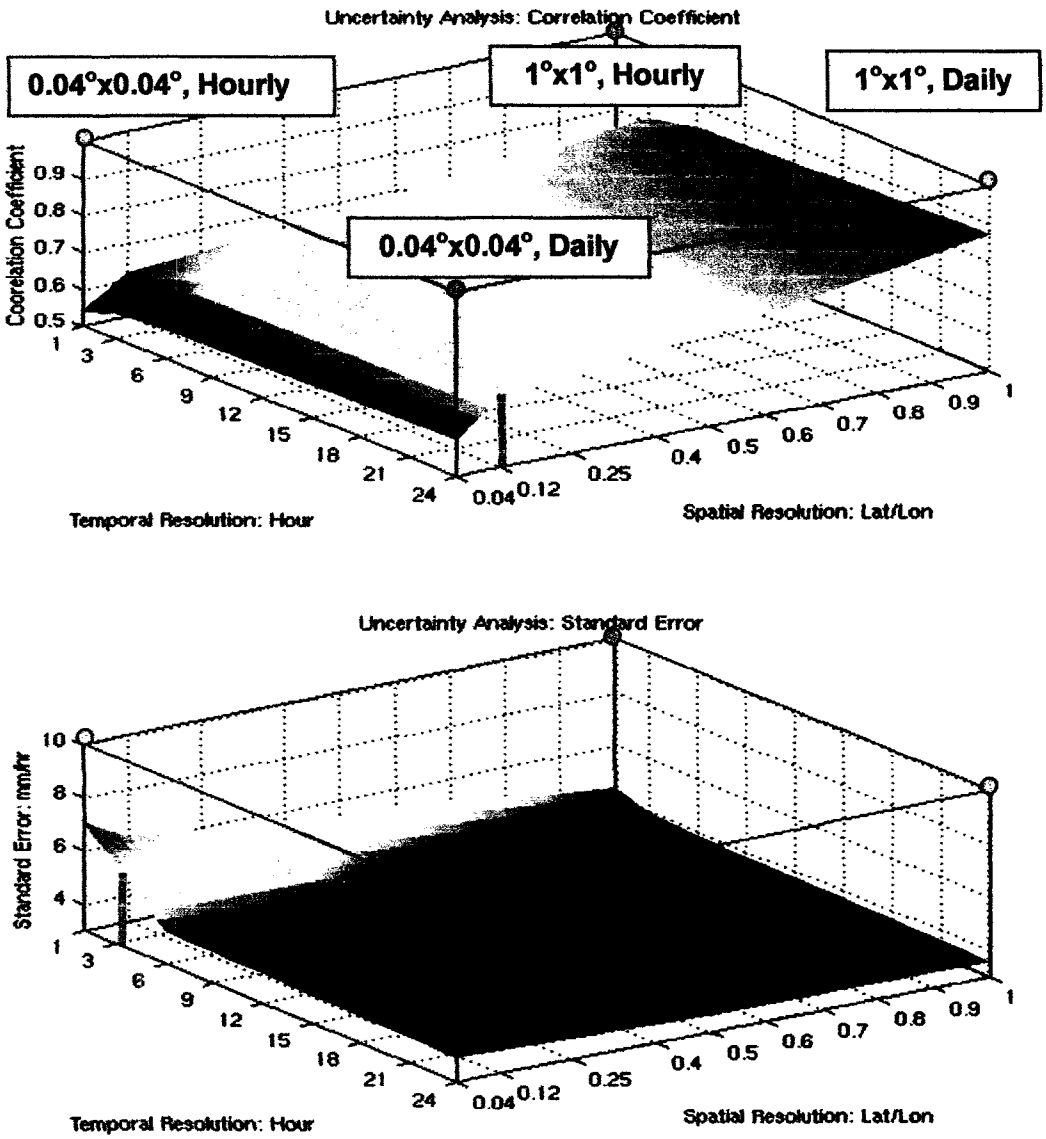

Figure 5.19 Model performance analysis of MIRACCS product vs. NEXARD radar data over a range of spatial and temporal scales (sampling data from monthly average at 30°-40°N and 105°-115°W region).

5.6 Summary and Conclusion

An adaptive algorithm from CCS model has been presented which aims to combine the organized comprehensive information of geostationary sensors with the more physically direct measurements of microwave instruments to produce accuracy estimates of rain rate at high temporal and spatial resolutions. This algorithm trained the CCS with the TRMM TMI microwave rain estimates, which is termed as combined Microwave/IR Rainfall Algorithm using Cloud Classification System (MIRACCS).

IR channel data provide near continuous temporal coverage and informative cloud patch features, which enable us to design a collective cloud classification system to organize cloud types using computational and intelligent strength of Self-Organizing Feature Mapping. This algorithm regards each of cloud clusters as an independent precipitation system and then approximates a nonlinear IR_{Tb}-RR relationship for different types of clouds using rainfall observation data. Unlike other existing MW/IR algorithms, MIRACCS inherits the model structure of Cloud Classification System and, therefore, exhibits great deal sensitivity in response to the variation of cloud-precipitation system. MIRACCS also provides the flexibility of model structure and adaptability of function approximation. The evaluation results point to three principle conclusions:

First, MIRACCS' performance outdistance passive MW related algorithm such as AGPI and UAGPI, particularly in correlation and the capability to catch the high variation of rainfall at small temporal/spatial scales, which demonstrates the advantage to determine diverse nonlinear IR_{Tb}-RR relationships based upon the classified cloud types as a distributed model instead of a simple lumped relationship.

Second, MIRACCS exhibits improvements in rainfall estimate accuracy compared to the IR algorithm such as AE, especially at classification of rain/no-rain pixels, bias, and root-mean-square-error, which demonstrates the strength of MIRACCS as a combined MW/IR algorithms.

Finally, coupled with MW rainfall estimates, MIRACCS retains the excellent monthly and daily rainfall characteristics of traditional IR algorithms (due to near continuous temporal sampling) and, meanwhile, lowers bias at the smallest possible temporal/spatial scale. Compared to AE, UAGPI, and PESIANN algorithms, the combined Microwave/IR Rainfall Algorithm using Cloud Classification System (MIRACCS) shows improvements of accuracy both in rainfall amount and in classification of rain/no-raining pixels at accumulated time/space scales and down to instantaneous pixel level.

There is a growing need to improve the spatial/temporal resolutions and accuracy of global-scale precipitation estimates for use in the investigation of weather/climate, hydrology, and environmental processes. The evaluation of current GOES IR-NEXRAD-TRMM TMI rainfall product from MIRACCS model indicates that this model provides a basis to build up an operational satellite-based rainfall estimation system to produce long-term/high-quality rainfall estimates at high temporal and spatial scale by using an adaptive procedure. The current MIRACCS algorithm is clearly capable of providing improved tropical rainfall products at relative high spatial and temporal resolution. The

results also support the effectiveness of the current strategies of combining geosynchronous and TRMM satellite instantaneous rain rate estimates.

Two strategies are considered as future work for MIRACCS: (1) using the satellite IR data from the ISCCP DX products and SSM/I microwave rain rate to produce a long term databank of 3-hourly rainfall estimation on 25km grids over the global tropical and subtropics from 1987 to present; (2) given the more likely accurate TRMM TMI/PR data, a TRMM adaptive procedure of MIRACCS could implement operationally in the future to compensate the moderate spatial resolution of PERSIANN products to 0.12^{o} or even 0.04^{o} from 0.25^{o} at near real time.

CHAPTER 6

CONCLUSION AND FUTURE WORK

6.1 Introduction

It was anticipated from the beginning of this analysis that different types of clouds yield various distribution and amount of rainfall. Especially, the relationship between cloud-top temperature and surface rain rate significantly varies from cloud patch to patch. It was also felt that high quality of precipitation estimation at small scales cannot be achieved without regard to development of distributed rainfall model that automatically classifies every cloud patch into sub-clusters and identifies a large number of event-sensitive functions to simulate the variable relations between cloud patches and their corresponding precipitation releases. Thus, how to segment IR images clearly, retrieve informative cloud features, classify cloud patches into well-organized types, and adaptively self-calibrate nonlinear functions were given utmost consideration throughout the analysis, which sets this study apart from other studies.

Outline of this study is first summarized in Section 6.1, followed by brief comparison between the proposed CCS model and previous PERSIANN system. Key contributions of this work are enumerated next in Section 6.2. Finally several recommendations for further work are offered in last section.

6.1.1 Summary of CCS

After elaborately reviewing prominent rainfall estimation algorithms (*IR, MW,* or *combined MW/IR*) and the limitations/uncertainty associated with them, the methodology of Cloud Classification System was presented in Chapter 2. The CCS is a synthetic system that consists of three sub-systems: (a) **Cloud Segmentation**, a hybrid segmentation procedure—Hierarchically Topographical Thresholding and Stepwise Seeded Region Growing (HTH-SSRG)—to segment satellite IR images into separate cloud patches; (b) **Cloud Feature Extraction**, a 3D cloud feature extraction procedure to retrieve both local-scale features of pixel and large-scale features of cloud patch at various vertical heights; (c) **an ANN model**, Self-Organizing Nonlinear Output (SONO) network, to classify the cloud patches into different clusters and then calibrate the cloud-precipitation nonlinear functions for each organized clusters.

Cloud Segmentation and Cloud Feature Extraction sub-systems (detailed in Chapter 3) function as preprocessors to separate cloud patches from IR imagery and retrieve cloud features as input so that SONO is able to process IR image at cloud patch level instead of pixel scale. SONO was developed as the core building block of the CCS rainfall system that copes with the primary limitations of previous approaches (GPI, UAGPI, PERSIANN, and other MW/IR algorithms) at fine temporal and spatial resolution. The SONO is modified from Self-Organizing Linear Output (SOLO) (Hsu et al., 2002) by redefining the linear output layer as nonlinear output function to meet the objectives of this study. Three consecutive components are comprised in SONO network: (1) SOFM—a cloud classification algorithm which groups cloud samples into well-organized cloud types; (2) PMM—a Probability Matching Method to match the Cumulative Probability

Distribution (CPD) of cloud IR and that of surface rain rate; (3) Nonlinear Output Mapping—a cloud-rainfall mapping algorithm to identify multi-parameter nonlinear functions between cloud types and their underneath surface precipitation characteristics.

The CCS model was calibrated with GOES IR and NEXRAD radar rainfall data located at US Southwest region (25°-45°N and 100°-130°W) in Chapter 4. The preliminary evaluation of CCS demonstrates advantages over GPI and PERSIANN to capture high variability of rain rate at the smallest possible temporal and spatial scales of satellite rainfall algorithms. The validation of CCS model performance also successfully provides insight into the diverse IR_{Tb}- rain rate relationships between cloud patches and output rainfall distribution curves. In Chapter 5, an adaptive CCS model that timely adjusts its parameters whenever new observation data available has been developed to estimate rainfall over extended areas and time periods (for year 2002 over region 10°-50°N and 65°-135°W). This adaptive mode was then validated over a range of temporal scales (hourly, 3-hour, 6-hour, daily, monthly) and spatial scales (0.04°, 0.12°, 0.24°, 0.5°, and 1.0°). The adaptability of CCS mode structure and the flexible functionality of IR_{Tb}-rain rate approximation improve model performance in estimate accuracy and correlation coefficient at small scales (3-hour and 0.12° x 0.12° grids) in comparison with other algorithms such as PERSIANN, UAGPI, and AE.

In summary, the CCS has the capability to (1) process large amounts of GOES IR, surface radar rainfall, and microwave imagery in real-time mode; (2) not only function as an "analyzer" to classify large amount of cloud patches into well-organized clusters but also function as "auto-approximator" to self-calibrate the nonlinear cloud-precipitation

function for each cloud cluster; (3) behave as a distributed model that dispatches the best-fitted curve in response to different types of clouds in order to capture the high variation of cloud-precipitation systems at small temporal and spatial scale; (4) update the network parameters to improve the model's transferability to extended seasons and regions. CCS estimates rainfall at relatively high spatial and temporal resolutions using data from GOES-8/10 IR brightness temperature, Next Generation Radar Network (NEXRAD) rainfall, and polar-orbiting TRMM TMI instantaneous rain rate estimates. The major characteristics of CCS rainfall model could be summarized in one phrase: an adaptive distributed cloud patch-based MW/IR rainfall estimation model using the strength of ANN to provide satellite-based rainfall estimates at high spatial and temporal resolution.

6.1.2 Difference of PERSIANN and CCS:

Satellite-based rainfall estimation is becoming increasingly important to the hydrological and climate researches because of its capability of sampling remote regions where ground-based cannot reach. To explore the use of multiple sources of information including the ground and satellite observations in the rainfall estimation, a satellite-based rainfall estimation system, named PERSIANN, has developed at The University of Arizona (Hsu et al., 1997, 1999; Sorooshian et al., 2000). This system estimate surface rainfall over 0.25^{o} x 0.25^{o} grid at every 30-minute time interval, and provides relatively accountable global rainfall products by accumulation to lower resolutions, such as daily at 1^{o} x 1^{o} latitude-longitude scale. PERSIANN is a pixel-based rainfall estimation algorithm, which uses Self-Organizing Linear Output (SOLO) network to fit local cloud

top temperature texture to pixel rain rates. The function relationship in between cloud top pixel temperature and surface rainfall, however, is complicated by many factors, which, as a result, is not unique. Although regression fitting may be calculated at fine scale, the rainfall estimates contain large uncertainty with which, in many cases, high intensity rain-rates are underestimated, while low intensity rain-rates are over estimated.

In this continuing study, a new version of the PERSIANN, named CCS, is proposed. As a new version of PERSIANN, CCS—a cloud patch-based distributed rainfall estimation model—couples the sophisticated preprocessors (Cloud Segmentation and Feature Extraction) and the Self-Organizing Nonlinear Output (SONO) network for rainfall estimation at high spatial and temporal resolution. Other than using local pixel texture in the original PERSIANN system, the CCS includes both local and regional cloud textures in classification of hundreds of cloud types, followed by different five-parameter exponential functions calibrated to represent the relations between precipitation and cloud-top property for each classified cloud types. Hourly rainfall from NEXARD and polar-orbiting TRMM TMI instantaneous estimates of rainfall are used to search for the parameters of the distribution functions. The CCS behaves as a distributed rainfall estimation model that automatically identifies and then dispatches the best-approximated nonlinear function for different cloud patches to address the high variation of cloud-precipitation processes. CCS simulates the current GOES IR-TRMM TMI-NEXRAD rainfall product at 0.04^{o} x 0.04^{o} every 30-minute time interval and provides relatively reliable products at 3-hour 0.12^{o} x 0.12^{o} resolution.

6.2 Summary of Key Contributions

6.2.1 Limitation of Existing Rainfall Algorithms Using Satellite IR image

A number of algorithms have been underway to estimate precipitation from satellite (*VIS, IR-brightness temperature, or microwave*) information because satellite observations can provide a uniquely detailed view and data unparalleled by ground-based observations of hydrologically relevant variables. In general, most of the widely used rain retrieval algorithms use infrared images as the basis to estimate precipitation because of the several advantages, such as: high frequency and high spatial resolution of the observations, easy accessibility of data, and the broad geographical area that they cover, in addition, by using IR data, the applicability of these algorithms extents to nighttime observations as well. After decades' efforts of research on rainfall algorithms using IR imagery as the basis, it has been more clearly that the limitations/uncertainty of IR-based satellite rainfall algorithms could be briefly summarized as the following.

(1) Limitation of IR pixel-based information retrieval;

(2) Difficulty of selection of comprehensive cloud features as input;

(3) Limitation of conventional lumped techniques to model the large variety of cloud-precipitation processes;

(4) Uncertainty of choice of IR threshold to define rain/no-rain cloud pixels;

(5) Uncertainty of cloud-top properties and precipitation mapping;

(6) Indirect/Nonlinear relationship between cloud-top temperature and rainfall rate;

(7) Limitation of model adaptability to address regional and seasonal variation;

(8) Relative low spatial and temporal resolution of rainfall estimates.

Various methods have been tried to improve precipitation retrieval from satellite IR-based imagery, usually by improving the limitations or reducing the uncertainty (Adler et al., 1993; Xie and Arkin, 1996; Hsu et al., 1997, 1999; Xu et al, 1999; Sorooshian et al., 2000; Huffman et al., 2001; Kuligowski, 2002). In this document, The proposed CCS rainfall model has been designed, so far one of the most sophisticated rainfall model, to take advantage of previous developments and cope with the above limitations or uncertainty. The following subsections from 6.2.2 to 6.2.9 summarize and enumerate how the major efforts and key contributions in CCS rainfall model to cope with the above limitations, respectively.

6.2.2 From Pixel to Cloud Patch-based Rainfall Algorithm

Geostationary satellites snapshoot high temporal and spatial resolution IR imagery that provides cloud-top temperature for rainfall modeling. Three basic kinds of information extraction approaches from IR imagery categorize IR rainfall algorithms as pixel-based, window-based, or patch-based algorithms. The pixel/window-based rainfall algorithms extract the local information and relate rain rata to local pixel brightness temperature. Therefore, pixel/window-based IR rainfall algorithms suffer from the uncertainty to identify precipitation characteristics from large-scale cloud features, resulting in inadequate reliability in estimates due to high variation of cloud-precipitation relations. Additional uncertainty is contributed by the spatial pixel-based displacements from IR imagery to Earth surface.

On the contrary, the advantage of cloud patch-based algorithms is to map the cloud-precipitation relationship by inclusion of synoptic cloud information. Various studies already prove that cloud patch-based algorithms seem to be the most promising method overall (Xu et al., 1997, 1999). However, the high variability of cloud system and the computational expense of processing dataflow at patch level challenge the practical application of cloud patch-based algorithms.

Previous cloud patch-based algorithms delimit cloud using a single temperature threshold (Griffith and Woodley, 1978, 1980; Xu et al., 1999), which introduces large uncertainty of the inclusion of no-rain cold clouds (cirrus) or the exclusion of raining warm clouds (Arkin and Xie, 1994). Moreover, simple IR thresholding method leads to biased features extraction, especially large-scale features such as geometry, global texture variation, as well as area coverage. Instead of using a simple threshloding method, a purpose-designed preprocessor module is developed to segment IR imagery into separated cloud patches and extract cloud patch features as input to enable the proposed CCS model to retrieve rainfall at cloud patch level in this document. In Section 3.2, an automatic segmentation algorithm, Topographical Hierarchical Thresholding and Stepwise Seeded Region Grow, (THT-SSRG), has been developed to segregate IR images into separated cloud patches. As a hybrid method, THT-SSRG retains all of Seeded Region Grow advantages-fast execution, robust segmentation, and no tuning parameters (Adams, 1994). Additionally, it is fully automatic and flexible by using topologically hierarchical thresholds method, which guarantees the automatic and dynamic seeding in different cloud height levels rather than manual seeds initialization.

The preprocessing module, cloud patch segmentation detailed in Section 3.2, enables the CCS rainfall model to extract information associated with large-scale features on cloud patch level and then classify the cloud patch samples into organized clusters. This procedure provides very first starting point to propagate information from not only pixels but also cloud patches into CCS rainfall estimation system.

6.2.3 Incorporation of Local and Large-scale Features Information

Pixel-based and window-based information are also called local-scale features whereas patch-based is called large-scale features. Local-scale information employed by pixel-based or window-based algorithms is limited to produce accurate rainfall estimates though they are easy to implement. For example, GPI is purely a local-scale IR algorithm only involving a simple binary function that assigns 3mm/hr rain rate value to pixels colder than 235K or no rain otherwise. As such, GPI is capable of providing reliable estimates after spatial and temporal accumulation at coarse spatial (2.5^{o} x 2.5^{o}) and temporal resolution (monthly). On the other hand, large-scale features depict properties of whole cloud patch. Although the IR rainfall algorithms based upon large-scale features have produced relatively good results in some applications (Petty, 1995), the features that had been employed are quite simple such as cloud area, mean temperature, and minimum temperature etc.

Both local-scale and large-scale feature-based rainfall algorithms have pro and cons. As a successful satellite rainfall estimation model using local-scale information, PERSIANN relates rain rate to target pixel IR temperature with the additional

information from surrounding pixels (3x3 or 5x5 window). Hsu et al. (1996, 1999) suggested future efforts needed to incorporate features associated with patterns on both large-scale and local-scale. In this study, Section 3.3 describes the preprocessing module-**Feature Extraction** that involves incorporation of features on both large-scale and local-scale information of the cloud. Although the selected features for CCS model fall under three groups (coldness, geometry, and texture), they could also be categorized into local-scale and large-scale features according to the size of information extraction. For example, the area, global texture variation, and shape index is the large-scale features that are retrieved from whole cloud patch while the pixel temperature, the standard deviation of local texture variation as well as the mean of local texture variation are the local-scale features. By combining these local-scale and large-scale features as input, the CCS model has been configured with a SONO network to classify cloud patches and their corresponding precipitation observations into clusters and then to redistribute rain rate into pixels of cloud by approximating a multi-parameter nonlinear mapping function for each cloud cluster. Besides horizontal feature retrieval, vertical information of both local-scale and large-scale features are extracted at incremental height levels (253K, 235K, and 220K) from IR cloud patch images, which gives rise of 3-D view of a cloud patch from 2-D IR imagery and provides better distinction between convective and stratiform clouds.

6.2.4 Not All Cloud Precipitate: A Distributed Rainfall Model

Global precipitation system is distributed over space and time due to the motion of global energy/water and heterogeneity of earth surface. Experiments have shown that the

relationships between cloud-top temperature and surface rain rate (IR_{Tb}-RR) vary significantly over space and time. Particularly, the variation of precipitation behaviors exists from cloud patch to patch.

Not all clouds precipitate. Different cloud types may have similar cloud-top temperatures but are associated with very different amounts of rainfall at the ground. For example, cirrus clouds are generally very cold, but they rarely produce surface rainfall. Even moderately thick cirrus clouds will thus convey a false precipitation signal to IR rainfall algorithms. Meanwhile, some rather shallow clouds are capable of producing significant precipitation, and these instances, often termed as warm rain, will go largely unnoticed by many IR technique. This complicates the task of developing instantaneous surface rainfall estimation algorithms and, therefore, many of existing approaches resort to considerable spatial aggregation and temporal accumulation to improve the statistical accuracy of the rainfall product. As such, a more sophisticated rainfall model that could discriminate the variation of cloud patches and then identify their diverse precipitation characteristics is needed.

Referenced from lumped or distributed hydrological watershed modeling, rainfall estimation approaches could also be clustered into two general categories: lumped and distributed rainfall estimation model. Because the lumped rainfall algorithms are essentially an area-time integral (ATI) approach, the rain estimates from the lumped techniques suffer one common feature: algorithms cannot capture the high variation of precipitating clouds and, therefore, model performance relies on the effects of accumulation to improve accuracy. The GPI, AGPI, and UAGPI fall under lumped

category for they all apply one calibrated IR_{Tb}-RR function to the area of interest. A single function curve for rainfall rate retrieval is appealing but has very limited application because of the variety of physical processes associated with rain generation. Obviously, development of distributed rainfall estimation model is needed to respond the large variability of clouds system over space and time.

Instead of searching for different curves for each sub-region during certain time period, CCS rainfall model is designed as a cloud patch-based distributed rainfall model that groups large number of cloud patches, separated by segmentation procedure, into different clusters by SOFM classifier and then investigates cloud-precipitation function for each cluster with multi-parameter nonlinear function approximation. Each node of SOFM matrix represents a type of clouds that have similar features. The number of distributed sub-models is determined by the arrangement of nodes on SOFM layer. All the nodes in the SOFM layer constitute a synthetic CCS rainfall model that dispatches its best-fitted sub-model (unit) to estimate rain rate for each target cloud patch.

As a result, CCS functions as a cloud patch-based distributed rainfall model because each unit of SOFM layer behaves as an independent rainfall sub-model that constitutes its own cloud-precipitation function (IR_{Tb}-RR) in response to specific cloud type. In Chapter 4, Figure 4.8b and Figure 4.13c demonstrate the high variation of calibrated cloud-precipitation relationship, which clearly prove that clouds with similar temperature but different geometry and texture would result totally different IR_{Tb}-RR. The insights provided by CCS model also prove that various cloud types behave significantly different precipitation characteristics.

6.2.5 Elimination of Universal IR Brightness Temperature Threshold

The implied physical sensible assumption of rainfall estimation using IR brightness temperature is that colder pixel has higher raining probability and gives higher rain rate, and vice verse. This highlights a fundamental limitation of IR threshold technique: all pixels colder than the threshold are labeled as "precipitating", and all those warmer are assigned with no rain. This assumption also indicates that IR brightness temperature threshold is one of the most important parameters for nearly all IR rainfall algorithms.

Screening IR images for precipitating clouds encompasses several problems. Clouds deemed cold enough to produce rain according to an IR_{Tb} threshold may have involved beyond the rain stage (e.g., inactive optical thick cirrus anvils); other clouds not deemed cold enough may be undergoing pre-ice-phase rain microphysics (e.g., orographic warm rain). There is no unique IR temperature threshold to separate no-rain pixel from rain pixel because the IR brightness at long wave channel (10.7*um*) is responding to cloud-top temperature, rather than hydrometeors within clouds. Todd et al. (1995) showed that optimum IR threshold values (calibrated by comparison to rain gauges) over East Africa are highly variable in time and space, as a result of sub-regional rainfall/cloud characteristics. AGPI (Adler et al., 1993) and UAGPI (Xu et al., 1999) also calibrated the thresholds of rain/no-rain in different study domains. Most of the efforts focus on calibrating an optimal IR threshold for a specific region and then apply it to the rest of the periods till update. However, the fundamental weakness of these approaches is the

unpractical assumption that all clouds within a region behave very similar precipitation characteristics over extended periods of time.

In this study, the CCS, a synthetic rainfall model, includes hundreds of sub-models. Each sub-model represents certain type of cloud-precipitation sub-system. Therefore, a large range of variation of IR thresholds could be derived from different sub-model by defining the IR temperature that corresponds to the rain rate 0.1mm/hr as optimum IR threshold. The CCS provides a large variety of IR thresholds suitable for rain/no-rain classification of within various types of cloud patches. Figure 4.8 in Chapter 4 shows the variation of IR thresholds in various cloud types ranged from 250K to 215K. The IR thresholds of majority of cloud types range between 225K-240K, which accounts for the 80% percent of rainfall in this study.

The variation of IR thresholds existing from cloud patch to cloud patch provides compelling evidence for the previous studies such as AGPI (Adler et al., 1993) and UAGPI (XU et al., 1999), which calibrated the optimum IR threshold for regional scale applications. However, CCS illustrates more variability and flexibility since the IR thresholds are derived from a large number of cloud patches instead of from a broad region.

6.2.6 Multi-parameter Nonlinear Mapping of Cloud-Precipitation Relations

Historically, the IR related algorithms include GPI (Arkin et al., 1987), AGPI (Adler et al., 1994), UAGPI (Xu et al., 1999), AE (Vicente et al., 1998), HE (Kuligowski et al., 2002), etc. all of these approaches attempt to model the relation of cloud-

precipitation by regressing the data pairs (IR_{Tb}, RR) with different formulas. GPI, AGPI, and UAGPI belong to the thresholding method that involves two parameters: the rain/no-rain IR threshold and the single rain rate for cloud pixel colder than the threshold. Like a binary function, any pixels colder than the threshold are assigned with the single rain rate, otherwise zero rain rates. Later on, the regressions of linear (Miller et al., 2001) and multiple linear functions (Vicente and Anderson, 1994) were also tested in relevant studies.

From the viewpoint of function regression, the GPI related methods behave like a binary function, which carry less amount of information than simple linear regression. However, all of these regression methods suffer a tendency that underestimates heavy rain rate and overestimates low rain rate primarily because extreme rain rates are outliers to such approaches. Miller et al. (2001) suggested that one possible solution to this problem is to convert the linear regression into a nonlinear function.

Nonlinear approximations are also explored in studies such as AE (Vicente et al., 1998), HE (kuligowski et al., 2002). HE is the improved version of AE and now is operationally producing daily rainfall estimates at National Environmental Satellite Data Information System (NESDIS). The basic formula of AE and HE is based on a calibrated power law function: $R=1.1183 \times 10^{11} \times exp(-0.036382 \times IR)$. The estimates are given by adjusting this basic function with other geophysical data such as soil moisture and precipitable water. In this study, a multi-parameter nonlinear function is used to approximate IR_{Tb}-RR relation for each cloud cluster. The rainfall estimates Z for cloud

patch p is thus computed from the nonlinear equation of the node outputs y_j in SOFM layer, the weights vector v_{kjl} in output layer, and the IR vector of N pixels.

$$z_{kjm} = \sum_{j}^{n_1} y_j . f(v_{kjl}, IR_m) = \sum_{j}^{n_1} y_j \times \{v_{kj1} + v_{kj2} \times \exp[v_{kj3} \times (IR_m + v_{kj4})]^{v_{kj5}}\} \; where \; m = 1,...,N(p)$$

Where j is the winning node in the SOFM layer; k is the counterpart node of i in Nonlinear Output layer and is turned "on" by SOFM "switchboard". The values of the network parameters i.e., connection weights such as w and v, are determined during the training process. This is a distributed multi-parameter nonlinear model that includes n_1 sub-functions (in this study, n_1=400 in fixed CCS model and 1600 in adaptive CCS model, the size of SOFM layer). The suitability of the structure of this distributed model is demonstrated at the Figure 4.7 and Figure 4.16. For the feasible distribution range between cloud-top temperature (180°K~300°K) and corresponding rain rates (0~100mm/hr) at 4x4km grid scale, the approximated functions show a variety of fitting curves that represent the whole practical training data domain. Compared with Figure 4.16b and 4.16c, the advantage of the distributed nonlinear functions approximation is obvious.

6.2.7 Utilization of Multi-sources of Observation Data (Ground and Satellite)

Geostationary IR brightness temperature data provides the basis for most of the satellite-based rainfall estimation algorithms because of its high spatial and temporal resolution, global coverage, as well as easy accessibility. Since the IR data originate in the cloud tops and not in the raindrops beneath, the relation between the IR_{Tb} and the

actual surface rainfall is indirect. Thus, observations from other sources are needed to train and validate IR-related rainfall models.

The CCS model is a satellite-based algorithm developed to estimate precipitation includes the use of high sampling geostationary Infrared, polar-orbiting microwave, and ground-based observations. Ground-based rainfall observations usually play as truth data to calibrate model parameters and validate model performance. For example, the Next Generation Weather Radar (NEXRAD) network, which was deployed between 1991 and 1997, is comprised of over 160 S-band Weather Surveillance Radar-1988 Doppler (WSR-88D) radars across the United States and has become an integral part of U.S. Federal weather services. NEXRAD creates a nearly seamless coverage of the continental U.S. and all of its coastal waters at a smallest spatial resolution of 0.025^{o} grid and a 15-minute temporal resolution, which provides an excellent source of ground-truth observations to calibrate or validate satellite-based precipitation algorithms. To compensate the absence of ground-based observations over extended areas, namely ocean, blocked mountains, or remote regions of the planet, instantaneous rain rate estimates from the Tropical Rainfall Measurement Mission (TRMM) are used to adaptively adjust the CCS network parameters and provide broader coverage of rainfall estimates over long term time periods. The sensor of TRMM Microwave Imager (TMI) directly relate to rain rate because it has the ability to penetrate into the clouds and, hence, the instantaneous rain rate can be derived using radiative transfer models of emission-absorption process within that hydrometeor column.

The author's current GOES IR-NEXRAD-TRMM TMI based product covers the region 10°N-50°N, 65°W-135°W from Feb 2002 to present. The coverage of this product will extend to the region of North American Monsoon Experiment (NAME) over 0°N-55°N, 60°W-135°W from June 2003 to September 2004 at hourly 4 km grid resolution.

6.2.8 The Adaptability of CCS model

The high variation of earth surface condition, climate, geography, and energy flux transportation etc. over time and space necessitates that the proposed CCS rainfall model is capable to adjust model behaviors from new observations such as radars, gauges, microwave rain rate, or meteorological modeling results. The adaptability of CCS would be critical to generalize or localize this model to perform more precisely and sensitively in responses to regional and seasonal variation.

The structure of CCS model enables us to adaptively train the model either by readjusting the approximation function of cloud-precipitation relation or by dynamically adding new SOFM nodes to account for function approximation of new cloud clusters. Chapter 4 is studies of fixed CCS model calibrated over the Southwest of United States (100°-130°N and 25°-45°W) and Chapter 5 implements the adaptability of CCS model to estimate rainfall for extended region of North America Monsoon Experiment (65°-135°N and 10°-50°W) and periods by adaptively adjusting the network parameters with instantaneous rain rate observations from TRMM TMI product 2A12 and ground data from NEXRAD. Validation results show that the accuracy of the rainfall product is

improved and, additionally, the adaptive mode is capable to learn new cloud-precipitation characteristics.

6.2.9 High Resolution of CCS Rainfall Estimates

The CCS was calibrated over the Southwest of United States (100°-130°N and 25°-45°W) first and then adaptively adjusted to the study region of North America Monsoon Experiment (65°-135°N and 10°-50°W) using observations from GOES IR imagery, NEXRAD rainfall network, and TRMM TMI rain rate estimates. CCS functions as a distributed model that first identifies cloud patches and then dispatches different but the best matching cloud-precipitation function for each cloud patch to estimate instantaneous rain rate at high spatial resolution (4km) and full temporal resolution of GOES IR images (every 30-minute).

Evaluated over a range of spatial and temporal scales (from 0.04° x 0.04° hourly to 1.0° x 1.0° daily) for long-term period, the performance of CCS compared favorably with GPI, UAGPI, PERSIANN, and AE algorithms consistently. Particularly, the large number of calibrated nonlinear functions and optimum IR-rain rate thresholds of CCS are highly variable, reflecting the complexity of dominant cloud-precipitation processes from cloud patch to cloud patch over various regions. As a result, CCS can more successfully capture variability in rain rate at small scales than existing algorithms and potentially provides rainfall product from GOES IR-NEXARD-TRMM TMI (SSM/I) at 0.12°x0.12° and 3-hour resolution with relative low standard error (not larger than 3.0mm/hr) and high correlation coefficient (not less than 0.65).

6.3 Recommendation and Future Works

6.3.1 Incorporation of Static and Dynamic Input Features

From any single snapshot of satellite image, one can only derive the current cloud information (called static information). The status of cloud development such as growing or decaying factor (called dynamical information) is also important because cloud exhibits diverse precipitation characteristics at different life stages. For convective clouds, more intensive rainfall precipitates during the growing stage than the decaying period. Propagation of the dynamical information into model could provide extra insight into the cloud-precipitation complex processes. The feasibility to do so requires investigation of consecutive satellite IR images. Therefore, it is doable in the foreseeable future that the dynamic features could be incorporated into the proposed rainfall estimation system.

6.3.2 Incorporation of Earth Surface and Climatic Region Information

6.3.2.1 Orographic Rainfall

Incorporation of Earth's surface information into this model would further refine the classification of precipitating cloud patterns. Besides the convective and stratiform precipitation systems, the orographic rainfall is another major form of rainfall systems. By including the surface environmental information such as elevation and land cover

types into CCS model, orographic rainfall types could be identified and calibrated using the adaptability of the proposed model structure.

6.3.2.2 Regional Climatic Information

Although the cloud behaviors on the scale of cloud patch are important to determine rainfall associated with cloud patches, the weather system at synoptic scales are also critical to infer rainfall of individual clouds. Inclusion of information on regional climatic system would improve the cloud-precipitation relationships.

6.3.3 More Advanced Adaptability of SOFM Network (MTS-SOFM)

6.3.3.1 Static and Dynamic SOFM Structure

The standard SOFM structure is predefined and retains the same during the implementation, i.e. the dimensionality, the number, and the arrangement of neurons are fixed, which renders as **static SOFM**. But if the nature of input data is unknown or may alter, the fixed structure of SOFM could be obstacle to the potential success of the model. A number of adaptive SOFM structures have been introduced in recent years, which dynamically adapt the structure of the network to respond data input space. These so called **dynamic SOFM** are able to dynamically decide upon the number and the structure of the nodes required to classify the input data, thus avoiding the problems of under-classification or over-classification of unknown input data.

Following a first proposal by Koikkalainen & Oja [1990], a dynamic SOFM mode, Tree-Structure SOFM (TS-SOFM), was described in [Koikkalainen, 1994]. TS-SOFM is

a dynamically growing, hierarchically organized network structure where regular SOFM algorithm is used to train the active layer. As shown in Figure 6.1, the TS-SOFM starts with a smaller layer and, once the actual layer is trained, it is fixed to serve as speed-up for the best matching neuron (*bmn*) searching the training of the subsequent layers. Since the TS-SOFM has topological connections between neurons of both the fixed and the adaptive layers, transition of borders given by the decision regions of parent node is easily possible. We developed a Modified TS-SOFM (MTS-SOFM) by coupling the regular SOFM and the TS-SOFM to take advantages of both structures.

6.3.3.2 Modified Tree-Structure SOFM for Adaptation (MTS-SOFM)

The MTS-SOFM is designed for the suitability of our studying problem. Figure 6.2 shows the structure of this model, which consists two components. The first one is a standard SOFM layer at the top. The second part is TS-SOFM, each associated with one parent node from the standard SOFM layer. The SOFM layer maintains the clustering strength and the operational simplicity of self-organizing mapping algorithm while each node behaves as parent to connect/incorporate the children nodes, TS-SOFM, to represent possible new patterns from changing input data. Besides the virtues of SOFM network for adaptation as mentioned in Section 5.2, the advantages of the MTS-SOFM dynamical hierarchical neural networks include:

3. Scalability. Statistical methods that perform lower dimension clustering, generally in 2 dimensions, are only able to cope with data sets of a limited dimensionality

and size. MTS-SOFM is capable to classify much large data sets into space of higher dimensionality-3 dimensions.

4. Inheritance. Natural hierarchies that exist in the input data set may be represented in the tree structure of the network. This multi-dimensional hierarchical classification may be important in some situations for those associated with biological or physical processes.

6.3.4 Incorporation of Correction Factors into Cloud-Precipitation Relations

One of the most important assumptions about rain clouds used in IR-based rainfall algorithms is that clouds with colder top temperature produce more rainfall than those with warmer top. However, indirectness exists between IR cloud-top temperature and surface rain rate. Therefore, correction factors such as moisture factors, structural analyses of the cloud-top temperature distribution on a pixel basis, as well as temporal evolution of the cloud systems using consecutive images, help to locate the precipitation pixel and to correct the pixel rain rate.

6.3.5 Extension the Study to Global Coverage

The current proposed model is applied over the region (10^{o}-50^{o}N and 65^{o}-135^{o}W) at 30 minutes 0.04^{o} x 0.04^{o} lat/long resolution. For application to larger coverage, the large amount of satellite imagery and the possible smallest spatial and temporal resolution necessitate high computation efficiency for a global product.

Two directions are under-considering for the possible model extension to global coverage. The first solution might be to partition the global into several geographical sub-regions by running separate computers or CPUs in parallel to improve the processing speed. The other alterative is the use of separate models for each specific climatic regions of the planet using the strategy of one computer-one model-one climatic region, and the parameters and structure of each model is tuned to suit the specific features of that local climatic region. Global microwave SSM/I and TRMM TMI data will be used to train this model for extended time periods and åreas where ground truth observations are absent. The global application of CCS model will be further explored in the future.

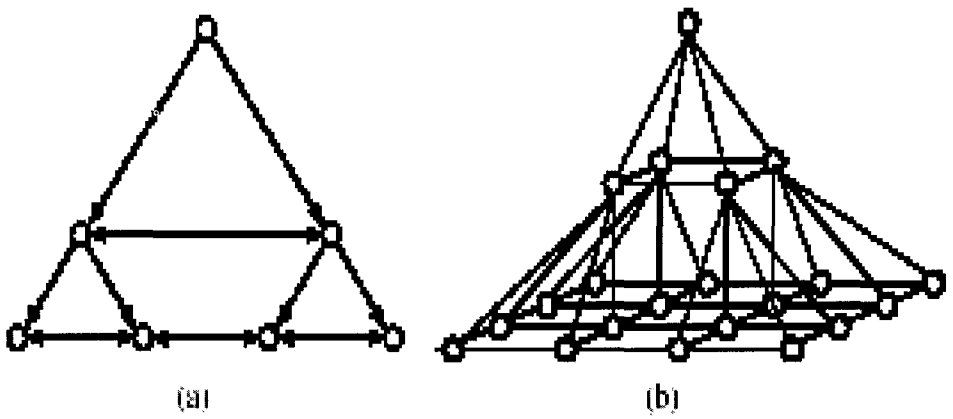

Figure 6.1 The structure of Tree-Structure SOFM: (a) one dimensional TS-SOFM; (b) two dimensional TS-SOFM.

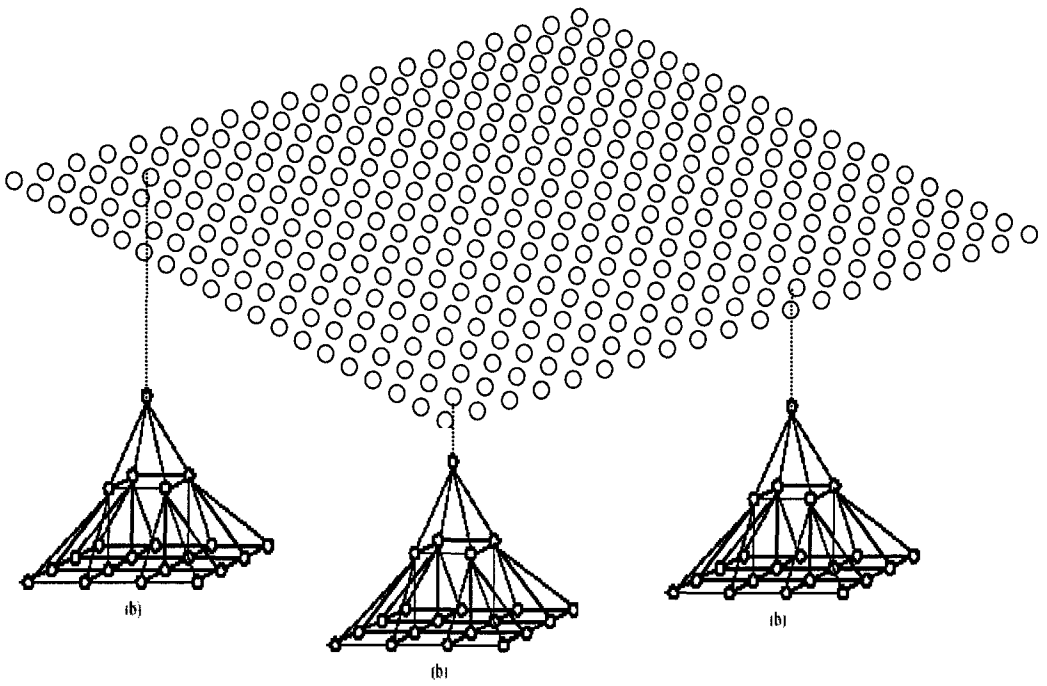

Figure 6.2 The Modified TS-SOFM. Top: a 20x20 SOFM as the basic classification layer; Bottom: 2 dimension TS-SOFM to represent any new cloud patterns from new training domain.

REFERENCES

Adams, R., Bischof, L., 1994: Seeded region growing. *IEEE Trans. Pattern Anal. Machine Intell.* **16(6)**, 641-647.

Adler, R. F. and R. A. Mack, 1984: Thunderstorm cloud height-rainfall rate relations for use with satellite rainfall estimation techniques, *J. Climate Appl. Meteor.*, 23, 280-296.

Adler, R. F. and A. J. Negri, 1988: A satellite infrared technique to estimate tropical convective and stratiform rainfall, *J. Appl. Meteor.*, 27, 30-51.

Adler, R. F., A. J. Negri, P. R. Keehn and I. M. Hakkarinen, 1993: Estimation of monthly rainfall over Japan and surrounding waters from combination of low-orbit microwave and geosynchronous IR data, *J. Appl. Meteor.*, 32, 335-356.

Arkin, P. A., 1979: The relationship between fractional coverage of high cloud and rainfall accumulations during GATE over the B-scale array, *Mon. Wea. Rev.*, 107, 1382-1387.

Arkin, P. A., and B. Meisner, 1987: The relationship between large-scale convective rainfall and cold cloud over the Western Hemisphere during 1982-1984, *Mon. Wea. Rev.*, 115, 51-74.

Arkin, P.A., 1988: Estimating climatic scale tropical precipitation from satellite observations. Tropical Rainfall Measurements, J. Theon and N. Fugono, Eds., A. Deepak, 151-157.

Arkin, P.A. and P. E. Ardanuy, 1989: Estimating climatic-scale precipitation from space: a review. J. Climate, **2**, 1229-1238.

Arkin, P. A. And Xie, P., 1994: The global precipitation climatology project: frist algorithm intercomparison project, *Bulletin of the American Meteorological Society*, 401-419.

Atlas, D., D. Rosenfeld, and D.B. Wolff, 1990: Climatologically tuned reflectivity-rainrate relations and links to area-time integrals. J.Appl. Meteor., **29**, 1120-1135.

Bankert, R. L., 1994: Cloud classification of AVHRR imagery in maritime regions using a probabilistic neural network. *J. Appl. Meteor.*, **33**, 909-918.

Baraldi, A. and F. Parmiggiani, 1995: An investigation of the textural characteristics associated with gray level cooccurrence matrix statistical parameters. *IEEE Trans. on Geoscience And Remote Sensing*, **33**(2), 293-304.

Barret, E. C., 1970: The estimation of monthly rainfall from satellite data. *Mon. Wea. Rev.*, **98**, 322-327.

Barrett, E. C. and D. W. Martin, 1981: The Use of Satellite Data in Rainfall Monitoring, Academic Press.

Barrett, E.C., G. D'Souza, and C. H. Power, 1986: Bristol techniques for the use of satellite data in rain cloud and rainfall monitoring, *Journal of British Interplanet Society*, 39, 517-526.

Barrett, E.C., G. D'Souza, C. H. Power, and C. Kidd, 1988: Toward trispectral satellite rainfall monitoring algorithms. Tropical Rainfall Measurements, J. Theon and N. Fugono, Eds., A. Deepak, 285-292.

Barrett, E. C. and C. Kidd, J. O. Bailey, and G. C. Collier, 1990: The great storm of 15/16 October 1987: passive microwave evaluations of associated rainfall and marine wind speeds, *The Meteorological Magazine*, 119, 177-187.

Battiti, B., 1992: First and second order methods for learning: between steepest descent and Newton's method, *Neural Computation*, 4(2), 141-166.

Beaulieu, J. and M. Goldberg, 1989: hierarchy in pictures segmentation: A stepwise optimization approach. *IEEE trans. on pattern Analysis and Machine Intelligence,* 11(2), 781-784.

Bellon, A., A. Kilambi, G. L. Austin, and M. R. Duncan, 1992: A satellite and radar rainfall observational and forecasting system, *Preprint Vol., AMS 6th Conference on Satellite Meteorology and Oceanography*, Atlanta, Georgia, J110-J116.

Bellerby, T, J. and E. C. Barrett, 1993: A strategy for the calibration by collateral data of satellite rainfall estimates for shorter periods. *J. Appl. Meteor.*, **32**, 1365-1378.

Bellerby, T, J., M. Todd, D. Kniveton, and C. Kidd, 2000: Rainfall estimation from a combination of TRMM precipitation radar and GOES multispectral satellite imagery through the use of an artificial neural network. *J. Appl. Meteor.*, **39**, 2115-2128.

Bhat, N. V., P. A. Minderman, T. McAvoy, and N. S. Wang, 1990: Modeling chemical process systems via neural computation, *IEEE Control Systems Magazine*, 80, 24-30.

Blum, E.K. and L.K. Li, 1991: Approximation theory and feedforward networks, *Neural Networks*, 4, 511-515.

Bourbakis, N. G., 1995: Knowledge extraction and acquisition during real-time navigation in unknown environments. *International J. Pattern Recognition and Artificial Intelligence*, **9**(1), 83-99.

Bow, S. T., 1992: Pattern recognition and image preprocessing. Marcel Dekker, Inc., New York.

Chen, D. W., S. K. Sengupta, and R. M. Welch, 1989: Cloud field classification based upon high spatial resolution textural features 2: simplified vector approaches. *J. Geophys. Res.*, **94**, 14,749-14,765.

Cheng, H. D., and X. Cheng, 1995: Shape recognition using a fixed-size VILI architecture. *International J. Pattern Recognition and Artificial Intelligence*, **9**(1), 1-21.

Chang, A.T.C. and L. Tsang, 1992: A neural network approach to inversion of snow water equivalent from passive microwave measurements, *Nordic Hydrology*, 23, 173-182.

Charalambous, C., 1992: Conjugate gradient algorithm for efficient training of artificial neural networks, *IEE Proceedings*, vol. 139, no. 3.

Chen, F.C. and H. K. Khalil, 1995: Adaptive control of a class of nonlinear discrete-time systems using neural networks, *IEEE Trans. on Automatic Control*, Vol. 40(5), 791-801.

Croall, I. and J. P. Mason, 1991: Industrial application of neural networks, Springer-Verlag, New York.

Duan, Q., 1991: A global optimization strategy for efficient and effective calibration of hydrologic models. Ph.D dissertation, The University of Arizona, Tucson, AZ.

Duan, Q., S. Sorooshian, and V. K. Gupta, 1992: Effective and efficient global optimization for conceptual rainfall runoff models. *Water Resour. Res.*, **28(4)**, 1015-1031.

Duan, Q., V. K. Gupta, and S. Sorooshian, 1993: A shuffle complex evolution approach for effective and efficient global minimization. *J. Optimi. Theory*, **73(3)**, 501-521.

Daunucht, W., DEFAnet-a deterministic neural network concelt for function approximation, *Neural Networks*, 4, 839-845, 1991.

Dayhoff, J.E., 1990: Neural Network Architectures: An Introduction, Van Nostrand Reinhold.

Digabel, H. and Lantuejoul, C., "iterative algorithms:, in Proc. 2nd European Symp.

Quantitative Analysis of Microstructure in Material Science, Biology and Medicine, Caen, France, Oct., 1997, J.L. Chermant, Ed. Stuttgart, West Germany: Riederer Verlag, 1978, pp. 85-90.

Ebert, E., 1987: A pattern recognition technique for distinguishing surface and cloud types in the polar regions. *J. Climate Appl. Meteor.*, **26**, 1412- 1427.

Ebert, E. E., M. J. Manton, P. A. Arkin, R. J. Allam, G. E. Holpin, and Arnold Gruber, 1995: Results from the GPCP Algorithm Intercomparison Programme. *Bull. Amer. Meteor. Soc.*, **77**, 2875-2886.

Ebert, E.E., 1996: Results of the 3rd Algorithm IntercomparisonProject (AIP-3) of the Global Precipitation Climatology Project (GPCP). *Bureau of Meteorology Centre, Report N° 55*, Melbourne, Australia.

French, M.N., W.F. Krajewski, and R.R. Cuykendall, 1992: Rainfall forecasting in space and time using a neural network, *Journal of Hydrology*, 137, 1-31.

Funahashi, K.I., 1989: On the approximation realization of continuous mappings by neural networks, *Neural Networks*, 2, 183-192.

Fayyad, U. M., 1991: On the induction of decision trees for multiple concept learning. Ph.D Dissertation, The University of Michigan.

Fu, K.S. and J.K. Mei, 1981: A survey on image segmentation. *Pattern Recognition*, **13**, 3-16.

Gallant, A.R. and H. White, 1992: On learning the derivatives of an unknown mapping with multi-layer feedforward networks, *Neural Networks*, 5, 129-138.

Garand, L., 1988: Automatic recognition of oceanic cloud pattern. Part I: methodology and application to cloud climatology. *J. Climate*, **1**, 20-39.

Gilberto A.V. et, 1998: The operational GOES infrared rainfall estimation technique. Bulletin of the American Meteorological Society, Vol.79, No.9

Gong, G., D. Entekhabi, and G. D. Salvucci, 1994: Regional and seasonal estimates of fractional storm coverage based on station precipitation observations. *J. Climate*, **7**, 1495-1505.

Grassotti, C. and L. Garand, 1994: Classification-based rainfall estimation using satellite data and numerical forecast model fields. *J. Appl. Meteor.*, **33**, 159-178.

Graves, C. E., J. B. Valdes, S. S. Shen, and G. R. North, 1993: Evaluation of sampling errors of precipitation from spaceborne and ground sensors. *J. Appl. Meteor.*, **32** 374-385.

Griffith, C. G., W. L. Woodley, P. G. Grube, D. W. Martin, J. Stout., and D. N. Sikdar, 1978: Rain estimation from geosynchronous satellite imagery—visible and infrared studies. *Mon. Wea. Rev.*, **106**, 1153-1171.

Griffith, C. G., 1987: Comparisons of gauge and satellite rain estimates for the central United States during August 1979. *J. Geophys. Res.*, **92**, 9551-9566.

Griffith, C. G., J. A. Augustine, and W. L. Woodley, 1981: Satellite rain estimation in the U.S. high plains. *J. of Appl. Meteor.*, **15**, 972-975.

Grossberg, S., 1969: Embeding fields: A theory of learning with physiological implications, *J. of Math. Psych.*, 6, pp209-239.

Grossberg, S., 1971: Embedding fields: underlying philosophy, mathematics, and applications to psychology, anatomy, *J. Cyber.*, 1(1), pp28-50.

Haralick, R. M., K. Shanmuban, and Its'hak Dinstein, 1973: Texture features for image classification. *IEEE Trans. on System, Man, and Cybernetics*, SMC-3, No. **6**, 610-621.

Haris, K, 1998: Hybrid image segmentation using watersheds and fast region growing. *IEEE Trans. Pattern Anal. Machine Intell. 7(12).*

Hayden, C. M., and G. S. Wade, 1996: Derived Product imagery from GOES-8. *J. Appl. Meteor.*, **35**, 153-162.

Haykin, S., 1994: Neural Networks: A Comprehensive Foundation, New York, Macmillan College Publishing Company.

Hecht-Nielsen, R., 1987a: Komogorov's mapping neural network existence theorem, *Proceedings of the International Conference on Neural Networks*, 3, 11-13, IEEE Press, New York.

Hecht-Nielsen, R., 1987b: Counterpropagation networks, *Proceedings of the International Conference on Neural Networks*, 2, 19-32, IEEE Press, New York.

Hecht-Nielsen, R., 1988: Applications of counterpropagation networks, *Neural Networks*, 1, 131-139.

Hecht-Nielsen, R., 1990: Neurocomputing, Addison-Wesley, Inc.

Hertz, J., A. Krogh, and R. G. Palmer, 1991: Introduction to the Theory of Neural Computation, Reading, MA: Addison-Wesley.

Holton, J. R., 1992: An Introduction To Dynamic Meteorology. *Academic Press, Inc.*, New York.

Ho, S.Y. and K.Z. Lee, 2001: An efficient evolutionary image segmentation algorithm. *Pattern Recognition* 24, 1327-1334.

Hong, Y., Hsu, k., Gao, X., Sorooshian, S., 2003, *"A Cloud-patch Distributed High Resolution Precipitation Estimation System using Combined Satellite Infrared, Passive Microwave, and Ground Radar", in manuscript*

Hong, Y., Hsu, k., Gao, X., Sorooshian, S., 2003, *"A Combined Passive Microwave and IR Algorithm using Cloud Classification System for Estimation of Precipitation", submitted to Journal of Hydrometeorology*

Hong,Y., Hsu, K., Gao, X., Sorooshian, S., 2003,*" Precipitation Estimation from Remotely Sensed Imagery Using Artificial Neural Network-Cloud Classification System"*, submitted to Journal of Applied Meteorology.

Hong, Y., Hsu, K., Gao, X., Sorooshian, S., 2003, "*A Cloud Patch-based MW/IR Rainfall Estimation Algorithm*", in Proceedings of 30th International Symposium on Remote Sensing of Environment, Honolulu, Hawaii.

Hong, Y., Hsu, K., Gao, X., Sorooshian, S., 2001, *"Diurnal Variability of Tropical Rainfall Retrieved from Combined GOES and TRMM Satellite Information", Eos Trans. AGU, 82(47), Spring Meet. Suppl., Abstract B51A-17.(published in J. Climate,**15(9)**,983-1001)*

Hong, Y., Hsu,K., Gao, X., Sorooshian, S., 2002: "Toward High-quality Precipitation Estimation: Correlating Satellite Precipitation Features with MM5 Simulation of Cloud Microphysics: A Case Study of Flash Flood in Las Vegas". *Eos Trans. AGU*, 83(19), *Spring Meet. Suppl., Abstract H22A-22.*

Hong, Y., Mahani, S., Li, J., Gao, X., Hsu, K., and Sorooshian, S., 2002: Precipitation Estimation from Satellite Cloud Infrared Imagery., *Proceeding Of* National Science foundation SAHRA 2nd Annual meeting, S14.

Hopfield, J.J., 1982: Neural networks and physical systems with emergent collective computational abilities, *Proceedings of National Acaddemy of Science*, USA, 79, 2554-2558.

Hornik, K., M. Stinchcombe, and H. White, 1990: Universal approximation of an unknown mapping and its derivatives using multi-layer feedforward networks, *Neural Networks*, 3, 551-560.

Houze, R. A., 1993: Cloud dynamics. Academic Press, Inc., New York.

Hsu, K., 1996: Rainfall estimation from satellite infrared imagery using artificial neural networks. Ph.D Dissertation, The University of Arizona, Tucson, AZ.

Hsu, K., S. Sorooshian, V. K. Gupta, and X. Gao, 1994a: Application of artificial neural network models in rain rate retrieval from satellite passive microwave imagery, Presented at AGU Spring Meeting, Baltimore, Maryland, May 23-27, 1994, published by *American Geophysical Union in EOS Abstract Supplement*, p.91.

Hsu, K., S. Sorooshian, V. K. Gupta, and X. Gao, 1994b: Application of artificial neural network models in rain rate retrieval from satellite passive microwave imagery, Presented at the Western Pacific Geophysics Meeting, Hongkong, July 25-29, 1994, Published by *American Geophysical Union in EOS Abstract Supplement*, p.31, June 21.

Hsu, K., Monthly rainfall estimation using satellite infrared imagery, Presented at the 5th Annual Hydrology Research Exposition, "EL Dia Del Agua," March 22, 1995, Published by the *Department of Hydrology and Water Resources*, The University of Arizona, March 1995a.

Hsu, K., X. Gao, and S. Sorooshian, Monthly rainfall estimation using satellite infrared imagery, Presented at AGU Spring Meeting, Baltimore, Maryland, May 30-June 2, 1995, Published by *American Geophysical Union in EOS Abstract Supplement*, p.S108, 1995b.

Hsu, K., H. V. Gupta, and S. Sorooshian, 1995: Artificial neural network modeling of the rainfall-runoff process, *Water Resources Research*, 31(10), 2517-2530.

Hsu, K., H. V. Gupta, and S. Sorooshian, A superior training strategy for 3-layer feedforward artificial neural networks, Technical Report, HWR No.96-030, Published by *Department of Hydrology and Water Resources*, University of Arizona, March, 1996.

Hsu, K., X. Gao, S. Sorooshian, and H. V. Gupta, 1997: Precipitation Estimation from Remotely Sensed Information using Artificial Neural Networks, *J. Appl. Meteorol.*, **36**, 1176-1190.

Hsu, K., H. V. Gupta, X. Gao, and S. Sorooshian, 1999: Estimation of physical variables from multichannel remotely sensed imagery using a neural network: Application to rainfall estimation, *Water Resour. Res., 35(5)*, 1605-1618.

Hsu, K., H. V. Gupta, X. Gao, S. Sorooshian, and B. Iman, 2002: Self-organizing linear output (SONO): An artificial neural network suitable for hydrologic modeling and analysis, *Water Resour. Res., 38(12)*, 1302-1318.

Huffman, G.J., R.F. Adler, B.Rudolf, U. Schneider, and P.R. Keehn, 1995: Global precipitation estimates based on a technique for combining satellite-based estimate, rain gauge analysis, and NWP model precipitation information. J. Climate, **8,** 1284-1295.

Huffman, G.J., Adler, R.F. et al., 2001: *Global Precipitation at One-Degree Daily Resolution from Multisatellite Observations.* J. Hydrometeorology, vol. 2, 36-50.

Huffman, G., R. Adler, M. Morrissey, D. Bolvin, S. Curtis, R. Joyce, B. McGavock, and J. Susskind, 2001: Global precipitation at one-degree daily resolution from multisatellite observations. Journal of Hydrometeorology. **2**. 36-50.

Ito, Y., 1992: Approximation of continuous functions on $\mathbf{R}^n$ by linear combinations of shifted rotations of a sigmoid function without scaling, *Neural Networks*, 5, 105-115.

Jacobs, R. A., 1988: Increase rates of convergence through learning rate adaption, *Neural Networks*, 1, 295-307.

Johnston, P.R. and D. Pilgrim, 1976: Parameter optimization for watershed models, *Water Resources Research*, Vol. **12(3)**, 477-48.

Kang, K.W., C.Y. Park, and J.H. Kim, 1993: Neural network and its application to rainfall-runoff forecasting, *Korean Journal of Hydrosciences*, 4, 1-9.

Kidder, S. Q. and T. V. Haar, 1995: Satellite Meteorology: An introduction. Academic Press, New York.

Kohonen, T., 1982: Self-organized formation of topologically correct feature maps, *Biol. Cybern.*, 43, 59-69.

Kohonen, T., 1984: Self-organization and associative memory, Springer-Verlag, Berlin.

Kolmogorov, A.N., 1957: On the representation of continuous functions of several variables by superposition of continuous functions of one variables and addition, *Dokl. Akad. Nauk. SSSR*, 114, 369-373.

Kosko, B., 1992: Neural networks for signal processing, Prentice-Hall, New Jersey.

Kuligowski, R.J., 2002: A self-calibrating real-time GOES rainfall algorithm for short-term rainfall estimates. Journal of Hydrometeorology, **3**, 112-130.

Kummerow, C. and L. Giglio, 1995: A method for combining passive microwave and infrared eainfall observations. J. Atmos. Oceanic Technol. **12**, 33-45.

Kummerow, C., W. Barnes, T. Kozu, J. Shiue, and J. Simpson, 1998: The Tropical Rainfall Measuring Mission (TRMM) sensor package. *J. Atmos. Oceanic Technol.*, **15**, 809-817.

Kummerow, C., Simpson, J., Thiele, O., Barnes, W., Chang, A. T. C., Stocker, E., Adler, R. F., Hou, A., Kakar, R., Wentz, F., Ashcroft, P., Kozu, T., Hong, Y., Okamoto, K., Iguchi, T., Kuroiwa, H., Im, E., Haddad, Z., Huffman, G., Ferrier, B., Olson, W. S., Zipser, E., Smith, E. A., Wilheit, T. T., North, G., Krishnamurti, T., Nakamura, K. 2000: The Status of the Tropical Rainfall Measuring Mission (TRMM) after Two Years in Orbit. *Journal of Applied Meteorology*: Vol. 39, No. 12, pp. 1965–1982.

Kummerow, Christian, Hong, Y., Olson, W. S., Yang, S., Adler, R. F., McCollum, J., Ferraro, R., Petty, G., Shin, D.-B., Wilheit, T. T.. 2001: The Evolution of the Goddard Profiling Algorithm (GPROF) for Rainfall Estimation from Passive Microwave Sensors. *Journal of Applied Meteorology*: Vol. 40, No. 11, pp. 1801–1820.

Lagarias, J.C., J. A. Reeds, M. H. Wright, and P. E. Wright, "Convergence Properties of the Nelder-Mead Simplex Method in Low Dimensions," SIAM Journal of Optimization, Vol. 9 Number 1, pp. 112-147, 1998.

Lee, T. H., J. E. Janowiak, and P. A. Arkin, 1991: Atlas of products from the algorithm intercomparison project 1: Japan and surrounding oceanic regions June-August 1989, University Corporation for Atmospheric Research, Boulder, Colorado.

Leese, J. L., C. S. Novak, and B. B. Clark, 1971: An automated technique for obtaining cloud motion from geosynchronous satellite data using cross correlation. *J. Appl. Meteor.*, **10**, 118-132.

Lin, J. H. and J. S. Vitter, 1991: Complexity results on learning by neural nets. *Machine*

Learning, **6**, 211-230.

Lippmann, R. P., 1987: An introduction to computation with neural nets, *IEEE ASSP Magazine*.

Lovejoy, S. and G. L. Austin, 1979: The source of error in rain amount estimating schemes from GOES visible and IR satellite data. *Mon. Wea. Rev.,* 107, 1048-1054.

Lorentz, G. G., 1976: The 13-th problem of Hilbert, *Proc. of Symposia in Pure Math.*, 28, 419-430, Am. Math. Soc.

Lovejoy, S. and G. L. Austin, The delineation of rain areas from visible and IR satellite data for GATE and mid-latitudes, *Atmosphere-Ocean*, 17, pp77-92, 1979.

Lovell, B. C. and A. P. Bradley, 1996: The multiscale classifier. *IEEE Trans. on Pattern anal. And Machine Intelligence*, **18**(2), 124-136.

Manobianco, J., S. Koch, V.M. Karyampudi, and A.J. Negri, 1994: The impacts of assimilating satellite-derived precipitation rates on numerical simulations of the ERICA IOP 4 cyclone. Mon. Wea. Rev., **122**, 341-365.

Maddox, R. A., 1980: Mesoscale convective complexes. *Bull. Amer. Meteor. Soc.*, **61**(11), 1374-1387.

Maddox, Robert A., Zhang, Jian, Gourley, Jonathan J., Howard, Kenneth W. 2002: Weather Radar Coverage over the Contiguous United States. *Weather and Forecasting*: Vol. 17, No. 4, pp. 927–934.

Mathur, M. B., H. S. Bedi, T. N. Krishnamurti, M. Kanamitsu, and J. S. Woollen, 1992: Use of satellite-derived rainfall for improving tropical forecasts. *Mon. Wea. Rev.,* **120**, 2340-2560.

Miller, S.W., Arkin, P.A., and Joyce, R., 2001: A combined microwave/infrared rain rate algorithm. INT. J. Remote Sensing, Vol 22, No. 17, 3285-3307.

Moghaddamzadeh, A. and N. Bourbakis, 1997: A fuzzy region growing approach for segmentation of color images. Pattern recognition, **30(6)**, 867-881.

Morrissey, M. L. and J. S. Greene, 1993: Comparison of two satellite-based rainfall algorithms using pacific atoll raingage data. *J. Appl. Meteor.*, **32**, 411-425.

Motell, C. E. and B. C. Weare, 1987: Estimating tropical pacific rainfall using digital satellite data, *J. Climate and Applied Meteorology*, 26, 1436-1446.

Negri, A. J. and R. F. Adler, 1981: Relation of satellite-based thunderstorm intensity to radar-estimated rainfall. *J. Appl. Meteor.*, **20**, 288-300.

Negri, A. J., R. F. Adler, and P. J. Wetzel, 1984: Rain estimation from satellites: An examination of Griffith-Woodley Technique, *J. of Climate. Appl. Meteor.*, 23, pp102-116.

Negri, A. J., and R. F. Adler, 1987: Infrared and visible satellite rain estimation. part I: a grid cell approach. *J. Climate Appl. Meteor.*, **26**, 1553-1564.

Negri, A. J., and R. F. Adler, 1987: Infrared and visible satellite rain estimation. part II: a cloud definition approach. *J. Climate Appl. Meteor.*, **26**, 1565-1576.

Negri, A. J., R. F. Adler, 1993: An intercomparison of three satellite infrared rainfall techniques over Japan and surrounding waters, *J. of Applied Metroro.*, 32, 357-373.

Pal, N.R. and S.K. Pal, 1993: A review of image segmentation techniques. *Pattern Recognition.* **26(9)**, 1277-1294.

Paola, J. D. and R, A, Schowengerdt, 1995: A detail comparison of Backpropagation neural network and maximum-likelihood classifiers for urban use classification, *IEEE Trans. on Geoscience and Remote Sensing*, 33(4), 981-996.

Parker, D. B., 1987: Optimal algorithms for adaptive networks: second-order backpropagation, second-order direct propagation, and second order Hebbian learning, *Proc. 1st Int. Conf. Neural Networks*, vol. 2, 593-600.

Patrick, W. S., W. D. Hogg, and P. A. Arkin, 1995: The role of visible data in improving satellite rain-rate estimation. *J. Appl. Meteor.*, **34**, 1608-1621.

Peak, J.E., P.M., Tag, 1994: Segmentation of satellite Imagery using hierarchical thresholding and neural networks. Journal of Applied meteorology. **33**, 605-616.

Penn, B. S., A. J. Gordon, and R. F. Wendlandt, 1993: Using neural networks to locate edges and linear features in satellite images. *Computer and Geosciences*, **19**(10), 1545-1565.

Petty, G. W., 1995: The status of satellite-based rainfall estimation over land. *Remote Sens. Environ.*, **51**, 125-137.

Plank, V. G., D. Atlas, and W. H. Paulsen, 1955: The nature and detectability of cloud and precipitation as determined by 1.25 cm radar, *J. Meteorol.*, 12, 358-378.

Qing-Yun, S. and K. S. Fu 1983: A method for the design of binary tree classifiers. *Pattern Recognition*, **16:6**, 593-603.

Quinlan, J. R., 1986: Induction of decision tree. *Machine Learning*, **1**, 81-106.

Quinlan, J. R., 1987: Simplifying decision tree. *International Journal of Man-Machine Studies*, **27**, 221-234.

Quinlan, J. R., and R. L. Rivest, 1989: Inferring decision tree using the minimum description length principle. *Information and Computation*, **80**, 227-248.

Quinlan, J. R., 1990: Learning logical definitions from relations. *Machine Learning*, **5:3**, 239-266.

Quinlan, J. R., 1990: Decision tree and decision making. *IEEE Trans. on Systems, Man, and Cybernetics*, **20**, 2, 339-346.

Quinlan, J. R., 1993: C4.5: Programs for Machine Learning. Morgan Kaufmann Publisher, San Mateo, California.

Richards, F. and P. Arkin, 1981: On the relationship between satellite-observed cloud cover and precipitation. *Mon. Wea. Rev.*, **109**, 1081-1093.

Rodgers, E. B. and H. F. Pierce, 1995: A satellite observational study of precipitation characteristics in western north pacific tropical cyclones. *J. Appl. Meteor.*, **34**, 2587-2599.

Rumelhart, D.E., E. Hinton, and J. Williams, 1986: Learning internal representation by error propagation, in Parallel Distributed Processing, Vol. 1, 318-362, Massachusetts Institute of Technology Press, Cambridge, Massachusetts.

Scalero, R.S. and N. Tepedelenlioglu, 1992: A fast new algorithm for training feedforward neural networks, *IEEE Transactions on Signal Processing*, 40(1), 202-210.

Scofield, R. A. and Oliver, V. J. , 1977: A scheme for estimating convective rainfall from satellite imagery, NOAA Tech. Mem., NESS, 86, Washington, D. C..

Scofield, R. A., The NESDIS operational convective precipitation technique, *Monthly Weather Review*, 115:1773-1792, 1987.

Serpico, S. B. And F. Roli, 1995: Classification of multisensor remote sensing images by structured neural networks, *IEEE Trans. on Geoscience and Remote Sensing*, 33(3), 562-578.

Shaw, K.B., and M.C. Lohrenz, 1992: A survey of digital image segmentation algorithms. NOARL Report 32, 21pp. [Available from Naval research Laboratory. Stennis Space Center, MS 39529-5004]

Sinclair, M. R., 1994: A diagnostic model for estimating orographic precipitation. *J. Appl. Meteor.*, **33**, 1163-1175.

Singh, V.P., editor, 1995: Computer Models of Watershed Hydrology, ISBN 0-918334-91-8.

Sofield, R. A., 1987: The NESDIS operational convective precipitation estimation technique. *Mon. Wea. Rev.*, **115**, 1773-1792.

Sorooshian, S., K. Hsu, X. Gao, H.V. Gupta, B. Iman, and D. Braithwaite, 2000: Evolution of PERSIANN system satellite-based estimates of tropical rainfall, *Bul. Am. Meteorol. Soc.*, 81(9), 2035-2046.

Sorooshian, S., Gao, X., Hsu, K., Maddox, R. A., Hong, Y., Gupta, H. V., Imam, B. 2002: Diurnal Variability of Tropical Rainfall Retrieved from Combined GOES and TRMM Satellite Information. *Journal of Climate*: Vol. 15, No. 9, pp. 983–1001.

Spillane, K. T. and Yamaguchi, 1962: Mechanisms of rain producing system systems in sourthern Australia, *Meteorolo. Mag.*, 39, 1-19.

Sprecher, D.A., 1965: On the structure of continuous functions of several variables, *Transactions of American Mathematical Society*, 115, 340-355.

Stevevs, C. F., *The neuron, Scentific American, 241, 54-65.*

Stout, J. E., D. W. Martin and D. N. Sikdar, 1979: Estimating GATE rainfall with geosynchronous satellite images. *Mon. Wea. Rev.*, **107**, 585-598.

Styblinski, M. A. and T. S. Tang, 1990: Experiments in nonconvex optimization: stochastic approximation with function smoothing and simulated annealing., *Neural Networks*, vol. 3, 467-483.

Sumner, Graham, 1988: Precipitation Process and Analysis. John Wiley & Sons Ltd. Press.

Takahashi, Y., 1993: Generalization and approximation capabilities of multi-layer networks, *Neural Computation*, 5, 132-139.

Thoma and Wyner, Neurocontrol, Springer-Verlag, New York, 1992.

Todd, M. C., E. C. Barrett, and M. J. Beaumont, 1995: Satellite identification of rain days over upper Nile River basin using an optimum infrared rain/no-rain threshold temperature model. *J. Appl. Meteor.*, **34**, 2600-2611.

Todd, M.C., Kidd, Chris et al., 2001: *A Combined Satellite Infrared and Passive Microwave Technique for Estimation of Small-Scale Rainfall.* Journal of Atmospheric and Oceanic Technology, Vol. 18, p742-755

Tollenaere, T., SuperSAB, 1990: fast adaptive back propagation with good scaling properties, *Neural Networks*, 3, 561-573.

Ueda, N. and K. Mase, 1995: Tracking moving contours using energy-minimizing elastic contour models. *International J. Pattern Recognition and Artificial Intelligence*, **9**(3), 465-484.

Vemuri, V.R. and R.D. Rogers (editors), 1994: Artificial neural networks: forecasting time series, IEEE Computer Society Press, Los Alamitos, California.

Vicente, G.A., and J.R. Anderson, 1994: A new rain retrivel technique that combines geosynchronous IR and MW polar orbit data for hourly rainfall estimates. Preprints, Seventh Conf. On Satellite Meteorology and Oceanography, Monterey, CA, Amer. Meteo, Soc., 34-37.

Vicente, G.A., R. A. Scofield, and W.P. Menzel, 1998: The Operational GOES Infrared Rainfall Estimation Technique., *Bul. Am. Meteorol. Soc.* 79(9), 1883–1898.

Vogl, T.P., J.K. Mangis, A.K. Rigler, W.K. Zink, and D.L. Alkon, 1988: Accelerating the convergence of back-propagation method, *Biol. Cybern.*, 59, 257-263.

Wallace, J. M. and P. V. Hobbs, 1977: Atmospheric Science: An Introductory Survey. Academic Press, New York.

Wang, Z, A. Guerriero, and M. De Sario, 1996: Comparison of several approaches for the segmentation of texture images. *Pattern Recognition Letters*, 17, 509-521.

Welch, R. M., K. S. Kuo, B. A. Wielicki, S. K. Sengupta, and L. Parker, 1988: Marine stratocumulus cloud fields off the coast of southern California observed using Landsat imagery, I, structural characteristics. *J. Appl. Meteor.*, **27**, 341-362.

Welch, R. M., S. K. Sengupta, and K. S. Kuo, 1988: Marine stratocumulus cloud fielsds off

the coast of southern California observed using Landsat imagery, II textural analysis. *J. Appl. Meteor.*, **27**, 363-378.

Welch, R. M., M. S. Navar, and S. K. Sengupta, 1989: The effect of spatial resolution upon textural-based cloud field classifications. *J. Geophys. Res.*, **94**, 14,767-14,781.

Weszka, J. S., C. R. Dyer, and A. Rosenfeld, 1976: A comparative study of texture measures for terrain classification. *IEEE Trans. On System, Man, and Cybernetics*, SMC-3, No. **4**, 269-285

White, H., 1990: Connectionist nonparametric regression: multi-layer feedforward networks can learn arbitrary mappings, *Neural Networks*, 3, 535-549.

Widow, B. And Hoff, M. E., 1960: Adaptive switching circuits, 1960 IREWESCON Convention Record, pp96-104, New York.

Woodley, W. L., C. G. Griffith, J. S. Griffin, and S. C. Stroomatt, 1980: The inference of GATE convective rainfall from SMS-1 imagery. *J. Appl. Meteor.*, **19**, 338-408.

Wu, R., J. A. Weinman, and R. T. Chin, 1985: Determination of rainfall rates from GOES satellite images by a pattern recognition technique. *J. Atmos. Oceanic Tech.*, **2**, 314-330.

Xie, P., and P. A. Arkin, 1996: Analyses of global monthly precipitation using gauge observations, satellite estimates, and model predictions, *J. Climate.*, **9**, 840-858.

Xu, L., 1997: Estimating rainfall from satellite infrared imagery: Cloud Patch analysis. Ph.D. Dissertation, The University of Arizona, 198 pp.. [Available from Main Library, University of Arizona, Tucson, AZ, 85721]

Xu, L., X. Gao, Sorooshian S., P.A. Arkin, and B. Imam, 1999: A microwave Infrared Threshold Technique to Improve the GOES Precipitation Index. *J. Appl. Meteor.*, 38,569-579.

Yoshihisa, H., R. G. Atkins, R. T. Shin, J. A. Kong, S. H. Yueh, and R. Kwok, 1995: Application of neural networks for sea ice classification in Polarimetric SAR images, *IEEE Trans. on Geoscience and Remote Sensing*, 33(3), 740-748.

Zhang, M., Fulcher, J., and Scofield, R.A., 1997: Rainfall estimation using artificial neural network group, *Neurocomputing*, **16**, 97-115.

Zhang, Y.J., 1997: Evaluation and comparison of different segmentation algorithms. *Pattern recognition Letters*, **18**, 963-974.